

Autonomous Rock Science Analysis System For Planetary Exploration



Lilan Pan

Department of Computer Science

Aberystwyth University

Thesis submitted for the degree of

Doctor of Philosophy

January 2016

Declaration and Statement

DECLARATION

This work has not previously been accepted in substance for any degree and is not being concurrently submitted in candidature for any degree.

Signed *Lilan Pan* (candidate)

Date 2016/1/14

STATEMENT 1

This thesis is the result of my own investigations, except where otherwise stated. Where **correction services**¹ have been used, the extent and nature of the correction is clearly marked in a footnote(s).

Other sources are acknowledged by footnotes giving explicit references. A bibliography is appended.

Signed *Lilan Pan* (candidate)

Date 2016/1/14

STATEMENT 2

I hereby give consent for my thesis, if accepted, to be available for photocopying and for inter-library loan, and for the title and summary to be made available to outside organisations.

Signed *Lilan Pan* (candidate)

Date 2016/1/14

¹This refers to the extent to which the text has been corrected by others.

Abstract

A major mission driver for space exploration is to minimise ground-based human intervention and hence associated operations costs, thereby maximising science data return. Future robotic exploration such as the ESA ExoMars mission will require rovers to be equipped with greater autonomy.

In line with such a requirement, a new autonomous system named *Autonomous Rock Science Analysis System* (ARSAS) is proposed in this thesis for the purpose of identifying and accessing scientific rocks during exploration. ARSAS consists of three components: rock detection, rock science value evaluation and related executive agent.

Three approaches are presented in the rock detection component. A number of image processing and machine learning techniques have been employed, including multispectral sampling, fuzzy-rough feature selection, classification, clustering, thresholding and saliency methods.

The rock science evaluation component is primed by a human planetary geology expert. Some visual features are selected as the indicators of some geological attributes and then a fuzzy expert system is used to convert the rock attributes to corresponding science value. In contrast with previous works, the proposed science evaluation mechanism is more autonomous and geology-oriented.

The executive agent mainly consists of a pair of cameras and a robotic arm, together with a series of algorithms for coordinate transformation. It serves as a platform to support the previous two components. Experiments have been conducted on this platform to demonstrate the usefulness, stability and repeatability of the proposed system.

The details of design, implementation and experimentation of all components are elaborated in the thesis.

Acknowledgements

Firstly, I would like to express my uttermost gratitude to my previous supervisor Prof. Dave Barnes for providing the opportunity to start my PhD degree. Without his guidance, I cannot determine the direction of my study. He will never be forgotten.

I am also grateful to my current supervisor Dr. Frédéric Labrosse for accepting me at the middle stage of my PhD study and giving me great help in the writing phase. Without him, I cannot complete my thesis.

Dr. Laurence Tyler also deserves my gratitude. As my second supervisor, he plays an important role throughout my PhD career.

My special thanks to Dr. Derek Pullan from Leicester University for providing geological ground truth. His generous and patient guidance is the beacon in the geological aspect of my research.

I would like to thank Dr. Gui Chen, a senior fellow researcher in my laboratory. The discussions with him are stimulating.

I would like to express my appreciation to the academic, administrative, technical, and support staff in the Institute of Mathematics, Physics and Computer Science, for their assistance throughout my entire study. I am especially grateful to Prof. Qiang Shen, Prof. Mark Lee, Dr. Changjing Shang, Dr. Richard Jensen, Ian Izett and Peter Todd.

I would also like to thank all my friends, especially the Chinese student community in Aberystwyth for their continuous support.

TO MY LOVING PARENTS

Contents

Contents	v
List of Figures	x
List of Tables	xv
1 Introduction	1
1.1 General background to the research	1
1.1.1 Exploration history	2
1.1.2 Purpose of exploration	4
1.1.3 Rover-based exploration	7
1.2 Need for autonomy	9
1.2.1 Why Mars rover exploration needs autonomy	10
1.2.2 Current stage of rover autonomy	13
1.3 Motivation and objectives	16
1.4 Main contributions	16
1.5 Thesis outline	17
2 Autonomous Science System Review	19
2.1 OASIS	19
2.2 AEGIS	21
2.3 CREST autonomous robotic scientist	23
2.4 ASTIA	26
2.5 Summary	29

3	Rock Detection	30
3.1	Introduction	30
3.2	Classification methods using spectral data	32
3.2.1	Raw data	33
3.2.2	R^* data	36
3.2.3	Feature generation	36
3.2.4	Feature selection	39
3.2.5	Classifiers	39
3.2.6	Experiments, results and evaluation	40
3.2.6.1	Image-based “local” rock detection	41
3.2.6.2	Scene-based “global” rock detection	43
3.2.6.3	Cluster results by selected features	46
3.2.7	Summary	48
3.3	Two-threshold methods	48
3.3.1	Algorithms	49
3.3.1.1	Otsu’s method (Otsu)	50
3.3.1.2	Two-threshold Otsu method (TO)	51
3.3.1.3	Restricted two-threshold Otsu method (RTO1)	52
3.3.1.4	Restricted two-threshold Otsu method with new σ_B^2 (RTO2)	52
3.3.1.5	Two-fold Otsu method (TFO)	53
3.3.1.6	Probability ratio method (PR)	53
3.3.1.7	Normal distribution method (ND)	55
3.3.1.8	Direct probability method (DP)	56
3.3.2	Experiments and results	57
3.3.2.1	Image source	58
3.3.2.2	Performance evaluation criteria	58
3.3.2.3	Parameter setting	59
3.3.2.4	Performance comparison of each algorithm	61
3.3.3	Summary	64
3.4	Saliency methods	65

3.4.1	Saliency algorithms	66
3.4.1.1	Itti's method (ITTI)	66
3.4.1.2	Graph-based visual saliency (GBVS)	67
3.4.1.3	Context aware (CA)	67
3.4.1.4	Spectral residue (SR)	67
3.4.1.5	Image signature saliency (IS)	68
3.4.2	Experiments and results	68
3.4.2.1	Image source	68
3.4.2.2	Scale parameter configuration	70
3.4.2.3	Experiment of rock detection	71
3.4.2.4	Rock novelty level representation	76
3.4.2.5	Novelty detection	76
3.4.3	Summary	78
4	Autonomous Rock Science Evaluation	80
4.1	Introduction	80
4.2	Visual features and corresponding algorithms	84
4.2.1	Basic grey level statistics algorithms	84
4.2.2	Basic direction statistics algorithms	85
4.2.3	Region shape-based algorithms	86
4.2.4	Canny-based algorithms	90
4.2.5	Gabor-based algorithms	96
4.2.6	Corner density	100
4.2.7	Co-occurrence matrix algorithms	101
4.2.7.1	Grey level co-occurrence matrix algorithms	103
4.2.7.2	Direction co-occurrence matrix algorithms	104
4.2.8	Taruma texture algorithms	104
4.3	Mapping Procedures	105
4.3.1	Rock images	105
4.3.2	Expert scoring of the geological attributes	107
4.3.3	Mapping of visual features and geological attributes	108
4.3.3.1	Single feature mapping	108

4.3.3.2	Linear combination feature mapping	112
4.3.4	Summary	126
4.4	Fuzzy expert system	127
4.4.1	Membership function	128
4.4.1.1	Structure	129
4.4.1.2	Texture	129
4.4.1.3	Composition	132
4.4.1.4	Output	134
4.4.2	Rule base	135
4.5	Examples of science value calculation	138
4.6	Summary	139
5	Executive Agent	140
5.1	Introduction	140
5.2	Camera Agent	140
5.2.1	Cameras	141
5.2.2	Multispectral Filters	142
5.2.3	Camera mount	143
5.2.4	Coordinate transformation	144
5.3	Arm Agent	148
5.3.1	Robotic arm	148
5.3.2	Kinematic analysis	149
5.3.2.1	Forward kinematics	150
5.3.2.2	Inverse kinematics	153
5.3.3	Workspace of the arm	156
5.4	Camera to arm	157
5.5	Summary	160
6	Experiments and Demonstrations	162
6.1	System integration	163
6.1.1	Image capture and preprocessing	164
6.1.2	Rock detection	166

6.1.3	Attribute extraction and science value calculation	170
6.1.4	End effector manipulation	172
6.2	Repeatability experiments	172
6.3	Summary	179
7	Conclusion	180
7.1	Summary of the thesis	180
7.2	Thesis contributions	183
7.3	Future work	183
7.3.1	Macro issues	184
7.3.2	Micro issues	185
	Appendix A Output of Science Evaluation	188
	References	195

List of Figures

1.1	Layering structure detected by cameras of Mars rovers	6
1.2	Drawings of Mars rover structures	8
1.3	The data transmission of Curiosity rover	11
1.4	Typical communication procedure for a target analysis	12
1.5	ARSAS architecture	17
2.1	OASIS framework	20
2.2	AEGIS framework	22
2.3	CREST system framework	24
2.4	SARA architecture	25
2.5	ASTIA Framework	27
2.6	KSTIS architecture	28
3.1	Multispectral curves of rocks and regolith	34
3.2	Flow chart of the proposed classification method	35
3.3	Example of 24 feature maps	38
3.4	“Local” selected features and the classification results by these features	42
3.5	Detection results of selected feature set and other feature sets	44
3.6	“Global” classification results	45
3.7	Detection result of a non-training image	46
3.8	Clustering results using different feature sets	47
3.9	Grayscale image of the famous Mars “Heat Shield” rock and its histogram	49

3.10	Schematic diagram of the two-fold Otsu method	54
3.11	Schematic diagram of the probability ratio method	55
3.12	Schematic diagram of the normal distribution method	56
3.13	Schematic diagram of the direct probability method	57
3.14	Example of a MER Pancam image and corresponding labeled image	58
3.15	Example of a laboratory image and corresponding labeled rock regions	59
3.16	Performance of the PR method with different values of p_R	60
3.17	Performance of the ND method with different values of r	60
3.18	Performance of the DP method with different values of p_T	61
3.19	Rock detection result of a MER image	62
3.20	Rock detection result of a laboratory image	63
3.21	Uncommon region to interesting region to rock region	66
3.22	Images for saliency experiments	69
3.23	Example of conversion from multispectral data to RGB data	70
3.24	Saliency rock detection results on MER images	71
3.25	Saliency rock detection results on <i>McMurdo</i> images	72
3.26	Saliency rock detection results on PATLab images	72
3.27	ROC curves of the saliency detection results on MER images	73
3.28	ROC curves of the saliency detection results on <i>McMurdo</i> images	74
3.29	ROC curves of the saliency detection results on PATLab images	74
3.30	Saliency result comparison between the images before and after adding a meteorite	77
3.31	Saliency methods to detect a Martian	78
3.32	Saliency methods to detect vehicles on Mars	78
4.1	Procedure comparison between the proposed system and other ex- isted systems	82
4.2	Examples of L_{min}	87
4.3	Example of rock template	88
4.4	Examples of the bounding box and the convex hull	88
4.5	Examples of the fitted ellipses	89
4.6	Example of edges detected by the Canny operator	91

4.7	Phenomena of circular and bifurcated edges	92
4.8	Preprocessing for generating the final edge map	93
4.9	Images of cross-bedding and graded-bedding	94
4.10	Hough lines detected from the Canny edges	95
4.11	Normalised Gabor filters with four scales and eight directions	97
4.12	Gabor feature maps of the image of a layered rock	98
4.13	Corner detection result of the image of an angular rock sample	101
4.14	Corner detection result of the image of a round rock sample	102
4.15	Rock images from different sources with red labeled rock regions	106
4.16	GUI of the rock evaluation software	107
4.17	Correlation between a specified attribute and the combination features with different combination ratios	115
4.18	Correlation values of the combination features generated from the best feature sets under different feature number limitation	117
4.19	Pseudocode of the fast greedy method	118
4.20	Correlation results of the combination features with the combination weights calculated by the fast greedy algorithm	120
4.21	Correlation values of the combination features corresponding to different values of λ	122
4.22	Test set correlation results of the combination features calculated by the enumeration method	124
4.23	Test set correlation results of the combination features generated by the fast greedy algorithm	124
4.24	Test set correlation results of the combination features generated by the Lasso algorithm	125
4.25	MATLAB fuzzy toolbox interface	128
4.26	Membership functions of Layering (SP_{Cpixel})	129
4.27	Membership functions of Lustre (grayscale intensity)	130
4.28	Membership functions of Relief (Den_{SIFT})	131
4.29	Membership functions of Angularity ($Compactness$)	131
4.30	Membership functions of Hue	132
4.31	Membership functions of Coloured/BW	133

4.32	Membership functions of Albedo	134
4.33	Membership functions of the output: the science value of a rock . . .	134
4.34	Example of science value evaluation on a smooth rock	138
4.35	Example of science value evaluation on a layered rock	138
5.1	Analogue experimental platform	141
5.2	Filter wheel structure	142
5.3	Camera mounting	144
5.4	Camera coordinate frame	145
5.5	Offsets of camera lens	146
5.6	Image coordinate frame to world coordinate frame	147
5.7	Simulation of coordinate transformation	148
5.8	Robotic arm at the “0” position	149
5.9	Directions of the rotation of the seven joints	150
5.10	Establishment of the DH coordinates	151
5.11	Solving procedure of the J_1	154
5.12	Solving procedure of J_2 , J_4 and J_6	154
5.13	GUI of the kinematic simulation system	156
5.14	Workspace of the end effector	158
5.15	Projections of the workspace on the three base coordinate planes . .	159
5.16	Procedure of the transformation between arm and camera	160
5.17	Integration of the camera agent and the arm agent	160
6.1	Experimental environment	163
6.2	Relation between the three components of proposed system	164
6.3	Example of an RGB image captured by the camera system	165
6.4	Pancam calibration target	166
6.5	Experimental R^* data	166
6.6	Detection results of multispectral classification algorithms on the example image	167
6.7	Detection results of thresholding algorithms on the example image .	168
6.8	Detection results of saliency algorithms on the example image . . .	169

6.9	Rock labels for the experiment	170
6.10	Robotic arm controlled to reach the rock which has highest science value	173
6.11	Results of experiment I	174
6.12	Results of experiment II	174
6.13	Results of experiment III	175
6.14	Results of experiment IV	175
6.15	Results of experiment V	176
6.16	Results of experiment VI	176
6.17	Results of experiment VII	177
6.18	Results of experiment VIII	177

List of Tables

1.1	Comparison between Mars and Earth	2
1.2	Chronology of Mars spacecraft exploration	3
1.3	Future exploration missions	4
1.4	Mars questions	5
1.5	ECSS autonomy levels for mission nominal operations execution . .	10
1.6	Summary of sample types needing to be collected for the sample return project	15
3.1	MER Pancam filter characteristics	36
3.2	Feature meaning and reference number	37
3.3	Quantitative performance comparison between classifiers	43
3.4	Performance comparison of thresholding algorithms	64
3.5	AUCs of saliency algorithms	73
4.1	Correlation results of the features generated by basic grey level and direction statistics algorithms	108
4.2	Correlation results of the features generated by shape-based algo- rithms	109
4.3	Correlation results of the features generated by Canny-based algo- rithms	109
4.4	Correlation results of the features generated by Gabor-based algo- rithms	110
4.5	Correlation results of the densities of corners	110
4.6	Correlation results of the features generated from co-occurrence ma- trices	111

4.7	Correlation result of the Tamura features	111
4.8	Feature reference number	113
4.9	Feature reference number(s) in the best feature sets under different feature number limitations	117
4.10	Additional features of each iteration during the process of the greedy method	119
4.11	Selected features through the Lasso algorithm with different λ . . .	121
4.12	Single original feature's correlation results of the test set data . . .	123
4.13	Fuzzy system configuration	127
5.1	Camera specifications	142
5.2	Filter specifications	143
5.3	DH parameter settings of the arm	150
6.1	Attribute extraction	171
6.2	Science value calculation	171
6.3	Mapping between original and new labels	178
6.4	Rock science value comparison between different experiment runs .	179
A.1	Attribute output of experiment I	188
A.2	Science value output of experiment I	189
A.3	Attribute output of experiment II	189
A.4	Science value output of experiment II	189
A.5	Attribute output of experiment III	190
A.6	Science value output of experiment III	190
A.7	Attribute output of experiment IV	190
A.8	Science value output of experiment IV	191
A.9	Attribute output of experiment V	191
A.10	Science value output of experiment V	192
A.11	Attribute output of experiment VI	192
A.12	Science value output of experiment VI	193
A.13	Attribute output of experiment VII	193
A.14	Science value output of experiment VII	193

A.15 Attribute output of experiment VIII 194

A.16 Science value output of experiment VIII 194

Chapter 1

Introduction

Since the first satellite was launched by the Soviet Union in 1957, humans have carried on space exploration for about 60 years. After the first satellite, a great number of milestones have been reached, including first human spaceflight in 1961, the first spacewalk in 1965, and the first Moon human landing in 1969 and first space station in 1971. After successfully conquering the Moon many times, the fervour of spacial exploration is shifting to the well-known but mysterious planet — Mars.

1.1 General background to the research

Mars is the fourth planet from the Sun in the Solar system. It is often described as the “Red Planet” because of the iron oxide prevalent on its surface. Although there are many differences between Mars and Earth (A characteristic comparison is exhibited in Table 1.1), Mars is the planet most similar to Earth in the Solar system.

In addition, Mars is the second closest planet to Earth. Approximately every 26 months, Mars close approach will happen. In 2003, Mars reached a closest distance to Earth of about 56 million kilometres. Due to both the environment similarity and relatively close distance to Earth, Mars becomes the most preferable planet to be explored.

Table 1.1: Comparison between Mars and Earth

	Mars	Earth
Distance to Sun (average)	2.279×10^8 km	1.496×10^8 km
Radius (equatorial)	3397 km	6378 km
Volume	1.6318×10^{11} km ³	1.083×10^{12} km ³
Mass	6.4185×10^{23} kg	5.9722×10^{24} kg
Gravity (surface)	3.711 m/s ²	9.807 m/s ²
Tilt of Axis	25.2°	23.5°
Atmosphere (composition)	Carbon dioxide (95.32%) Nitrogen (2.7%) Argon (1.6%) Oxygen (0.13%)	Nitrogen (77%) Oxygen (21%) Argon (1%) Carbon dioxide (0.038%)
Atmosphere (pressure)	7.5 millibars	1013 millibars
Length of Day	24 hours 37 minutes	23 hours 56 minutes
Length of Year	687 Earth days	365 days
# of Satellites	2 (Phobos and Deimos)	1 (Moon)
Temperature (average)	-63 °C	14 °C

1.1.1 Exploration history

The recorded history of Mars observation dates back to the era of the ancient Egypt in the 2nd millennium BCE. Ancient Babylonian, Chinese, Indian, Greek astronomers also have recorded the observation and approximate measurement of Mars. In the 16th century, Johannes Kepler calculated a more accurate elliptic orbit for Mars based on Nicolaus Kepler's heliocentric model. The first telescopic observation of Mars was done by Galileo Galilei in 1610. From then on, with the improvement of telescopic technology, a series of researches have been done to acquire Mars information, including refined mapping, approximate surface temperature measurements and atmosphere component estimations.

During the recent decades, the exploration of Mars has entered the age of spacecrafts. Compared to telescopic instruments, the spacecrafts can observe Mars closer and in more detail thereby providing more accurate and useful information. Recently, multiple robotic spacecrafts have been sent to explore Mars from its orbit

Table 1.2: Chronology of Mars spacecraft exploration

Mission	Country	Year	F	O	L	R	S
Marsnik 1	USSR	1960	•				
Marsnik 2	USSR	1960	•				
Sputnik 22	USSR	1962	•				
Mars 1	USSR	1962	•				
Sputnik 24	USSR	1962	•				
Mariner 3	USA	1964	•				
Mariner 4	USSR	1964	•				
Zond 2	USSR	1964	•				
Mariner 6	USA	1969	•				
Mariner 7	USA	1969	•				
Mariner 8	USA	1971	•				
Kosmos 419	USA	1971			•		
Mars 2	USSR	1971		•	•		
Mars 3	USSR	1971		•	•		
Mariner 9	USA	1971		•			
Mars 4	USSR	1973		•			
Mars 5	USSR	1973		•			
Mars 6	USSR	1973		•	•		
Mars 7	USSR	1973		•	•		
Viking 1	USA	1975		•	•		
Viking 2	USA	1975		•	•		
Phobos 1	USSR	1988		•	•		
Phobos 2	USSR	1988		•	•		
Mars Observer	USA	1992		•			
Mars Global Surveyor	USA	1996		•			
Mars 96	USSR	1996		•	•		
Mars Pathfinder	USA	1996			•	•	
Nozomi (Planet-B)	Japan	1998		•			
Mars Climate Orbiter	USA	1998		•			
Mars Polar Lander	USA	1999			•		
Mars Odyssey	USA	2001		•			
Mars Express	Europe	2003		•			
Beagle 2	UK	2003			•		
MER-A Spirit	USA	2003				•	
MER-B Opportunity	USA	2003				•	
Mars Reconnaissance Orbiter	USA	2005		•			
Phoenix	USA	2008			•		
Fobos-Grunt	Russia	2011			•		•
Yinghuo-1	China	2011		•			
MSL Curiosity	USA	2011				•	
Mars Orbiter Mission	India	2013		•			

Successful missions are highlighted in yellow. Mission type: F = Flyby, O = Orbiter, L = Lander, R = Rover, S = Sample Return.

to its surface. A timeline of the Mars spacecraft exploration is listed in Table 1.2.

It can be seen that, in the early stages, the spacecraft missions were limited to flyby missions. Even so, due to the immature launching technology, flyby missions were often unsuccessful. Before the 21st century, approximately 70% of spacecraft missions failed. Recently, as the technology improved, the success rate of Mars spacecraft missions has been increasing. The Mars missions in 21st century achieve a success rate more than 70%, which arouses worldwide enthusiasms for Mars exploration. Nowadays, not only USA and Russia, but many countries such as Europe (Germany, UK, etc.), China and India also have plans to undertake spacecraft exploration on Mars. Partial future Mars exploration missions are listed in Table 1.3.

Table 1.3: Future exploration missions (partial)

Mission	Country	Year	F	O	L	R	S
InSight	USA	2016				•	
ExoMars	Europe&Russia	2016		•	•		
		2018			•	•	
Mangalyaan 2	India	2018		•	•		
Mars 2020	USA	2020					•

Mission type: F = Flyby, O = Orbiter, L = Lander, R = Rover, S = Sample Return.

1.1.2 Purpose of exploration

There are many questions of the red planet that are still to be answered (some questions are listed in Table 1.4), which attract exploration of the wild planet. As can be seen, most questions are of particular relevance to life, which is the key purpose of Mars exploration.

One way to search for life is to directly search for biosignatures that provide scientific evidence of past or present life. Viking landers had three experiments [Klein, 1978] attempting to detect signs of metabolism. The result of one experiment was positive but others showed negative results. Recently, reanalysis has been done on the old data [Bianciardi et al., 2012; Biemann and Bada, 2011; Navarro-Gonzalez et al., 2010], but the results still remain inconclusive. Currently, organic molecules, a kind of biosignature, have been found by the Curiosity Rover during the drilling process [Webster et al., 2015].

The other strategy for searching for life is to “follow the water”, given that

Table 1.4: Mars questions

Past	Was Mars suitable for life?
	Has life ever existed on Mars?
	Was the life on Mars the same as the life on Earth?
	Did Earth life come from Mars?
	When and why did Mars become a dry desert?
Present	How much liquid water was there in the past?
	Is there any liquid water under Mars surface?
	Is current Mars environment suitable for life?
	Is there life on Mars now?
	What is the condition to generate life?
Future	What is the condition to support life?
	Is Mars a planet good enough for colonization?
	Is there anything that can be done to make the planet more habitable?

water is a fundamental element of life on Earth. Although the Phoenix rover determined the existence of ice on the north pole of Mars, it is believed that no large standing bodies of liquid water exist due to the low atmosphere pressure. However in the past, Mars probably was wetter than today and has been warm enough to sustain liquid water at the surface for a period of time [Kargel, 2004]. Hence, the related researches focus on finding evidence of the existence of ancient liquid water. Currently, the investigation of ancient liquid water mainly refers to geological concepts, looking for geological signs of past aqueous activity. Compared with directly searching for biosignatures, the exploration associated with geology depends less on specialised instruments. For example, only with on-board cameras, the layered structure (see Fig. 1.1) can be captured which implies previous sedimentary deposit caused by water. Unlike Earth, whose terrains have suffered reformation and hence look different from their ancient form, Mars, on the other hand, keeps its form more primitively. Such primitiveness facilitates the geological exploration of Mars. Furthermore, geological information can provide guides to the experiment of searching for biosignatures. For example, through geological analysis, locations with higher possibility to be microbial habitat may be found, by which the search for biosignatures will perhaps be improved.

The geological exploration refers to several existing missions. The Mars Exploration Rover (MER) mission is the mission particularly designed for the geological exploration [Squyres et al., 2003], with the scientific objectives as following [NASA, 2015b]:

- Search for and characterise a variety of rocks and soils that hold clues to past water activity. In particular, samples sought will include those that have minerals deposited by water-related processes such as precipitation, evaporation, sedimentary cementation, or hydrothermal activity.
- Determine the distribution and composition of minerals, rocks, and soils surrounding the landing sites.
- Determine what geologic processes have shaped the local terrain and influenced the chemistry. Such processes could include water or wind erosion, sedimentation, hydrothermal mechanisms, volcanism, and cratering.
- Search for iron-containing minerals, identify and quantify relative amounts of specific mineral types that contain water or were formed in water, such as iron-bearing carbonates.
- Characterise the mineralogy and textures of rocks and soils and determine the processes that created them.
- Search for geological clues to the environmental conditions that existed when liquid water was present. Assess whether those environments were conducive to life.



Figure 1.1: Layering structure detected by cameras of Mars rovers. Left is the image captured by MER Spirit Pancam; Right is the image captured by MSL MastCam. Images courtesy of NASA/JPL.

In addition, the Curiosity Rover also has some geological and geochemical objectives [NASA, 2015a]:

- Investigate the chemical, isotopic, and mineralogical composition of the Martian surface and near-surface geological materials.
- Interpret the processes that have formed and modified rocks and soils.

It can be seen that geological information has been regarded as a key theme of Mars exploration. Many future Mars exploration missions, especially the rover-based exploration such as ExoMars [Vago, 2010], involve geological exploration.

1.1.3 Rover-based exploration

Recently, with significant technological advancements, Mars exploration missions with a rover become mainstream. Rovers can carry sophisticated science instruments which can be applied to detect biosignatures. In addition, the close distance to Mars surface allows them to observe geological features in more detail. Unlike orbiter units which can only gain geological features such as “volcano”, “canyon” and “channel”, rovers are subtle observers, capturing more informative features such as “layered cliff”, “soil pore” or even “meteorite”. Compared with landers which can only perform exploration surrounding the landing location, rovers can move around Mars to explore different sites thereby acquiring more comprehensive information. In addition, as it is similar to a real human exploration, a rover may discover latent hazards that will be encountered by future human missions.

Generally, a rover consists of a rover body, a computer, wheels, cameras, a robotic arm, science instruments, antennas, energy units and other auxiliary parts. The schematic structures of MER and MSL rovers are illustrated in Fig. 1.2.

- A rover body is a “box” with a strong, outer layer which protects the rover computer, electronics and some science instruments and keep them warm.
- The computer, the rover’s “brain”, processes the commands given by the Earth control panel, monitoring the status of the rover, controlling and manipulating the movement of other parts.
- Wheels provide the mobility of the rover. Like the MER and MSL rovers, a general rover will have six wheels, each with its own individual motor. Such a design is to support a special suspension system to keep balance.

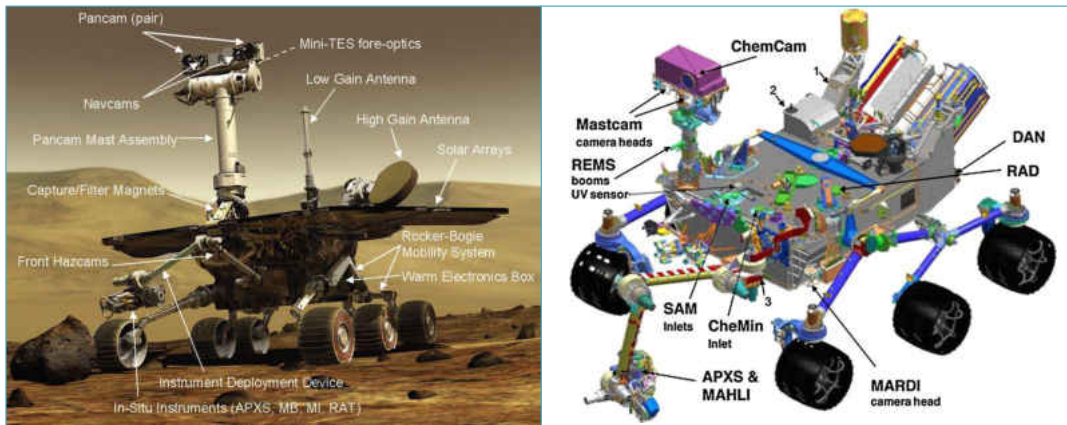


Figure 1.2: Drawings of Mars rover structures. Left: Mars Exploration Rover (MER) [Crisp et al., 2003], Right: Mars Science Laboratory (MSL) [Grotzinger et al., 2012]. Image courtesy of NASA/JPL.

- Cameras are the “eyes” of the rover. Different cameras have different functions. Commonly, a rover will have panoramic cameras for capturing colour or multispectral images of interesting science targets, stereo navigation cameras for generating 3D imagery to guide the rover movement and hazard cameras for avoiding potential hazards. Cameras can be regarded as science instruments to some extent. Particularly, the Curiosity rover was equipped with a ChemCam, which can fire a laser and analyse the elemental composition of vaporised materials.
- The robot arm of a rover holds some science instruments which are used in a closeup or contact condition. The flexibility of the arm can maneuver the instruments into specified positions and gestures for accurate analysis. Moreover, some devices such as drills and grinders for sample preparation functions will be also mounted on the end of the arm.
- The science instruments play key roles in Mars exploration. It can be said that a rover’s other parts are for the purpose of supporting and serving the deployment of science instruments. The various on-board instruments are designed for different scientific objectives. A well-known instrument is Alpha particle X-ray spectrometre (APXS) [Rieder et al., 2003], providing the capability to determine the abundance of specific elements. Another famous instrument, the Sample Analysis at Mars (SAM) [Mahaffy et al.,

2013] carried by the Curiosity rover, can investigate the elements related to life.

- A rover’s antennas serve as both its “mouth” and “ears”, sending the Mars information to Earth and receiving command update from Earth. Generally, multiple antennas will be equipped for back-up options.
- Energy units provide the power required by the rover to perform any operation. Previously, the energy units of rovers were solar arrays, which will still be adopted by many future missions. However recently, the MSL rover has carried a radioisotope power system which can provide more persistent, durable and powerful energy.

Due to good mobility and also carrying sophisticated science instruments, rover exploration is the most suitable and preferable way to unveil the mysterious planet, both biologically and geologically. Hence, in this thesis, the main discussion focuses on rover-based exploration.

1.2 Need for autonomy

Although manned missions to Mars have been under study, they are still debatable due to reasons such as unrealisation of return process, requirement of feeding, warming and recycling, risk of contamination and partly cost. Currently, rovers have dominated Mars exploration as they can simulate human exploration in many aspects. However, an essential difference between manned exploration and rover exploration is that rover cannot “think” as humans can do. A rover cannot autonomously decide which action it should do, and hence needs to receive human’s commands to perform operations. Without the intervention of human, a rover can hardly do any exploration. Currently, technology has reached a level where autonomy is becoming feasible. Thus, the autonomy in rover exploration has been presented to alleviate the manned dependency and to make the rovers’ action more similar to that of humans.

Particularly, the European Cooperation for Space Standardisation (ECSS) has defined robotic autonomy within a planetary exploration context (see Table 1.5). These levels can also be regarded as a standard to assess autonomous systems for rover exploration.

Table 1.5: ECSS autonomy levels for mission nominal operations execution

Level	Description	Functions
E1	Mission execution under ground control. Limited on-board capability for safety issue.	Real-time control from ground for nominal operation. Execution of time-tagged commands for safety issues.
E2	Execution of pre-planned, ground-defined, mission operations on-board.	Capability to store time-based commands in an on-board scheduler.
E3	Execution of adaptive mission operations on-board.	Event-based autonomous operations. Execution of on-board operations control procedures.
E4	Execution of goal-orientated mission operations on-board.	Goal-oriented mission replanning.

1.2.1 Why Mars rover exploration needs autonomy

Autonomy, if safe enough, is more desirable in Mars rover exploration than in normal robotic exploration because of the problems caused by the distance between Mars and Earth. The long distance generates a large communication delay. Even if the signals travel at the speed of light between Mars and Earth, the travel time will take 3–22 minutes. Thus, it is impossible to execute a real-time rover control.

The large transmission time is by no means the only problem of Mars-Earth communication. A rover mission will also suffer the challenges of limited communication windows and down-link bandwidth. For example, the MSL rover (Curiosity), currently the most advanced rover, has two communication methods (see Fig. 1.3): direct-to-Earth and orbiter relay, both of which require the Deep Space Network (DSN) as the data receiver. The data rate of direct-to-Earth is very limited, from 500 bits per second to about 30000 bits per second. On the other hand, the data rate to Mars Reconnaissance Orbiter can be as high as 2 million bits per second.

In addition, both communication methods will be limited by communication timing. In the case of orbiter relay communication, the communication only occurs when the orbiter passes over the rover for about eight minutes at a time per sol. In that time, between 100 and 250 megabits of data can be uploaded. Such amount of data will take up to 20 hours through the direct-to-Earth method whose communication time is also limited. The rover can only transmit direct-to-Earth for a

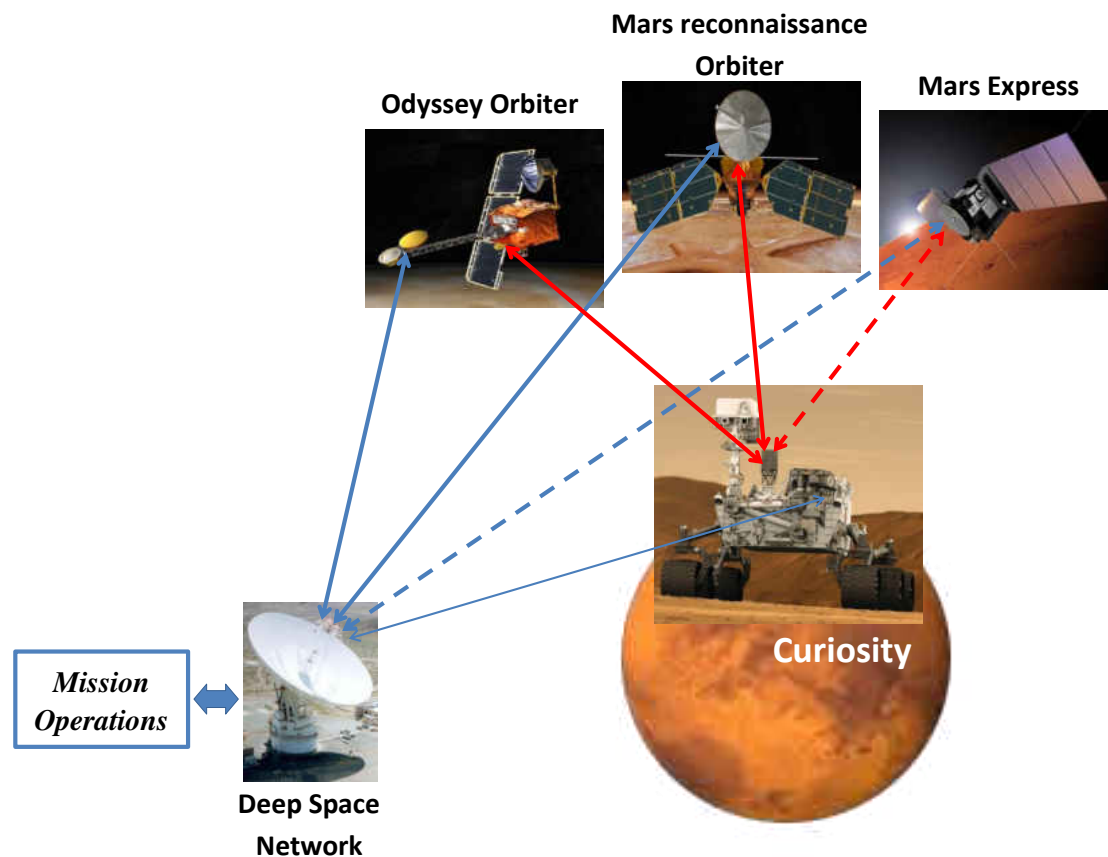


Figure 1.3: The data transmission ways of the Curiosity rover: to Earth directly or via three relay satellites in Mars orbit. Both ways need the DSN as the receiver. Image courtesy of NASA.

few hours a day due to power limitations, conflicts with other planned activities or uncommunicable orientation of Mars. Thus, even though maximum transmission is made, only about 250 megabits of data can be transmitted to Earth per sol.

Not only the amount of data, the interval between two communications will also restrict the rover's activities. If a rover is fully controlled by an Earth-bound panel (ground scientists and engineers), the procedure of target analysis is similar to Fig. 1.4. Images and data recorded by the rover need to be transmitted back to Earth where scientists perform analysis and upload a new set of commands for the rover to follow. As can be seen, to gain the final science result of only one analysis, three days will be spent to guarantee all activities are under supervision in safe range. The rover can only be at a stand for a sol even though the data required for the commands is less than the bandwidth. Generally, data can be obtained

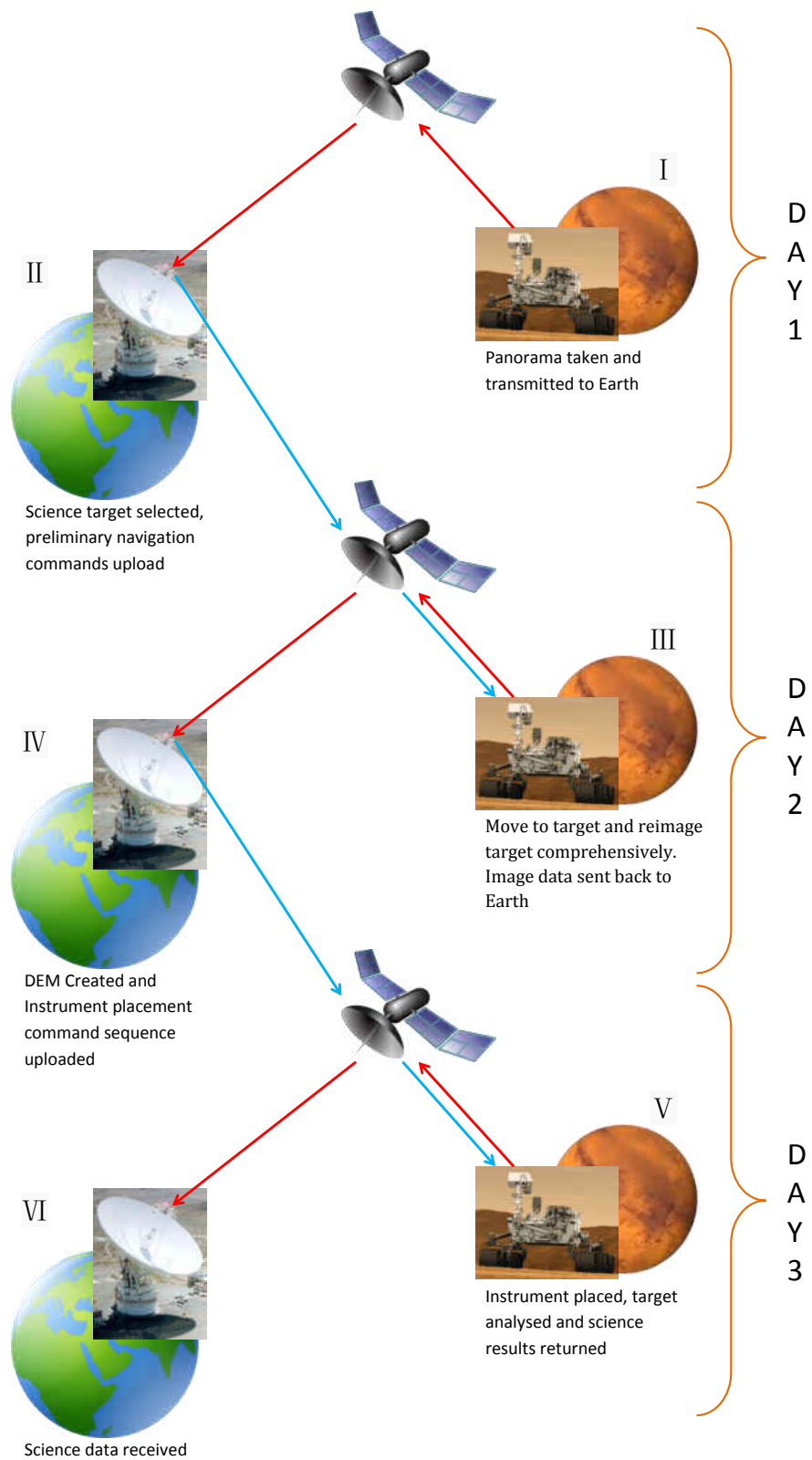


Figure 1.4: Typical communication procedure for a target analysis

far quicker than it can be successfully transmitted to Earth. Thus, pauses are introduced inevitably when a command sequence has been completed and the data must be processed by Earth scientists and engineers before the next move can be decided. Both the pauses and the delays lead to the inefficiency of Mars exploration.

With increased autonomy, some Earth-bound decisions could be delegated to the rover, hence reducing the requirements of communication between the ground control panel and rovers. If full autonomy (E4 in Table 1.5) in rover exploration is fulfilled, no input from Earth except the list of goals is necessary and hence transmission bandwidth can be saved. Also some intermediate data such as workflow images need not be down-linked at all. Thus, the limited bandwidth can be mostly used for transmitting significant data thereby maximising science return. Even if the autonomy level cannot reach E4, giving a rover some rudimentary autonomous capabilities can speed up the process of exploration and hence improve the efficiency of exploration.

Another benefit of autonomy is reducing the degree of dependence on Earth operators. If autonomous systems are applied, the workload of ground-based staff such as scientists and engineers would be reduced. They would not need to work 24×7 , waiting for responses from rovers and designing new plans “immediately” as an autonomous system does. Moreover, in the case of an expeditious rover driving site to site, scientists cannot perform detailed examination of all terrain targets and thus may miss some targets with high scientific values. Applying autonomous systems to detect science targets can reduce the probability of the failure of capturing those opportunistic objects.

1.2.2 Current stage of rover autonomy

Although full autonomy has not been achieved and cannot be achieved in a short period, a lot of efforts have been made to develop autonomous systems for rover exploration. Prior to regular exploration, during the entry, descent and landing (EDL) phase of a rover, some autonomous systems have been applied. In some periods of the EDL phase, full autonomy is required since the round-trip time for communications will be much longer than the time between entering the atmosphere and landing [Maimone et al., 2007]. For example, the Descent Image Motion Estimation System (DIMES) [Cheng et al., 2005] was adopted in the EDL stage of the MER mission for horizontal velocity estimation during the last

2000 meters, thereby guaranteeing the safe landing. In the EDL phase of the MSL rover, the onboard computer executed an autonomous system to perform all navigation by integrating acceleration and attitude data provide by an Inertial Measurement Unit (IMU) after the Cruise Stage Separation (CSS) [Prakash et al., 2008; Way et al., 2007]. Autonomous navigation systems have also been used in general exploration. As for the MER rovers, the onboard system used the Sum of Absolute Difference (SAD) metric to generate full 3D measurements of points from stereo images [Goldberg et al., 2002]. Then from the 3D point cloud, an autonomous system called Grid-based Estimation of Surface Traversability Applied to Local Terrain (GESTALT) was employed to detect geometric hazards around the rover. Through the output of GESTALT, the rover can autonomously select a safe and short path towards the specified target position [Carsten et al., 2007]. Some other technology such as Visual Odometry also facilitates autonomous navigation/driving of the MER rovers [Biesiadecki and Maimone, 2006]. The Curiosity rover also carried autonomous navigation system similar to the MER's to allow its autonomous driving [Webster, 2015].

After autonomous navigation systems paving the way, autonomous science systems can be used. Autonomous systems for science are another important branch of autonomy in Mars rover exploration. The objective of an autonomous science system is to search for interesting targets with high scientific value and collect scientific information about them. Although there are some autonomous systems designed for analysing the data gained by other instruments [Gazis and Roush, 2001], most autonomy studies for Mars rovers focus on the image data captured by onboard cameras, including feature detection (dust devil detection [Castano et al., 2007a], rock detection [Song, 2008; Thompson and Castano, 2007], layering detection [Gulick et al., 2001], life detection [Wettergreen et al., 2005]), novelty detection [Thompson et al., 2006] and feature representation (rock classification [Dunlop, 2006; Pedersen, 2000], surface classification [Bekker et al., 2014; Brooks and Iagnemma, 2007; Shang and Barnes, 2013], geological analysis [Thompson et al., 2005b]). Specifically, these studies often focus on isolated or float rocks. In addition, for the sample requirements of the Mars Sample Return project [MEPAG, 2008], rocks are also selected as high-priority targets (see Table. 1.6).

Rocks are obvious targets on Mars surface and hence easy to approach. In contrast to another widespread feature—regolith, rocks can maintain geological information with higher science value. Rocks are relatively solid and hence can keep their structures (shapes) and composition for thousands of years. By inves-

Table 1.6: Summary of sample types needing to be collected for the sample return project [MEPAG, 2008]

Ref.	Goal	Objective Nickname	Rocks				Other				
			Sedimentary suite	Hydrothermal suite	Low-T W/R suite	Igneous Suite	Depth-Resolved Suite	Regolith	Dust	Ice	Atmospheric Gas
1	I	Habitability	H	H	L	L	M	L		L	L
2	I	Pre-biotic, life	H	H	L		M			M	L
3	III	water/ rock	H	H	H			M			
4	III	Geochronology	M	M		H					
5	III	Sedimentary record	H		M						
6	III	Planetary evolution				H		M			M
7	III	Regolith					M	H	M		
8	IV	Risks to human explorers					L	H	H	M	
9	I	Oxidation			H		H	M	M		
10	II	Gas Chemistry	M	M		M					H
11	II	Polar							M	H	M

Note: Priorities are expressed as relative High, Medium, and Low.

tigating the shapes of rocks, the ancient configuration of Mars may be derived. In addition, more detailed biological and geological information can be obtained through the deeper analysis of rock composition, especially the composition of rock interiors. Moreover, unlike soil which is easily spread, rocks can reflect more local information. Due to the pervasiveness and relatively high science value of rocks, many autonomous science systems have been built with the emphasis on rock science evaluation. Hence, four existing autonomous rock science systems are specifically reviewed in Chapter 2. Moreover, rock science evaluation is also a key issue discussed in this thesis.

As well as navigation and science, studies have been done about other applications of autonomous system such as instrument placement [Backes et al., 2005; Huntsberger et al., 2005; Pedersen et al., 2005], target rock tracking [Kim et al., 2009; Maimone et al., 1999], graspability analysis [Cadapan, 1997], touchability analysis [Gui et al., 2013], autonomous drilling [Helmick et al., 2013] and even system architecture [Volpe et al., 2001].

1.3 Motivation and objectives

As mentioned above, in the current modality of Mars exploration, geology plays a vital role and rocks are the most important targets. Onboard cameras and science instruments mounted on a robotic arm are the main tool to investigate rocks. Crucially, like the emphasis of other studies, autonomy becomes the key issue in Mars exploration. Therefore, it is important to build an **autonomous** system which links **computer vision**, **geological knowledge** and **robotics** together.

A new system is proposed which has a similar structure to the *Autonomous Science Target Identification and Acquisition (ASTIA)* system¹. Compared to ASTIA, the proposed system has better autonomous science capabilities. For reference, the proposed system is called *Autonomous Rock Science Analysis System (ARSAS)*. The architecture of ARSAS is illustrated in Fig. 1.5.

Like most classic autonomous systems related to Mars exploration, the proposed system mainly contains three components: rock detection, rock science value evaluation and executive agent. When all three components have been integrated together, it can reach E3 autonomy level (see Table 1.5), which allows a rover to execute an event (i.e. searching for rocks with high science values and accessing them) autonomously.

1.4 Main contributions

As stated before, the objective of this thesis is to establish an autonomous system with a higher autonomy level. In following chapters, a number of techniques have been used for achieving such an objective, which can be regarded as the key contributions of this thesis. Specifically, three different rock detection methods have been introduced and a novel rock evaluation mechanism has been proposed and implemented. Compared to previous systems, the proposed system obtains better rock detection performance and evaluates rock science value in a more geology-oriented way.

¹Brief descriptions of this system are presented in Section 2.4. More details can be found in [Barnes et al., 2009].

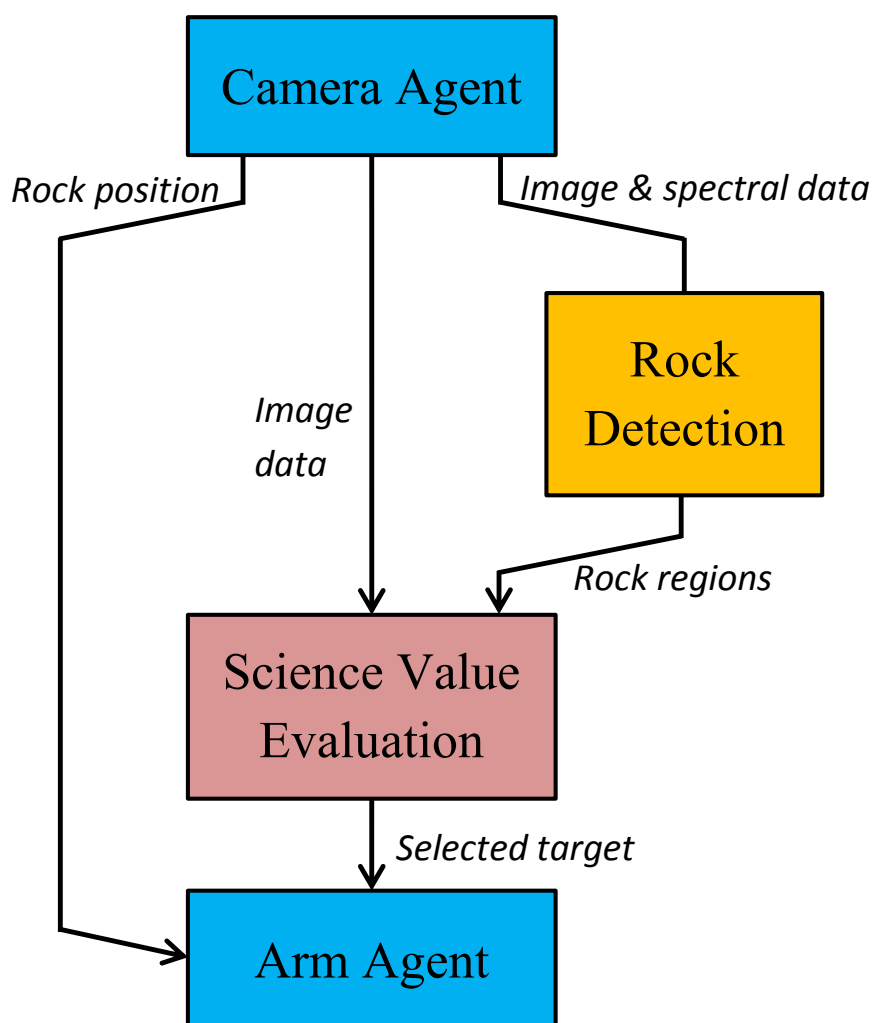


Figure 1.5: ARSAS architecture. The rock detection part is discussed in Chapter 3. The rock science value evaluation issue is discussed in Chapter 4. Camera agent and arm agent are both included in the executive agent part which discussed in Chapter 5.

1.5 Thesis outline

Corresponding to the three components of the proposed system, the rock detection, science value evaluation and execution agent are introduced in different chapters. In each component, several novel algorithms are presented. Finally, these three components are integrated together. A simulated experimental environment has been established in which demonstrating experiments have been conducted to show

how the integrated system works.

The thesis has been divided into seven chapters, which are organised as follows:

Chapter 2: Autonomous Science System Review This chapter provides an introduction of four existing autonomous science systems. The content of system architecture and corresponding algorithms is reviewed.

Chapter 3: Rock Detection This chapter presents three kinds of rock detection approaches. The first approach utilizes a series of machine learning techniques to address the multispectral data. The second approach contains several two-threshold thresholding methods, separating the relatively brighter and darker regions of rock from the monotonous background. The third approach applies some methods in saliency aspects, detecting rocks in a bottom-up way.

Chapter 4: Autonomous Rock Science Evaluation This chapter proposes a methodology for converting image data to science. This methodology bridges the gap between analytic geology representation and computerized visual processing. A number of image processing algorithms such as Canny operator, SIFT corner and colour space transformation are used for generating visual features from which some features are chosen as the indicators of geological attributes. Based on the knowledge and experience of a geologist, a fuzzy expert system is designed to calculate science values of rocks through their geological attribute values.

Chapter 5: Executive Agent This chapter describes a platform whose structure is similar to a partial rover. This platform provides the hardware system as well as corresponding control system to support the rock detection and rock science value evaluation components.

Chapter 6: Experiments and Demonstrations This chapter integrates the components described in the preceding three chapters. Experiments have been done to demonstrate the whole procedure of ARSAS from initial image data acquisition to final arm manipulation.

Chapter 7: Conclusions This chapter summarises the main contributions made by the thesis, together with a discussion of future research. Both general issues and immediately achievable tasks are considered.

Chapter 2

Autonomous Science System Review

In this chapter, four autonomous systems for Mars rover exploration are reviewed with emphasis on autonomous science of rocks, from which many lessons can be learnt for developing our system. The four systems are: *Onboard Autonomous Science Investigation System (OASIS)*, *Autonomous Exploration for Gathering Increased Science (AEGIS)*, *CREST Autonomous Robotic Scientist* and *Autonomous Science Target Identification and Acquisition (ASTIA)*. In particular, the *ASTIA* system is a prototype of the autonomous system proposed in this thesis.

2.1 OASIS

The Onboard Autonomous Science Investigation System (OASIS) [Castano et al., 2007a,b] has been developed to endow a rover with the capability to identify and react to serendipitous science opportunities. These science opportunities can include dust devils and clouds but mainly refer to rocks. The framework of OASIS is illustrated in Fig. 2.1.

It can be seen that, OASIS mainly consists of three components:

- **Feature Extraction:** This component concentrates on extracting visual features from located rocks.
- **Data Analysis:** This component uses the extracted features to determine scientific value of rocks and scenes.

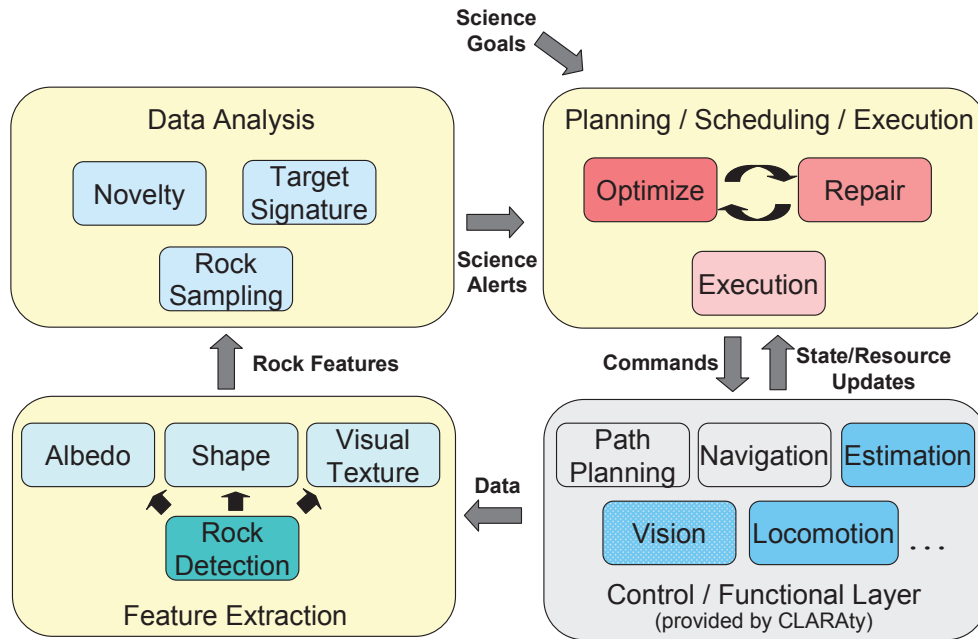


Figure 2.1: Framework of the Onboard Autonomous Science Investigation System (OASIS). This diagram shows how the decision-making capabilities interact within OASIS (yellow boxes) and how OASIS interacts with low-level robotic control software (gray box). Figure from [Estlin et al., 2007].

- **Planning/Scheduling/Execution:** This component dynamically modifies the rover’s plan to accommodate new observations.

The system firstly identifies rocks from collected images of the surrounding terrain using an algorithm called *rockfinder* [Thompson and Castano, 2007]. The position of rocks can be measured and translated into a frame relative to the centre of the rover. After detection and location, rock features/properties (geological attributes) are extracted for further analysis. The properties currently estimated by OASIS include shape, texture and albedo. The albedo of a rock is used as an indicator of the reflectance which implies the composition of the rock. OASIS measures albedo by computing the average gray-scale value of the rock pixels segmented from the rock image. Identified texture information can be used to gather information about rocks’ history and composition. OASIS utilizes Gabor filters to represent the visual texture of observed rocks [Castano et al., 1999]. The shapes of rocks may provide knowledge about the provenance (source and formation of rocks) and about the environmental conditions that rocks have been

exposed to. The eccentricity of the fit ellipse, as well as the error, is computed to describe the shape of rocks [Fox et al., 2002].

In the property analysis and prioritisation module, the scientific values of rocks are assessed using the extracted features. Three different techniques have been used to prioritise rocks. The first technique, called “key target signature”, tries to recognise a pre-specified rock signature which has been identified by the science team as data of high scientific value. There are two ways to set the rock signatures. In the first method, the importance of specific feature/property values is directly set by scientists through which the science value of rock can be calculated. In the second way, the target signature is specified by selecting an identified rock with interesting properties and hence with high science value. Thus, rocks which resemble this particular rock will be given a high priority. The second technique, novelty detection, is for identifying the unusual signatures that do not conform to the statistical norm for the region. Such a technique can detect uncommon rocks (e.g. meteorites) which may hold extremely high science values. The third technology, known as representative sampling, prioritises rocks for the aim of understanding the region where the rover traversed. The representative rocks are selected for comprehensive analysis of the whole region rather than the rocks themselves. The prioritisation results generated from all three techniques can be used as the input of Planning/Scheduling model.

The planning and scheduling module enables dynamic modification of the current rover command sequence (or plan) to accommodate new science requests generated from the data analysis module, the content of which surpasses the subject of this thesis and hence no more discussion is provided.

The procedure of OASIS is instructive to subsequent researches. It is designed as a full autonomous system and shows impressive preliminary test results [Castano et al., 2005]. From many other autonomous systems for rover-based planetary exploration, the trace of OASIS can be found.

2.2 AEGIS

The Autonomous Exploration for Gathering Increased Science (AEGIS) system was originally developed as a part of OASIS, providing automated targeting capability for remote sensing instruments (e.g. Pancam and ChemCam) for Mars exploration [Estlin et al., 2009]. It has been operated on the MER Opportunity rover and the MSL Curiosity rover [Estlin et al., 2012, 2014]. Unlike OASIS, which

tries to build a fully integrated platform, AEGIS concentrates on the acquisition of interesting rocks by Pancam. The framework of AEGIS is shown in Fig. 2.2. It can be seen that, as a successor, AEGIS has many components similar to OASIS such as target detection, feature extraction, and target prioritisation.

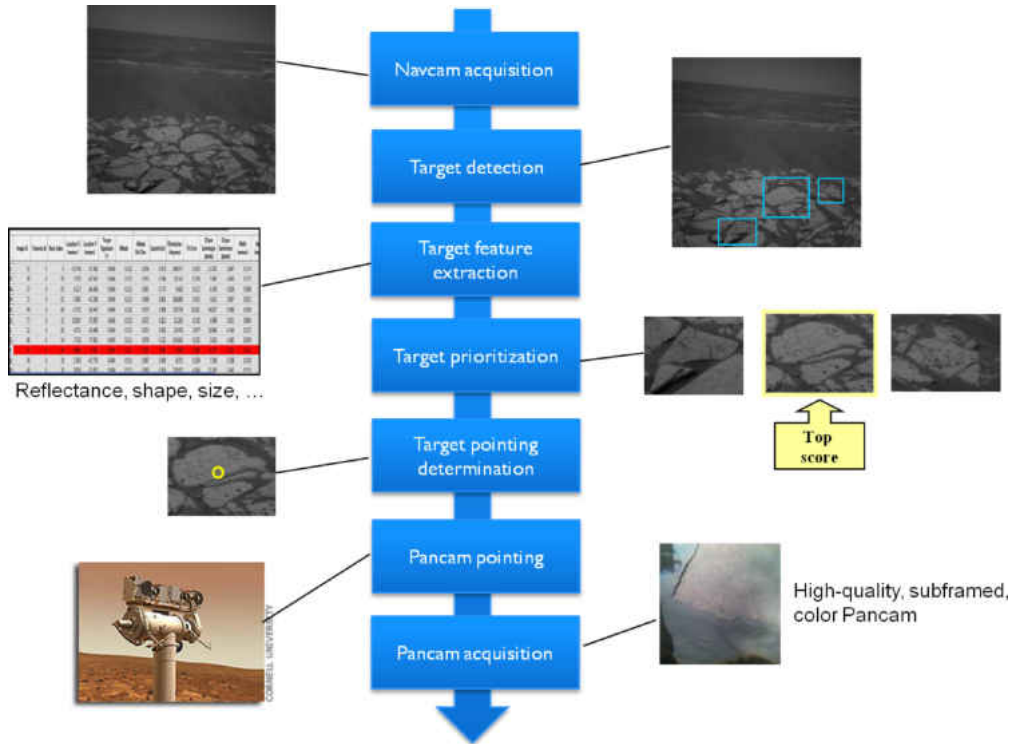


Figure 2.2: Framework of AEGIS system. This series of steps has been executed onboard the MER Opportunity rover. Figure from [Estlin et al., 2009].

In terms of the rock detection component in AEGIS, an algorithm called *ROCKSTER* was used. This algorithm firstly identifies raw edge segments using a procedure similar to Canny edge detection [Canny, 1986]. Then a gap-filling mechanism is applied to join nearby contour edge fragments. Finally, the edge fragments are regrouped into coherent contours through a background flood method.

Once candidate rocks are identified, their albedo, shape and size features are extracted. With regards to albedo features, not only the mean of the grayscale value but also the moments of the pixel intensity distribution including variance, skewness and kurtosis are included. As to shape feature extraction, identical to OASIS, the eccentricity of a fitted ellipse as well as fitting error are calculated. Particularly, AEGIS extracts the size information of rocks while OASIS doesn't.

For one rock target, the size is represented by the pixel area, the radius of the largest inscribed circle and the lengths of major and minor axes of the fitting ellipse.

For the target prioritisation component, AEGIS applies a strategy similar to first method of the “target signature” in OASIS: stipulating the importance of each particular feature by a geological expert. In particular, AEGIS can give each candidate rock target a score corresponding to a weighted sum of up to two features. Supposing the two features are x_1 and x_2 , the final score f can be computed as:

$$f = \alpha_1 x_1 + \beta \alpha_2 x_2, \alpha_i \in \{-1, 1\}, \beta \in [0, 1] \quad (2.1)$$

where α_1 and α_2 are the coefficients to control “absolute” importance of the two features while β is to describe the comparative importance which can be set as 0 in the case only using one feature.

After the best scoring candidate rock has been determined, AEGIS points the remote sensing instrument at the target to acquire more detailed data (e.g. multispectral data).

AEGIS is also a typical autonomous system dedicated to a specified mission. It is the prototype of many other autonomous targeting systems such as the Automatic Pointing and Image Capture (APIC) system [Pugh et al., 2010b].

2.3 CREST autonomous robotic scientist

The primary task of the CREST robotic scientist is to demonstrate opportunistic science in a representative ExoMars [Vago et al., 2006; Van Winnendael et al., 2005] rover environment. The system attempts to establish an initial scientific methodology for the autonomous science assessment and planning based on human terrestrial field practice [Shaw et al., 2007; Woods et al., 2008a,b]. The prototype framework of the CREST system is shown in Fig. 2.3. As can be seen, the system mainly consists of three components: *Timeline Validation, Control and Repair* (TVCR), *Science Assessment and Response Agent* (SARA) and *Arm Agent and Perception Interface* (AAPI).

TVCR is the autonomous planning component in CREST. Similar to the planning and scheduling of OASIS, TVCR is developed to support goal-based arbitration and time line replanning to response to opportunistic science [Woods et al.,

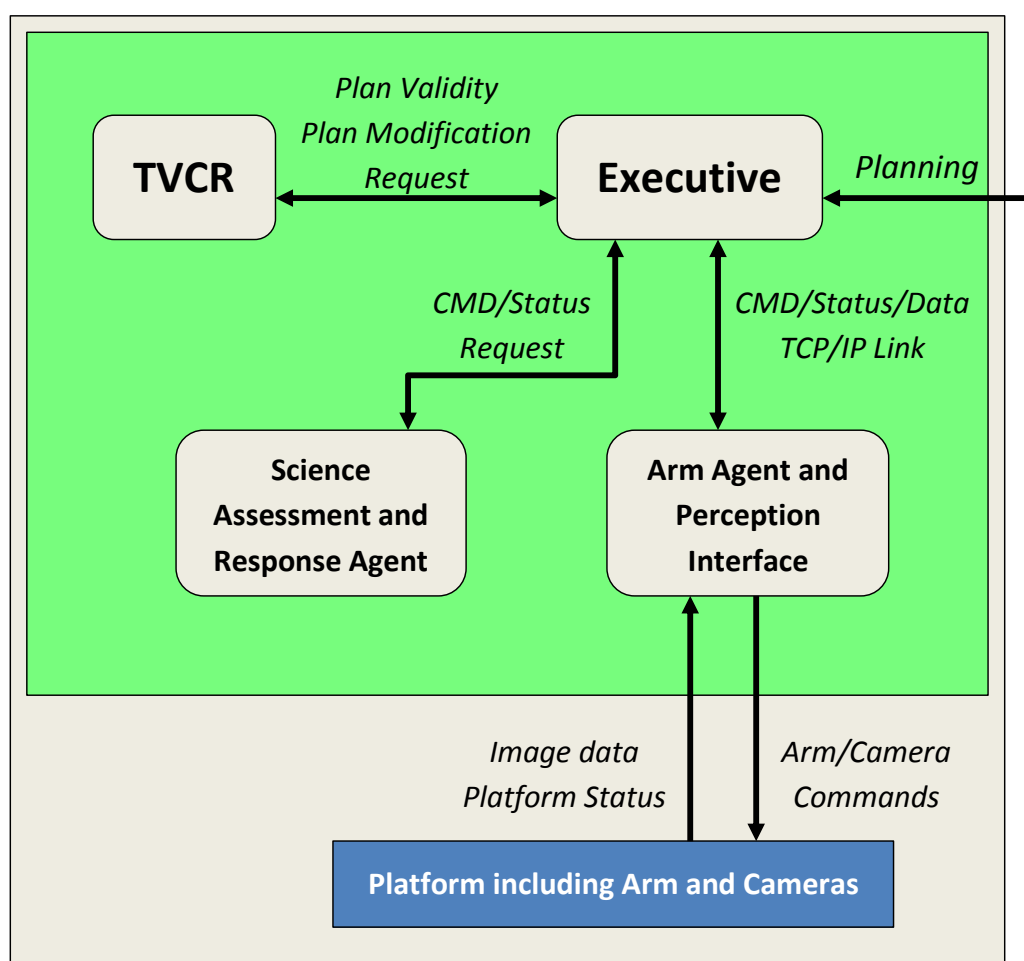


Figure 2.3: Framework of the CREST system (On-board part). The original image can be found in [Woods et al., 2008a].

2006]. AAPI is the hardware executive component, manipulating the rover instruments such as camera, pan and tilt unit (PTU), chassis and robotic arm. SARA is the key component of CREST system which is responsible for the identification and assessment of science targets and hence more attention is paid to it.

SARA is developed on an underlying scientific scoring framework outlined in [Pullan, 2006] (also can be found in [Pugh, 2010]). In the framework, a planetary geology domain expert enumerates some criteria to deconstruct the process of the rock assessment by humans into relevant attribute analysis. Thus, in contrast to the science component of OASIS and AEGIS which consider the rock attributes

in a computer vision view, SARA evaluates the science values of rocks in a more geology-oriented manner. The expert asserts that the comprehensive assessment of rocks can be broken down into three geological aspects (see Fig. 2.4): Structure (macroscopic geometric shape, e.g. bedding type and scale), Texture (surface characteristic, e.g. luster and relief) and Composition (mineralogy appearance, e.g. albedo and colour).

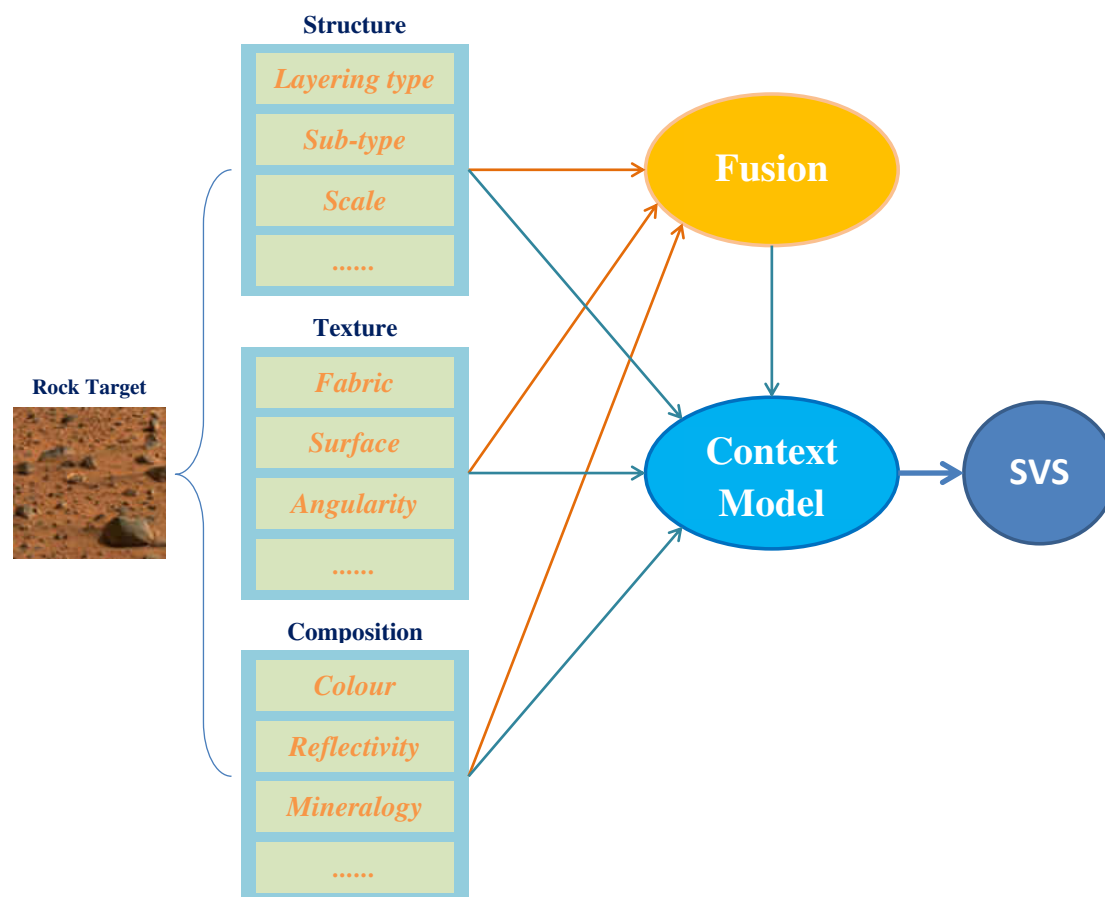


Figure 2.4: Architecture of the SARA module in CREST system. The original image can be found in [Woods et al., 2008a].

In each aspect, geological attributes/features are defined for analysing the science value of rocks. A set of rules [Pugh, 2010] based on expert knowledge is established, by which the science score of a rock in each geological aspect can be calculated. Finally, combining the scores of all three aspects of rock features together, the numerical Science Value Score (SVS) of a rock can be estimated by a

contextual model [Woods et al., 2009] which can be simply expressed as:

$$\text{svs} = \left(\sum A_s + \sum A_t + \sum A_c + A_x \right) \cdot Q \cdot B \quad (2.2)$$

where $\sum A_s$ is the overall structural attribute score, $\sum A_t$ is the overall textural attribute score and $\sum A_c$ is the overall compositional attribute score. Specifically, A_x is a composite score which can be given to a composite group of related attributes which shows little value when they are evaluated separately but produce a desirable target when they are combined together. Q is a quality factor, which is used to represent the quality of the image or an identified target. This value is generally smaller than 1 to degrade the science value while acquiring images with low quality. B is a bias factor for adjusting the value of certain kinds of targets. For example, if the system has already identified a basalt rock with a very high priority, the basalt rocks found in future exploration will be given lower scores.

CREST autonomous robotic scientist provides the concept to develop an autonomous science system where the geological knowledge plays a more important role. However, as that duration and budget for developing the system is limited and that the domain of geological knowledge is too broad, the system has not been developed completely. However, the mechanism which analyses rock science value in an analytic geological way is heuristic. In addition, through the limited results of the system [Woods et al., 2009], it can be found that such a mechanism is very promising.

2.4 ASTIA

Autonomous Science Target Identification and Acquisition (ASTIA) [Barnes et al., 2009] is a system designed for the purpose of autonomous science target (rock) identification surface and sample acquisition with the framework shown in Fig. 2.5.

The ASTIA framework resembles previous reviewed autonomous systems, especially the CREST autonomous scientist, consisting of the components of rock identification (Rock Ident), science assessment (KSTIS) and executive agents (pan/tilt camera agent, arm agent, etc.). The rock identification component detects rocks in images using a region growing algorithm. The executive agents build some 3D models to map the science targets' positions relative to the rover and calculate the kinematics of the onboard instruments (camera and arm), allowing them to access the science targets. Here, we present more details on the science mod-

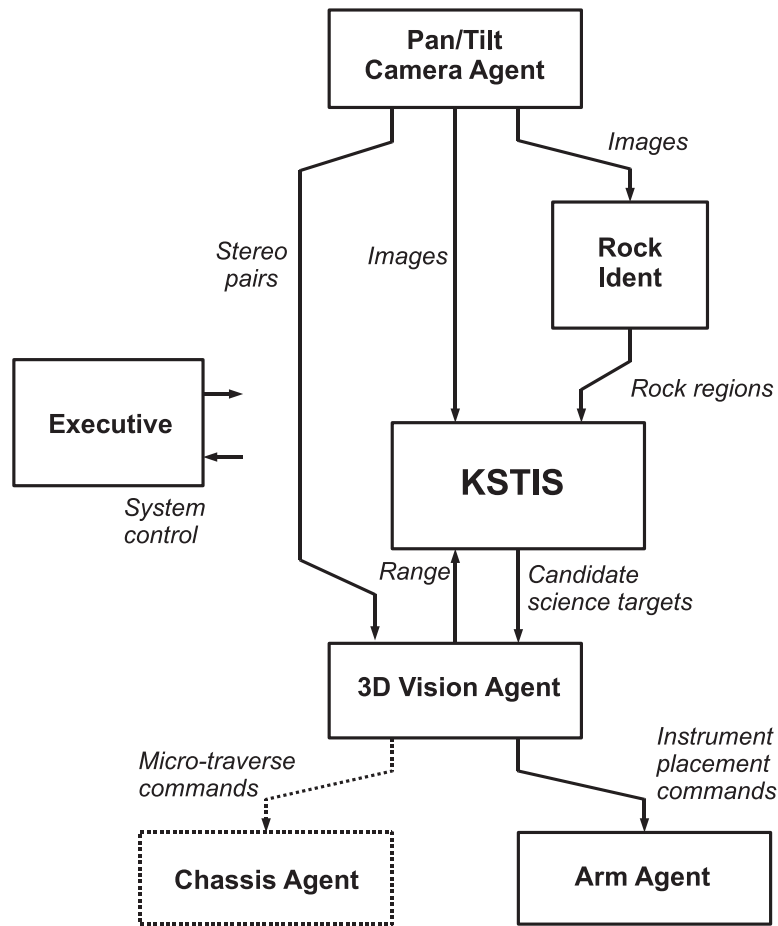


Figure 2.5: Schematic diagram of the ASTIA framework. Figure from [Barnes et al., 2009].

ule Knowledge-based Science Target Identification System (KSTIS) [Barnes et al., 2009; Pugh et al., 2010a], whose architecture is shown in Fig. 2.6.

It can be seen that the architecture of KSTIS is derived from the SARA system which classifies rock features/attributes into three categories: Structure, Texture and Composition. Specifically, unlike SARA which uses a contextual model to combine the science values of geological attributes, fuzzy logic [Zadeh, 1965] has been introduced into KSTIS. In other words, a fuzzy expert system has been established for the assessment of the science values of rocks. The introduction of the fuzzy concept not only makes the representation of combining features closer to the way that a real geologist makes a judgement but also reduces the uncertainty

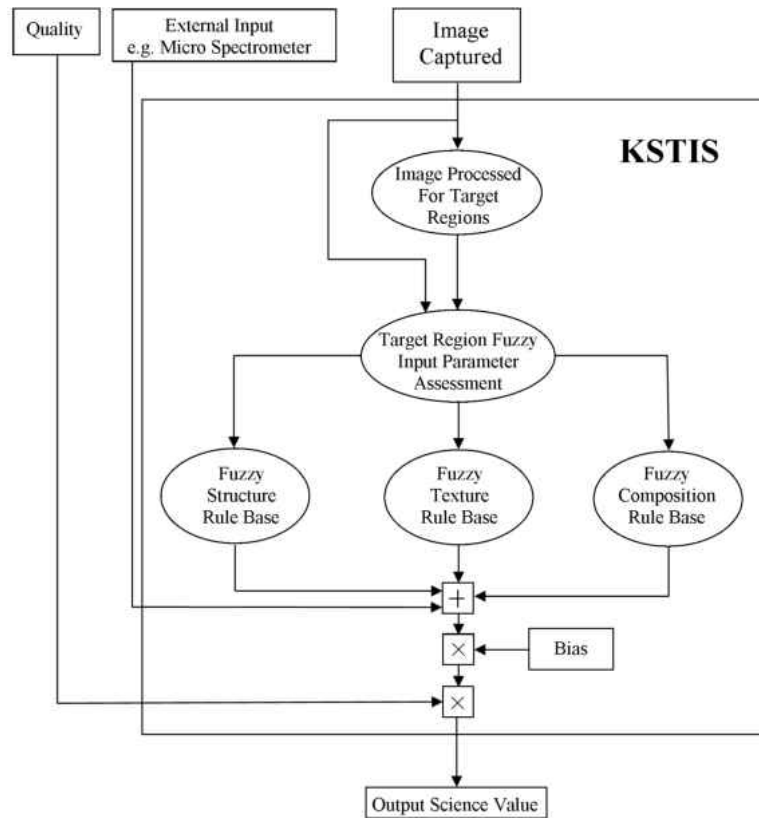


Figure 2.6: Architecture of KSTIS. Figure from [Pugh et al., 2010a].

encountered during target assessment. In the first version of KSTIS [Barnes et al., 2009], the inputs of the fuzzy system are albedo, colour, whiteness, roundness, surface, sphericalness, disk-likeness, rod-type, scale, stratification, curviness and lenticularity. The membership functions and relative rules have been designed in collaboration with a geological expert, through which the values of input features can be transferred to a final numerical science.

However, due to the difficulty of extracting the geological features/attributes information from images, only four of the twelve input parameters were calculated automatically (albedo, whiteness, colour and roundness) while the other eight needed humans to score them. Thus, KSTIS cannot be implemented without human interaction. Such a shortcoming has extended to the later version of KSTIS [Pugh et al., 2010a]. A tradeoff has been made which maintains the architecture of the fuzzy expert system (membership functions and rules) but receives inputs all provided by human being, thereby degrading the original system

for autonomous planetary exploration to an Earth-based tool for facilitating the assessment of rocks [Pugh, 2010].

2.5 Summary

This chapter has presented a comprehensive review of four existing autonomous science systems. A number of techniques¹ pertaining to image processing and machine learning have been involved into these systems, including edge detection, histogram, fuzzy system, etc. From the systems reviewed, much can be learned about how to develop an autonomous rock science system. The underlying architecture of the reviewed systems deeply inspire the framework development of our proposed system.

On the other hand, the systems presented above also have their shortcomings. For example, in OASIS and AEGIS, some visual features are arbitrarily specified to represent geological attributes. To overcome the shortcomings of previous systems, amelioration has been made in the proposed system whose details are described in the following chapters.

¹More techniques which are used to detect rocks and calculate rock science value but have not been used in any relatively integrated system are reviewed in Chapters 3 and 4 where they are relevant.

Chapter 3

Rock Detection

3.1 Introduction

It can be seen that, in many previous autonomous systems for rover-based planetary exploration, rocks are regarded as the most important science target. The rock detection is always the fundamental step, paving ways for subsequent components. Currently, the most common way to detect rocks is to identify rocks in images. Hence, the rock detection concept discussed in this chapter refers to the rock detection in images.

Rock detection faces many challenges. Firstly, “rock” is not a clearly defined object. Rocks were formed under different conditions and by different geological process. Sedimentary rocks and igneous rocks can be defined as “rocks” although they may look extremely different in shape, texture and colour. In addition, from large boulders to small pebbles, even tiny crumbs can be considered as rocks as well. Such a “vague” definition makes it difficult to label ground truth for rock detection. Moreover, even a given rock will look different under different light conditions. Different illuminations and directions of light will cause different shade and shadow. In addition, rocks will always be covered partially by sand/soil or occluded by other rocks, increasing the difficulty of rock detection as well.

Although challenges exist, many image processing methods have been proposed for identifying rocks in images. Here, some rock detection methods are reviewed, whether for planetary exploration or for non-planetary objectives.

The most straightforward rock detection methods are based on grayscale intensity thresholding [Castano et al., 2004; Crida and De Jager, 1994; Gor et al., 2001;

Mkwelo, 2004]. The distribution of intensity such as variance provides information to recognise rocks as well [Thompson et al., 2005b]. RGB colour, which can be regarded as 3-channel grayscale intensity, provides more information in rock recognition [Pedersen, 2000; Shaukat et al., 2013; Wagner et al., 2001]. In addition, derived colour features such as hue and saturation have also been applied for detecting rocks [Pan et al., 2013; Thompson et al., 2005a].

Edge information is another important part of features for rock detection. Many rock detection methods regard edges as the key feature to segment rocks [Gui et al., 2012; Song, 2008], including the detection algorithms in OASIS and AEGIS systems [Castano et al., 2007a; Estlin et al., 2009]. Unlike intensity information which describes rocks directly, the edge-based methods attempt to find the boundaries between rocks and background. The pixels enveloped by the boundaries will be labeled as rocks. Generally, the initially detected edges are discontinuous and hence extra algorithms are needed to link the edge fragments [Estlin et al., 2009; Gui, 2015].

Texture has also been used to generate the features in rock detection widely. Indeed, texture can describe rock surface more explicitly. The texture features that have been used for rock recognition include spatial frequency [Kachamuban and Udomhunsakul, 2007], Gabor filter features [Castano et al., 1999; Lepistö et al., 2003a], fractal dimension [Niekum, 2005] and gray-level co-occurrence matrix [Lepistö et al., 2003b; Partio et al., 2002; Wang, 1995].

Region-based methods have achieved good performance in rock detection. The related algorithms involve superpixel [Dunlop et al., 2007; Gong and Liu, 2012], region growing [Pugh et al., 2010a], and the watershed method [Farfán et al., 2001].

Geometry can be applied to determine the position of rocks in image. For example, [Gulick et al., 2001] proposed a rock detection method that need not detect rocks in an image directly but detects the shadows of rocks firstly. Once the shadows have been identified, they can be used to infer the locations of rock candidates with the time-of-day information. Another type of algorithm for detecting rocks is to extract 3D information through stereo images. Such method is especially suitable for searching for relatively large rocks [Di et al., 2013; Gor et al., 2001; Li et al., 2007; Pedersen, 2002].

Machine learning techniques have played an important role in rock detection, which can exploit the features mentioned above to generate better detection results. The machine learning methods used for rock detection include k-nearest neighbour (KNN) [Lepistö et al., 2006], K-means [Fink et al., 2008; Song and Shan,

2006], neural network [Gilmore et al., 2000], Bayesian belief network [Niekum, 2005; Pedersen, 2000], fuzzy-rough methods [Shang and Barnes, 2013; Shang et al., 2009], classifier combination [L. Lepistö et al., 2005] and support vector machine (SVM) [Shang and Barnes, 2010; Song, 2008; Thompson et al., 2005b].

Taking the previous works as reference, three new methods are proposed for detecting rocks in different aspects. The first method attempts to classify rocks and soil using multispectral data. The second method tries to find two adaptive thresholds by which the rocks can be segmented from the background. The third method refers to saliency concepts, intending to identify novel objects in images. Details of the three methods are discussed in Sections 3.2, 3.3 and 3.4 respectively.

3.2 Classification methods using spectral data

Classification methods have been widely used to identify rock regions from images. The process of classification is analogous to finding the differences between rocks and background. Generally, for each pixel in an image, a feature vector will be generated to represent the properties of the pixel. A feature vector can show obvious differences between rocks and the background and hence can be used to train a classifier with better classification results. Currently, the features that have been used for classification include pixel intensities and the relations between pixels (so-called texture features). Colour information has also been used in some publication [Shang et al., 2011; Thompson et al., 2005a]. However, to the best of the author's knowledge, no research refers to using multispectral features to detect rocks in a Mars environment.

Multispectral data can be acquired by the multispectral cameras that are carried by recent Mars rovers (MER Pancam [Bell et al., 2003] and MSL Mast-Cam [Bell et al., 2012]) and will be carried by some future Mars rovers (e.g. ExoMars PanCam [Griffiths et al., 2006]). In contrast to grayscale and RGB colour images, multispectral data can provide more information to represent the composition properties of rocks. Compared to texture or shape properties, composition of rocks is less affected by the surrounding environment (e.g. wind erosion) and hence is relatively invariant. Thus, as an indicator of rock composition, the multispectral data has potential to generate good features to identify rocks. Examples to show the multispectral differences between rocks and regolith are exhibited in Fig. 3.1. It can be seen that the spectra of rocks and regolith overlap at some wavelengths. If only the grey level image of the wavelength where the spectral values of rocks

and regolith are same or similar is used, it is hard to distinguish them. However, if multispectral data is introduced, the difference between them will be enlarged and hence better classification results could be expected.

On the other hand, rocks will often be covered by regolith dust, narrowing the difference between rocks and background. A rock will show diverse appearances under different light condition. Shadows or overexposure will also weaken the relationship between some multispectral features and the essence of a rock. Even so, it is believed that there exists some multispectral data or derived features that will always hold the differences between rocks and soil. Hence, a method inspired by [Shang and Barnes, 2013] is proposed to deal with the multispectral data. The flowchart of the method is given in Fig. 3.2.

As can be seen, the raw multispectral data is firstly transferred to R^* data, normalising the scale of reflection. A group of features are then derived from the R^* data. A feature selection method is applied to pick good features which can reflect the difference between rocks and regolith. The feature vectors of each pixel are generated using the selected features. Finally, with labeled ground truth, a classifier is trained, by which the rock regions are segmented from the background. Details of each process are presented below.

3.2.1 Raw data

The multispectral data used for the classification is captured by the Pancam of the MER Spirit rover. The raw data is downloaded from the NASA planetary data system (PDS) in the .img format. The .img file consists of not only spectral data but also the status information of data acquisition such as exposure time. Particularly, the downloaded data has been radiometrically-calibrated and hence no more radiometric correction is necessary.

The Pancam system of the Spirit rover (the same as the Opportunity rover) contains a pair of stereo cameras. A filter wheel with eight filter slots is mounted in front of each camera, providing the capability to capture multispectral images. The filters of left cameras (L1-L8) and right camera (R1-R8) are different. The detailed wavelength and bandpass of each filter are shown in Table 3.1. Particularly, the L1 filter slot is left empty to maximise sensitivity during low light. The L8 and R8 filter are designed as “solar” filters. They are used for direct sun imaging rather than rock/regolith imaging. On the other hand, the filters L2-L7 and R1-R7 are designed for geological purposes.

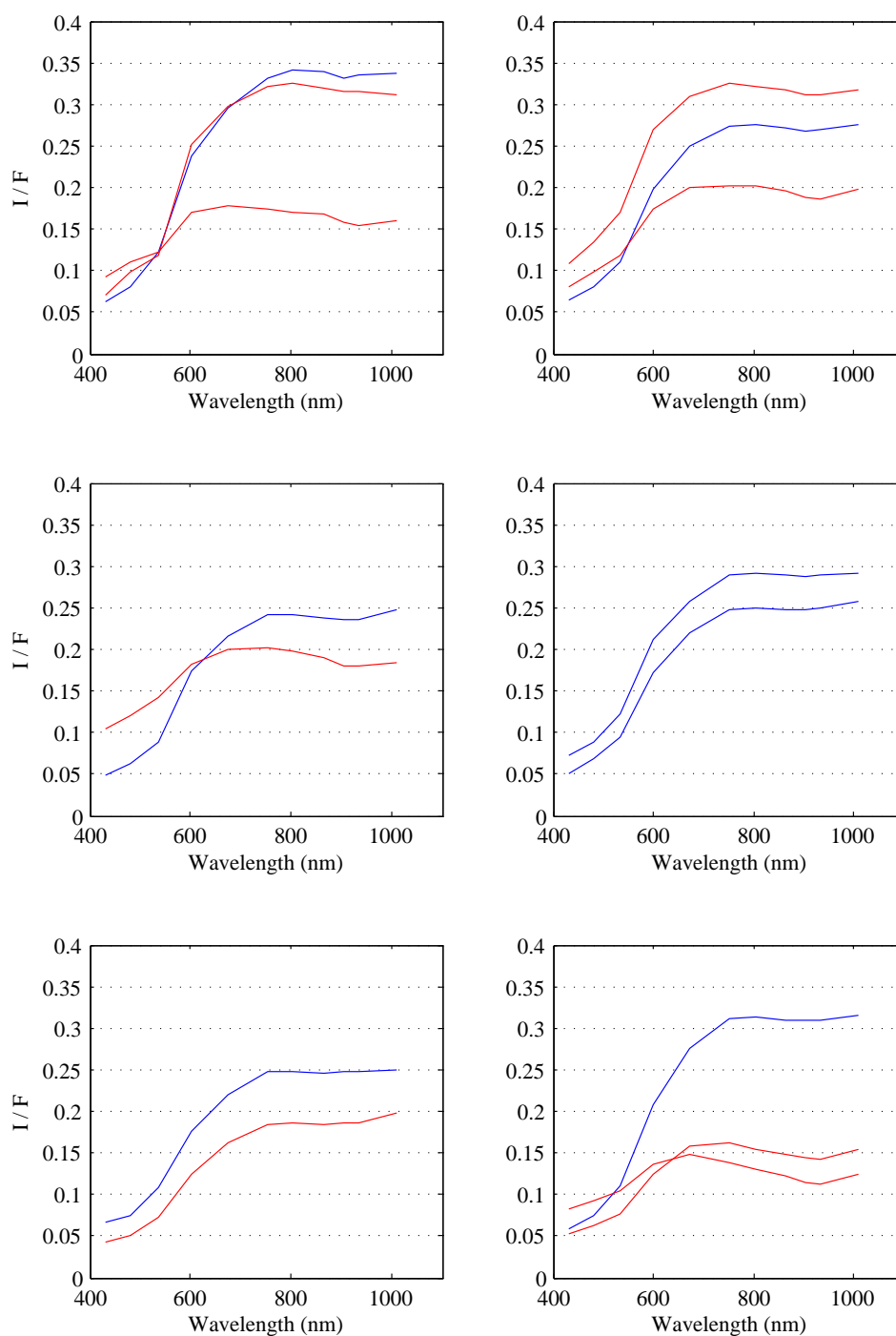


Figure 3.1: Some multispectral curves of rocks and regolith using I/F as the radiometric unit, where I is the measured radiance and πF is the incident irradiance of sunlight at the top of Martian atmosphere. Red curves represent rocks and blue curves represent soil (regolith). More details can be found in [Bell et al., 2004].

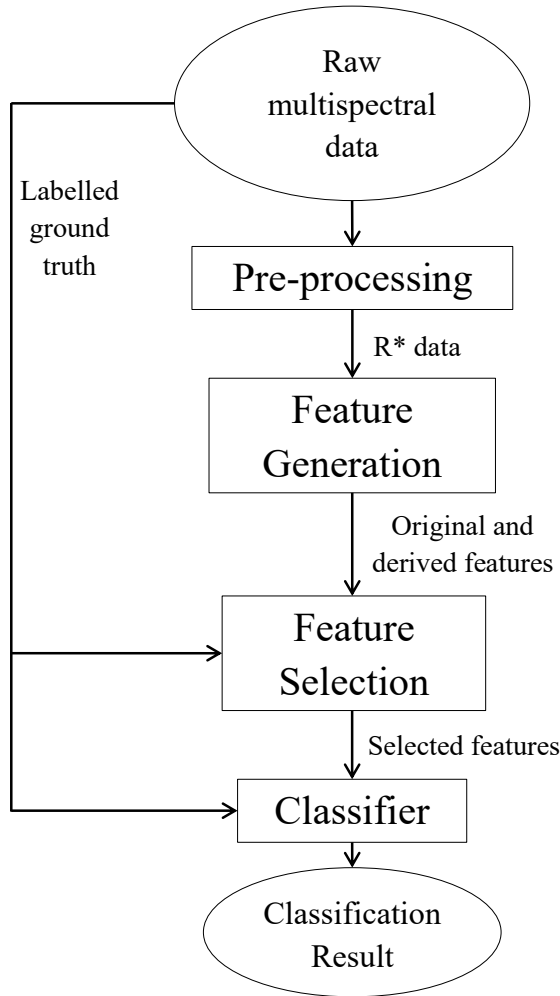


Figure 3.2: Flow chart of the proposed classification method

While the multispectral data is downloaded, the data of each filter can be transferred to a 512×512 image. The image pixel intensities reflect the response corresponding to the wavelength of the filter.

If the multispectral data of left and right cameras is used, it is necessary to use image registration techniques. In addition, as can be seen from Fig. 3.1, the curve portions become flat when the spectral values are greater than 800 nm. Thus, for convenience, we only choose the geological multispectral data sampled by the left camera (i.e. spectral data of filters L2 to L7, the spectral range from 432 nm to 753 nm) for experiments.

Table 3.1: MER Pancam filter characteristics

Left Camera			Right Camera		
Name	Wavelength (nm)	Bandpass (nm)	Name	Wavelength (nm)	Bandpass (nm)
L1	739	338	R1	436	37
L2	753	20	R2	754	20
L3	673	16	R3	803	20
L4	601	17	R4	864	17
L5	535	20	R5	904	26
L6	482	30	R6	934	25
L7	432	32	R7	1009	38
L8	440	20	R8	880	20

3.2.2 R^* data

R^* (“R-star”) was defined as “the brightness of the surface divided by the brightness of an RT (Radiometric Calibration Target) scaled to its equivalent Lambert reflectance” [Reid et al., 1999]. It can be calculated as follows:

$$R^* = I \times S_r + O_r \quad (3.1)$$

where I denotes the multispectral image (the intensities of the image indicate the spectral values). S_r denotes the radiance scaling factor and O_r denotes the radiance offset. Both S_r and O_r parameters have been packaged in the `.img` file. R^* data is useful as that it normalises spectra captured under varied lighting conditions, allowing for direct comparison between spectra taken at different times of day, and more straightforward comparison with laboratory spectra [Bell et al., 2006]. Such an uniformity also enables us to combine the data of images in different scenes together for the training of classifiers.

3.2.3 Feature generation

In this step, 24 features are extended from the R^* data. For easy cross-referencing, the features are labeled as Table 3.2.

As mentioned before, the original data used for the experiments is made up of the spectra of six wavelengths corresponding to the filters of left camera (L2 to L7). The R^* data of these spectra is firstly applied as the features. Specifically, the features are sorted in the ascending order of spectral wavelength. Thus, the first to sixth features correspond to the wavelength of 432nm, 482nm, 535nm, 601nm,

Table 3.2: Feature meaning and reference number

Feature No.	Meaning
1 – 6	Original spectral features
7 – 11	Slope features
12 – 13	Mean and variance
14 – 15	PCA features
16 – 18	CIEXYZ
19 – 21	RGB
22 – 24	CIELab

673nm and 753nm, respectively. These six features are called “original spectral features” since the other 18 features are derived from them.

The simplest derived features are the mean and variance of the original spectral features. The mean value can represent the overall intensity while the variance can reflect the fluctuation of spectra.

Spectral slope features are also extracted, denoting the difference between any two adjacent spectral values. For example, the slope between 432nm and 482nm is $(R_{*482\text{nm}} - R_{*432\text{nm}})$. As only differences between adjacent spectral data are considered, five slope features can be calculated from six original spectral features.

Principal component analysis (PCA) is a statistical procedure which can convert possibly correlated data into linearly uncorrelated variables (so-called principal components). It has been proven as a useful tool for interpreting compositional variation of MER spectral data [Anderson and Bell, 2013]. Hence, it can also be used to generate features from the original features¹. Originally, six original features can generate six derived features. However, in most cases in our data, through PCA, the proportion of the cumulative energy of the first two components is more than 99%. Accordingly, the last four features’ energy only occupies less than 1%, meaning that they express very little information. Hence, only the first two components generated from PCA are regarded as features, being called PCA features.

In addition, colour information can be used to generate features since all multispectral data we use are in the range of visible light. Hence, in this way, the spectral data is mapped to three 3-channel colour spaces: CIEXYZ, CIELab and RGB. The CIEXYZ space can reflect the light tristimulus values of the human eye.

¹The PCA processes in our experiments are performed on a per “image” basis. A so-called “image” is equivalent to six original spectral features.

The CIELab space represents lightness and colour information in different channels. The RGB space is the most popular space to represent colour in computer vision. The detailed procedure of mapping spectral data to colour space can be found in [Barnes et al., 2011]. After mapping, the value of each channel of each colour space is regarded as one feature. Thus, nine features are generated.

The feature generation of each pixel is independent, which means the features of a pixel are generated from the spectral values of that pixel and no information of neighbourhood pixels has been involved. After feature generation, a pixel can produce 24 features values and hence 24 feature maps can be generated from the original six spectral images. Here, examples of 24 visualised feature maps are shown in Fig. 3.3, by which the difference between features of rocks and soil can be observed. The reference numbers of the feature maps correspond to Table 3.2.

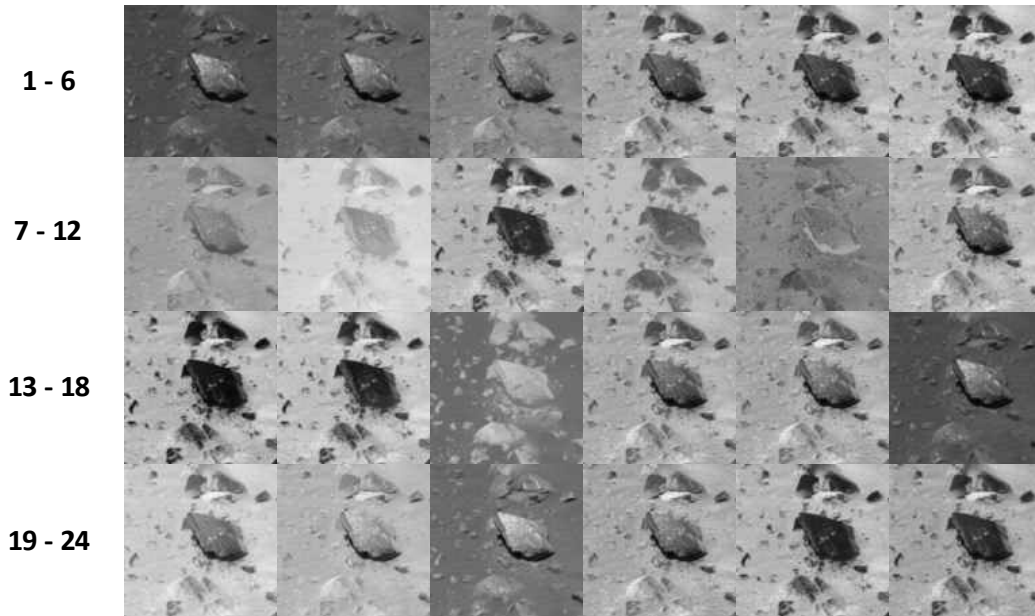


Figure 3.3: Examples of all 24 feature maps derived from the original spectral data. Some feature values are very small, and hence cannot be directly displayed by images. For illustration, we show here a normalisation of the original maps. The intensities displayed are therefore not equal but proportional to the real feature values.

It can be seen that the spectral information is enriched after the feature generation process. Thus, it is more likely to find features which clearly determine rocks. On the other hand, although the features are generated through different ways, some feature maps look very similar (e.g. 12th and 16th feature maps in Fig. 3.3).

Thus, a feature selection process is necessary for the purpose of selecting good features which can separate rock and regolith regions efficiently and also removing redundant features which represent spectral information in similar ways.

3.2.4 Feature selection

Feature selection (FS) [Dash and Liu, 1997; Jensen and Shen, 2008] addresses the problem of selecting the features that are most informative. It is highly recommended to have a feature selection process before training classifiers. Firstly, it can find out less informative features which cannot discriminate rocks and background (e.g. noise). Through removing those bad features, the distance between foreground (i.e. rocks) and background will be increased and hence the accuracy of classification may be improved. Moreover, the redundancy of the data can be decreased through a feature selection process. The complexity of classifiers can therefore be reduced, increasing the training and prediction efficiency.

In this thesis, a fuzzy-rough feature selection (FRFS) algorithm based on fuzzy similarity relations is applied for selecting informative features which can facilitate separating rocks from the background. The reason for using this FS method is because it has successfully been used for Mars *McMurdo* image classification [Shang and Barnes, 2013]. Details of the method can be found in [Jensen and Shen, 2009].

3.2.5 Classifiers

Four classic classification methods were applied to train the classifier to identify rocks. These are: K-nearest neighbours (KNN), naive Bayes (Bayes), decision tree (Dtree) and support vector machine (SVM) with Sequential Minimal Optimization (SMO).

The KNN algorithm is one of the simplest learning methods for constructing classifiers. The training phase of the algorithm consists only of storing the feature vectors and class labels of the training samples. During the classification phase, unlabeled data is classified by assigning the most frequent label among the K training samples most similar to the unlabeled data. Particularly, in our experiment, the parameter K is defined as 1 and 5, which will be mentioned as 1NN and 5NN in the experiment section.

The Naive Bayes classifier is a probabilistic classifier. The posterior probability of each class is calculated by the prior probabilities based on Bayes' theorem in

the training phase. The unlabeled data is then assigned to the class which has the highest posterior probability (so-called maximum likelihood).

A decision tree-based classifier uses a tree-like model to determine the classes of unclassified data. The tree model is learnt from training data through an iterative process of choosing features and splitting them. In this research, the popular J48 algorithm [Mitchell, 1997] is used to generate decision trees.

The support vector machine method firstly maps original training data to a high-dimensional space and then tries to find a hyperplane which can split the data with the largest distance between data points and hyperplane. In this research, the sequential minimal optimisation method [Platt, 1998] is used to optimise the training of SVM methods.

In addition, the clustering method K-means is also involved in the experiment. K-means clustering, as an unsupervised method, does not need labeled ground truth for training. It only partitions the observations (unlabeled data) into K clusters in which each observation belongs to the cluster with the nearest mean. In our experiments, two classes of rocks and regolith are required, and hence the parameter K of clustering is set to two, meaning that only two clusters need to be created.

3.2.6 Experiments, results and evaluation

Three experiments have been conducted to test the algorithms. The first experiment performed feature selection and classifier training image-independently and hence is called “local”. Parts of an image were labeled as ground truth for selecting features and training classifiers. Then the trained classifiers were used to predict the rock regions in the whole image. The second “global” experiment addressed the data of several images in a specified scene rather than of a single image. Thus the trained classifiers could be suitable for predicting the rock regions in the scene. Finally, in the third experiment, the selected feature numbers were inherited from the first and second experiments and a 2-means clustering method was used on unlabeled data to partition them into two clusters corresponding to rocks and regolith.

The qualitative evaluation of the detection results mainly focused on five multispectral images. The detection results were illustrated by binary images: rock regions were represented by white pixels and regolith regions were represented by black pixels. In terms of quantitative evaluation, the rock regions in images were

labeled for evaluating corresponding performance. Like general pattern recognition systems, the *Precision/Recall* coefficients were used to judge the detection results quantitatively. *Precision* refers to the proportion of detections that are actually true, while *Recall* denotes the proportion of regions in the image that are detected. In addition, the F_1 score is applied to balance those two evaluative indicators as well, which is the harmonic mean of *Precision* and *Recall*:

$$F_1 = 2 \cdot \frac{\textit{Precision} \cdot \textit{Recall}}{\textit{Precision} + \textit{Recall}} \quad (3.2)$$

Because the F_1 score can comprehensively evaluate the performance of rock detection, it is regarded as the primary index for evaluating the detection performance.

On the other hand, because that parts of rock regions are small and scattered and that some boundaries between rocks and regolith are vague, the ground truth was not labeled perfectly. The contours of labeled rock regions may not be the real rock boundaries and some tiny rocks were discarded. Such imperfect labeled ground truth would lead to some biases in quantitative evaluation. These biases could be mainly reflected in the decrease of *Precision* because that the tiny rocks which could be detected have not been labeled.

3.2.6.1 Image-based “local” rock detection

This experiment is called “local” as it just addresses rock detection problems based on single images. It means that, for the rock detection of one image, the training data (for feature selection and classification) were all extracted from the image. In terms of the training settings of this experiment, 100 pixel positions of rock and regolith regions were labeled in each image manually, 50 pixels for rocks and 50 pixels for regolith. From the pixel position, ground truth feature vectors were extracted for later feature selection and classifier training. For one image, the labeled data occupied a proportion less than 0.2% of all data. These labeled data can indicate the difference of rocks and regolith, by which efficient features can be selected and classifiers can be trained. After training, the classifiers were used to predict the classes of unlabeled pixels in the images. Here, some detection results (predictions) using different classifiers are illustrated in Fig. 3.4. The corresponding selected feature numbers of each image are also given.

The average quantitative performance of the five classifiers is listed in Table 3.3. It can be seen that, all classifiers generate detection results with high *Precision*






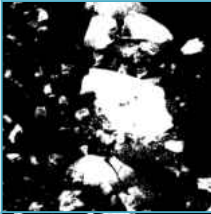

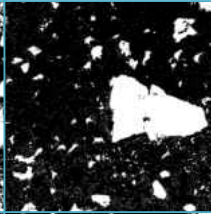
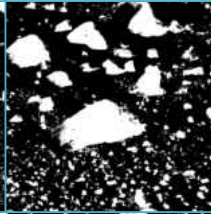



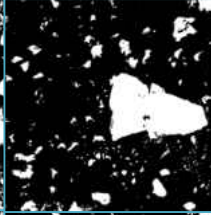
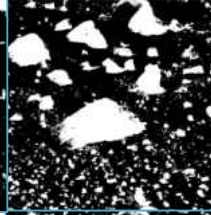



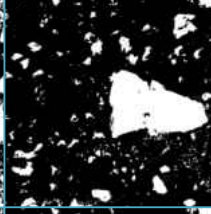
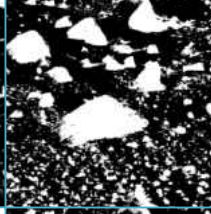
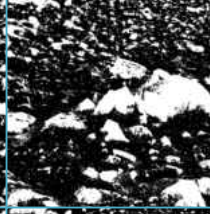


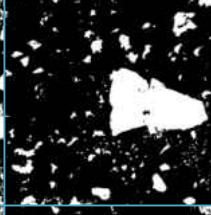
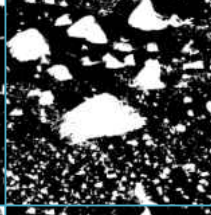



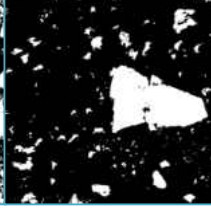
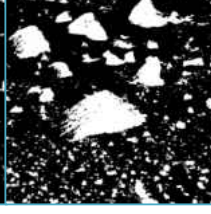
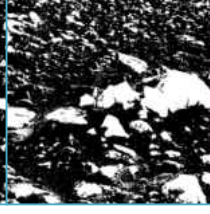
Colour Image					
Selected Features	4, 10	1, 7, 11, 13, 23	1,3,7,10,11,12	1, 14	5, 10, 15, 21
INN					
SNN					
Bayes					
SMO					
J48					

Figure 3.4: “Local” selected features and the classification results by these features using different classification algorithms

even if the imperfect labeled ground truth may affect the accuracy. In particular, comprehensively considering the *Precision* and *Recall* evaluation (i.e. the F_1 measure), the Bayes classifier obtained the best detection performance.

Table 3.3: Quantitative performance comparison between classifiers

Classifier	<i>Precision</i>	<i>Recall</i>	F_1
1NN	0.87	0.783	0.824
5NN	0.93	0.767	0.841
Bayes	0.909	0.818	0.862
SMO	0.946	0.743	0.832
J48	0.918	0.695	0.791

Moreover, another experiment has been done to test the efficacy of feature selection. For simplicity, the Bayes classifier was chosen as the only classifier in this experiment. The classification results of selected feature sets¹, full feature sets², original feature sets³ and some random feature sets⁴ are compared qualitatively and quantitatively. The comparison is shown in Fig. 3.5.

It can be seen that, compared to using original spectral features directly, the processes of feature generation and selection can indeed improve the detection performance, especially the *Precision* performance. In addition, judged by the comprehensive measure F_1 , the classification results using the selected feature sets generates best performance, even slightly better than classification results using full features. It proves that, through the feature selection method, we can not only obtain feature sets with reduced number of features but also feature sets containing efficient features which can facilitate classifier training. Hence both the speed and performance of classifiers trained by the selected features could be improved.

3.2.6.2 Scene-based “global” rock detection

In the “local” classification, although having generated competent performance, the rock detection of an image is based on the image itself. Therefore, an attempt

¹i.e. the feature set with selected feature(s).

²A full feature set denotes the feature set containing all generated features (i.e. all 24 features listed in Table 3.2).

³An original feature set denotes the feature set only containing the six original spectral features (i.e. the 1-6 features listed in Table 3.2).

⁴A random feature set denotes a feature set containing random selected features (different to selected feature set). Specifically, to reflect the efficacy of feature selection, the feature number of the random feature sets using in the experiment are same to the selected feature set.




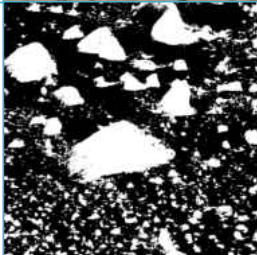

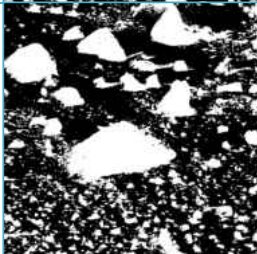

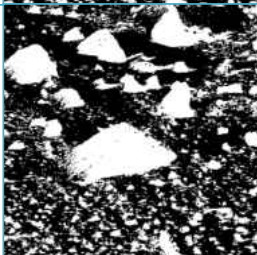

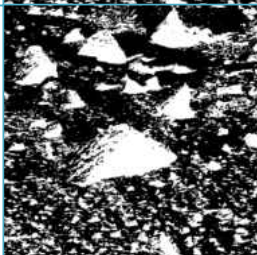
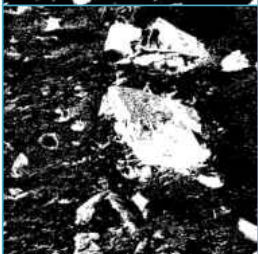

Colour Image		
Selected Features	 <i>Precision</i> = 0.956 <i>Recall</i> = 0.648 $F_1 = 0.773$	 <i>Precision</i> = 0.918 <i>Recall</i> = 0.923 $F_1 = 0.921$
Full Features	 <i>Precision</i> = 0.951 <i>Recall</i> = 0.645 $F_1 = 0.769$	 <i>Precision</i> = 0.833 <i>Recall</i> = 0.943 $F_1 = 0.885$
Original Features	 <i>Precision</i> = 0.943 <i>Recall</i> = 0.653 $F_1 = 0.772$	 <i>Precision</i> = 0.793 <i>Recall</i> = 0.92 $F_1 = 0.852$
Random Features 1	 <i>Precision</i> = 0.951 <i>Recall</i> = 0.619 $F_1 = 0.75$	 <i>Precision</i> = 0.72 <i>Recall</i> = 0.789 $F_1 = 0.753$
Random Features 2	 <i>Precision</i> = 0.764 <i>Recall</i> = 0.573 $F_1 = 0.655$	 <i>Precision</i> = 0.743 <i>Recall</i> = 0.791 $F_1 = 0.766$

Figure 3.5: Detection results of selected feature subset and other feature sets. All detections are through Bayes classifiers.

has been made to establish a “global” classifier for a certain scene on Mars. For such a purpose, we mixed the labeled ground truths of five images in a same scene together and hence obtained a training set which has 250 rock instances and 250 soil instances. After feature selection, a reduced feature set was generated which contains eight features: 1, 4, 7, 10, 11, 13, 15 and 23. As the labeled data was extracted from different images in a scene, the corresponding selected features could probably reflect the “global” differences between rock pixels and regolith pixels. A classifier was then trained selected feature vectors through the Bayes method. The performance of this classifier on the five images which contain labeled pixels is shown in Fig. 3.6.

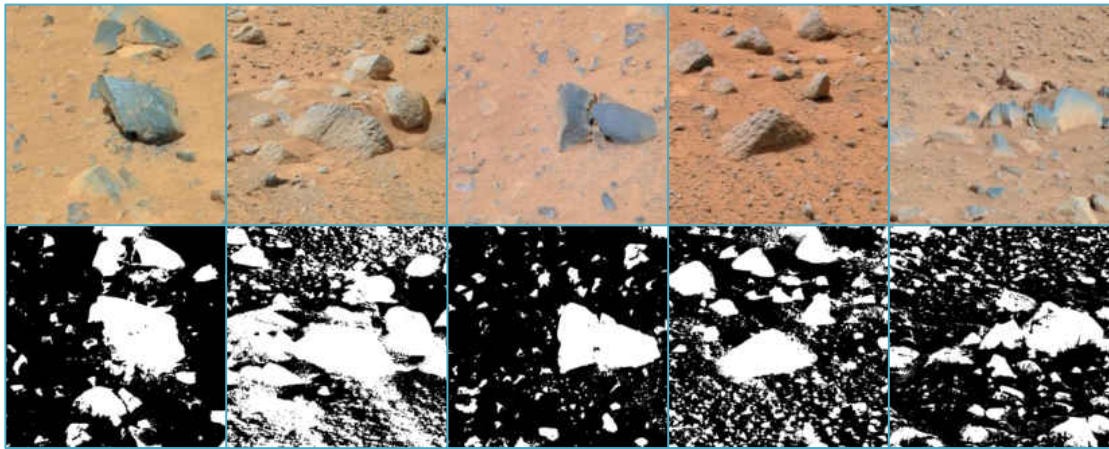


Figure 3.6: “Global” classification results of the five images in which ground truth were labeled

It can be seen that, although only using one classifier, the rock regions in all five images can be detected properly. The average *Precision* and *Recall* of the “global” detection results were 0.898 and 0.823, hence obtaining an overall F_1 measure about 0.859 which was just slightly lower than the “local” results (see Table 3.3). It proves that, through our method, the “global” classifier can be generated to identify rocks. In addition, we tested the “global” classifier on some Mars images which were captured from the same scene as the five training images but not used in the training stage. An example of the detection result is shown in Fig. 3.7. The average *Precision*, *Recall* and F_1 of the detection results on those non-training images have reached 0.896, 0.808 and 0.849 respectively which are very closed to the performance of training images. It indicates that a classifier trained by a part of images in a specified scene can really identify the difference

between rocks and regolith in the scene and hence can be used to predict rock regions in the scene.



Figure 3.7: Detection result of a non-training image

3.2.6.3 Cluster results by selected features

Besides the classification approaches, cluster methods can be used to distinguish rock and regolith regions. A 2-class cluster can perform detection faster than classification methods because no training phase is needed. Here, the 2-means (i.e. two cluster K-means) method was applied as the clustering demonstrator. The clusterings were carried on both “local” and “global” selected feature sets. In addition, clusterings using full feature sets, original feature sets and random feature sets have been done as well. The comparison of clustering results using different feature sets is shown in Fig. 3.8.

It can clearly be seen that the detection results of the feature sets after selection, whether global or local, have generated better performance. In particular, rocks in the right column images, although covered by dust, can be clustered into the rock part using selected features. On the other hand, if feature selection is not performed, the corresponding clustering was affected severely by the dust coating, making the detection performance worse. In addition, clustering results using selected features performed even better than the results of clustering using full feature sets. It proves that, through feature selection, the features which highlight the difference between rocks and regolith will be extracted and irrelevant features will be removed. Using those selected features, better clustering results can be expected.





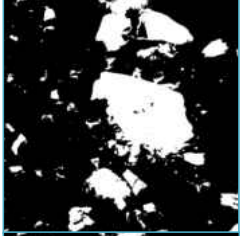


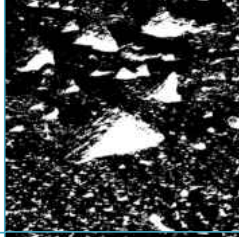

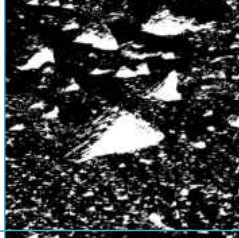

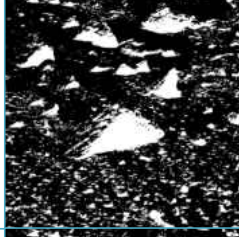

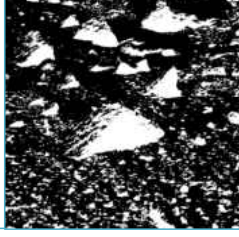
Colour Image		
Local Features	 <p><i>Precision</i> = 0.961 <i>Recall</i> = 0.601 F_1 = 0.739</p>	 <p><i>Precision</i> = 0.858 <i>Recall</i> = 0.865 F_1 = 0.862</p>
Global Features	 <p><i>Precision</i> = 0.964 <i>Recall</i> = 0.579 F_1 = 0.723</p>	 <p><i>Precision</i> = 0.823 <i>Recall</i> = 0.841 F_1 = 0.832</p>
Full Features	 <p><i>Precision</i> = 0.97 <i>Recall</i> = 0.541 F_1 = 0.694</p>	 <p><i>Precision</i> = 0.847 <i>Recall</i> = 0.622 F_1 = 0.717</p>
Original Features	 <p><i>Precision</i> = 0.969 <i>Recall</i> = 0.536 F_1 = 0.69</p>	 <p><i>Precision</i> = 0.841 <i>Recall</i> = 0.604 F_1 = 0.703</p>
Random Features 1	 <p><i>Precision</i> = 0.962 <i>Recall</i> = 0.482 F_1 = 0.642</p>	 <p><i>Precision</i> = 0.816 <i>Recall</i> = 0.604 F_1 = 0.694</p>
Random Features 2	 <p><i>Precision</i> = 0.537 <i>Recall</i> = 0.695 F_1 = 0.606</p>	 <p><i>Precision</i> = 0.803 <i>Recall</i> = 0.708 F_1 = 0.753</p>

Figure 3.8: Clustering results using different feature sets

3.2.7 Summary

In this section, a rock detection approach based on multispectral data is proposed. The concepts of feature extension (generation), feature selection and classification have been involved in this approach. By visual observation and quantitative evaluation, the method has the potential to deal with the rock detection with relatively high accuracy. Currently, the spectral data used for the experiments is only captured by the filters of the left camera of the MER rover. In future work, through image registration, the spectral information of the right camera can be used to enrich the original data. In addition, more features can be derived in the feature generation phase such as band depth and red/blue ratio [Anderson and Bell, 2013]. Thus more optimised feature sets can be expected by which better classification or clustering performance may be obtained.

3.3 Two-threshold methods

Although multispectral data can provide more information, efforts towards rock detection are mainly made on grayscale images. Compared to multispectral images, grayscale images are easier to acquire. Not only the panoramic cameras (Pancam), the navigation cameras and other cameras on rovers can also be used to capture gray level images. In addition, although containing less content, by applying appropriate algorithms, rock detection using grayscale images can probably gain similar results to the detection using multispectral data in less time thereby being more suitable for on-board implementations. Thresholding methods, as the most classic and straightforward image segmentation methods, may be regarded as the fast methods to deal with the rock detection problem in grayscale images.

A grayscale Mars rock image with its histogram is illustrated in Fig. 3.9. As can be seen, rocks will be influenced more strongly by sunlight. The surfaces of rocks are relatively smooth and hence cause direct (specular) reflection rather than diffuse reflection more frequently. In addition, due to the sizes and shapes of rocks, sunlight is likely to be blocked thereby generating shadows. Therefore, in contrast with soil (regolith) regions, the intensities of rock regions will be darker or brighter. This phenomenon can be reflected in histograms. The regions of rocks are located in the two sides of the histogram, and the centre region of histogram represents regolith. Thus, to separate rock and soil regions, traditional thresholding methods which only use one threshold are not suitable.

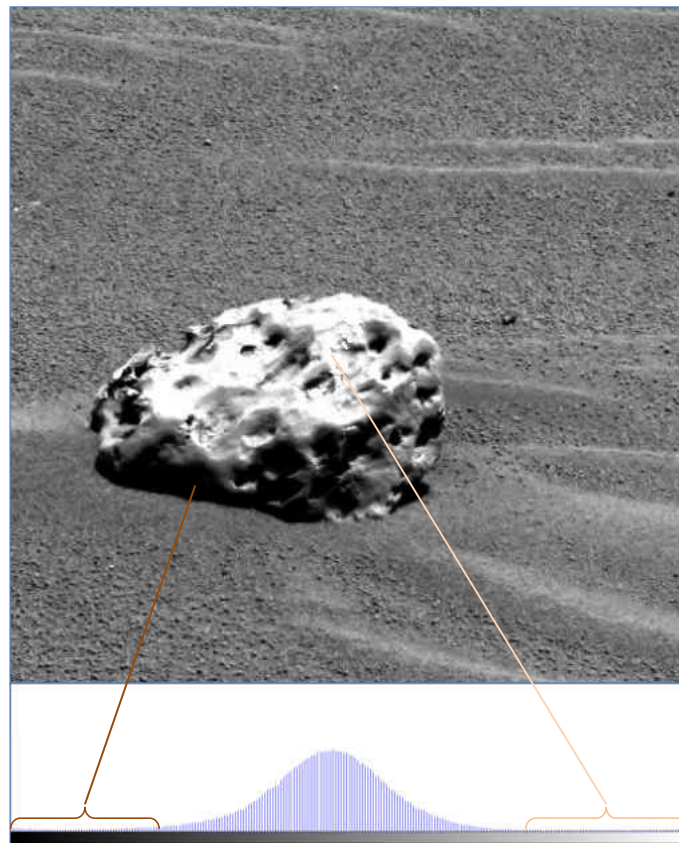


Figure 3.9: Grayscale image of the famous Mars “Heat Shield” rock (meteorite) and its histogram. The rock region is divided into a dark part and a bright part.

Hence, a series of two-threshold thresholding algorithms are proposed and reviewed, which are able to segment the pixels of images into three parts representing dark rock regions, background regions and bright rock regions respectively. The pixels with intensity values below the low-threshold or above the high-threshold are regarded as the rock pixels and the region between the two thresholds represents the background (regolith) pixels.

3.3.1 Algorithms

The most traditional thresholding method is the Otsu algorithm [Otsu] which originally aims at bi-level (one threshold) thresholding. From the original one-threshold Otsu method, the two-threshold Otsu method (TO) has been derived [Liao et al., 2001]. In addition, six new two-threshold methods are proposed. There are: **Re-**

stricted two-threshold Otsu method (RTO1), Restricted two-threshold Otsu method with new σ_B^2 (RTO2), Two-fold Otsu method (TFO), Probability ratio method (PR), Normal distribution method (ND) and Direct probability method (DP). The details of these methods are described below. In addition, since some proposed methods are related to the original Otsu method (Otsu) and the two-threshold Otsu method (TO), the details of those are also reviewed.

3.3.1.1 Otsu's method (Otsu)

Since some proposed two-threshold algorithms are derived from the traditional Otsu algorithm, here we introduce the one-threshold thresholding method firstly.

An image contains N pixels whose gray levels range from 1 to L . Supposing that the number of pixels with the i th gray level is n_i , the probability of the i gray level, p_i , can be defined as:

$$p_i = n_i/N \quad (3.3)$$

To divide the pixels of an image into two classes C_1 and C_2 , a threshold t is selected. Thus, C_1 contains gray levels $[1, \dots, t]$ and C_2 contains gray levels $[t + 1, \dots, L]$. The probabilities of the two class ω_1 and ω_2 are:

$$\omega_1 = \sum_{i=1}^t p_i \quad (3.4)$$

$$\omega_2 = \sum_{i=t+1}^L p_i \quad (3.5)$$

Also, the mean intensities μ_1 and μ_2 of the two classes are:

$$\mu_1 = \sum_{i=1}^t i p_i / \omega_1 \quad (3.6)$$

$$\mu_2 = \sum_{i=t+1}^L i p_i / \omega_2 \quad (3.7)$$

Thus, the mean intensity of the whole image μ_T can be obtained as:

$$\mu_T = \mu_1\omega_1 + \mu_2\omega_2 \quad (3.8)$$

Otsu defined the between-class variance σ_B^2 as:

$$\sigma_B^2 = \omega_1(\mu_1 - \mu_T)^2 + \omega_2(\mu_2 - \mu_T)^2 \quad (3.9)$$

An alternative function of the bi-level between-class variance is:

$$\sigma_B^2 = \omega_1\omega_2(\mu_2 - \mu_1)^2 \quad (3.10)$$

Then, through exhaustive search, the threshold t^* with maximum σ_B^2 is chosen.

$$t^* = \operatorname{argmax}_{1 \leq t < L} \sigma_B^2(t) \quad (3.11)$$

As the Otsu's definition, t^* is the threshold giving the best separation of the classes in gray levels.

3.3.1.2 Two-threshold Otsu method (TO)

To solve multi-threshold problems, Eqn. (3.9) can be extended. Assuming that there are $M-1$ thresholds (t_1, \dots, t_{M-1}), which divide an image into M classes, the between-class variance can be rewritten as follows [Liao et al., 2001]:

$$\sigma_B^2 = \sum_{k=1}^M \omega_k(\mu_k - \mu_T)^2 \quad (3.12)$$

In our case, two thresholds t_1 and t_2 are required, and hence σ_B^2 is defined as:

$$\sigma_B^2 = \omega_1(\mu_1 - \mu_T)^2 + \omega_2(\mu_2 - \mu_T)^2 + \omega_3(\mu_3 - \mu_T)^2 \quad (3.13)$$

Thus, the best threshold set $\{t_1^*, t_2^*\}$ should satisfy the condition that the σ_B^2 in Eqn. (3.13) reaches the maximum value.

$$\{t_1^*, t_2^*\} = \operatorname{argmax}_{1 \leq t_1 < t_2 < L} \sigma_B^2 \quad (3.14)$$

To distinguish with other methods derived from the original Otsu method, we

named this method as two-threshold Otsu method (TO).

3.3.1.3 Restricted two-threshold Otsu method (RTO1)

It can be found that, in most Mars images, soil pixels are in the majority. Therefore, we make a supposition that the gray level with highest probability p_{max} is the gray level which represents background. This gray level is defined as t_{most} . As mentioned above, the region between t_1 and t_2 corresponds to the background part. Hence, t_{most} must be in the position between t_1 and t_2 . By adding this restriction, it can be ensured that the background part includes the background gray level t_{most} thereby avoiding the wrong segmentation in which the two thresholds are both on the same side. The function to search for the optimal thresholds t_1^* and t_2^* can be expressed as:

$$\{t_1^*, t_2^*\} = \underset{1 \leq t_1 < t_{most} < t_2 < L}{\operatorname{argmax}} \sigma_B^2 \quad (3.15)$$

in which σ_B^2 is expressed in Eqn. (3.13). Since this method adds a restriction, we called it the restricted two-threshold Otsu method (RTO1).

3.3.1.4 Restricted two-threshold Otsu method with new σ_B^2 (RTO2)

Derived from the Eqn. (3.10) which is for the bi-level situation, a new measure $\sigma_{B^*}^2$ is derived from Eqn. (3.10) for tri-level situation, defined as:

$$\sigma_{B^*}^2 = \omega_1 \omega_2 (\mu_2 - \mu_1)^2 + \omega_3 \omega_2 (\mu_3 - \mu_2)^2 \quad (3.16)$$

This equation does not contain the mean intensity of the whole image μ_T , only considering the differences between classes. The first term relates to the between-class variance between dark foreground and background and the second term relates to the between-class variance of background and light foreground. The term $\omega_1 \omega_3 (\mu_3 - \mu_1)^2$ has been ignored because it is only related to the foreground. Using $\sigma_{B^*}^2$ rather than σ_B^2 , Eqn. (3.15) can be applied to calculate the optimum thresholds t_1^* and t_2^* . To distinguish with the restricted two-threshold Otsu method (RTO1), this method is abbreviated as RTO2.

3.3.1.5 Two-fold Otsu method (TFO)

As supposed above, the gray level t_{most} must be included into the background. Using t_{most} as the boundary, the pixels in an image are segmented into 3 parts: the dark part with the gray levels $[1, \dots, t_{most} - 1]$, the bright part with the gray levels $[t_{most} + 1, \dots, L]$ and the part with the gray level t_{most} . Thus, we can apply the traditional Otsu algorithm on the dark part and the bright part respectively. By such an approach, two thresholds can be generated on both sides of t_{most} . One threshold t_1 divides the dark part into the dark foreground part ($[1, \dots, t_1]$) and the dark background part ($[t_1 + 1, \dots, t_{most} - 1]$). Likewise, the other threshold t_2 can divide the light part into the light background part ($[t_{most} + 1, \dots, t_2]$) and the light foreground part ($[t_2 + 1, \dots, L]$). Finally, the background (regolith) region is composed of the dark background part, the light background part and the t_{most} part and hence the gray level range of the background is from $t_1 + 1$ to t_2 . Accordingly, the gray levels ($[1, \dots, t_1]$) and ($[t_2 + 1, \dots, L]$) represent rock region. Since this method folds the gray levels and performs twice Otsu operation respectively, it is named as two-fold Otsu methods (TFO). The schematic diagram of TFO method is illustrated in Fig. 3.10.

3.3.1.6 Probability ratio method (PR)

Through observing histograms of Mars images (e.g. Fig. 3.11), it can be found that the shape of the histogram which represents the background is relatively steep and the shape of the foreground (rock region) histogram is relatively flat. Hence, a method is proposed to distinguish background (regolith) and foreground (rock) using the shape of the histogram. Hence, we defined a parameter named as probability ratio (pr), which denotes the ratio of the probabilities of two adjacent gray levels. For convenience, pr_i of the gray level i is calculated in different directions on the two sides of t_{most} , defined as:

$$pr_i = \begin{cases} p_{i-1}/p_i & \text{if } i < t_{most} \\ p_{i+1}/p_i & \text{if } i > t_{most} \end{cases} \quad (3.17)$$

The probability ratio pr can reflect the variation degree of the probability of adjacent gray levels. If pr is far larger than 1, a steep histogram shape is detected. On the other hand, pr near to 1 means that similar values are detected and hence indicate that the corresponding region is relatively flat. Thus, a parameter p_R was

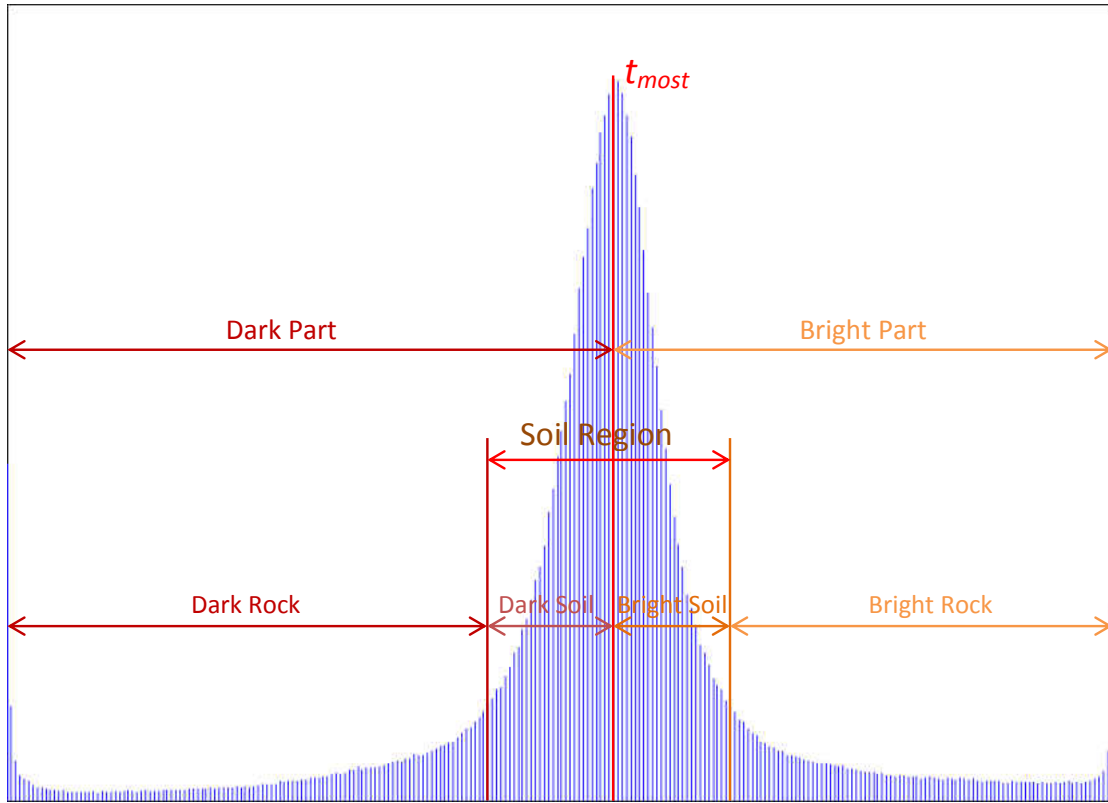


Figure 3.10: Schematic diagram of the two-fold Otsu method

introduced to determine if a gray level is in the flat region. To avoid the gray level fluctuations near t_{most} , those gray levels with probabilities higher than the half of p_{max} were extracted into a set T . In the set T , the minimum and maximum gray levels t'_1 and t'_2 are chosen as the initial gray levels to search for t_1^* and t_2^* . Thus, in the region $[1, \dots, t'_1]$, the probabilities of the gray levels were approximately monotonically increasing and conversely approximately monotonically decreasing in the region of gray level $[t'_2, \dots, L]$. Starting from gray level t'_1 to 1, if the pr values of three consecutive gray levels are larger than the parameter p_R , it can be considered that the gray level has entered into a flat region, and thus the optimal t_1^* was the first gray level in the flat region. Likewise, t_2^* can be found out as the boundary between the steep part and the flat part in the range of $[t'_2, \dots, L]$. Since the probability ratio was introduced in this method, we named this method the probability ratio method (PR).

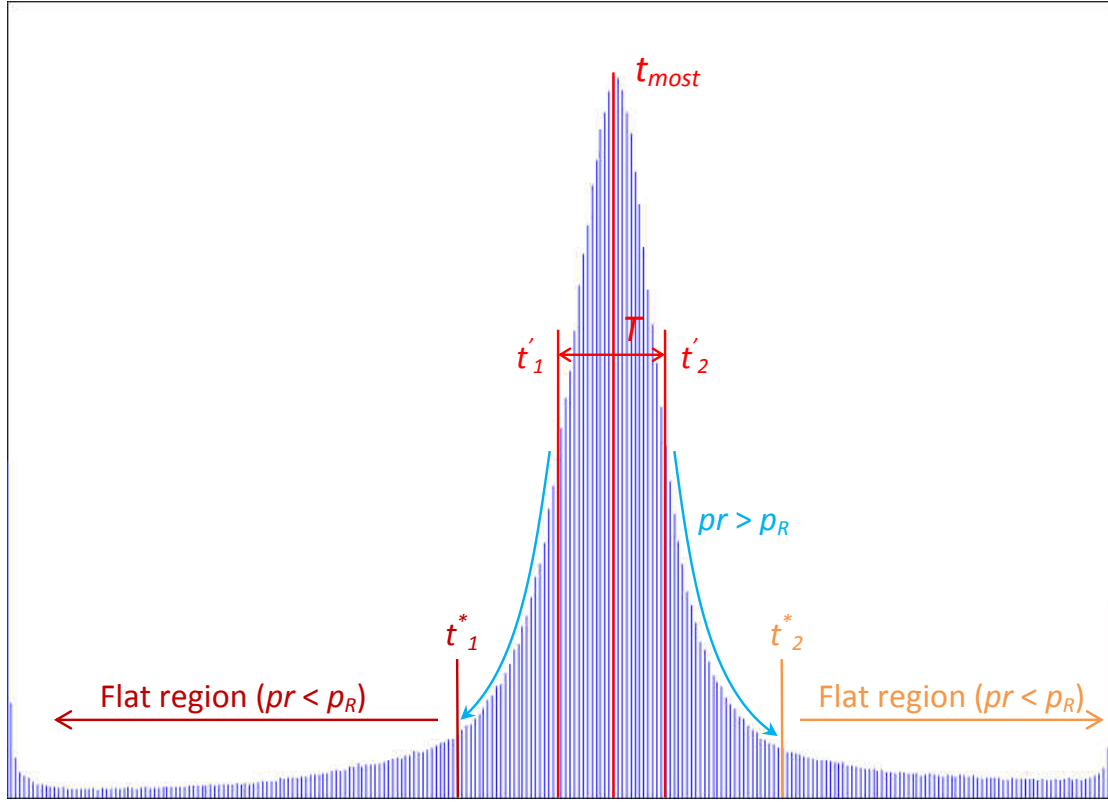


Figure 3.11: Schematic diagram of the probability ratio method

3.3.1.7 Normal distribution method (ND)

As can be seen in Fig. 3.12, the histogram has a shape similar to that of a normal distribution. Thus, the normal distribution method (ND) is proposed under the assumption that the gray levels of the background follow a normal distribution. Thus, the mean μ_T and the standard deviation σ_T of all pixels of an image can be calculated to describe the shape of the histogram. Hence, inspired by the tolerance interval concept in statistics, a scale factor r is introduced to scale the impact of σ_T , thereby determining the gray level interval of the background. Specifically, the thresholds t^*_1 and t^*_2 can be calculated as follows:

$$t^*_1 = \mu_T - r \sigma_T \quad (3.18)$$

$$t^*_2 = \mu_T + r \sigma_T \quad (3.19)$$

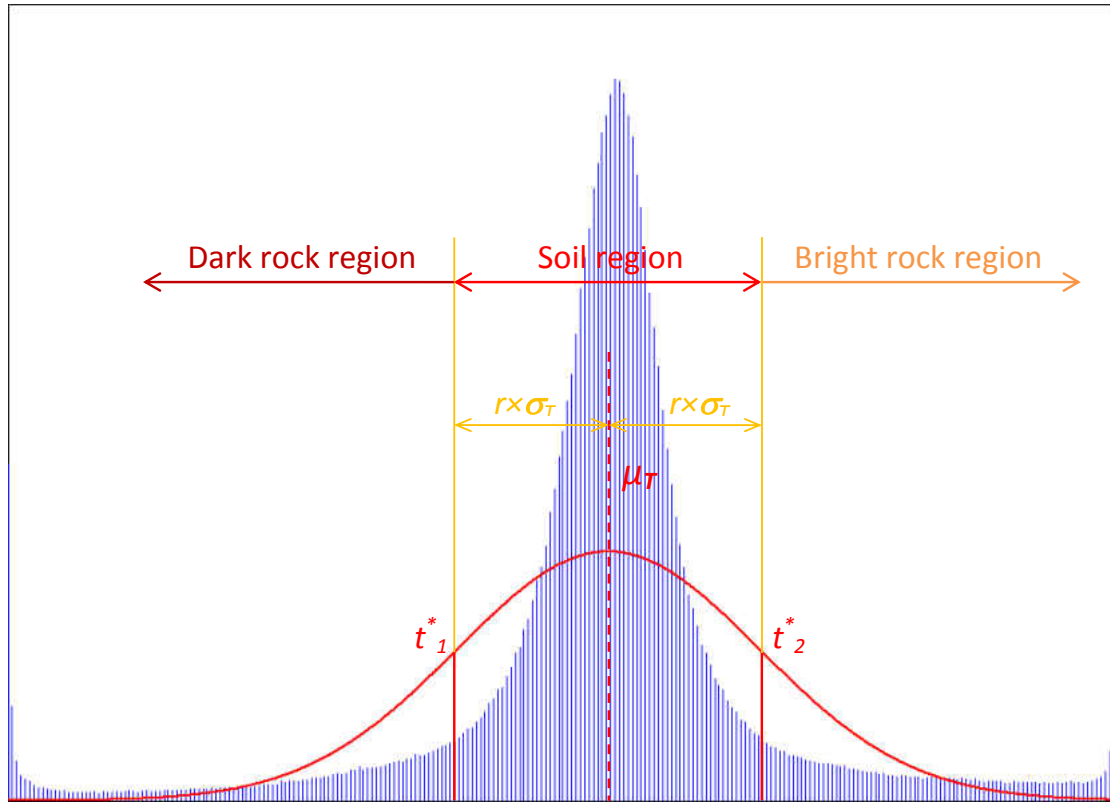


Figure 3.12: Schematic diagram of the normal distribution method

3.3.1.8 Direct probability method (DP)

The direct probability method (DP) distinguishes the rock and the background based on gray level probability p_i directly. It can be seen in Fig. 3.13 that, the probability of the gray levels included in background are generally larger than the rocks'. Hence, a parameter p_T has been defined as a probability threshold, by which the rocks and regolith can be differentiated. The gray levels with p_i higher than p_T are categorised into the class of background. The gray levels with smaller p_i are regarded as foreground. That is:

$$t \in \begin{cases} \text{foreground} & \text{if } p_i \leq p_T \\ \text{background} & \text{if } p_i > p_T \end{cases} \quad (3.20)$$

In some cases, the darkest gray level (0) and brightest gray level (255) will have larger probabilities due to the shadow and the overexposure. As mentioned before, the rock regions in an image, are more likely to be influenced by these

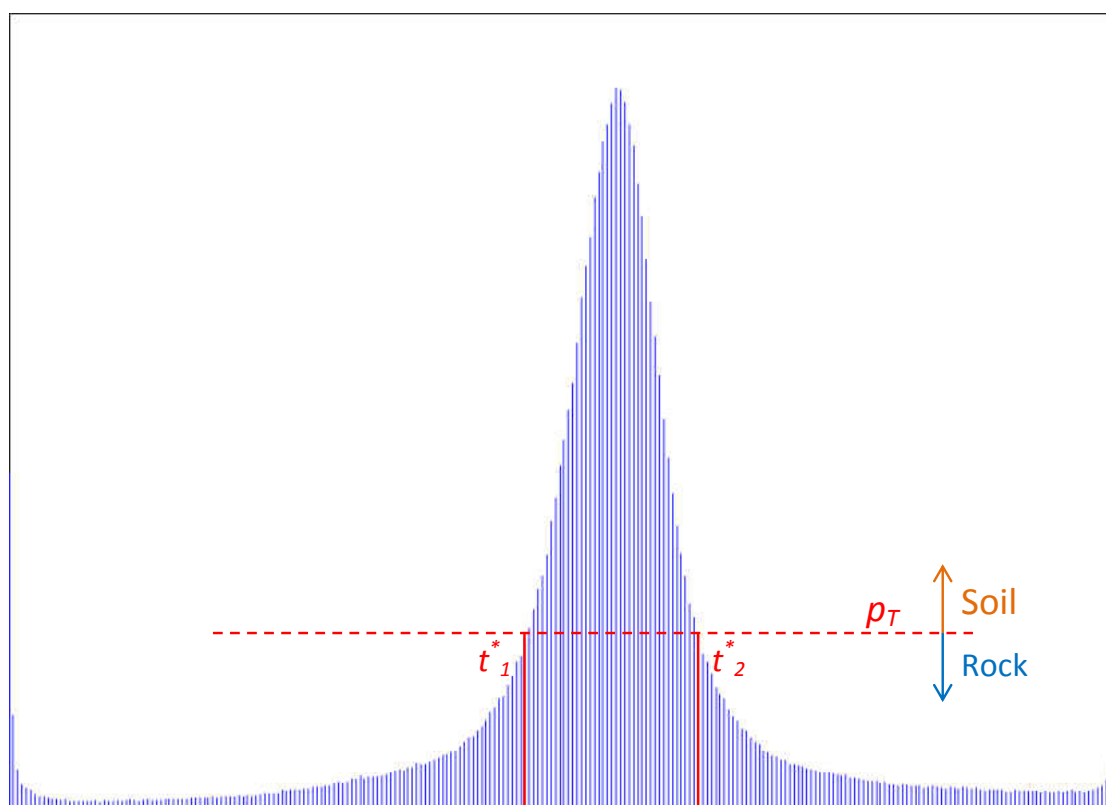


Figure 3.13: Schematic diagram of the direct probability method

phenomenon. Hence in this method, even if the probabilities of the gray level 0 and 255 are higher than p_T , they are defined into the rock region specifically.

3.3.2 Experiments and results

Images from different sources were collected in which the rock regions are labeled manually. Before going through algorithms, all original images were blurred by a 5×5 Gaussian filter to reduce the influence of noise. Thereafter, the parameters of the various algorithms (p_R , r and p_T) were determined firstly using part of images. Then, all algorithms were tested on all images and the detection results of the algorithms are compared.

3.3.2.1 Image source

The images for evaluating the performance of each algorithm come from two sets. One set is constituted by the images captured from the Mars Exploration Rover (MER) Spirit panoramic camera (MER images). The other set consists of rock specimen images captured by a camera similar to that of the Aberystwyth University Pancam Emulator (AUPE) [Pugh et al., 2012] in a laboratory environment (laboratory images). For the quantitative evaluation of algorithms, both image sets were manually labeled¹ with ground truth of rock regions. The labeling refers to the manual identification of each rock pixel. However, due to the complexity of Mars images, some small rocks were not well-labeled and some typical non-rock content such as shadows and sedimentary features were labeled as rock regions. These will cause a small bias in the result evaluation but the labeled region can still be used as the reference to compare the performance of each algorithm. On the other hand, the rocks in laboratory images were relatively well-labeled. Examples of the two kinds of images are shown in Figs. 3.14 and 3.15.

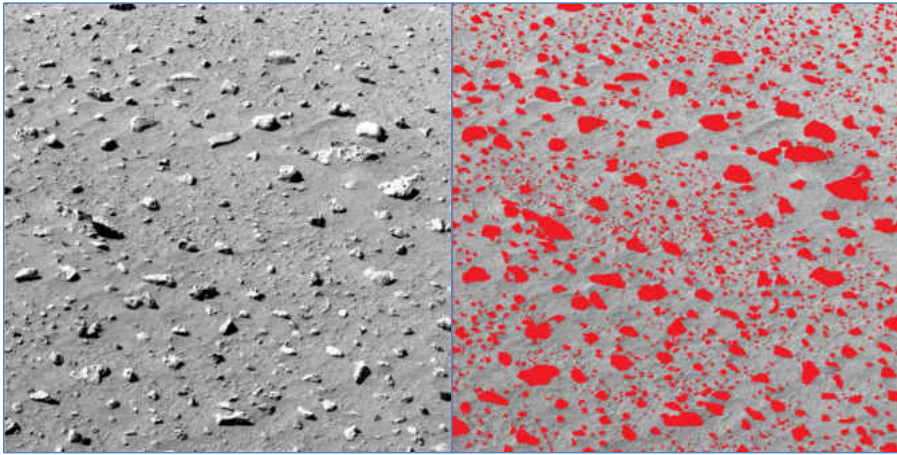


Figure 3.14: Example of a MER Pancam image and corresponding labeled rock regions. Left: original image; Right: labeled ground truth (rock regions are labeled in red).

3.3.2.2 Performance evaluation criteria

The same as the multispectral detection experiments, *Precision*, *Recall* and F_1 are selected as the criteria to evaluate the performance of each thresholding algorithms.

¹The labeling is done by the author.

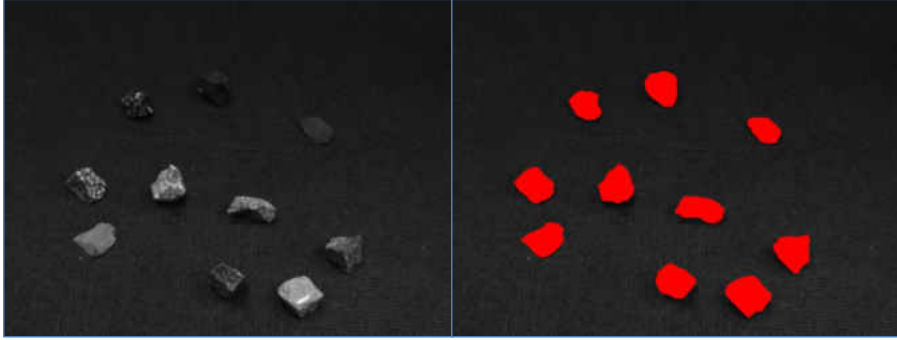


Figure 3.15: Example of a laboratory image and the corresponding labeled image. Left: original image; Right: labeled ground truth (rock regions are labeled in red).

In particular, F_1 is regarded as the main evaluative indicator as well.

3.3.2.3 Parameter setting

There was no need to configure parameters for the methods related to the original Otsu method (Otsu, TO, RTO1, RTO2, TFO). However, in the other algorithms, some parameters are needed to be configured. Those parameters are the p_R in the PR methods, the r in the ND method and the p_T in the DP method. With different parameter settings, the algorithms usually show obvious performance variations. Here, due to the difference of environments, the parameters of the MER data and the laboratory data were adjusted separately. Half of the images from each set were chosen to search for the “optimal” parameter values of each algorithm. The “optimal” parameter values calculated from partial data were regarded as the “optimal” parameter values of the algorithms and kept unchanged. The average performance curves of p_R , r and p_T of two partial sets are illustrated in Figs. 3.16, 3.17 and 3.18 respectively. The x -axis denotes the values of the algorithm parameters and the y -axis denotes the performance evaluative values with the corresponding parameter settings.

With regard to the PR and ND algorithms, it can be seen that *Precision* is approximately monotonically increasing while *Recall* is approximately monotonically decreasing. Since the increasing and decreasing speeds are different, the F_1 curves are mountain-like. The *Precision* and *Recall* variations of the PR algorithm were relatively little in the range from 0.80 to 0.98, leading to the F_1 curves of this algorithm having relatively flat peaks. On the other hand, as to the ND algorithm, the *Recall* curves are decreasing stable while the *Precision* curves reach

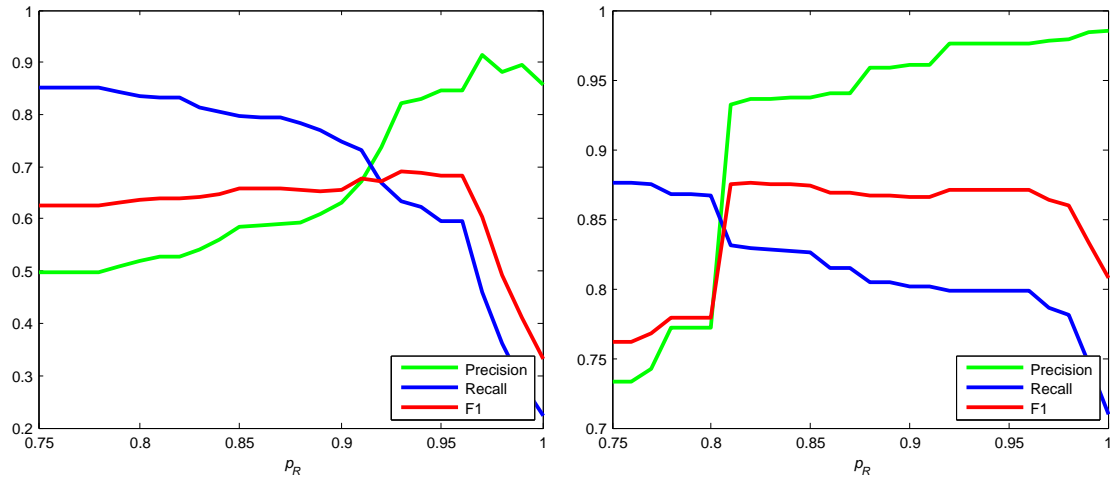


Figure 3.16: Performance of the probability ratio method (PR) with different values of p_R . Left: MER images. Right: Laboratory images.

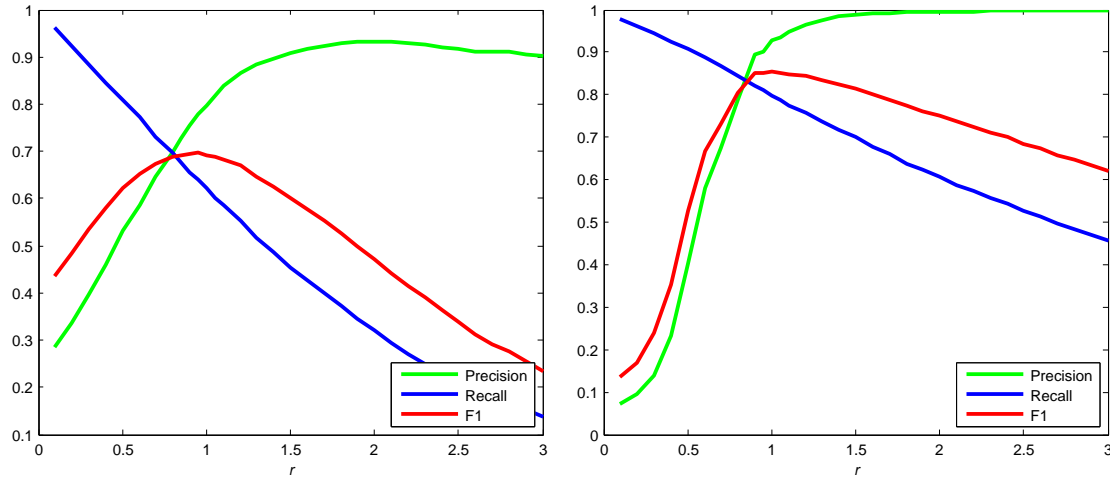


Figure 3.17: Performance of the normal distribution method (ND) with different values of r . Left: MER images. Right: Laboratory images.

their peaks fast. Thus, the peaks of the F_1 curves of the ND algorithm are relatively narrow. As to these two algorithms, although the shapes of the F_1 curves have some differences, the peak positions of the F_1 curves are almost same while addressing different image sets (MER and laboratory images). Hence, judged by the F_1 performance, the p_R parameter of the PR algorithms was set to 0.9 and the r parameter of the ND algorithm was set to 1 for both two kinds of data during the experiments. However, although the performance curve shapes of the DP

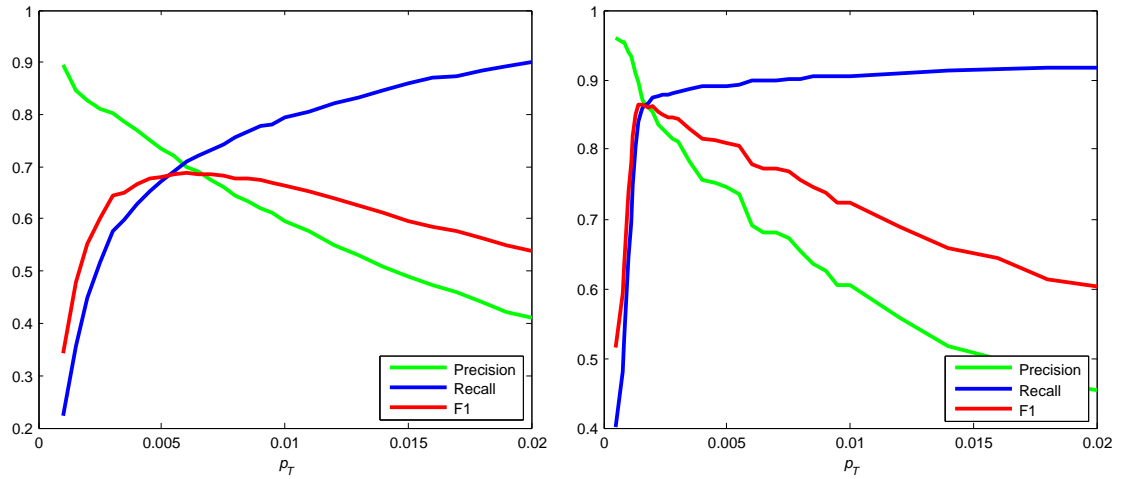


Figure 3.18: Performance of the method directly based on grey level probability (DP) with different values of p_T . Left: MER images. Right: Laboratory images.

algorithm are similar to those of the ND algorithm, when dealing with different data sets, the F_1 peak positions are different. It may prove that the algorithm directly depending on the probability is less adaptive. Compared to the ND algorithm, the DP algorithm lacks a scaling parameter such as σ_T for adapting to different histogram shapes corresponding to different environments. Thus, dealing with different environments, the p_T parameters should be set to different values for pursuing “optimal” rock detection performance. Hence, in our experiments, the p_T values for the MER and laboratory data were set to 0.007 and 0.0015 respectively.

3.3.2.4 Performance comparison of each algorithm

After the parameters were determined, all images in both image sets were used to test all seven two-threshold algorithms (TO, RTO1, RTO2, TFO, PR, ND, DP). The performance of the traditional Otsu method was also tested for comparison. Since the one-threshold Otsu method can only separate the pixels of an image into two classes, it is not clear which class of the segmentation result is a more appropriate representation of rock regions. Hence, the class which gained a higher F_1 performance was considered as the Otsu result. Here, the performance on the MER and laboratory data is presented separately. Examples of the rock detection results of a MER image and a laboratory image are illustrated in Figs. 3.19 and 3.20, where the white pixels represent the detected rock regions.

By visual inspection, compared to the traditional Otsu method, some new two-

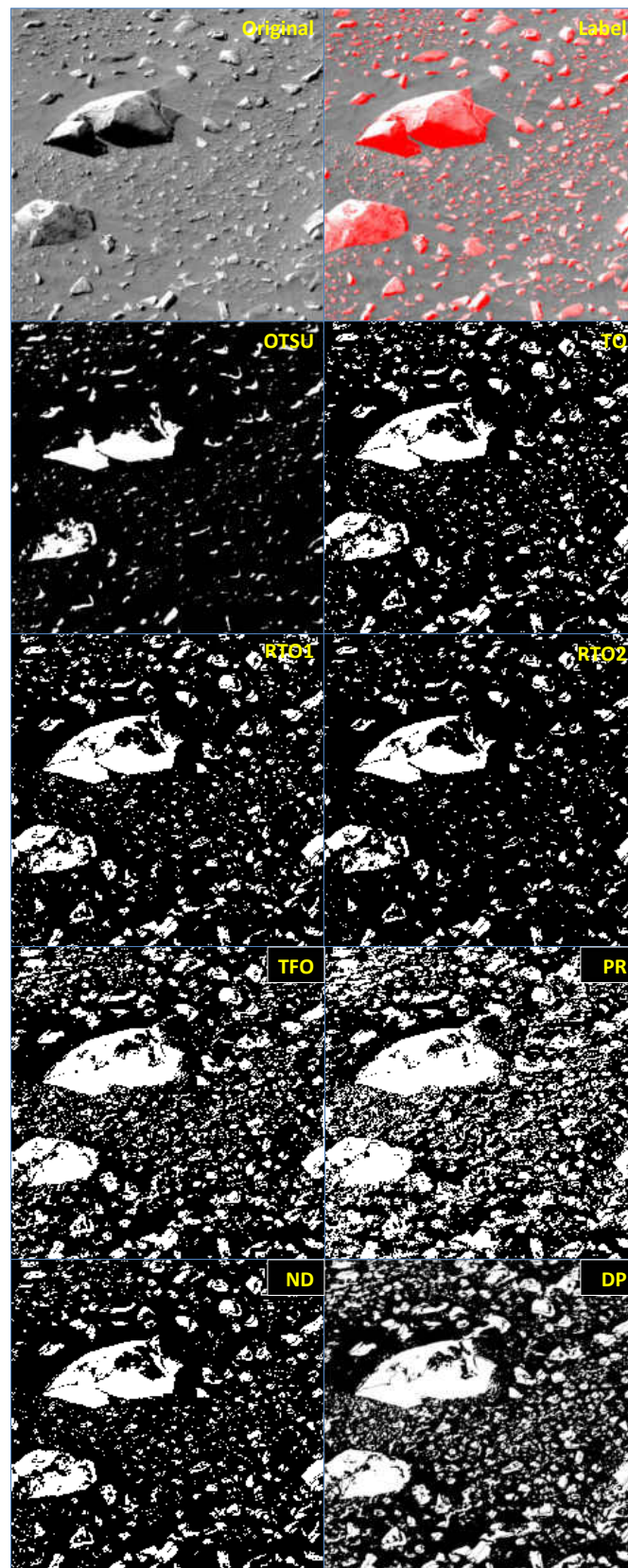


Figure 3.19: Rock detection results of an image captured by MER spirit

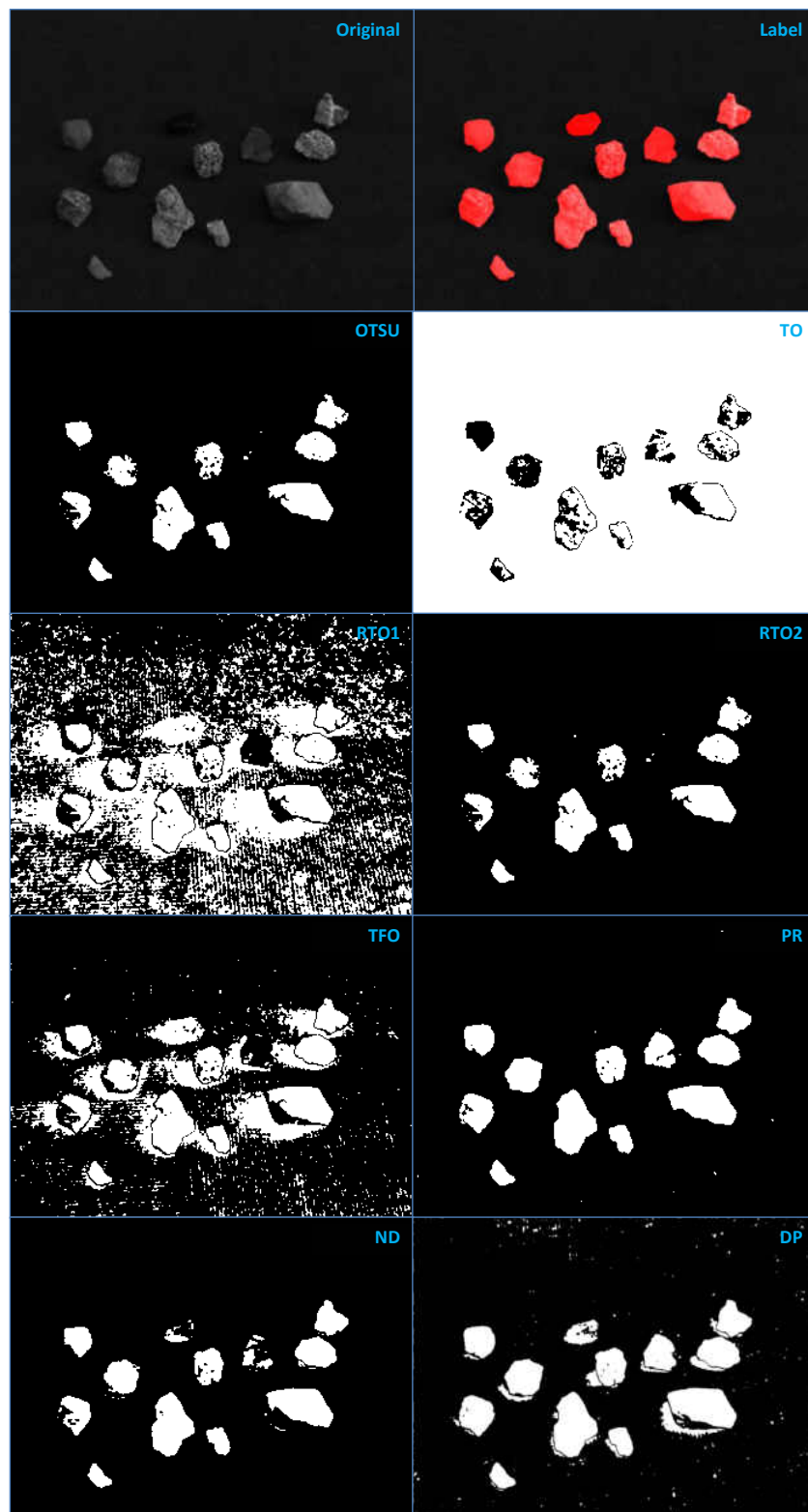


Figure 3.20: Rock detection results of an image captured in the laboratory environment

threshold methods (e.g. PR) can detect more intact rock regions. The quantitative performance is also presented using the labeled ground truth. Here, the *Precision*, *Recall* and F_1 of every image in both sets were averaged in order to reflect the comprehensive performance of each algorithm. The comparison of the averaged performance is given in Table 3.4.

Table 3.4: Performance comparison of thresholding algorithms

Method	MER Data			Laboratory Data		
	<i>Precision</i>	<i>Recall</i>	F_1	<i>Precision</i>	<i>Recall</i>	F_1
Otsu	0.731	0.480	0.501	0.997	0.516	0.669
TO	0.558	0.652	0.560	0.041	0.547	0.076
RTO1	0.575	0.654	0.576	0.117	0.581	0.193
RTO2	0.887	0.522	0.652	0.926	0.537	0.671
TFO	0.603	0.748	0.658	0.314	0.682	0.422
PR	0.602	0.749	0.644	0.963	0.794	0.862
ND	0.784	0.612	0.682	0.899	0.778	0.830
DP	0.655	0.726	0.673	0.895	0.827	0.857

The quantitative performance¹ shows that, to deal with the MER image data, the two-threshold methods obtained generally better performance than the traditional Otsu method. However, some two-threshold methods (the methods based on the between-class variance) generated bad results when they dealt with laboratory images. The PR, ND and DP algorithms achieved adequate performance on both the MER and laboratory data. Although some parameters need to be configured firstly, the algorithms (especially PR and ND) exhibit good adaptabilities with fixed parameters.

3.3.3 Summary

In this section, we have explained the rationale for introducing two-threshold methods into rock detection in Mars images. In contrast with the multispectral methods mentioned above, two-threshold methods need to process smaller amount of data and hence run fast.

Seven two-threshold algorithms were presented, in which TO, RTO1, RTO2 and TFO are derived from traditional Otsu thresholding and the PR, ND and DP methods are based on other histogram information. Two image sets (MER and

¹As mentioned, we mainly use F_1 as the indicator to evaluate the performance of proposed algorithms. Hence, the good or bad performance discussed below refers to F_1 .

laboratory) were established in order to test the performance of those algorithms. F_1 , as a coefficient which combines *Precision* and *Recall*, was selected as the primary coefficient for evaluating the performance of each algorithm.

The PR, ND and DP algorithms rely on an adjustable parameter. These parameters were firstly determined by the detection performance of part of images in two different image sets and were kept unchanged in the evaluation experiment. The optimal parameter values of the DP algorithm are different while processing different data. The ND method was sensitive to the setting of the parameter r . However, when the parameter r was set as 1, the detection performance of the MER and laboratory data both approximated to the best values. Other the other hand, the performance of the PR algorithm was stable over a large range of parameter value p_R thereby making this algorithm more adaptive with a fixed p_R .

After the parameters were calculated and fixed, experiments were conducted on all images in both image sets. The results show that, by applying appropriate two-threshold methods, better detection results than one-threshold methods can be obtained. Specifically, the PR and ND algorithms can generate rock detection results both with high accuracy (judged by F_1) and good stability.

3.4 Saliency methods

Both multispectral methods and two-threshold methods detect rocks in a top-down way. That is to say that these methods give the definitions to describe rocks firstly. In multispectral methods, classifiers are trained to understand the rocks' properties while in two-threshold algorithms, rock pixels are defined as being brighter or darker than soil pixels. The definitions are then used as the criteria for searching for rocks. If the conditions of a pixel (or region) satisfy the definitions, the pixel (or region) will be regarded as a part of a rock. That is so-call top-down. On the other hand, bottom-up methods also can be applied to "detect" rocks, which means that no prior knowledge is involved during the "rock detection" process.

Without prior knowledge, rock regions cannot be clearly recognised. Hence, a tradeoff has been made which is to detect "interesting" regions rather than "rock" regions. So what is an "interesting" region? Here we propose that the region which is uncommon (rare) in an image is a region of interest (ROI). The rarity level of a region can be used to reflect the interest level of the region. Thus, detecting the ROI of an image is equivalent to finding the regions less frequently appearing in the image. And in most cases, compared to the soil (regolith) regions, the rock regions

are relatively uncommon in an image and hence can be detected by such method. Even if the detected region does not represent rocks, its rarity makes it become a “novelty” object and hence researchers would probably pay more attention to it.

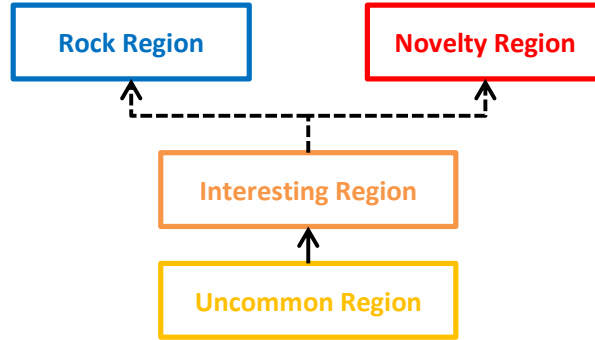


Figure 3.21: Uncommon region to interesting region to rock region

The concept of detecting uncommon regions is in harmony with some bottom-up saliency methods which also need no prior knowledge or manual labels. For convenience, some existing saliency algorithms were tested to validate the idea that rocks can be detected in a bottom-up way.

3.4.1 Saliency algorithms

Five popular saliency algorithms¹ were chosen for the experiment, those are **Itti’s Method** (ITTI) [Itti et al., 1998], **Graph-based visual saliency** (GBVS) [Harel et al., 2007], **Context-aware algorithm** (CA) [Goferman et al., 2010], **Spectral residual** (SR) [Hou and Zhang, 2007] and **Image signature saliency** (IS) [Hou et al., 2012]. Brief introductions to these algorithms follow.

3.4.1.1 Itti’s method (ITTI)

Itti’s saliency method is the most primitive saliency method which establishes a visual attention model inspired by the behaviour and neuronal architecture of the human visual system. It firstly extracts features including intense features, colour features and texture (orientation) features from the original image. These features are then used to generate initial feature maps based on the center-surround theory. Initially, the feature maps were generated by the subtraction of features in

¹The source codes are downloaded from the web sites of corresponding authors or papers. Small modifications have been made for allowing them to run through our data.

different scales of a Gaussian pyramid. In later research [Itti and Koch, 2000], a 2-D difference-of-Gaussian algorithm was introduced to optimize the model. Afterwards, the feature maps of all features are integrated into three “conspicuity maps” through across-scale combinations and normalization (activation), which represent intensity, colour and texture respectively. The summation of these three conspicuity maps is regarded as the final saliency map.

3.4.1.2 Graph-based visual saliency (GBVS)

Graph-based visual saliency is a saliency model based on graph theory computation. It supposes that a feature map is a undirected graph in which each pixel is a node. It defines the weights between two nodes based on the dissimilarity and distance information between them. Then a random walk is performed between nodes according to the weights between nodes (as transition probabilities). The walker is more likely to arrive at the nodes that are highly dissimilar to the nodes surrounding them. The activation maps are generated by counting the quantity of visits to each node. The normalisation of activation maps is done using a Markov chain method to highlight the “salient” regions and thus the final saliency map can be generated.

3.4.1.3 Context aware (CA)

Context-aware saliency is a saliency method aimed at detecting the image regions that represent the scene. In this method, the dissimilarity between a pair of pixels (or patches) is calculated by using the distance of colour and position between them. The saliency value of a patch can be obtained by the dissimilarity between the patch and the K most similar patches. Multi-scale information is introduced into the saliency computation to enhance the contrast of salient and non-salient regions. The final saliency map is formed through an optimisation process following the Gestalt laws.

3.4.1.4 Spectral residue (SR)

The spectral residue method is a saliency method in the frequency domain. The authors found that the spectral residual of an image contains the innovations which are salient in the image. In this method, the image is firstly transformed to a frequency spectral map by using the Fourier transform. The amplitude map

from the Fourier transform is then taken through a logarithmic transformation to gain the log spectrum. A local average filter is adopted to obtain the average log spectrum. The spectral residual can be calculated by subtracting the average log spectrum from the log spectrum. Finally, the saliency map is obtained by the inverse Fourier transform of the sum of the spectral residual and the phase map which is preserved during the process.

3.4.1.5 Image signature saliency (IS)

The image signature approach is also a frequency domain method. Unlike the SR method which uses the Fourier transform, IS method uses the discrete cosine transform (DCT) to convert images into the frequency domain. In this method, the image signature which can reflect the saliency level is defined as:

$$\text{ImageSignature}(x) = \text{IDCT}(\text{sign}(\text{DCT}(x))) \quad (3.21)$$

in which x denotes an image, and sign means an entrywise sign operator. That is to say that, through an inverse discrete cosine transform (IDCT) on a signed DCT signal of an image, a reconstructed image highlighting and isolating the salient regions can be formed. The final saliency map is generated by smoothing the reconstructed image. As for a colour image, the saliency map of each channel (e.g. RGB) is calculated independently. The saliency maps of three channels are simply summed into a final saliency map.

3.4.2 Experiments and results

3.4.2.1 Image source

Since some saliency algorithms used in experiments require colour information, especially traditional RGB colour information, the images used for the experiments are all 3-channel RGB colour information. The colour images come from three different sources. Each type of image contains ten colour images. The first type of images are colour images generated from the multispectral data captured by the MER Spirit Pancam. The second type of images are images cropped from the *McMurdo* panorama image. The third type of images are colour photos taken in the Mars yard in the Planetary Analogue Terrain Laboratory (PATLab) [Barnes et al., 2008] of Aberystwyth University. Fig. 3.22 shows typical images from the

three sets.



Figure 3.22: Three types of images used in saliency experiments, from left to right: synthesized MER Pancam image (MER image), cropped *McMurdo* image (*McMurdo*), and the image of the PATLab Mars yard (PATLab image).

MER image: As mentioned before, the Pancam of MER rover is able to sample multispectral data but not traditional RGB data. Hence, in order to gain the traditional RGB images for saliency processing, the multispectral data within the range of visible light is transformed into the CIEXYZ space and then to the RGB space. The transformation processing referred to the eye tristimulus of each bandwidth. The related details can be found in [Barnes et al., 2011]. An example of a synthesized RGB image generated from multispectral data is shown in Fig. 3.23. Due to the lack of relative spectral power information, the colour of synthesized images is distorted but is still better than a false colour image directly composed by three spectral images. Particularly, the synthesized images have the same size of 512×512 pixels.

McMurdo image: The 360-degree view *McMurdo* panorama image was obtained from the panoramic camera (Pancam) on the Spirit rover and was manually adjusted to approximately true colour. It is constructed from 1449 Pancam images and is 20480×4124 in size. Some rock detection experiments have been done directly on the *McMurdo* images [Shang and Barnes, 2013]. However, dealing with such a large image is very time-consuming and a large part of the image contains no rock but only desert-like land. Therefore we cropped the whole image into small images (512×512) and ensure that there are some “salient” rocks in each chopped image.

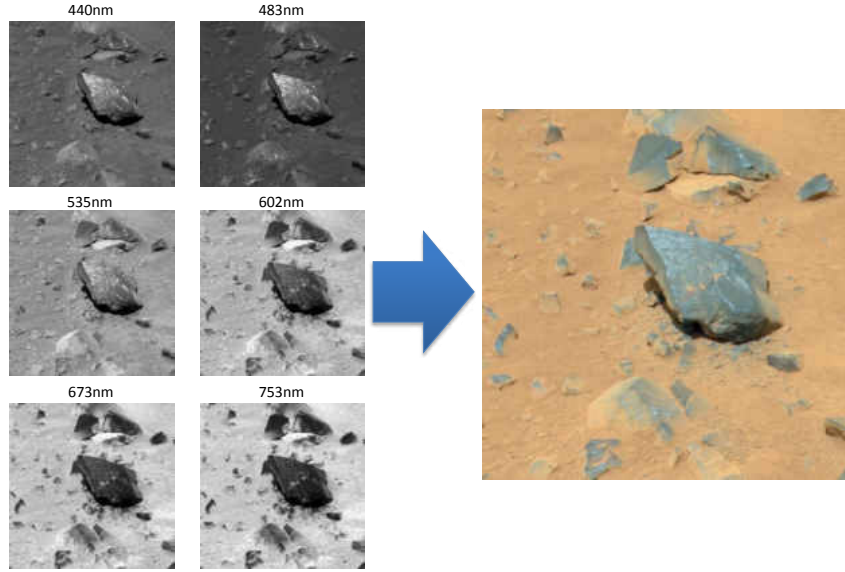


Figure 3.23: Example of conversion from multispectral data to RGB data

PATLab image: The PATLab aims to perform comprehensive mission operations emulation experiments. It has a 50m^2 terrain region (Mars yard) composed of Mars Soil Simulant-D where some fully characterised science target rocks are distributed. Some field tests have been performed in the laboratory [Pugh, 2010; Woods et al., 2009]. In our experiments, the original PATLab rock photos are colour images with the size of 2304×1704 corresponding the capturing camera. For uniformity, we cropped the images to a size of 512×512 .

3.4.2.2 Scale parameter configuration

In saliency algorithms, an input image is first rescaled to a small image in order to accelerate the speed of generating saliency maps. And the final resultant saliency map is obtained by resizing the small-scale saliency map to the original size. Since existing codes were used, the images were scaled according to default settings. The maximum saliency map length of ITTI, GBVS, SR and IS is 64. This means that if an original image is 1:1, it will be resized to 64×64 , and if an original image is 4:3, it will be resized to 64×48 . For the CA algorithm, the default maximum length of the saliency map is 250.

3.4.2.3 Experiment of rock detection

Firstly, we tested the rock detection performance of all five mentioned saliency methods. Different types of images were tested respectively. Partial results are shown in Figs. 3.24, 3.25 and 3.26.

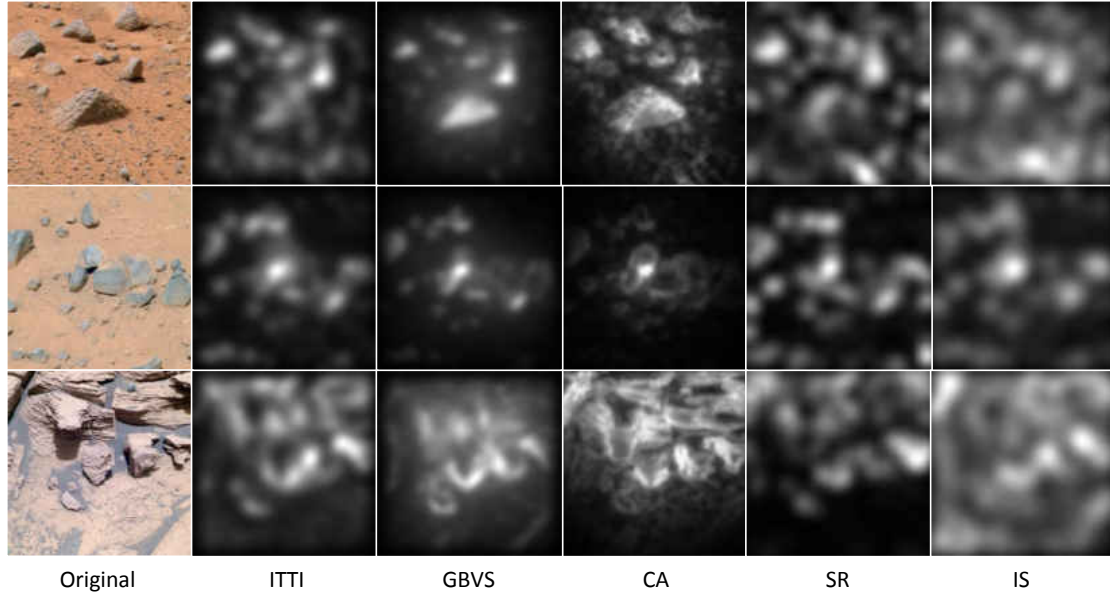


Figure 3.24: Saliency rock detection results on MER images

To reflect the performance of each saliency algorithm more comprehensively and precisely, the results are evaluated quantitatively. Unlike the multispectral classification and two-threshold thresholding methods, the output of saliency methods is not binary. Hence it is hard to represent the quantitative performance of saliency algorithms only by a pair of *Precision/Recall* as well as one F_1 coefficient. Therefore, the receiver operating characteristic (ROC) curve¹ has been used as the criteria to evaluate the performance of the five saliency methods mentioned above. The curve is represented by plotting the true positive rate (i.e. *Recall*) against the false positive rate² at various threshold settings³, and hence can address saliency output. In addition, the curve does not refer to the *Precision* information, hence

¹It is the most popular manner to estimate the performance of saliency methods.

²It can be regarded as the *Recall* coefficient of background regions (i.e. the proportion of the background pixels which are correctly identified).

³To every specified threshold setting, the pixels with saliency intensities above the threshold were regarded as the pixels belonging to rock regions.

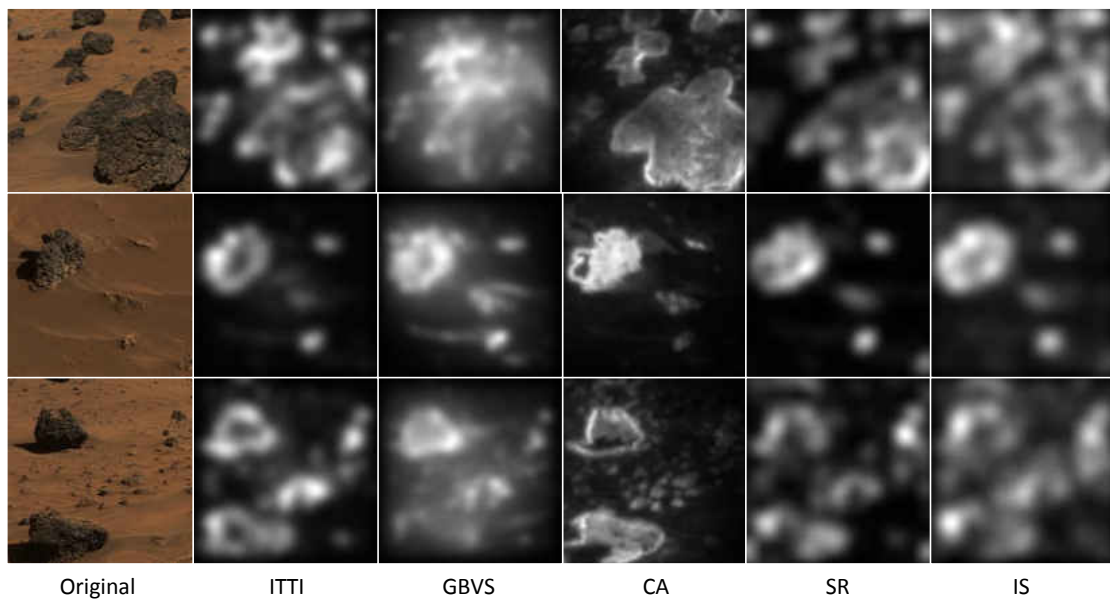
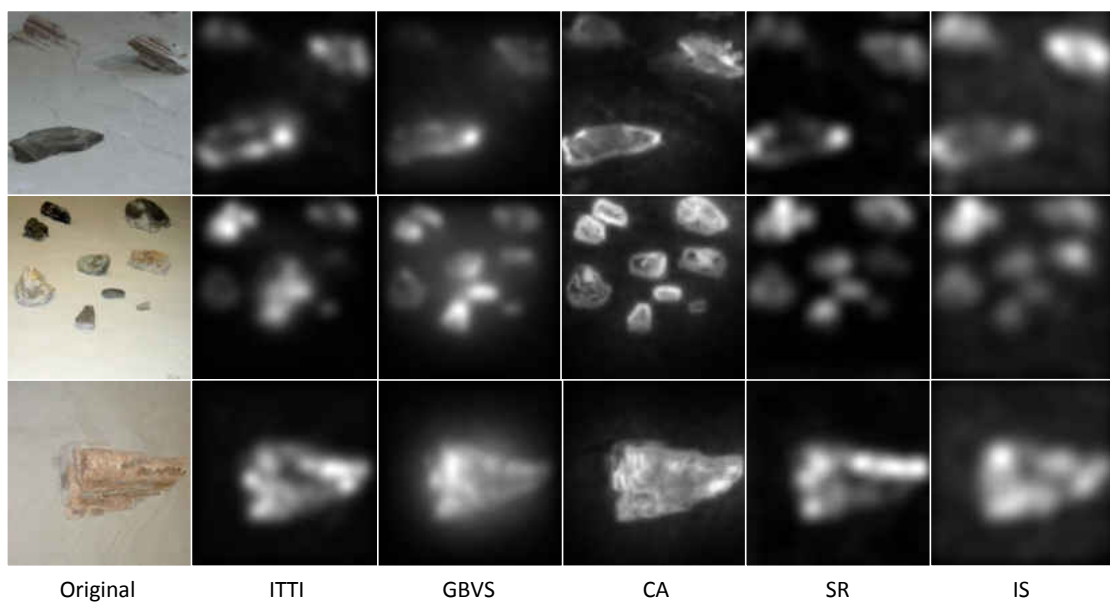
Figure 3.25: Saliency rock detection results on *McMurdo* images

Figure 3.26: Saliency rock detection results on PATLab images

overcoming the problem that the saliency method may detect some non-rock novel objects.

We plotted ROC curves for each of the three image types (MER, *McMurdo* and PATLab) respectively. For each, 256 thresholds were used and the results

averaged over the 10 images of the corresponding datasets. The ROC curves are illustrated in Figs. 3.27, 3.28 and 3.29.

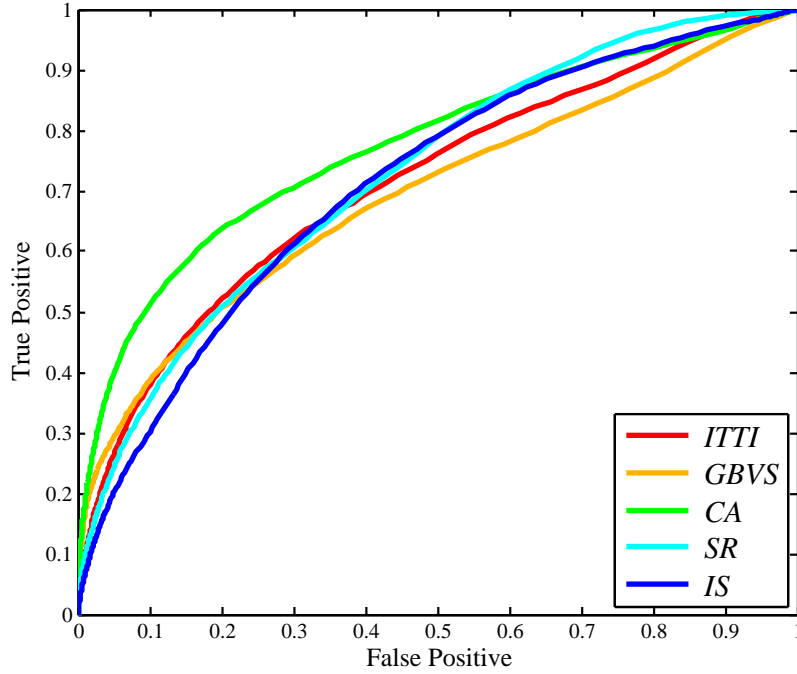


Figure 3.27: ROC curves of the saliency detection results on MER images

In addition, the area under a ROC curve (AUC) can reflect the performance of corresponding algorithms more directly. Here, the AUCs are calculated through trapezoidal approximation. The AUC of each saliency algorithm is listed in Table 3.5. Generally, the larger a ROC area is, the better performance the corresponding algorithm generates.

Table 3.5: AUCs of saliency algorithms

	ITTI	GBVS	CA	SR	IS
MER	0.712	0.693	0.773	0.727	0.712
<i>McMurdo</i>	0.868	0.747	0.895	0.901	0.832
PATLab	0.93	0.898	0.969	0.947	0.958
Average	0.837	0.779	0.879	0.858	0.834

It can be seen that, for laboratory images with distinct rock regions and simple background, the performance of saliency algorithms is generally very good. It proves that saliency methods can find out the “salient” rocks if these rocks are indeed “salient” in images. On the other hand, for some real Mars images

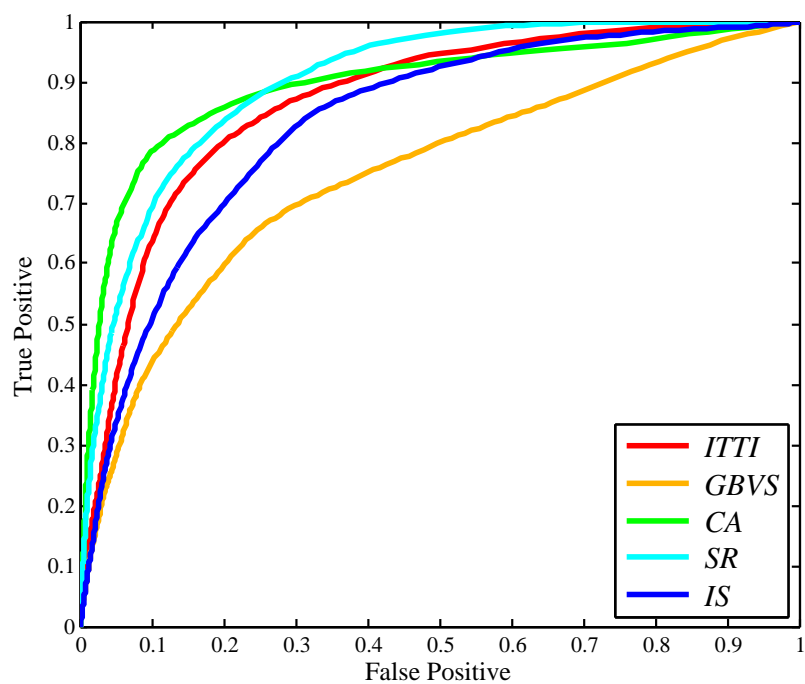
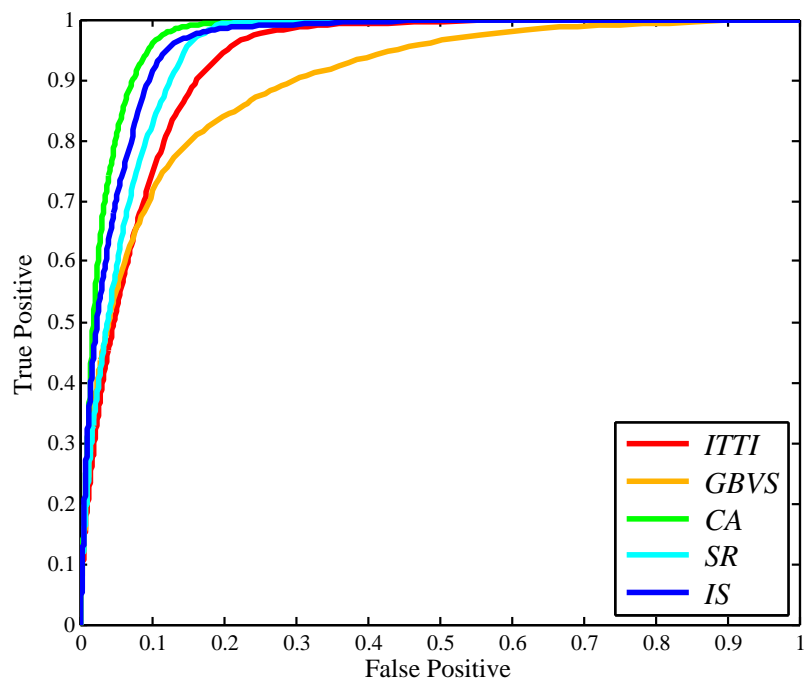
Figure 3.28: ROC curves of the saliency detection results on *McMurdo* images

Figure 3.29: ROC curves of the saliency detection results on PATLab images

(MER and *McMurdo* images) which contain less distinct rocks and more complex environment background, saliency algorithms generate relatively worse detection results. For some detection results¹, the detected “salient” regions nearly covered whole the images and hence cannot highlight the real rock regions.

In terms of the performance comparison of the five saliency algorithms, considering the average AUC of all three images types, the CA algorithm obtains the best average AUC (0.879) while the GBVS algorithm generates relatively worse performance (AUC = 0.779). Specifically, the SR algorithm, as a frequency domain algorithm (with relatively fast running speed), obtains good performance, specially in the detection of *McMurdo* images.

Compared to top-down methods, since no prior knowledge is given, detecting rocks in a bottom-up way (saliency methods) is unnecessary to define different rules to identify different rocks. Rocks with different attributes can all be detected by one saliency method only if they are salient. Hence, even if a novel rock which has not been defined as rock target appears in front of a rover, due to its saliency, it will be recognised as well.

Nevertheless, the saliency methods have their shortcomings. For example, they are sensitive to edges. Intense edges will often be detected as salient objects because that edge shape is regarded as special (rare) texture. In addition, saliency maps may also focus on the region of shadows, because shadows are locally different and often stand out from an image. Therefore, the saliency methods may perhaps gain an improved performance if the shadows have been removed in a pre-processing stage. Moreover, the saliency methods do not generate binary map which can separate rock and regolith regions directly. It needs an extra processing such as thresholding to convert the saliency output to rock regions. Thus, the rock regions generated by this way may be less reliable than the regions generated through top-down algorithms. Hence, in some precise operation, the detection results of saliency methods might be less useful. However, saliency methods can be at least used to point out the positions of salient objects and remove redundant background. In addition, saliency methods may be able to be used to reflect the novelty level of rocks. Except for rocks, other novel objects can be detected through the bottom-up way as well.

¹e.g. The IS detection results of MER images in Fig. 3.24.

3.4.2.4 Rock novelty level representation

According to the theory of saliency methods, if a rock looks extraordinarily different to other rocks, its saliency will be higher than other normal rocks. On the other hand, if all rocks in an image have similar properties, less attention will be paid to them. Thus, the saliency method can be used not only for detecting rocks but also for representing rocks' novelty level. In order to test the representing capability of saliency methods, a meteorite (i.e. the famous "Heat Shield" rock) which is very uncommon in Mars exploration was pasted into some images containing only common rocks. The saliency results of the images before and after adding the meteorite were compared. The comparison examples are shown in Fig. 3.30. Heat maps have been used to demonstrate the intensity values of saliency maps. The red regions indicate the region with higher saliency level.

It can be observed that in the original images without the meteorite, the salient regions are distributed around rocks with emphasis on the rock pile regions. After the meteorite has been added, the saliency focus is transferred to the meteorite region. It verifies that the saliency method can reflect the novelty level of rocks which is also an important attribute to evaluate the rock science value.

3.4.2.5 Novelty detection

As mentioned before, not only rocks but also novelty objects may be detected through such a bottom-up detection approach. Although currently most research focuses on rocks, other uncommon objects deserve attention as well. For example, if a human or animal-like creature has been found, it may overturn the present rock-centred exploration mode. Also debris, whether human's (e.g. Beagle 2 [Amos, 2015]) or alien's, is extremely scientifically valuable. However, since some novelty objects are extraordinary rare or even non-existent on Mars, it is impossible to place them into a regular exploration schedule. Nevertheless, the saliency method may work for identifying them. Interestingly, some imagined images of Mars that contain novelty objects were processed through the saliency algorithms. The corresponding results are shown in Figs. 3.31 and 3.32.

In the resultant images, the detected salient regions are in agreement with what scientists would consider interesting, proving that the saliency methods can be used for detecting novelty objects even if the objects are not in the schedule.

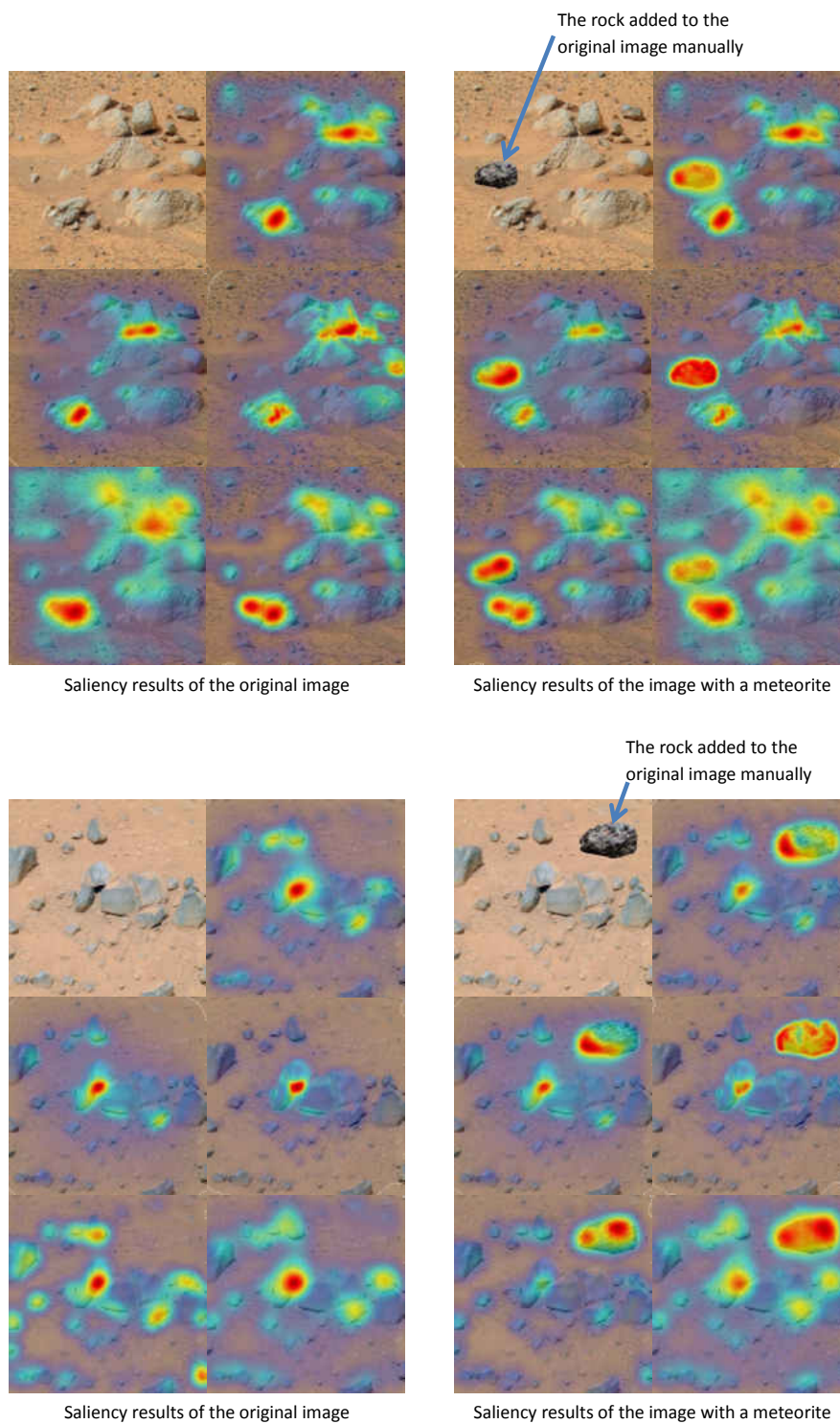


Figure 3.30: Saliency result comparison between original images and images with a meteorite. In each subfigure, from left to right, and top to bottom: original RGB colour image, ITTI saliency result, GBVS saliency result, CA saliency result, SR saliency result and IS saliency result.

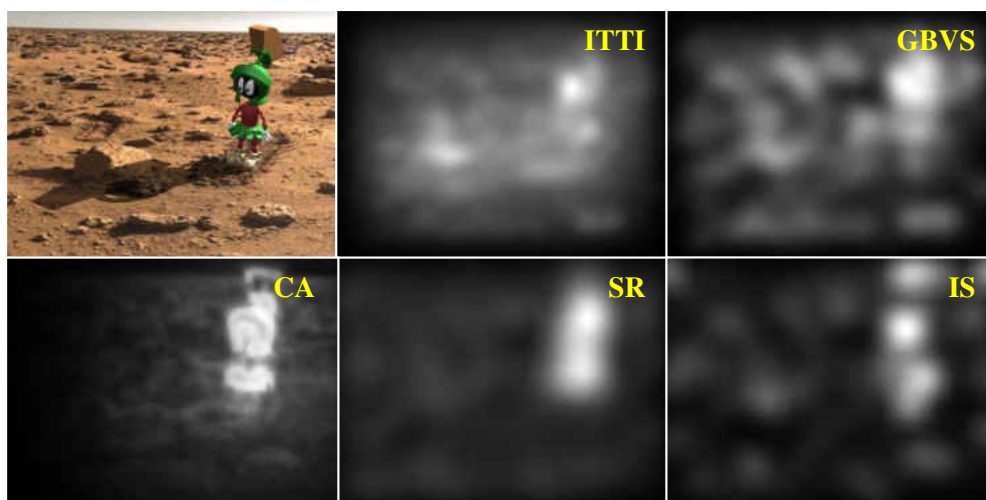


Figure 3.31: Saliency methods to detect a cartoon Martian

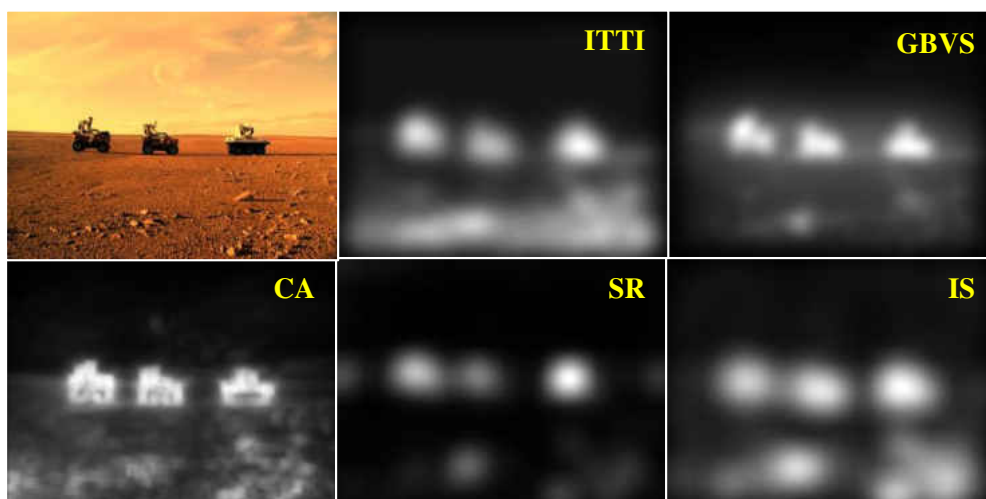


Figure 3.32: Saliency methods to detect vehicles on Mars

3.4.3 Summary

In this section, bottom-up concepts have been proposed to identify rock regions without prior knowledge. Five well-known saliency algorithms were presented to demonstrate the rock detection process in a bottom-up way. In most cases, rock regions can be approximately detected and the repetitious background regions can be removed through using saliency methods. In addition, the saliency methods can evaluate the rarity of rocks and hence reflect their novelty level, which also can

be regarded as an important indicator to assess rocks' scientific values. Besides rocks, saliency methods can also identify other novelty objects. On the other hand, saliency methods have shortcomings. They cannot detect rock regions with clear boundaries. Objects with less science value such as edges and shadows will probably be highlighted.

Although having some shortcomings, saliency methods which detect rocks in a bottom-up way can be complementary to the general top-down detection methods such as thresholding and classification methods. Combining the bottom-up and top-down methods together, better rock detection abilities could be expected.

Chapter 4

Autonomous Rock Science Evaluation

4.1 Introduction

Detecting rocks automatically on the planetary surface is significant. It provides the rover with the abilities to safely travel and avoid dangerous obstacles. Detected rocks can also be regarded as science targets. Moreover, by transmitting these extracted “interesting” regions instead of whole images, the efficiency of data transmission will be improved and the limited bandwidth can be fully utilized.

On the other hand, rock detection is only the preliminary step in autonomous exploration. Indeed, the aim of planetary exploration is to discover some objects (rocks) with desirable science values. Only detecting rock regions is not enough to accomplish such an aim. The rock regions still need to be sent back to Earth where scientists perform analysis and evaluate their science value. After analysis and evaluation, the control centre uploads a new set of instructions depending on the scientists’ decision for the rover to follow. For example, if scientists are interested in one particular rock, the uploaded instructions would guide the rover to move to the rock for close-up observation and further analysis with the onboard instruments. These data and command exchanges will also cost the limited bandwidth. In addition, the scientists have to wait for the rover’s information and the rover needs to wait for the feedback, thereby decreasing the efficiency of exploration. If the science values of rocks could be assessed onboard automatically, the efficiency of exploration would be dramatically improved.

There are a number of works related to autonomous rock science representation. However, many works only focused on extracting features of rocks but did not mention how to utilise these features [Di et al., 2013; Fink et al., 2008; Thompson et al., 2005b]. In order to automatically evaluate the science value of rocks, it is necessary to establish an automatic mechanism to use the extracted features. In terms of existing autonomous systems, OASIS [Castano et al., 2003, 2007a,b] implemented a method similar to weighted sum for enabling scientists to efficiently and easily stipulate the importance of each feature, by which the science priority of rocks can be ranked based on the extracted features and the importance weights. AEGIS [Estlin et al., 2009, 2012] also applied such a strategy to incorporate the information of extracted features. In the CREST Autonomous Robot Scientist (ARS) system [Woods et al., 2008a], the science evaluation subsystem SARA [Woods et al., 2009] is based upon the methodology produced by Dr. Derek Pullan¹ from the University of Leicester [Pullan, 2008], attempting to emulate human field geologists' thinking: identifying key attributes, scoring them as scientific values and then combining them together. Compared to OASIS and AEGIS, the rock science evaluation mechanism in SARA involved more geological concepts, addressing "geological attributes" rather than only "computer vision features". Particularly, geological attributes in this mechanism were divided into three parts: structure, texture and composition. It is believed that such a mechanism can generate evaluation results more scientifically and geologically. However, due to heavy constraints in both time and manpower, the SARA system has not been implemented completely. While in later research, a system named Knowledge-based Science Target Identification System (KSTIS) has been designed as a feasible rock science value evaluation model based on SARA's evaluation mechanism [Pugh, 2010; Pugh et al., 2010a]. Accordingly, KSTIS analysed rock attributes in three parts. The structure part concerned layering (bedding) information, containing three attributes: layering presence, layering scale and layering type. In the texture part, three attributes were selected: surface lustre, surface relief and angularity. The attributes of the composition part were mainly hue and albedo. Specifically, fuzzy logic has been introduced into KSTIS. A fuzzy expert system was established for converting geological attribute values to science values. In contrast with the previous systems which use linear methods to integrate the feature/attribute information, the introduction of a fuzzy system allows KSTIS to analyse rocks' attributes more similarly to humans. However, due to time constraints, KSTIS did not achieve full autonomy. The input parameters of the expert system need to

¹The ground truth in this chapter is also provided by Dr. Derek Pullan.

be evaluated by a human, leading the system to being not applicable in real planetary exploration. If automatic input was to be implemented, the system would become more practicable and efficient.

It can be seen that, although the geology-oriented mechanism was proposed and applied in the CREST and KSTIS systems, the unsolved problem is how to automatically generate geological attributes from previously detected rock regions. Here, in order to fulfill full automation, we propose a new approach (see Fig. 4.1) of generating rock science value. Derived from the OASIS and AEGIS systems, the proposed approach (system) extracts visual features from rock regions. And derived from KSTIS, a fuzzy expert system has been applied for calculating the science value of rocks through geological attributes. However, there is a gap between visual features and geological attributes. Visual features are extracted using computer vision concepts but geological attributes are described using geological concepts. Hence, a mapping procedure has been introduced to map visual features to geological attributes.

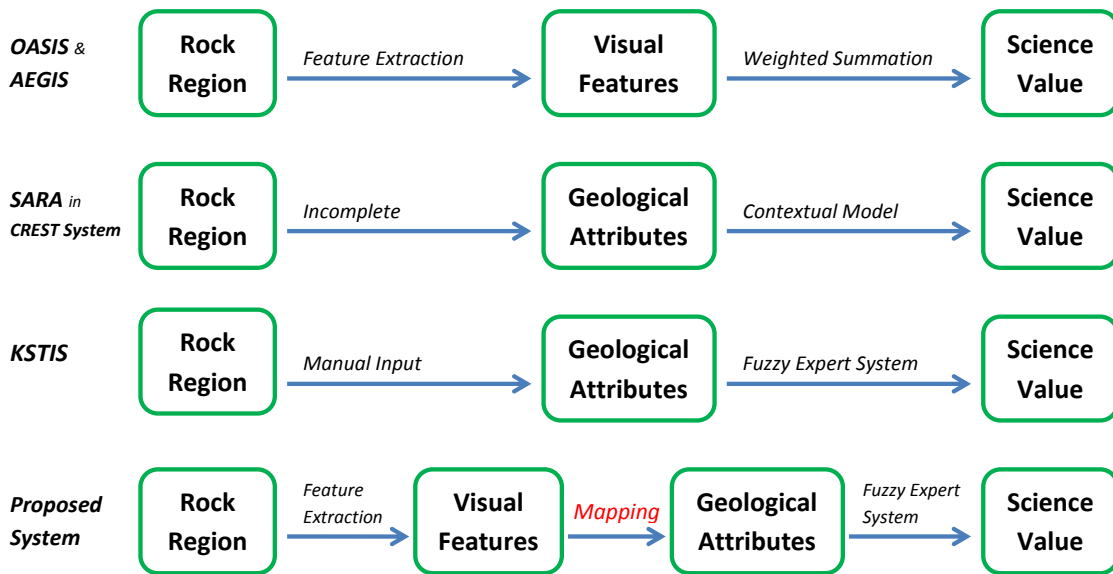


Figure 4.1: Procedure comparison between the proposed system and other existed systems

Since the geological mechanism is inherited from KSTIS, the geological attributes and fuzzy expert system of our proposed system are very similar to those of KSTIS. KSTIS divides the geological attributes into structure attributes (layering presence, layering scale and layering type), texture attributes (surface lustre,

surface relief and angularity) and composition attributes (hue and albedo). Hence, in our system, the geological attributes are classified in such way.

With regard to the composition part, once the rock regions have been defined, it can be relatively easy to extract the composition information (i.e. hue and albedo) directly. It means that the visual features hue and albedo are equivalent to the geological attributes hue and albedo. Thus, it is unnecessary to have an extra mapping process. On the other hand, the structure and texture attributes are more abstract. It is difficult to know which visual feature can be a good representation of a specified attribute. Thus, the mapping procedure is needed.

Since distance information is lacking from some rock data, the layering scale attribute cannot be recovered. Moreover, because the attribute layering type is rather abstract, it is hard to deliver it by a simple computation concept. During early consultation with a domain expert, it was agreed to use a new attribute “layering” to represent the distinct level of the layering (bedding) structure. In addition, lustre is also difficult to determine from images because it relies on direct illumination and specularly of the target surface. Moreover, it is similar to the composition attribute “albedo”. Hence, as a suggestion from the geological expert, the lustre attribute was represented by the average gray level intensity of a rock region. Thus, the attributes that should be mapped are surface relief (*Relief*), angularity (*Angularity*) and layering (*Layering*). Since the colour of images is irrelevant to these three attributes, the rock images for experiments were converted to grayscale. For the sake of simplicity, in each image, only one rock was regarded as the target that needs to be analysed and its region was labeled manually. Rough scores of three geological attributes of these rock targets were provided by a geologist and a series of algorithms were tested on the rock regions in images to extract the visual features. Correlation between attribute scores and feature values were calculated in order to find out the best feature to represent each geological attribute respectively (i.e. mapping process). After the geological attributes were mapped from corresponding visual features, they were used as the inputs of the fuzzy expert system to generate the science values of rocks.

The features and corresponding algorithms are given in Section 4.2. Details of the mapping procedure are shown in Section 4.3. And the fuzzy system is discussed in Section 4.4.

4.2 Visual features and corresponding algorithms

In this section, 63 visual features are selected for representing different characteristics of rock regions. One group of features such as *Mean* and *Compactness* have been mentioned in other people's works. In addition, some new features are created especially for the purpose of representing specific attributes. For example, Gabor filters have been used to search parallel edges which seems to have some connection with the *Layering* attribute. It is believed that these features or combinations of them could represent geological attributes in a way similar to geologists and hence can be used for mapping.

4.2.1 Basic grey level statistics algorithms

Statistical measures can be used to create features that reflect pixel intensity distribution, providing useful information about surface properties of rocks. In AEGIS [Estlin et al., 2012], the statistical features *Mean*, *Variance*, *Skewness* and *Kurtosis* were used. These features can be defined as:

$$Mean = \frac{1}{n} \sum_{x \in R} x \quad (4.1)$$

$$Variance = \frac{1}{n} \sum_{x \in R} (x - \bar{x})^2 \quad (4.2)$$

$$Skewness = \frac{\frac{1}{n} \sum_{x \in R} (x - \bar{x})^3}{(\frac{1}{n} \sum_{x \in R} (x - \bar{x})^2)^{3/2}} \quad (4.3)$$

$$Kurtosis = \frac{\frac{1}{n} \sum_{x \in R} (x - \bar{x})^4}{(\frac{1}{n} \sum_{x \in R} (x - \bar{x})^2)^2} - 3 \quad (4.4)$$

in which, R denotes the rock region, n denotes the number of pixels in the rock region and x denotes the grey level value of each pixel.

Moreover, the coefficient of variation (CV), which is a normalised measure for integrating the *Mean* and the *Variance*, is also selected as a feature for the mapping experiment:

$$CV = \frac{Variance^{1/2}}{Mean} \quad (4.5)$$

The entropy of grey level intensity is another statistic feature to reflect the intensity distribution of rocks [Pedersen, 2000], which can be calculated by:

$$Entropy = - \sum_i P(x_i) \log P(x_i) \quad (4.6)$$

where $P(x_i)$ denotes the probability of x_i .

An 8-bin grey level histogram was constructed to reduce uncertainty and simplify calculation of *Entropy*. In order to distinguish grey level entropy from other entropies, it is called *Ent_{gl}*.

4.2.2 Basic direction statistics algorithms

Additionally to the grey level information, direction information is also significant. The Sobel operator, having been applied in some previous science evaluation system such as SARA [Woods et al., 2009], was employed to provide direction information in our experiments. The operator uses two 3×3 kernels which are convolved with the original images to calculate approximations of the derivatives (horizontal and vertical gradients). Then, the approximate direction of each pixel can be calculated through using the two gradients. Unlike the intensity information, the direction information is periodic, creating the difficulty in the calculation of some statistical features such as variance, kurtosis and skewness. Hence, the entropy became an appropriate feature to represent the dispersion of the direction distribution. Here, the entropy of direction is named *Ent_{dir}*. Similar to *Ent_{gl}*, the directions, in the range of $[0, 2\pi)$, were partitioned into eight equal-sized intervals. Each direction is mapped to its interval thereby forming a histogram which can facilitate the calculation of the *Ent_{dir}*. The equation of *Ent_{dir}* is the same as the entropy function of grey level intensity (Eqn. (4.6)) but replaces intensity information with direction information.

Since the kurtosis of directions cannot be calculated, a new feature entitled *Sharpness* is proposed to reflect the ‘‘peakedness’’ of the direction distribution. It is defined as follows:

$$Sharpness = \sum_i L_{\min}(i)^2 \times P(x_i) \quad (4.7)$$

in which $P(x_i)$ refers to the probability of x_i . Supposing that the peak position of the maximum $P(x_i)$ is i_{max} , $L_{\min}(i)$ denotes the minimum distance to i_{max} in a

cycle. A simple way to calculate $L_{\min}(i)$ is:

$$L_{\min}(i) = \min(|i - i_{max}|, |i - i_{max} - \lambda|, |i - i_{max} + \lambda|) \quad (4.8)$$

where λ is the wavelength of a cycle. If the original direction information is applied, $\lambda = 2\pi$. Since a histogram was used, the value of λ equaled the number of histogram bins¹. Examples of L_{min} are shown in Fig. 4.2.

By using *Entropy* and *Sharpness*, it is feasible to measure the dispersion and constringency of the distribution of directions. In the statistics of directions discussed below, the concept of *Sharpness* will be mentioned many times. Here, the *Entropy* and *Sharpness* of the direction distribution of a whole rock region are named Ent_{dir} and SP_{dir} .

4.2.3 Region shape-based algorithms

Shape-based features focus on the shape characters of rock regions but neglect the content inside. It can be said that shape-based algorithms only perform processing on rock templates (labeled rock regions) but not original rock images. The example of a rock template is demonstrated in Fig. 4.3.

Currently, 15 kinds of features have been selected to represent the shape information of rocks. They are: *Area*, *Extent*, *Solidity*, *Compactness*, the ratio of perimeter R_p , eccentricity of fitted ellipse *Eccentricity*, the error of fitting Err_{fit} , Hu moments I_1 to I_7 , and the bending energy BE .

Area indicates the number of pixels in a rock template, representing the size of the rock. Although it seems to be irrelevant to the geological attributes which need to be mapped, it is an important feature used in many autonomous systems and prototypes [Di et al., 2013; Estlin et al., 2009] and can be used to derive other features.

Extent specifies the ratio of pixels in the rock region to that in its bounding box, computed as the area of rock divided by the area of its bounding box. An example of a bounding box is shown in Fig. 4.4 (A).

Solidity, a measure similar to *Extent*, is the ratio of pixels in the rock region to that in its convex hull. Generally, the convex hull will express the rock region envelope more accurately. An example of a convex hull is illustrated in Fig. 4.4 (B).

Compactness is a measure of the similarity of the rock boundary to a circle.

¹Thus, λ is set to 8 in all calculation procedures of *Sharpness*

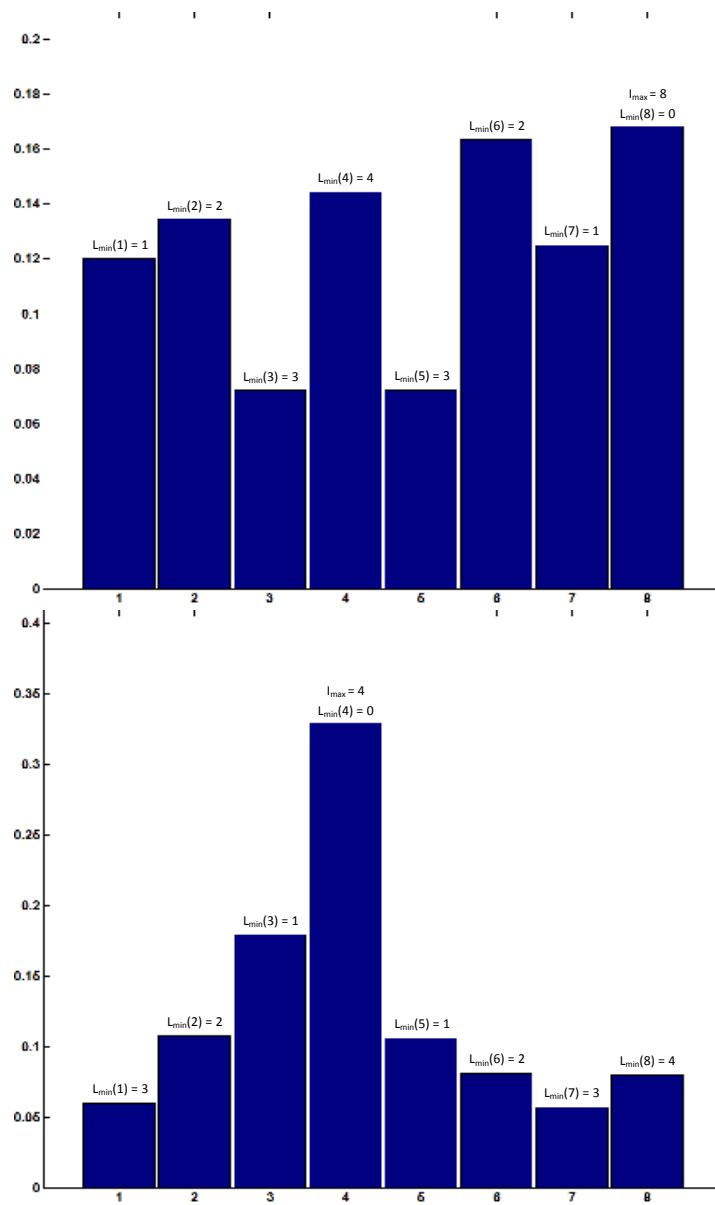


Figure 4.2: Examples of L_{min}

Compactness has been used to describe the angularity of rocks [Pedersen, 2000], calculated as:

$$Compactness = \frac{4 \times Area_{rock}}{Perimeter_{rock}^2} \quad (4.9)$$

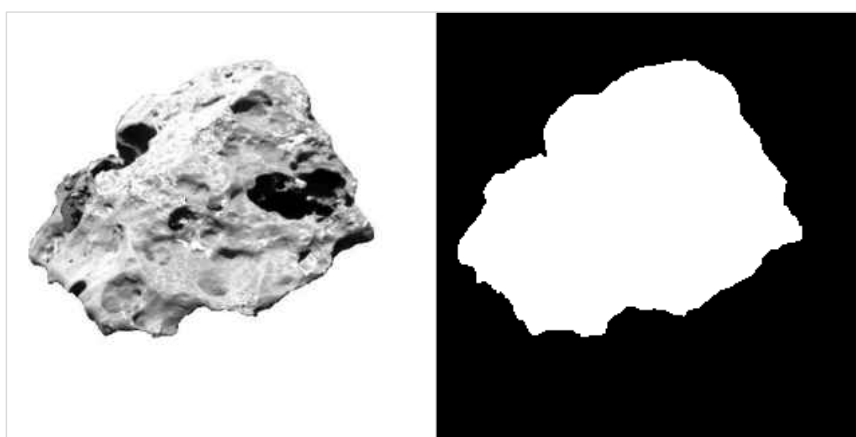


Figure 4.3: Example of rock template

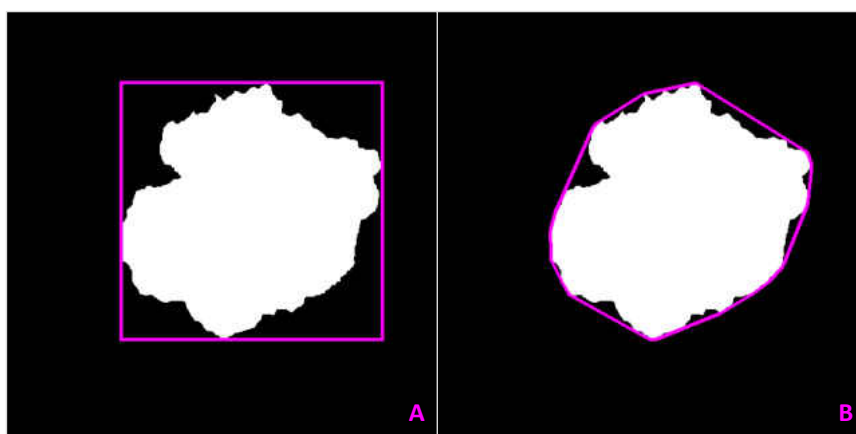


Figure 4.4: Examples of bounding box (A) and convex Hull (B)

The R_p means the ratio of perimeters of the convex hull and the rock region, describing the bending of rock contours as well.

Another way to describe a rock's shape is to fit an ellipse to it. The eccentricity and fitting error of the fitted ellipse have been mentioned to represent the angularity of rocks [Barnes et al., 2009; Castano et al., 2003; Di et al., 2013; Fox et al., 2002]. Here, a robust ellipse fitting method [Fitzgibbon et al., 1999] was adopted to fit the pixel point of the contour of rock. The ellipse is represented by

a general conic function:

$$F(x, y) = ax^2 + bxy + cy^2 + dx + ey + f = 0 \quad (4.10)$$

with the following constraint:

$$b^2 - 4ac < 0 \quad (4.11)$$

Examples of the fitted ellipses are illustrated in Fig. 4.5. After the parameters (a, b, c, d, e, f) of a fitted ellipse are obtained, *Eccentricity* can be calculated as:

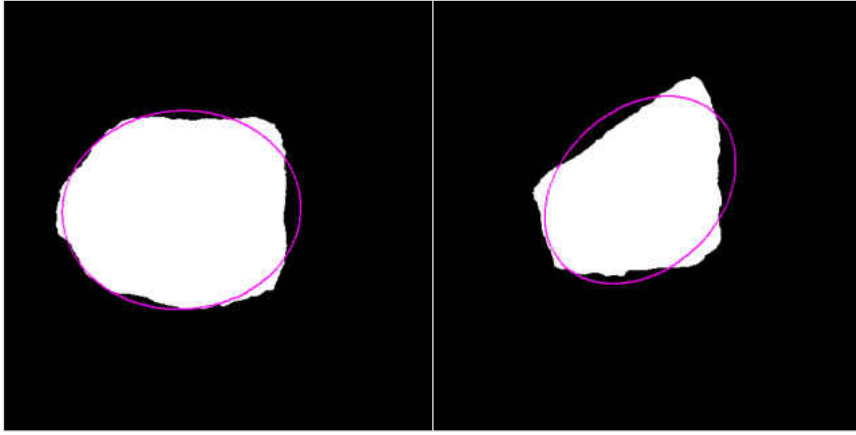


Figure 4.5: Examples of the fitted ellipses

$$Eccentricity = \sqrt{\frac{2\sqrt{(a-c)^2 + b^2}}{\eta(a+c)^2 + \sqrt{(a-c)^2 + b^2}}} \quad (4.12)$$

where $\eta = 1$ if the determinant of a 3×3 matrix:

$$\begin{bmatrix} a & b/2 & d/2 \\ b/2 & c & e/2 \\ d/2 & e/2 & f \end{bmatrix} \quad (4.13)$$

is negative or $\eta = -1$ if that determinant is positive. On the other hand, the fitting error Err_{fit} is represented by the square root of the mean of squares of the

fitted residual errors:

$$Err_{fit} = \sqrt{\frac{\sum_{i=1}^n F^2(x_i, y_i)}{n}} \quad (4.14)$$

An image moment is a certain particular weighted average of image pixels, describing the shape of objects. As shape encoders, Hu moments [Hu, 1962], which are invariant under translation, changes in scale and rotation, have been used to distinguish between different rock shapes automatically [Fink et al., 2008]. Here, the seven Hu moments are also selected as the features $I_1, I_2, I_3, I_4, I_5, I_6$ and I_7 .

Bending energy BE is another feature based on the contours of rocks. It is a measure to represent the angularity of the boundary [Pedersen, 2000], being analogous to the potential energy of a steel spring wrapped around the rock. Originally, it can be calculated as:

$$BE = \frac{\oint |\kappa(s)|^2 ds}{Perimeter} \quad (4.15)$$

where $\kappa(s)$ is the curvature of the directed boundary curve $\vec{x}(s)$. However, because the boundary of a rock in an image consists of discrete pixels, it is unable to calculate the curvature directly. Hence, the curvature of the boundary at each pixel is approximated as the curvature of a polygon fitted to the positions of the pixel and its neighbour pixels ($\kappa(x)$). Thus, the discrete BE can be calculated as follows:

$$BE = \frac{\sum_{i=1}^n \kappa(x_i)}{n} \quad (4.16)$$

where n is the number of pixels on the perimeter of the rock's shape.

4.2.4 Canny-based algorithms

The Canny edge detector [Canny, 1986] is an edge detection operator that uses a multi-stage algorithm to detect optimal edges in images. In some works, the Canny detector has been used as an important tool for the recognition of rock layering [Gulick et al., 2001; Roush, 2004].

The Canny operator can find continuous and smooth edges from rock regions, but rock attributes cannot be represented directly by these edges. It needs a

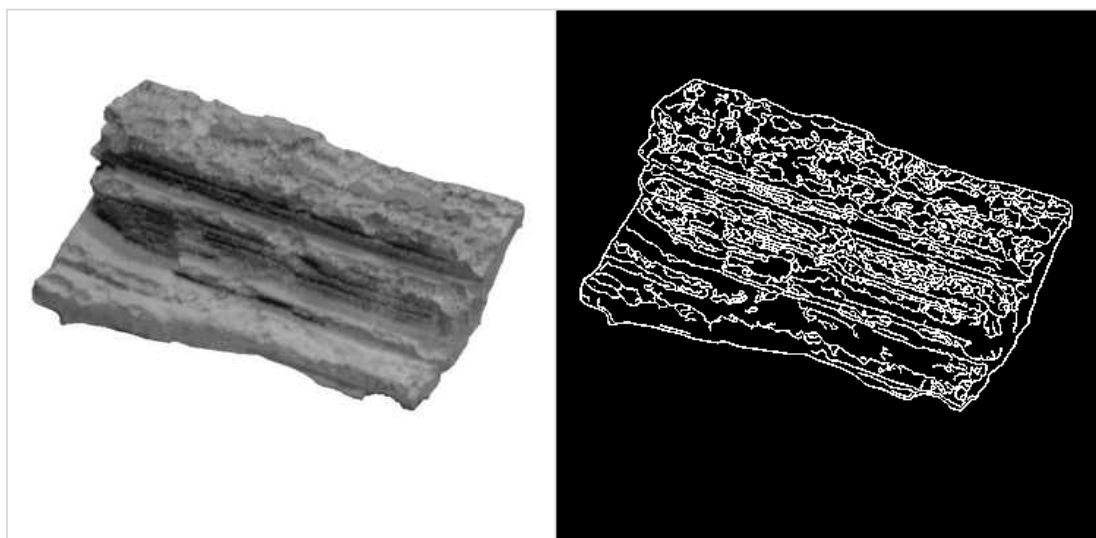


Figure 4.6: Example of edges detected by the Canny operator

statistic analysis of these edges to calculate attribute values. In [Gulick et al., 2001], a small, square window (59×59) is placed on the Canny edge map. Each edge in the window was examined as a series of pixel chains of a fixed length. The straight line between the endpoints of the chains was used to calculate the approximate local orientation (direction) of the edge. Afterwards, a histogram of directions was built and then the entropy of the directions was calculated to present the conformity of the layer. In addition, the number of edge pixels in a window was counted. Finally layer structure was represented by the entropy of direction histogram and the edge number of Canny edges. Since rock regions have already been labeled in our experiments, it is not necessary to set an extra window. The statistical analysis can be directly implemented on the rock region. An example of the edges detected by the Canny operator in a rock region is illustrated in Fig. 4.6. However, original Canny edge maps show phenomena such as circular edges and bifurcated edges (see Fig. 4.7), increasing the difficulty of direction calculation.

The direction near the branch of a bifurcated edge is ambiguous. In addition, there is no endpoint on a circular edge. Thus, the start point of a circular edge cannot be defined, making the direction of the edge meaningless. Hence, in order to perform a statistical analysis of the direction of the edges, some preprocessing needs to be done to solve the problems. Bifurcated edges can be regarded as a set of edges with different directions which intersect at some crossing points (connected

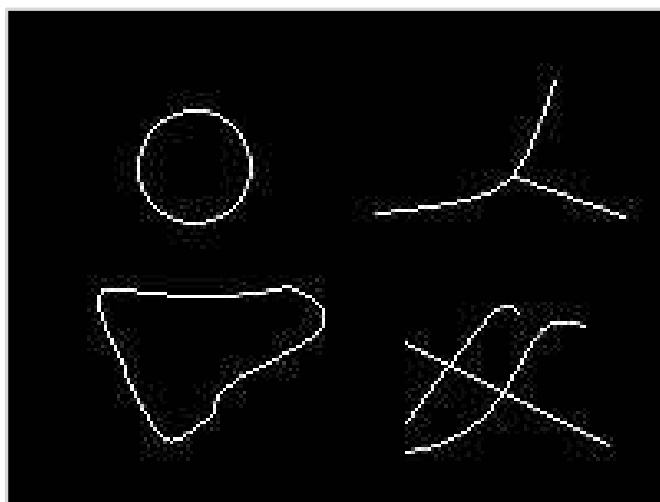


Figure 4.7: Phenomena of circular and bifurcated edges

points). Hence, by breaking these crossing points, except for the circular edges, all edges become simple edges. Each simple edge has two and only two endpoints and there is no branch between the two endpoints. Thus the edge can be easily represented as one or several chains, facilitating the calculation of edge direction. The connected points can be found as the pixels which have more than two edge points in their eight-connected neighbourhood. The circular edges can be found by counting the endpoint numbers of edges. If an edge has no endpoint (points that only have one edge point in their eight-connected neighbourhood), it can be defined as the circular edge. For convenience, circular edges were removed directly from the edge map. In addition, it is less important to calculate the edges shorter than a certain length. For example, the detected edges with only one or two pixels may be noise. Hence, edges that have less than five pixels were eliminated as well. After removing connected points, circular edges and short edges, the final Canny edge map can be obtained. An illustration of the preprocessing is shown in Fig. 4.8.

Although the connected points and circular edges were removed in our algorithm to gain a simple edge map, they may be useful in other applications. For example, combined with other attributes, connected points and circular edges can be applied to detect cross-bedding and graded-bedding (Fig. 4.9) respectively.

After the final Canny edge map has been obtained, the histograms of direction can be generated. Corresponding to the basic direction statistics algorithms, the

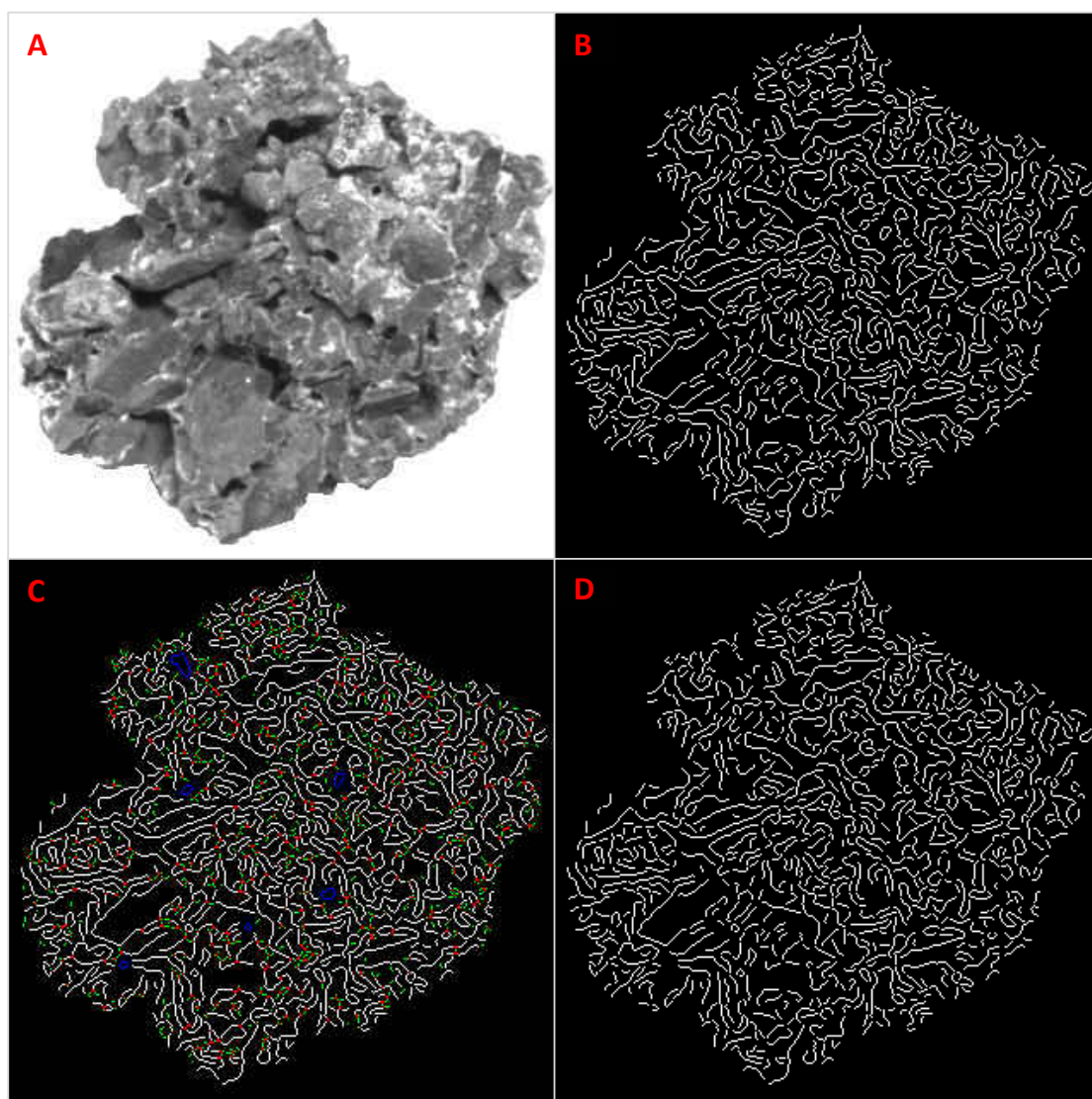


Figure 4.8: Preprocessing for generating the final edge map: (A) original grey level image, (B) original Canny edge map; (C) removing connected points (red), circular edges (blue) and short edges (green); (D) final Canny edge map.

histogram is 8-bin with the same interval. There are two ways to represent the direction directly by using the Canny edge. The first way is similar to [Gulick et al., 2001], considering that an edge consists of several chains with the same length. The direction of the edge is an integration of the directions of the chains. Here, the histogram generated by these directions was named Canny chain direction

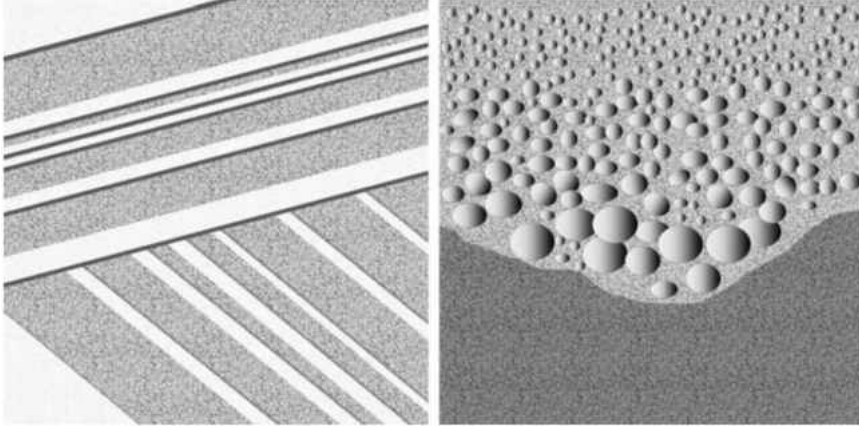


Figure 4.9: Synthetic images of cross-bedding and graded-bedding (from [Pullan, 2008]).

histogram. The other way directly uses each whole edge. Since every edge only has two endpoints, the direction angle of an edge can be directly calculated from the endpoints of the edge itself rather than of the chains. The histogram representing these directions was named Canny edge direction histogram.

Moreover, a method based on Canny edges was proposed which however did not use the Canny edges directly. This method considered that the pixels detected by the Canny operator are the pixels describing the real edge in a rock region appropriately. That is to say, the Canny operator can be regarded as a thresholding tool to select pixels. Hence the Canny edges were regarded as a set of pixels. The Sobel operator was employed on the original rock image to get the directions of the pixels at the Canny detected positions. The histogram representing the Sobel directions of detected Canny pixels was named Canny pixel direction histogram.

The *Entropy* and *Sharpness* of each histogram were calculated as features. The *Entropy* and *Sharpness* of the Canny chain direction histogram, Canny edge direction histogram, and Canny pixel direction histogram were abbreviated as Ent_{Chain} , SP_{Chain} , Ent_{Edge} , SP_{Edge} , Ent_{Pixel} and SP_{Pixel} respectively. Furthermore, the density of the Canny edges (denoted by Den_{Canny}), which means the ratio of the number of Canny edge pixels and the total pixels in the rock region, was also selected as a feature.

The Hough transform [Hough, 1962] has been used in autonomous science for line detection in edge maps [Roush, 2004]. The Hough line transform firstly represents the lines in polar coordinates, and then measures the edge map's response

to each line. Generally, a predefined number of lines having the highest response will be selected for further analysis. Hence, unlike the features mentioned before which used histograms to calculate the statistics, the statistics was directly performed on the lines with high responses. Firstly, the line with the highest response was extracted as the primary line. It is called L_0 and its direction is the primary direction θ_0 . Then, the next n lines with highest responses were selected as L_1 to L_n and their directions are θ_1 to θ_n . A measure was used to indicate the direction similarity between $[L_1, \dots, L_n]$ and L_0 . Since this measure is similar to the *Sharpness* of direction, it was named SP_{Hough} , which can be calculated as:

$$SP_{Hough} = \frac{\sum_{i=1}^n \min((\theta_n - \theta_0 - \lambda)^2, (\theta_n - \theta_0)^2, (\theta_n - \theta_0 + \lambda)^2)}{n} \quad (4.17)$$

where λ is the cycle length of direction. As the general direction range of Hough lines are $[-90, 89]$, λ was set as 180. The number of extracted Hough lines n was set to 20 in our case. An example of the lines detected by the Hough transform from the Canny edge map is shown in Fig. 4.10.

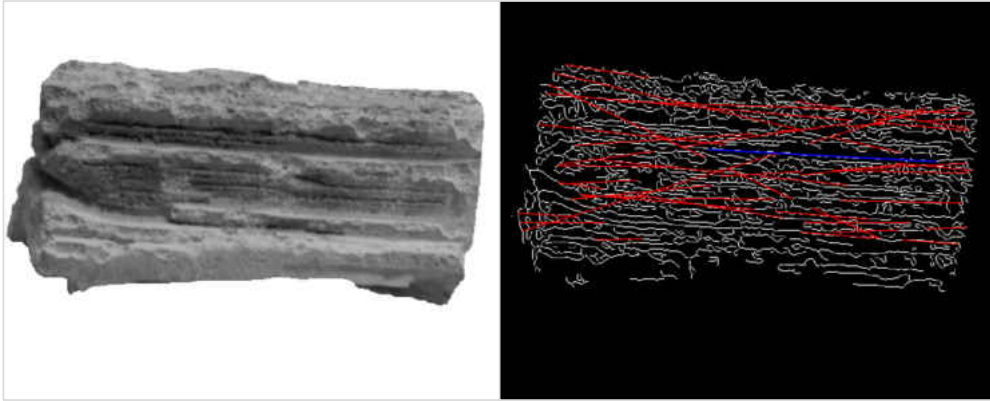


Figure 4.10: Hough lines detected from the Canny edges (red). The blue line is L_0 , denoting the primary direction.

Consequently, by using the edges generated by the Canny operator, eight features can be obtained. They are: Ent_{Chain} , SP_{Chain} , Ent_{Edge} , SP_{Edge} , Ent_{Pixel} , SP_{Pixel} , Den_{Canny} and SP_{Hough} .

4.2.5 Gabor-based algorithms

Gabor filters are a set of linear filters used for edge detection. The frequency and orientation representations of Gabor filters are similar to human visual perception, and they have been found to be particularly appropriate for texture representation and discrimination. As a tool that can represent not only the orientation information but also the scale information of texture, Gabor filters have been already used to describe and analyse the texture of rocks in some works on planetary exploration [Castano et al., 1999; Fink et al., 2008].

Generally, a Gabor filter has a real and an imaginary component. Both components are defined by a sinusoidal wave multiplied by a Gaussian function. In the 2D situation, a Gabor filter can be expressed as:

Real:

$$g(x, y; \lambda, \theta, \sigma, \gamma) = \exp\left(-\frac{x'^2 + \gamma^2 y'^2}{2\sigma^2}\right) \cos\left(2\pi \frac{x'}{\lambda}\right) \quad (4.18)$$

Imaginary:

$$g(x, y; \lambda, \theta, \sigma, \gamma) = \exp\left(-\frac{x'^2 + \gamma^2 y'^2}{2\sigma^2}\right) \sin\left(2\pi \frac{x'}{\lambda}\right) \quad (4.19)$$

where

$$x' = x \cos \theta - y \sin \theta \quad (4.20)$$

and

$$y' = x \sin \theta + y \cos \theta \quad (4.21)$$

in which λ is the wavelength of the sinusoidal wave, indicating the scale information, θ denotes the orientation of parallel stripes of a Gabor function, σ is the standard deviation of the Gaussian envelope, γ is the aspect ratio, specifying the ellipticity of a Gabor function. Moreover, because the imaginary component is too sensitive to edges, for simplicity, only the symmetric real component was applied.

In previous works, one Gabor filter was used to produce one feature. If 40 Gabor filters are applied, 40 features are generated. However each feature only indicates the character of a particular orientation and scale. In order to represent the rock attributes, it is necessary to summarise the features of different orientations and scales together to get more abstract features.

Moreover, a problem of the filter expressed by Eqn. (4.18) is that, if an image is directly convolved by such filters, the results obtained by filters with different σ

will have different result ranges. In addition, in image processing, data is discrete, causing another problem that the sum of a Gaussian distribution filter does not precisely equal to 1, which also introduces some biases of result ranges. Hence, due to the difference of ranges, the convolution results of different filters cannot be integrated directly. Therefore, a process of normalisation is required before the integration of Gabor features at different scales (σ). A normalised real Gabor filter derived from Eqn. (4.18) can be represented as:

$$g(x, y; \lambda, \theta, \sigma, \gamma) = \frac{\frac{1}{2\pi\sigma^2/\gamma} \exp\left(-\frac{x'^2 + \gamma^2 y'^2}{2\sigma^2}\right) \cos\left(2\pi\frac{x'}{\lambda}\right)}{\sum |g|} \quad (4.22)$$

Through using the Gabor features generated by the normalised filters, direct statistical analyses can be performed. In our experiments, four wavelengths and eight orientations were used. These were $[2, 4, 8, 16]$ and $[0, \pi/8, \pi/4, 3\pi/8, \pi/2, 5\pi/8, 3\pi/4, 7\pi/8]$. For each filter, $\sigma = 0.5\lambda$, and for all filters, the γ values were set to 1. Based on the three standard deviations of the filter with the largest σ , the size of the filter window was set as 49×49 . The images of all 32 Gabor filters are given in Fig. 4.11.

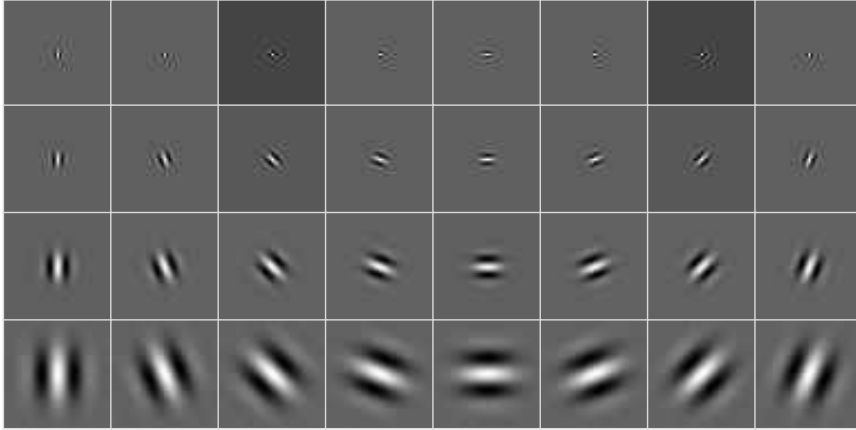


Figure 4.11: Normalised Gabor filters with four scales and eight directions

Convolved with the 32 normalised Gabor filters, a rock image can generate 32 feature maps. It can be found that a layer structure can produce a larger absolute response, whether positive or negative. Hence, the absolute value of the feature maps was used, making the value range of feature maps from 0 to 1. An example of feature maps of a layered rock image is shown in Fig. 4.12, from which it can

be seen that the image of a layered rock has an obviously prominent response to a particular filter (fourth scale and fourth direction).

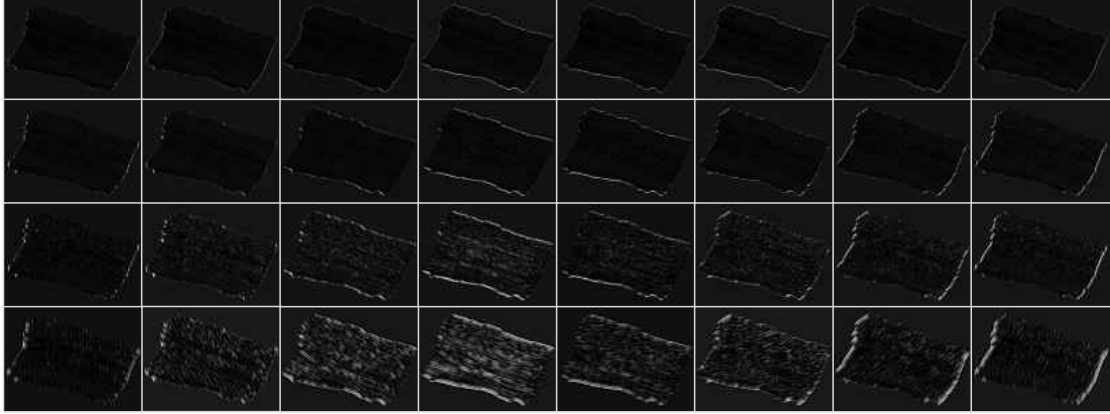


Figure 4.12: Gabor feature maps of the image of a layered rock (the original image is the left figure of Fig. 4.6). As the responses of some filters are too small, intensity of the feature map images are rescaled to $[0,1]$.

After normalisation and making absolute, the feature maps can be used to calculate abstract features. In our algorithms, the abstraction processing was started from each pixel. For each pixel in the rock region of the original rock image, 32 features can be obtained from the Gabor filters. Here, they are described by a feature matrix whose size is related to the number of scales (wavelengths) and directions (orientations). Because four scales and eight orientations were employed, the size of the matrix in our experiment is 4×8 . A matrix can be expressed as follows:

$$\begin{bmatrix} a_{11} & a_{12} & a_{13} & a_{14} & a_{15} & a_{16} & a_{17} & a_{18} \\ a_{21} & a_{22} & a_{23} & a_{24} & a_{25} & a_{26} & a_{27} & a_{28} \\ a_{31} & a_{32} & a_{33} & a_{34} & a_{35} & a_{36} & a_{37} & a_{38} \\ a_{41} & a_{42} & a_{43} & a_{44} & a_{45} & a_{46} & a_{47} & a_{48} \end{bmatrix} \quad (4.23)$$

Each element value of the matrix is the response value of the filters at corresponding scale and direction. For example, the a_{37} means the response value in the feature map convolved by the filter of third scale ($\lambda = 8$) and seventh direction ($\theta = 3\pi/4$). Here, we defined the primary scale and the primary direction by using the matrix. The primary scale and primary direction of a pixel corresponds to the

position of maximum value in the matrix. For instance, if a matrix is:

$$\begin{bmatrix} 0.130 & 0.184 & 0.144 & 0.233 & 0.242 & 0.265 & 0.243 & 0.255 \\ 0.222 & 0.027 & 0.143 & 0.179 & 0.344 & 0.235 & 0.256 & 0.278 \\ 0.231 & 0.068 & 0.046 & 0.317 & 0.289 & 0.004 & 0.134 & 0.028 \\ \mathbf{0.538} & 0.183 & 0.077 & 0.132 & 0.212 & 0.187 & 0.158 & 0.343 \end{bmatrix} \quad (4.24)$$

The maximum value is 0.538, and thus the primary scale is 4 ($\lambda = 16$) and primary direction is 1 ($\theta = 0$). After determining the primary scales and directions of all pixels, an 8-bin direction histogram and a 4-bin scale histogram are established, by which the entropies of them can be calculated to reflect the coherence of the rock's texture. Here the entropies are called Ent_{Gdir} and Ent_{Gscale} . In addition, the sharpness of the direction was also calculated, abbreviated as SP_{Gdir} .

With respect to abstract features of scale, a new feature called *Scale* is proposed to combine the scale and their distribution. This kind of feature is supposed to be able to reflect the coarseness of rock texture. For example, if a rock image is sensitive to the Gabor filters with small λ , it probably has fine texture. Two kinds of *Scale* called $Scale_{lvl}$ and $Scale_{\lambda}$ were used, which refer to the scale level ([1, 2, 3, 4]) and the wavelength ([2, 4, 8, 16]) respectively. They are:

$$Scale_{lvl} = \sum_{i=1}^4 i \times H(i) \quad (4.25)$$

$$Scale_{\lambda} = \sum_{i=1}^4 2^i \times H(i) \quad (4.26)$$

in which $H(i)$ is the value of the i -th bin of the scale histogram, denoting the probability of different primary scales of all pixels.

The features mentioned above only used the position of maximum value in the matrix (primary scale and primary direction) but ignored other elements in the matrix. By analysing the whole matrix, it is possible to find out more comprehensive information. For example, the conspicuousness of the primary scale and direction could be an important character to reflect rocks' texture. Here, for a matrix M corresponding to a specified pixel, two measures were generated to reflect how "primary" the primary scale and direction are. The first measure is the standard deviation of the matrix σ_M . The other measure $MaxMean_M$ is calcu-

lated from the maximum value (corresponding to the primary scale and direction) subtracting by the mean of all elements in the matrix. The definitions of these two measures are as follows:

$$\sigma_M = \sqrt{\frac{\sum_{i=1}^4 \sum_{j=1}^8 (a_{ij} - \mu_M)^2}{32}} \quad (4.27)$$

$$MaxMean_M = \max(M) - \mu_M \quad (4.28)$$

where μ_M the can be calculated as:

$$\mu_M = \frac{\sum_{i=1}^4 \sum_{j=1}^8 a_{ij}}{32} \quad (4.29)$$

After the two measures of every matrix of all pixels were obtained, the average values of the two measures of all pixels were taken to reflect the general situation of a rock region. These two averages are used as two features as well, named StD_G and $MaxMean_G$ respectively.

Consequently, seven features are generated based on the normalised Gabor filters: Ent_{Gdir} , Ent_{Gscale} , SP_{Gdir} , $Scale_{lwl}$, $Scale_\lambda$, StD_G and $MaxMean_G$.

4.2.6 Corner density

As mentioned in Section 4.2.3, some shape-based algorithms were used to generate features which could be able to represent rock angularity. Those algorithms only utilised rock template information and ignored the content inside a rock contour. This may introduce some bias while describing rocks. Hence an attempt has made to create features related to the angularity of rocks by using not only the rock template but also the intensity information inside the template. An assumption was made that an angular rock will have more corners than a round rock per unit of a rock region. Thus, the density of corners can reflect the rock angularity.

Four kinds of corner detection methods were used for finding corner points in rock regions. They are Harris corner [Harris and Stephens, 1988], Shi & Tomasi corner [Shi and Tomasi, 1994], SUSAN corner [Smith and Brady, 1995] and SIFT corner [Lowe, 2004]. Examples of the corner detection results of an angular rock and a round rock are shown in Figs. 4.13 and 4.14 respectively.

It can be observed that, for some corner detection methods (e.g. Harris method),

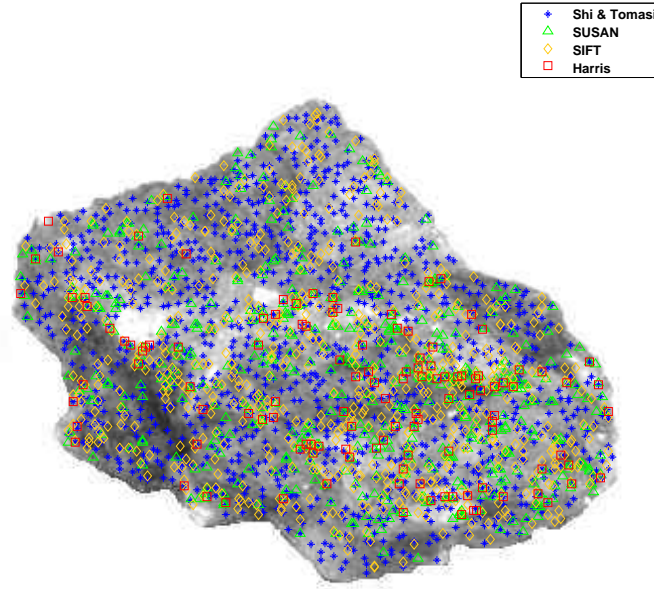


Figure 4.13: Corner detection result of the image of an angular rock sample

the corner densities are obviously different when dealing with the angular rock and the round rock. Here, the density features¹ of the four detection methods were abbreviated as Den_{Harris} , Den_{Shi} , Den_{SUSAN} and Den_{SIFT} .

4.2.7 Co-occurrence matrix algorithms

A co-occurrence matrix is a matrix that represents the distribution of co-occurring values at a given offset in a given image. It was used in [Haralick et al., 1973] to generate textural features. Mathematically, a co-occurrence matrix C can be defined over an $n \times m$ image, parameterised by an offset $[\Delta x, \Delta y]$, as:

$$C_{\Delta x, \Delta y}(i, j) = \sum_{p=1}^n \sum_{q=1}^m \begin{cases} 1, & \text{if } I(p, q) = i \text{ and } I(p + \Delta x, q + \Delta y) = j \\ 0, & \text{otherwise} \end{cases} \quad (4.30)$$

¹The “density” mentioned here is calculated as: $\frac{\text{Number of detected corner points}}{\text{Number of pixels in the rock region}}$.

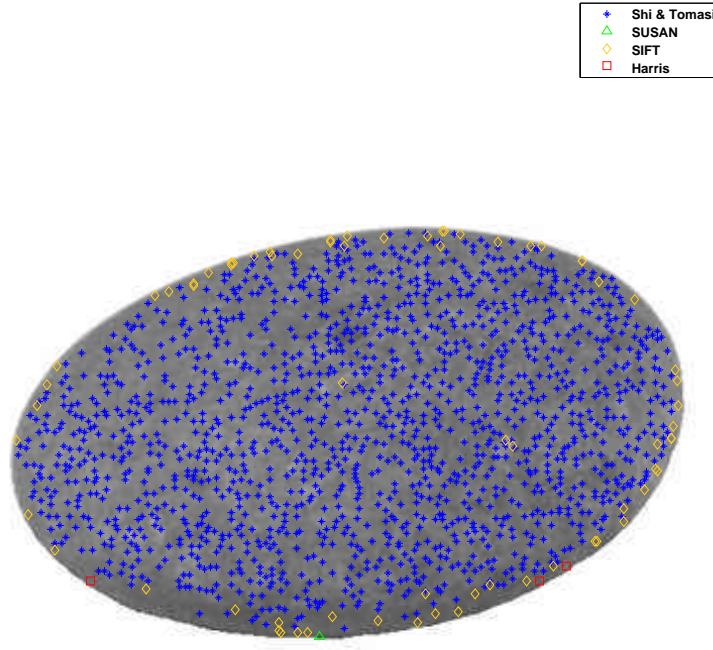


Figure 4.14: Corner detection result of the image of a round rock sample

Since only rock regions are concerned, the statistical analysis of the regions outside the rock contours is discarded. Therefore, unlike Eqn. (4.30) which analyses the whole image, the co-occurrence matrix can be redefined to focus on a rock region:

$$C_{\Delta x, \Delta y}(i, j) = \sum_{p=1}^n \sum_{q=1}^m \begin{cases} 1, & \text{if } I(p, q) = i, I(p + \Delta x, q + \Delta y) = j \text{ and} \\ & [p, q] \in R, [p + \Delta x, q + \Delta y] \in R \\ 0, & \text{otherwise} \end{cases} \quad (4.31)$$

where R means the rock region and I represents a property value of the image at the position. Grey level is the most common property used to construct co-occurrence matrix but other properties such as direction information and edge information can also be applied. Here, two kinds of co-occurrence matrices were used: the traditional grey level co-occurrence matrix (GLCM) and the direction co-occurrence matrix (DCM).

4.2.7.1 Grey level co-occurrence matrix algorithms

A GLCM is the co-occurrence matrix represented by the grey level. In our algorithm, the 0 – 255 grey intensities are divided into eight grey levels with the same intervals, and hence, the grey level co-occurrence matrices are of size 8×8 . Four kinds of the offsets $[\Delta x, \Delta y]$ were used. They are $[1, 0]$, $[1, 1]$, $[0, 1]$ and $[-1, 1]$, representing the co-occurring relations of two neighbouring pixels at 0° , 45° , 90° and 135° respectively. Thus, for each rock region, four matrices were generated. For convenience, every matrix was normalised to present the probability rather than the number of occurrence. After being normalised, for each matrix, five measures were calculated, which are *Entropy*, *Energy* (angular second moment), *Contrast*, *Homogeneity* (inverse difference moment) and *Correlation*:

$$Entropy = - \sum_{i=1}^8 \sum_{j=1}^8 C(i, j) \log C(i, j) \quad (4.32)$$

$$Energy = \sum_{i=1}^8 \sum_{j=1}^8 (C(i, j))^2 \quad (4.33)$$

$$Contrast = \sum_{i=1}^8 \sum_{j=1}^8 C(i, j)(i - j)^2 \quad (4.34)$$

$$Homogeneity = \sum_{i=1}^8 \sum_{j=1}^8 \frac{C(i, j)}{1 + (i - j)^2} \quad (4.35)$$

$$Correlation = \frac{\sum_{i=1}^8 \sum_{j=1}^8 (ij)C(i, j) - \mu_x \mu_y}{\sigma_x \sigma_y} \quad (4.36)$$

where μ_x , μ_y , σ_x and σ_y are the means and standard deviations in the x and y directions.

Finally, the average and standard deviation of each measure generated from all four matrices were calculated as features, labeled as *EntAvg_{GLCM}*, *EntStd_{GLCM}*, *EngAvg_{GLCM}*, *EngStd_{GLCM}*, *ConAvg_{GLCM}*, *ConStd_{GLCM}*, *HomAvg_{GLCM}*, *HomStd_{GLCM}*, *CorAvg_{GLCM}* and *CorStd_{GLCM}*.

4.2.7.2 Direction co-occurrence matrix algorithms

A DCM is similar to a GLCM but replaces grey levels with directional information. The Sobel operator was used to generate the direction of each pixel in the rock region. The direction range $[-\pi/2, \pi/2)$ was then partitioned into eight equal-size intervals thereby constructing another 8×8 matrix. Referring to the measures of each matrix, the formulas of *Entropy* and *Energy* of DCM are for the same as GLCM. However, because the ways to measure the distance of directions and grey levels are different (grey level information are linear but direction information is circular), *Contrast* and *Homogeneity* were calculated in slightly different manners:

$$Contrast = \sum_{i=1}^8 \sum_{j=1}^8 C(i, j) D(i, j)^2 \quad (4.37)$$

$$Homogeneity = \sum_{i=1}^8 \sum_{j=1}^8 \frac{C(i, j)}{1 + D(i, j)^2} \quad (4.38)$$

in which $D(i, j)$ is the distance between the i -th and j -th directions. This distance can be calculated as:

$$D(i, j) = \min(|i - j|, |i - j - 8|, |i - j + 8|) \quad (4.39)$$

Moreover, because it is hard to obtain μ and σ from the direction information, the *Correlation* has not been adopted as a measure of a DCM. The averages and standard deviations were then calculated to generate the eight DCM features: $EntAvg_{DCM}$, $EntStd_{DCM}$, $EngAvg_{DCM}$, $EngStd_{DCM}$, $ConAvg_{DCM}$, $ConStd_{DCM}$, $HomAvg_{DCM}$ and $HomStd_{DCM}$.

4.2.8 Taruma texture algorithms

[[Tamura et al., 1978](#)] proposed six texture features corresponding to human visual perception, namely, *coarseness*, *contrast*, *directionality*, *linelikeness*, *regularity* and *roughness*. Although these features have not been designed specifically for rocks, they can be used for rock images. Since *regularity* is a derivative of *coarseness*, *contrast*, *directionality* and *linelikeness*, and *roughness* is the sum of *coarseness* and *contrast*, these two features have not been used in the final experiments. Moreover, due to the high similarity between the feature *linelikeness* and the DCM feature

Con_{DCM} , *linelikeness* was discarded as well. Thus, three of the six features were utilised to describe rock geological attributes, labeled as $Coar_T$, Con_T and Dir_T .

4.3 Mapping Procedures

In the previous section, 63 computer vision features have been presented to describe different characteristics of rocks. This section discusses mapping the features onto geological concepts. Firstly, rock images from different sources were collected and labeled with rock regions. From these labeled regions, vision features were extracted through the algorithms mentioned above and the values of the three attributes (i.e. *Relief*, *Angularity* and *Layering*) were provided by a geologist. Correlation coefficients were used to reflect the similarity between each feature and attribute. If a feature has a high similarity to a specific geological attribute, the feature can probably be used for representing this geological attribute and thus a good mapping could be expected. In addition, linear combinations of features are discussed as well.

4.3.1 Rock images

One hundred and three images of rocks were collected for testing the algorithms. The rock images come from four sources. The first source is the real Mars images captured by the cameras of real Mars rovers: Mars Exploration Rover (MER) (Spirit and Opportunity rovers) and Mars Science Laboratory (MSL) (Curiosity rover). The images contain some famous rocks in Mars exploration such as the iron meteorite “Heat Shield”. The second source of images is from a series of rock specimens provided by Northern Geological Supplies. The specimens contain 15 igneous rocks (granite, basalt, etc.), 15 sedimentary rock (sandstone, shale, etc.) and 10 metamorphic rocks (slate, marble, etc.). The third source is images of float rocks at Clarach bay where the Planetary Robotics Vision Scout rover (PRoViScout) [Paar et al., 2012] has done some field experiments. The last kind of rock source is images of rocks in the Planetary Analogue Terrain Laboratory (PATLab) [Barnes et al., 2008] which were selected by geologists. Some of the rocks were used as the science targets of field trials [Woods et al., 2009]. The real Mars images were captured by different cameras including Pancam and Navcam of MER, MastCam and MAHLI of MSL. Hence, the resolutions of these images are different, from 384×384 to 1024×1024 . The rock specimen images were captured

on a white background by an industrial camera with resolution 1024×1024 . Since the sizes of specimens are relatively small, they only occupy small regions in the center of the original 1024×1024 images and other parts of images are blank background. Hence the images were cropped to 512×512 . The images of Clarach bay and the PATLab were both captured by a 2304×1704 CCD digital camera and were cropped and resized to 1024×768 . Examples of rock images with manual labeled regions from the four sources are illustrated in Fig. 4.15.

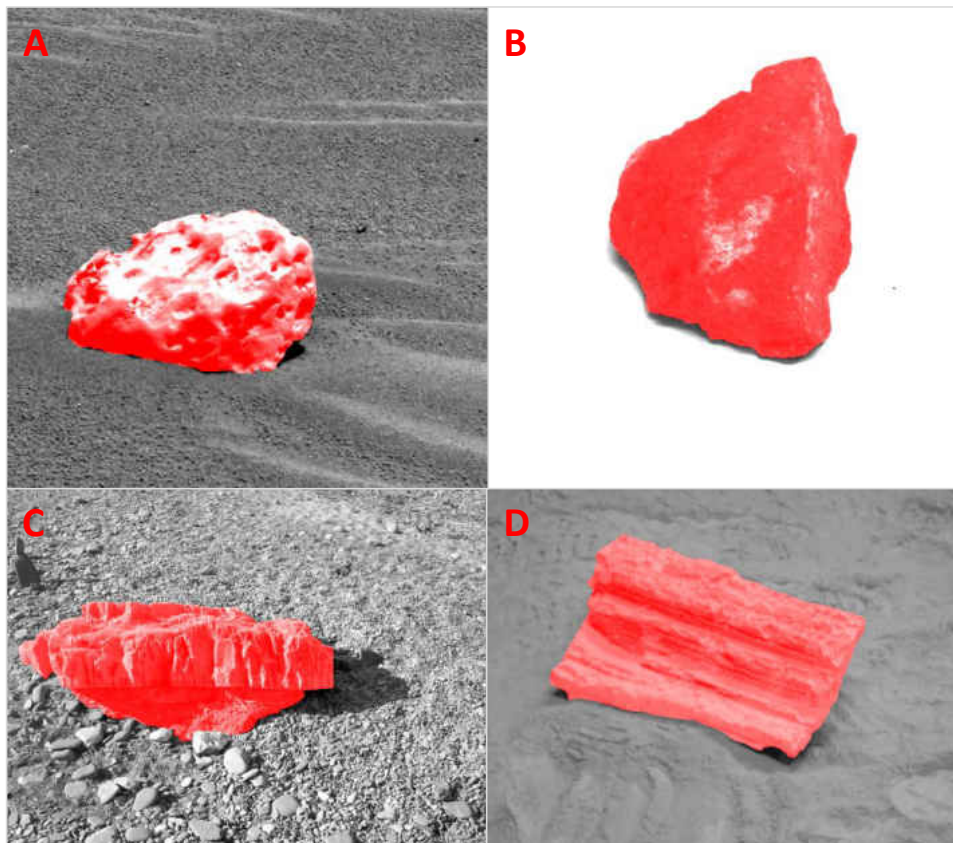


Figure 4.15: Rock images from different sources with red labeled rock regions: (A) MER image (“Heat Shield” meteorite); (B) specimen image (basalt); (C) the image of a rock at Clarach bay; (D) the image of a rock in PATLab with layering structure.

4.3.2 Expert scoring of the geological attributes

As mentioned before, our aim is to try to use the visual features calculated by computer to represent geological expert's knowledge. Therefore, an expert is indispensable in the experiment to provide the ground truth of every attribute of every rock. Altogether, three attributes of all 103 rock samples needed to be evaluated. Dr. Derek Pullan, the expert of geology and planetary exploration from University of Leicester, was invited to score every attribute of all 103 rock samples. In addition, software was developed to accelerate the process of the evaluation. The GUI of the software is displayed in Fig. 4.16. Using the software makes it more efficient to view all of the rock samples. And by sliding the slider, the score of each attribute of each rock can be rapidly graded. According to the requirement of the geological expert, the attribute scores were given on a scale from 0 to 10. For example, if a rock is extremely angular, its angularity score will be 10, and conversely, the angularity of a very round rock will be scored as 0. The expert mentioned that there could be some inconsistencies of scores across the data but they were adequate to be regarded as the ground truth for testing the algorithms and the visual features.

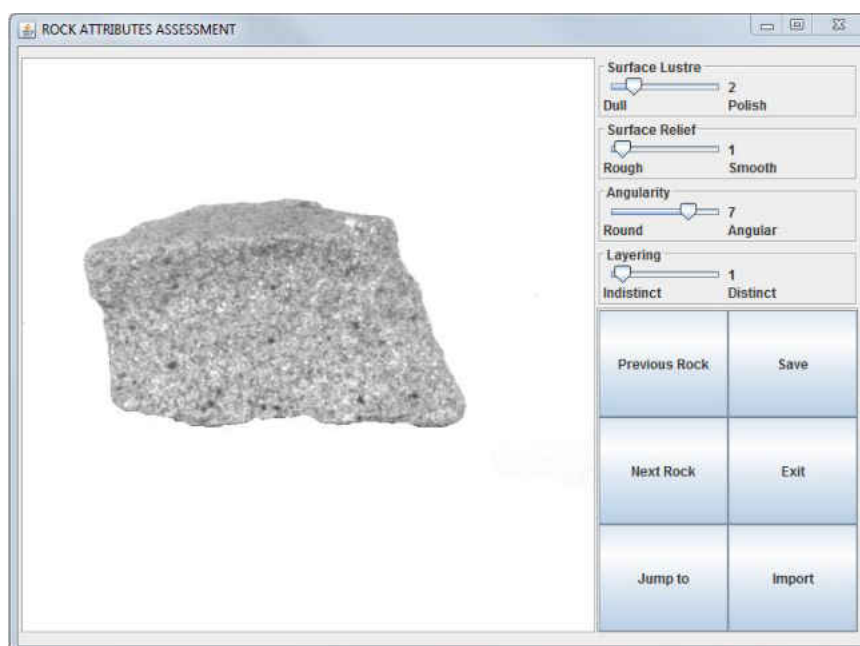


Figure 4.16: Graphic user interface of the rock evaluation software

4.3.3 Mapping of visual features and geological attributes

After 63 features were generated and three attribute scores were approximately graded by a geologist, it was time to investigate the relation between visual feature(s) and attributes. Attempts have been made to search for the visual feature(s) matching the specified attribute score most precisely. In other words, for each attribute, we try to find a feature (a single original feature or a feature composed of several original features¹) which can represent the expert's thinking (attribute score) most appropriately.

4.3.3.1 Single feature mapping

Original features, meaning the features directly generated by the algorithms without any processing such as normalisation, scaling and adding bias, were used for mapping geological attributes. Correlation measures were employed to calculate the dependence relation between each attribute and each single original feature. Two kinds of correlation coefficients were used. These were: Pearson's product-moment coefficient reflecting the linear dependence and Spearman's rank correlation which considers only the order consistency of the rank without requiring a linear relationship. Both correlation coefficients between all three geological attributes and all 63 features were computed through all 103 rock samples. The correlation results are shown in Tables 4.1, 4.2, 4.3, 4.4, 4.5, 4.6 and 4.7, catalogued by different algorithm types.

Table 4.1: Correlation results of the features generated by basic grey level and direction statistics algorithms

Feature	Pearson's Correlation			Spearman's Correlation		
	<i>Relief</i>	<i>Angularity</i>	<i>Layering</i>	<i>Relief</i>	<i>Angularity</i>	<i>Layering</i>
<i>Mean</i>	-0.115	-0.319	-0.359	-0.126	-0.328	-0.241
<i>Variance</i>	-0.242	-0.001	-0.109	-0.342	0.03	0.032
<i>CV</i>	-0.184	0.188	0.081	-0.221	0.252	0.211
<i>Skewness</i>	0.138	0.095	-0.024	0.089	0.215	0.051
<i>Kurtosis</i>	0.119	-0.194	-0.146	0.134	-0.053	-0.065
<i>Ent_{gl}</i>	-0.297	0.121	-0.067	-0.314	0.068	0.028
<i>Ent_{dir}</i>	-0.076	-0.223	-0.599	-0.015	-0.241	-0.593
<i>SP_{dir}</i>	-0.039	-0.277	-0.686	0.025	-0.241	-0.582

¹Also called combination feature.

Table 4.2: Correlation results of the features generated by shape-based algorithms

Feature	Pearson's Correlation			Spearman's Correlation		
	<i>Relief</i>	<i>Angularity</i>	<i>Layering</i>	<i>Relief</i>	<i>Angularity</i>	<i>Layering</i>
<i>Area</i>	-0.07	-0.048	0.239	0.048	0.064	0.324
<i>Extent</i>	0.222	-0.375	-0.099	0.252	-0.303	-0.037
<i>Solidity</i>	0.305	-0.267	-0.064	0.384	-0.243	-0.034
<i>Compactness</i>	0.186	-0.391	-0.424	0.232	-0.323	-0.368
<i>R_p</i>	0.467	-0.069	0.108	0.584	-0.079	0.084
<i>Eccentricity</i>	0.183	0.109	0.567	0.212	0.186	0.643
<i>Err_{fit}</i>	-0.162	0.165	0.046	-0.23	0.192	0.072
<i>I₁</i>	0.166	0.248	0.528	0.134	0.225	0.644
<i>I₂</i>	0.164	0.199	0.457	0.185	0.187	0.654
<i>I₃</i>	-0.048	0.14	0.085	-0.15	0.111	0.08
<i>I₄</i>	-0.003	0.099	0.138	-0.011	0.151	0.468
<i>I₅</i>	-0.031	0.082	0.046	0.01	0.041	0.419
<i>I₆</i>	0.031	0.065	0.112	0.07	0.118	0.483
<i>I₇</i>	0.057	0.107	-0.133	0.121	0.035	0.005
<i>BE</i>	-0.13	0.01	-0.099	-0.567	0.109	0.052

Table 4.3: Correlation results of the features generated by Canny-based algorithms

Feature	Pearson's Correlation			Spearman's Correlation		
	<i>Relief</i>	<i>Angularity</i>	<i>Layering</i>	<i>Relief</i>	<i>Angularity</i>	<i>Layering</i>
<i>Ent_{Cpixel}</i>	-0.128	-0.301	-0.648	-0.066	-0.285	-0.632
<i>SP_{Cpixel}</i>	-0.068	-0.332	-0.738	-0.007	-0.272	-0.625
<i>Ent_{Cedge}</i>	-0.063	-0.207	-0.583	-0.041	-0.209	-0.568
<i>SP_{Cedge}</i>	0	-0.315	-0.665	0.045	-0.255	-0.579
<i>Ent_{Cchain}</i>	-0.081	-0.242	-0.649	-0.024	-0.3	-0.626
<i>SP_{Cchain}</i>	-0.055	-0.312	-0.716	-0.019	-0.246	-0.6
<i>Den_{Canny}</i>	-0.481	-0.039	-0.401	-0.501	-0.14	-0.248
<i>SP_{Hough}</i>	0.142	-0.356	-0.127	0.016	-0.266	-0.17

Table 4.4: Correlation results of the features generated by Gabor-based algorithms

Feature	Pearson's Correlation			Spearman's Correlation		
	<i>Relief</i>	<i>Angularity</i>	<i>Layering</i>	<i>Relief</i>	<i>Angularity</i>	<i>Layering</i>
Ent_{Gdir}	0.044	-0.295	-0.636	0.079	-0.236	-0.543
SP_{Gdir}	-0.032	-0.215	-0.644	-0.025	-0.256	-0.603
Ent_{Gscale}	-0.188	-0.005	-0.334	-0.162	-0.053	-0.142
$Scale_{lwl}$	0.146	0.031	0.332	0.23	0.138	0.337
$Scale_{\lambda}$	0.222	0.05	0.349	0.291	0.154	0.333
StD_G	-0.46	-0.064	-0.234	-0.527	-0.076	-0.151
$MaxMean_G$	-0.428	-0.042	-0.146	-0.521	-0.03	-0.072

Table 4.5: Correlation results of the densities of different corners

Feature	Pearson's Correlation			Spearman's Correlation		
	<i>Relief</i>	<i>Angularity</i>	<i>Layering</i>	<i>Relief</i>	<i>Angularity</i>	<i>Layering</i>
Den_{Harris}	-0.417	-0.089	-0.293	-0.425	-0.1	-0.286
Den_{Shi}	-0.317	-0.056	-0.465	-0.323	-0.133	-0.33
Den_{SIFT}	-0.58	-0.041	-0.309	-0.617	-0.092	-0.171
Den_{SUSAN}	-0.423	-0.103	-0.25	-0.572	-0.073	-0.222

Table 4.6: Correlation results of the features generated from the grey level and direction co-occurrence matrices

Feature	Pearson's Correlation			Spearman's Correlation		
	<i>Relief</i>	<i>Angularity</i>	<i>Layering</i>	<i>Relief</i>	<i>Angularity</i>	<i>Layering</i>
<i>EntAvg_{GLCM}</i>	-0.445	0.066	-0.194	-0.45	0.003	-0.071
<i>EntStd_{GLCM}</i>	-0.437	0.076	0.164	-0.486	0.043	0.229
<i>EngAvg_{GLCM}</i>	0.438	-0.126	0.163	0.457	0.021	0.211
<i>EngStd_{GLCM}</i>	-0.143	0.116	0.319	-0.128	0.109	0.383
<i>ConAvg_{GLCM}</i>	-0.437	-0.087	-0.244	-0.576	-0.101	-0.237
<i>ConStd_{GLCM}</i>	-0.34	-0.118	-0.09	-0.58	-0.051	-0.068
<i>HomAvg_{GLCM}</i>	0.554	0.032	0.369	0.617	0.135	0.405
<i>HomStd_{GLCM}</i>	-0.509	0.001	0.011	-0.586	-0.054	0.072
<i>CorAvg_{GLCM}</i>	0.127	0.081	0.319	0.192	0.111	0.309
<i>CorStd_{GLCM}</i>	-0.304	-0.079	-0.173	-0.331	-0.068	-0.018
<i>EntAvg_{DCM}</i>	-0.201	-0.079	-0.546	-0.179	-0.066	-0.435
<i>EntStd_{DCM}</i>	0.196	-0.044	0.432	0.221	0.017	0.425
<i>EngAvg_{DCM}</i>	0.176	0.095	0.494	0.178	0.116	0.596
<i>EngStd_{DCM}</i>	0.169	0.073	0.53	0.173	0.064	0.537
<i>ConAvg_{DCM}</i>	-0.259	0.033	-0.426	-0.259	-0.02	-0.285
<i>ConStd_{DCM}</i>	-0.312	-0.048	-0.059	-0.289	-0.131	0.036
<i>HomAvg_{DCM}</i>	0.253	-0.01	0.438	0.264	0.068	0.447
<i>HomStd_{DCM}</i>	-0.06	-0.05	0.368	-0.078	-0.058	0.386

Table 4.7: Correlation result of the Tamura features

Feature	Pearson's Correlation			Spearman's Correlation		
	<i>Relief</i>	<i>Angularity</i>	<i>Layering</i>	<i>Relief</i>	<i>Angularity</i>	<i>Layering</i>
<i>Coar_T</i>	0.401	0.154	0.277	0.411	0.263	0.295
<i>Con_T</i>	-0.213	0.006	-0.07	-0.326	0.059	0.072
<i>Dir_T</i>	0.465	0.095	0.547	0.523	0.138	0.551

In terms of the single feature selection by the evaluation of correlation coefficients, we assumed that, to a specified geological attribute, the higher the absolute correlation value of a feature is, the better it represents the attribute. The reason for using absolute correlation value is that if a feature has a high negative correlation value to a geological attribute, a new feature that has a positive correlation with the same absolute value of the negative correlation can be constructed from the original feature by performing negation or being subtracted from the maximum value of the feature. Thus, the feature with the highest correlation to the score of one attribute will be regarded as the most appropriate feature to describe the attribute. For each attribute, the feature with highest absolute correlation values (Pearson's and Spearman's) is marked in red in the tables.

According to the Pearson's correlation, Den_{SIFT} , $Compactness$ and SP_{Cpixel} have the highest correlations to the geological attributes $Relief$, $Angularity$ and $Layering$ respectively. Nevertheless, the features with highest Spearman's correlation performance are $HomAvg_{GLCM}$, $Compactness$ and I_2 . There exists an inconsistency between two correlation coefficients.

As the Pearson's correlation reflects a linear relationship, a feature with a high Pearson's correlation value can be regarded as an indicator of the corresponding geological attribute directly or only with a linear transformation. However, because Spearman's correlation only reflects the order of rank, a feature with a high Spearman's correlation value may need a power, root or exponential transformation before being able to represent the geological attribute. In addition, a feature that has a high Pearson's correlation will probably have a high Spearman's correlation, but not vice versa. Moreover, due to the limited range of the expert score (0-10, 11 values), identical attribute scores of different rocks were inevitable and part of the ranks of these attributes will be the same. However, the algorithms rarely generate identical values, and hence generally the visual features have unique ranks. Such a difference of ranking may also introduce some uncertainty into the Spearman's correlation statistics. Given all that, the Pearson's correlation coefficient is preferable to Spearman's in correlation evaluation. Thus, judged by the Pearson's correlation coefficient, the best single representative features of $Relief$, $Angularity$ and $Layering$ are Den_{SIFT} , $Compactness$ and SP_{Cpixel} respectively.

4.3.3.2 Linear combination feature mapping

Although using original features directly can be able to represent geological attributes, it seems that a better mapping could be generated by combining two

or more features together. Indeed, the original features could be complementary while describing an attribute. For example, in terms of angularity, the shape-base features such as *Compactness* reflect the sharpness of a rock contour and the corner density such as *Den_{SIFT}* reflect the pointedness inside the rock contour. Combining them together has the potential to make a new feature that represents the *Angularity* attribute more closely.

Thus, the feasibility of combination features is discussed in this section. A combination feature will refer two or more original features generated from the visual algorithms mentioned above. For clarity, the original features are numbered as Table 4.8.

Table 4.8: Feature reference number

No.	Feature	No.	Feature	No.	Feature
1	<i>Mean</i>	22	I_7	43	$EntAvg_{GLCM}$
2	<i>Variance</i>	23	BE	44	$EntStd_{GLCM}$
3	<i>CV</i>	24	Ent_{Cpixel}	45	$EngAvg_{GLCM}$
4	<i>Skewness</i>	25	SP_{Cpixel}	46	$EngStd_{GLCM}$
5	<i>Kurtosis</i>	26	Ent_{Cedge}	47	$ConAvg_{GLCM}$
6	Ent_{gl}	27	SP_{Cedge}	48	$ConStd_{GLCM}$
7	Ent_{dir}	28	Ent_{Cchain}	49	$HomAvg_{GLCM}$
8	SP_{dir}	29	SP_{Cchain}	50	$HomStd_{GLCM}$
9	<i>Area</i>	30	Den_{Canny}	51	$CorAvg_{GLCM}$
10	<i>Extent</i>	31	SP_{Hough}	52	$CorStd_{GLCM}$
11	<i>Solidity</i>	32	Ent_{Gdir}	53	$EntAvg_{DCM}$
12	<i>Compactness</i>	33	SP_{Gdir}	54	$EntStd_{DCM}$
13	R_p	34	Ent_{Gscale}	55	$EngAvg_{DCM}$
14	<i>Eccentricity</i>	35	$Scale_{tol}$	56	$EngStd_{DCM}$
15	Err_{fit}	36	$Scale_{\lambda}$	57	$ConAvg_{DCM}$
16	I_1	37	Std_G	58	$ConStd_{DCM}$
17	I_2	38	$MaxMean_G$	59	$HomAvg_{DCM}$
18	I_3	39	Den_{Harris}	60	$HomStd_{DCM}$
19	I_4	40	Den_{Shi}	61	$Coar_T$
20	I_5	41	Den_{SIFT}	62	Con_T
21	I_6	42	Den_{SUSAN}	63	Dir_T

Due to the difficulty in finding a specified function to fit the original features, only linear combination methods are discussed in the current stage. A combination

feature can be expressed as:

$$F_{comb} = \beta_0 + \beta_1 F_1 + \beta_2 F_2 \cdots + \beta_n F_n \quad (4.40)$$

where F_n denotes the original feature and β_n ¹ denotes the combined weight of the relative feature, can be positive or negative. It can also be zero, which means the feature is not selected to calculate the combination feature. Thus the final problem is how to decide the weight of each original feature to express the knowledge of the expert more precisely. Similar to the case of single original features, the evaluation of matching degree was based on the Pearson's correlation coefficient. A high absolute correlation between a combination feature and a specified attribute can imply that the combination feature can express the attribute more precisely. Fig. 4.17 shows the correlation values between combination features and a specified geological attribute. In the example, the combination features were composed of *Compactness* and *Dens_{SIFT}* with different combination weight ratios, while the geological attribute was *Angularity*.

The ratios denote the ratios of weights applied in feature combinations. For example, the ratio 1 : 10 can mean combination features such as:

$$\begin{aligned} F_{comb} &= 1 \times Compactness + 10 \times Dens_{SIFT} \\ \text{or } F_{comb} &= 0.1 \times Compactness + 1 \times Dens_{SIFT} \\ \text{or } F_{comb} &= -1 \times Compactness - 10 \times Dens_{SIFT} \end{aligned} \quad (4.41)$$

The reason why we used the weight ratios but not the weights for the demonstration is that, in the calculation process of the Pearson correlation coefficient, the data is scaled by its standard deviation. Hence, the correlation value remains invariant when the combination weights of original features change proportionally. For example, in terms of a specified geological attribute, the three F_{comb} s in Eqn. (4.41) will obtain the same correlation value.

If we regard the mapping process between visual features and a specified geological attribute as an overdetermined regression, the least square method, a standard approach to calculate the approximate solutions of overdetermined systems, can be applied to find the optimised weights $\hat{\beta}$ by minimising the sum of the square

¹Particularly, β_0 is a constant which can facilitate the least square method discussed below.

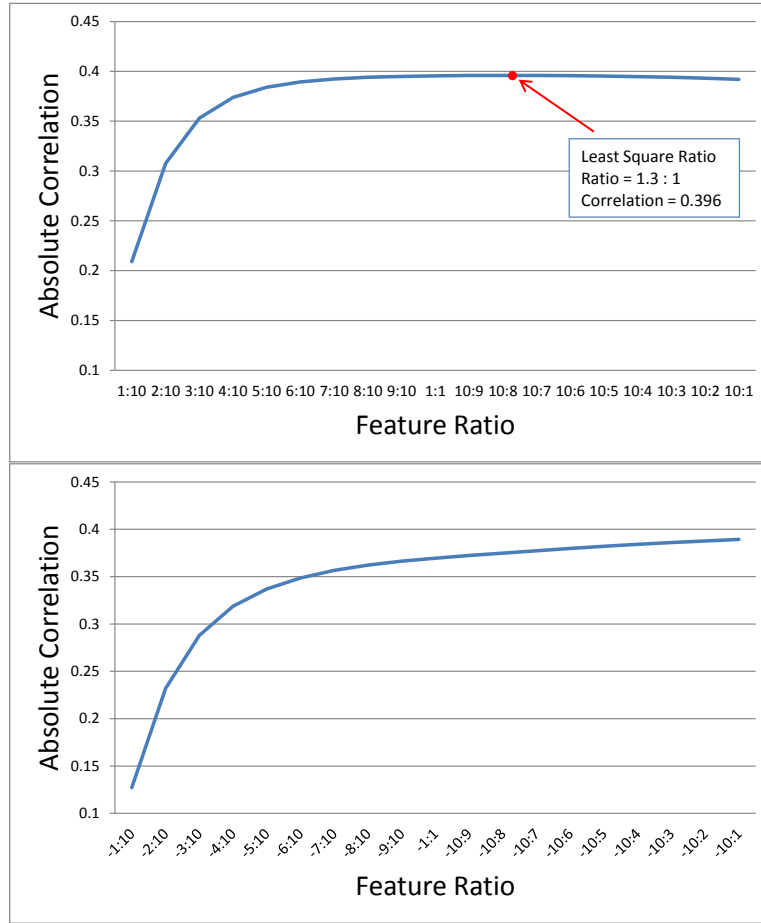


Figure 4.17: Correlation between a specified attribute (*Angularity*) and the combination features (combined by *Compactness* and *Dens_{SIFT}*) with different combination ratios. The red point position indicates the ratio of weights generated from the least square algorithm.

residues (i.e. the difference between combined feature $F\beta$ and attribute score S).

$$\hat{\beta} = \arg \min \sum (F\beta - S)^2 \quad (4.42)$$

In addition, we found that the Pearson's correlation of the combination feature with the weights generated by the linear least square method almost reaches the highest value. For example, combining the two original features *Compactness* and

Den_{SIFT} , the least square combination feature F_{LS} to represent *Angularity* is:

$$F_{LS} = 10.0532 - 21.8246 \times Compactness - 16.7953 \times Den_{SIFT} \quad (4.43)$$

The weight ratio of the two features is $21.8246/16.7863 \approx 1.3$. As can be seen in Fig. 4.17, the least square weight ratio is corresponding to the highest correlation.

Since the least square method can be used to calculate the combination feature with not only a minimum square residue sum but also a high correlation, it was applied to generate the combination features with optimised weights. On the other hand, overfitting is another problem which will occur in a combination process and will affect the performance of combination features. Generally, overfitting occurs when a model is excessively complex, such as having too many parameters relatively to the number of observations. In our case, as the number of observations (i.e. rock samples) is fixed, increasing the number of features for combination will also increase the probability of overfitting. Hence a tradeoff must be made between the correlation performance and the number of features for the combination. Here, three ways were attempted to find the best linear combination feature which is composed of a limited number of original features to represent each geological attribute. These were the enumeration method, a fast greedy method and the linear regression with L1-constraints (Lasso) method.

A. Enumeration method

This method firstly defines the number of original features for combinations. All possible sets with the specified number of original features are enumerated and then the combination features are calculated through the least square method. Particularly, the calculation of the combination weights of each geological attribute is independent. That is to say, under each limitation of feature number, three feature sets will be generated to represent the three geological attributes *Relief*, *Angularity* and *Layering* respectively. The combination feature with the highest absolute correlation value to each geological attribute is selected as the best combination feature to represent the corresponding attribute. The feature set which generates the best combination is therefore called best feature set.

For a n -feature combination, $\prod_{i=1}^n (63-i)/n!$ feature sets need to be calculated. In the case of 7-feature combination, the set number is 553,270,671. Hence, due to the huge calculation amount and the aim to restrict the number of original features, only the feature sets containing two to six original features were consid-

ered. Table 4.9 shows the feature indices (see Table 4.8) in best feature sets with different feature numbers, in which a 1-feature set is equivalent to the single original feature. Fig. 4.18 illustrates the correlation values of the combination features generated from those best feature sets.

Table 4.9: Feature reference number(s) in the best feature sets under different feature number limitations

	1	2	3	4	5	6
<i>Relief</i>	41	13, 41	13, 41, 46	13, 41, 46, 63	13, 38, 41, 50, 63	1, 4, 13, 33, 38, 50
<i>Angularity</i>	12	1, 10	1, 5, 10	1, 10, 45, 48	1, 25, 45, 50, 59	1, 10, 25, 45, 50, 59
<i>Layering</i>	25	25, 49	29, 37, 38	25, 26, 33, 37	4, 25, 26, 33, 47	4, 9, 25, 26, 33, 48

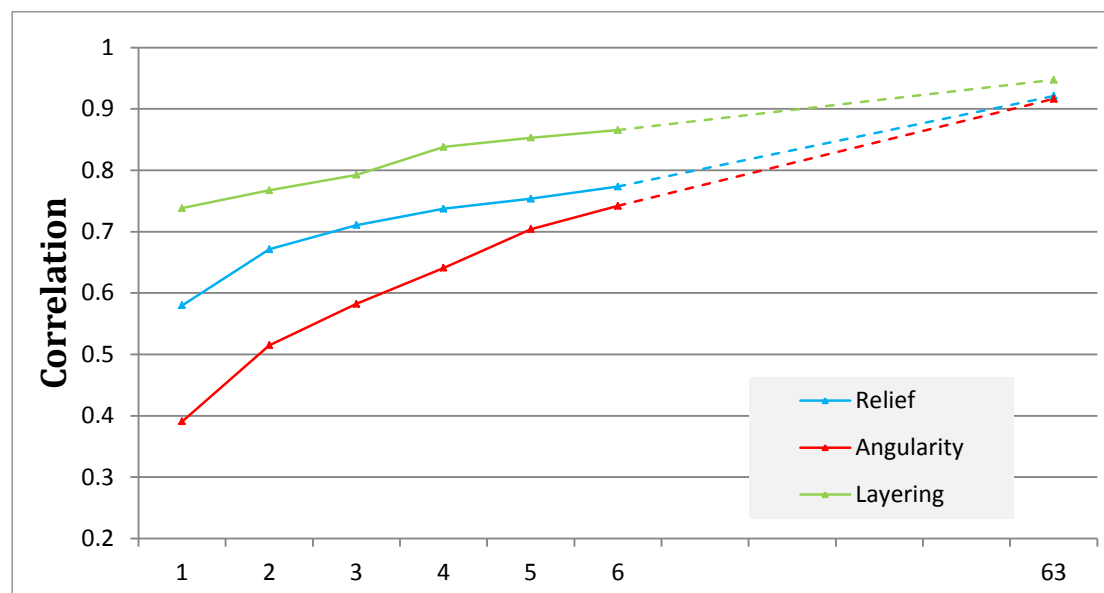


Figure 4.18: Correlation values of the combination features generated from the best feature sets under different feature number limitation

B. Fast greedy method

It can be seen in Table 4.9, for a specific attribute, a best feature set with more features tends to contain the elements in the best features with fewer features. For example, for the attribute *Relief*, the best 1-feature set ([41]) is a subset of the best

2-feature set ([13, 41]) and the best 2-feature is a subset of the best 3-feature set ([13, 41, 46]). Hence, a fast greedy algorithm (shown in Fig. 4.19) was proposed for the purpose of accelerating the calculation of the “best” feature sets.

\mathcal{F}_i is the “best” feature set in the i -feature case.

i_{max} is the maximum number of features. It is 63 in our case.

A is a specified attribute.

$C(\mathcal{F}, A)$ is the correlation value between the feature set \mathcal{F} and the attribute A .

```

1   $\mathcal{F}_0 \leftarrow \{\}$ 
2  for  $i = 1$  to  $i_{max}$  do
3     $T \leftarrow \mathcal{F}_{n-1}$ 
4    foreach  $x \in (\mathcal{F}_{all} - T)$ 
5      if  $C(\mathcal{F}_{n-1} \cup x, A) > C(T, A)$ 
6         $T \leftarrow \mathcal{F}_{n-1} \cup x$ 
7     $\mathcal{F}_n \leftarrow T$ 

```

Figure 4.19: Pseudocode of the fast greedy method

This method starts off with an empty set, and then the features will be added gradually while increasing the number of features. At a time (iteration), only one feature is added to previous “best” feature set to create the new “best” feature set with one more feature. The additional feature is the one that causes the greatest correlation increase to the previous set. The i -feature feature set will definitely be a subset of $(i+1)$ -feature feature set. Thus, it does not need to enumerate all possible feature sets thereby reducing the calculation time dramatically. For generating the best i -feature combination feature set, the number of calculation will decrease from $\prod_{i=1}^n (63 - i)/n!$ to $64 - i$. Therefore, by applying such a greedy method, the combination feature calculation will not be limited by the number of features. On the other hand, although this method will probably not find the global best feature set, due to the greedy property of this method, the combination features generated by the “best” feature sets will be relatively high-scoring as well. As an $(i+1)$ -feature set can be represented by an i -feature set plus an additional feature, the “best” feature sets of all attributes are presented by corresponding addition features, which are shown in Table 4.10. The overall correlation results of the combination features generated by these feature sets are shown in Fig. 4.20.

C. Linear regression with L1-constraints (Lasso)

The Lasso method is a shrinkage and selection method for linear regression [Tibshirani, 1996]. It minimises the usual sum of squared residues, with a bound on

Table 4.10: Additional features of each iteration during the process of the greedy method

No.	Relief	Angularity	Layering	No.	Relief	Angularity	Layering
1	41	12	25	33	35	18	21
2	13	1	49	34	36	62	16
3	46	31	33	35	56	49	20
4	63	40	26	36	7	43	41
5	37	48	4	37	61	36	60
6	40	5	9	38	55	60	54
7	54	10	48	39	53	46	50
8	52	54	11	40	59	52	14
9	11	6	32	41	4	55	57
10	47	25	10	42	27	37	34
11	10	14	27	43	22	41	46
12	51	2	62	44	24	28	52
13	58	50	43	45	60	51	7
14	44	33	45	46	1	34	56
15	33	63	5	47	49	38	1
16	20	47	12	48	6	57	53
17	29	9	17	49	30	45	28
18	16	58	40	50	23	30	8
19	34	20	6	51	2	44	63
20	28	22	42	52	32	56	29
21	42	3	23	53	15	26	35
22	18	39	39	54	45	23	36
23	62	42	61	55	12	8	38
24	39	53	55	56	26	24	37
25	21	35	44	57	14	59	59
26	19	61	3	58	3	4	31
27	17	19	24	59	9	11	47
28	38	16	58	60	50	27	51
29	8	13	2	61	31	7	13
30	5	17	15	62	48	32	19
31	25	21	30	63	57	29	18
32	43	15	22				

the sum of the absolute values of the weights (L1-norm). A simple expression of

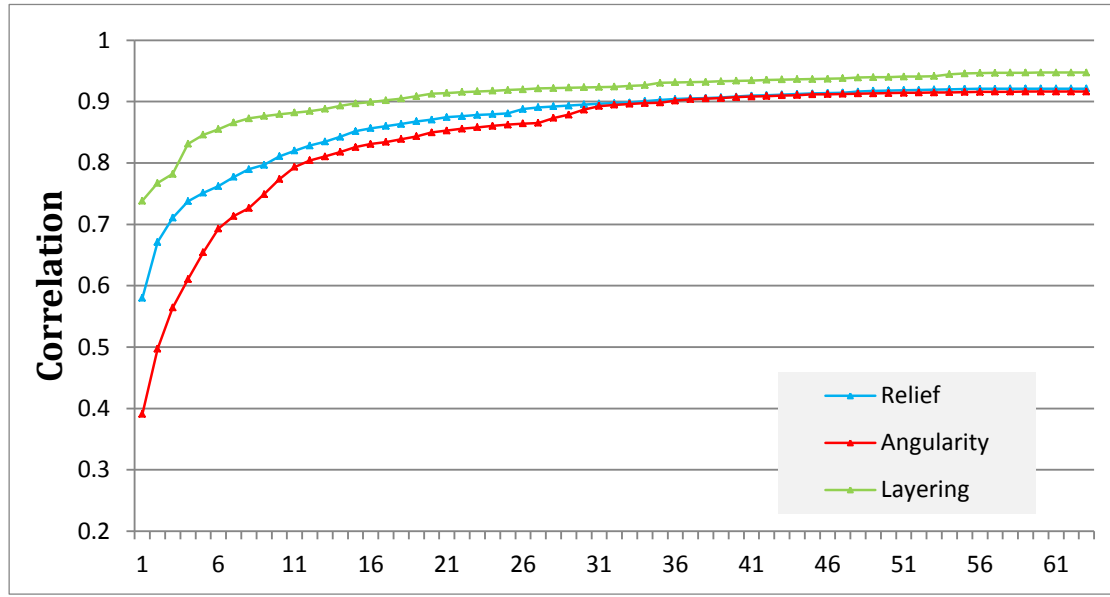


Figure 4.20: Correlation results of the combination features with the combination weights calculated by the fast greedy algorithm

the Lasso method can be written as a least square regression with a L1 penalty.

$$\hat{\beta} = \arg \min \sum (F\beta - S)^2 + \lambda \|\beta\|_1 \quad (4.44)$$

where $\|\beta\|_1$ is the L1-norm of the combination weights:

$$\|\beta\|_1 = \sum_{i=1}^n |\beta_i| \quad (4.45)$$

By increasing the L1 penalty coefficient λ , the combination weights of a combination feature will be driven to zero. Thus, the Lasso method can automatically deselect some features within the regression process and hence it is not necessary to predefine the number of original features. The combination features with limited numbers of original features can be generated directly with a suitable λ . Here we tested the Lasso method on our data with λ ranging from 0.1 to 1. Table 4.11 lists the “selected” original feature indices of the Lasso combination features generated by different λ values. It can be seen that, if λ reaches a certain value, the result is the same as for single feature selection. Fig. 4.21 shows the correlation results of the Lasso combination features.

Table 4.11: Selected features through the Lasso algorithm with different λ

λ	<i>Relief</i>	<i>Angularity</i>	<i>Layering</i>
0.1	1, 4, 9, 10, 13, 14, 16, 31, 36, 40, 41, 46, 57, 63	1, 5, 6, 9, 10, 12, 14, 20, 21, 22, 24, 25, 29, 31, 45, 48, 54, 57	1, 4, 5, 9, 13, 14, 21, 22, 25, 26, 29, 33, 35, 48, 50, 52, 62
0.2	9, 10, 13, 31, 41, 46, 57, 61, 63	1, 5, 10, 12, 25, 29, 31, 45, 48, 54, 57	1, 2, 9, 14, 22, 25, 29, 33, 36, 37, 48, 49, 52
0.3	13, 41, 46, 61, 63	1, 5, 10, 12, 31, 48	1, 9, 14, 25, 29, 33, 36, 42, 49
0.4	13, 41, 46, 50, 61, 63	1, 10, 12, 31	1, 9, 14, 25, 29, 33, 36, 49
0.5	13, 41, 61, 63	1, 10, 12, 31	1, 14, 25, 29, 33, 49
0.6	13, 41, 63	1, 10, 12, 31	1, 14, 25, 29, 33, 49
0.7	13, 41	10, 12, 31	1, 14, 25, 29, 33, 49
0.8	13, 41	12	1, 14, 25, 29, 49
0.9	13, 41	\emptyset	14, 25
1	41	\emptyset	25

As can be seen in the correlation results, whether the enumeration method, the greedy method or the Lasso method, the correlation tends to increase along with the number of original features for combination. It seems that the correlation can reach a certain level as long as the number of original features is enough. However, as mentioned before, increasing the number of original features will also increase the possibility of overfitting. Overfitting means that the combination feature excessively matches the “training” data and hence has poor adaptability and robustness. The overfitted combination feature will generally have poor predictive performance on other data.

Here, in order to judge the efficacy of the combination features, a test set of rock images has been established. The test set contains 30 images of rock samples and the attribute scores of each rock sample have been evaluated by the same geologist. Table 4.12 shows the Pearson’s correlation result for every original feature on the basis of test sets.

Specifically in the table, the highest absolute correlation values to each geological attribute is labeled in colour (red for training set, blue for test set, magenta for both). To distinguish with the test set, the original image set containing 103 samples was called “training set”. It can be found that, for each geological attribute, if the single feature selected by training set is applied for the test set’s

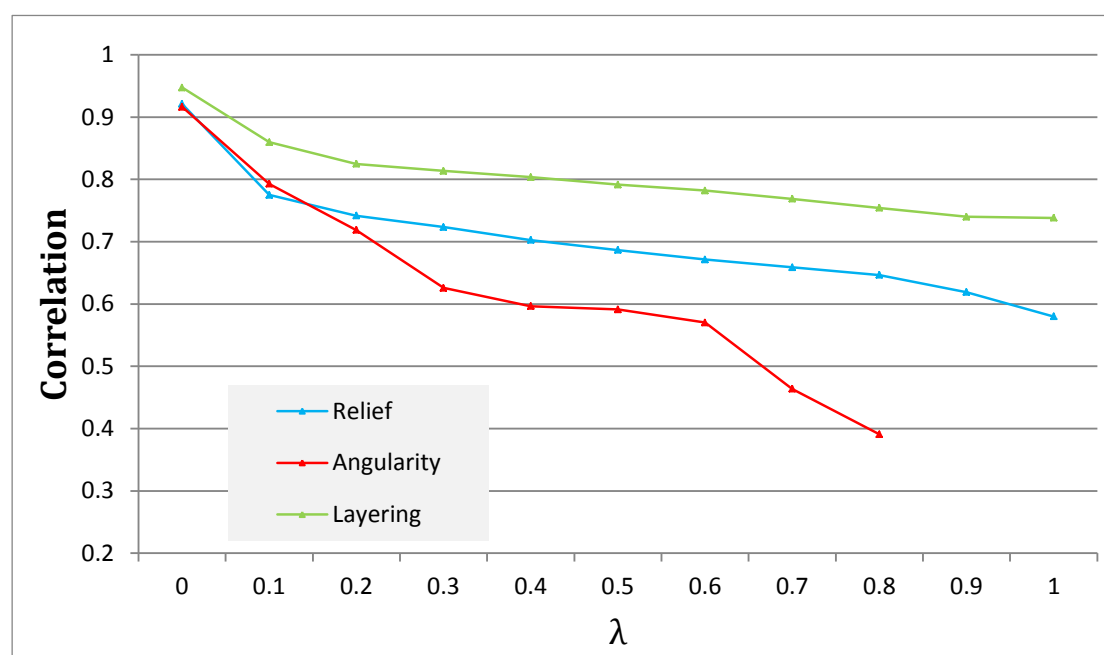


Figure 4.21: Correlation values of the combination features corresponding to different values of λ . In particular, when $\lambda = 0$, the Lasso method is equivalent to the least square method.

representation, the correlation performance is still good. In addition, the original single features' correlation values for the training set and the test set are similar, implying that a single feature is a relatively stable indicator to represent geological attributes, whether good or bad.

With regard to the combination features, for testing the adaptability, we did not recalculate combination weights again but used the weights calculated from the previous training set. Hence, by using the feature values generated from the test set and the weights generated from the training set, the combination features for the test set were constructed. The correlation performance of combination features with the weights calculated by the enumeration method, the fast greedy method and the Lasso method are illustrated in Figs. 4.22, 4.23 and 4.24.

It can be seen from the performance results of the test set that, for the geological attributes *Relief* and *Layering*, applying the combination features composed of a few (2 or 3) original features can gain a small correlation increase. However, in terms of the attribute *Angularity*, using combination features did not obtain better correlation performance. The single feature produced the best correlation

Table 4.12: Single original feature's correlation results of the test set data

<i>No.</i>	<i>Relief</i>	<i>Angularity</i>	<i>Layering</i>	<i>No.</i>	<i>Relief</i>	<i>Angularity</i>	<i>Layering</i>
1	-0.099	-0.077	-0.102	33	0.066	-0.151	-0.548
2	-0.237	0.025	-0.116	34	-0.121	-0.308	-0.002
3	-0.135	0.200	-0.066	35	0.138	0.404	0.133
4	0.153	-0.066	-0.204	36	0.251	0.476	0.149
5	0.317	0.015	-0.167	37	-0.500	-0.182	-0.174
6	-0.280	0.012	-0.108	38	-0.476	-0.121	-0.103
7	-0.006	-0.252	-0.707	39	-0.418	-0.348	-0.239
8	0.068	-0.204	-0.605	40	-0.417	-0.234	-0.142
9	-0.344	0.212	0.028	41	-0.585	-0.250	-0.157
10	0.141	-0.112	0.204	42	-0.509	-0.292	-0.215
11	0.218	-0.477	-0.201	43	-0.421	-0.099	-0.121
12	0.217	-0.470	-0.499	44	-0.474	-0.041	0.256
13	0.374	-0.291	-0.038	45	0.343	0.040	-0.011
14	-0.084	0.349	0.500	46	0.001	-0.020	0.499
15	-0.270	0.209	-0.155	47	-0.502	-0.290	-0.201
16	-0.027	0.206	0.507	48	-0.489	-0.204	-0.130
17	-0.016	0.147	0.431	49	0.608	0.345	0.180
18	-0.305	0.121	-0.133	50	-0.539	-0.190	0.181
19	-0.169	0.186	0.146	51	0.115	0.371	0.147
20	-0.143	0.150	0.008	52	-0.239	-0.380	-0.046
21	-0.060	0.163	0.103	53	-0.130	-0.173	-0.287
22	-0.020	-0.139	-0.013	54	-0.018	0.251	0.119
23	0.018	-0.045	-0.098	55	0.108	0.057	0.219
24	-0.103	-0.377	-0.779	56	0.032	0.198	0.287
25	-0.008	-0.287	-0.704	57	-0.167	-0.277	-0.009
26	-0.036	-0.309	-0.763	58	-0.504	-0.279	0.233
27	0.083	-0.237	-0.581	59	0.197	0.261	0.004
28	-0.118	-0.342	-0.810	60	-0.399	0.032	0.335
29	-0.047	-0.202	-0.679	61	0.511	0.431	0.077
30	-0.554	-0.372	-0.171	62	-0.242	0.026	-0.101
31	0.279	-0.268	0.063	63	0.304	0.290	0.456
32	-0.019	-0.235	-0.828				

result. The results show that, the linear combination method would not generate combination features with a considerable correlation improvement. Moreover, linear combination features could easily suffer from overfitting, especially in the case that the correlation values of single features are not high.

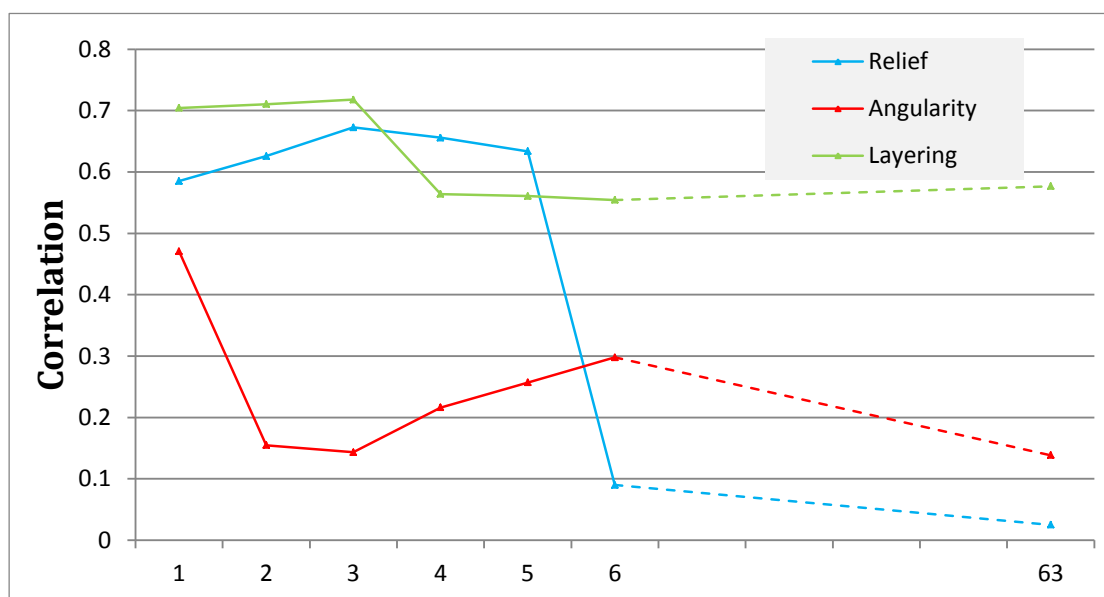


Figure 4.22: Correlation results of the combination features calculated by the enumeration method (test set)

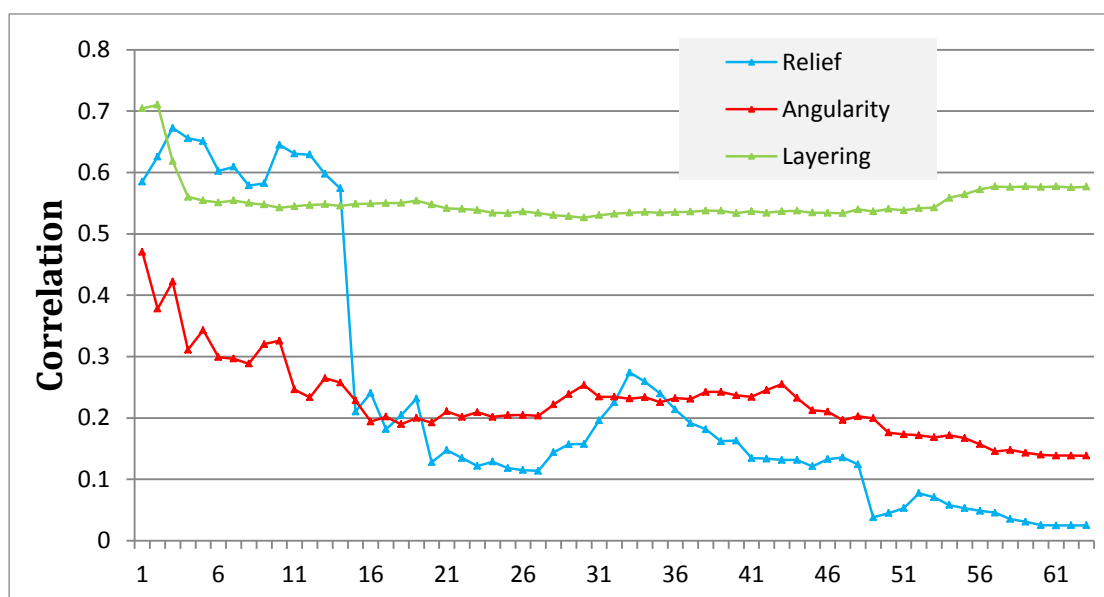


Figure 4.23: Correlation results of the combination features generated by the fast greedy algorithm (test set)

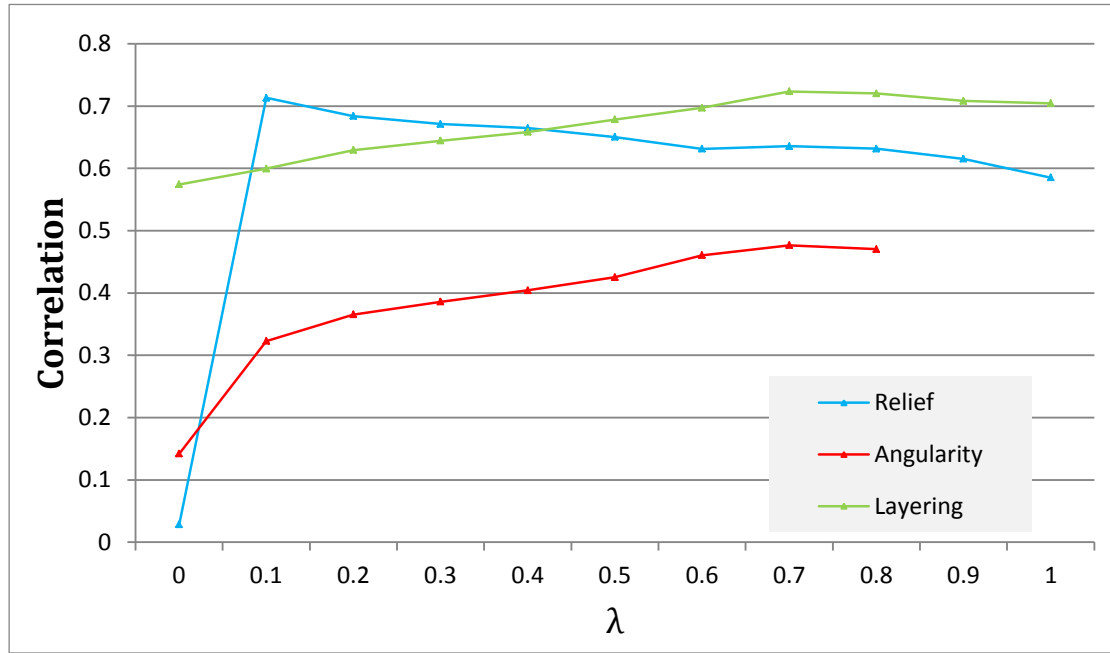


Figure 4.24: Correlation results of the combination features generated by the Lasso algorithm (test set)

In addition, we shuffled the original training and testing sets to rebuild several new training and testing sets. Four-fold cross validation experiments were conducted on the new sets. The correlation performance curves of the results generated from the new training and testing sets are similar to previous ones. However, the features (feature sets) for generating the best combination features calculated by different training sets showed some uncertainties, particularly in the cases of the combinations of more features. For instance, in the experiments of 2-feature combinations for *Layering* representation, for one training set, the feature elements in the best set for combination were SP_{Cpixel} and *Eccentricity*, but for another training set, the best features became the combination of SP_{Cpixel} and StD_G . Moreover, it can be found that linear combinations have a tendency to pick a primary feature which has a high correlation and then add other feature(s) to fine-tune the primary feature, making the values of the combination feature closer to the expert scores. Primary features were usually the same as the feature with highest correlation (i.e. best single feature) while the features used for fine-tuning were varied. Tables 4.9 and 4.11 also reflect such a phenomenon. It indicates that using single features to represent geologist attributes may obtain a better

repeatability and robustness than using combination features.

In addition, there are two extra strong points of using single features rather than combination features. Firstly, a single feature has a clear physical definition. For example, the feature SP_{Cpixel} was defined by the “order within chaos” of the directions of the strong edges in a rock region. This definition is very similar to how real geologists analyse the layering structure and hence is easy to make sense to them. Moreover, a clear definition will help to understand the geologists’ idea, which is an important evidence to adjust and improve the corresponding feature algorithm. Nevertheless, it is difficult to explain some combination feature sets (e.g. *Extent* plus *Mean*). Furthermore, the meanings of combination weights are also not easy to be explained. Secondly, as using a single feature requires only one feature to be calculated and it need not a combination process, it is faster to compute.

Although using combination features has potential to improve the performance of the correlation between features and attributes, currently in our research, only considering a linear combination using the weights calculated by the least square method, the correlation performance didn’t gain a remarkable improvement. Therefore, comprehensively taking the correlation performance, definition clarity and computative speed into consideration, we prefer to use single features to represent geological attributes at the preliminary stage.

4.3.4 Summary

In this section, a series of experiments has been described for finding an appropriate mapping between visual features generated from computer visual algorithms and the geological attribute evaluation in geologists’ thinking. Pearson’s correlation coefficient has been used as the most important index to evaluate the mapping performance. Both single features and combination features have been tested. Finally, due to stability and repeatability, single features are preferred to represent geological attributes. Thus, according to correlation values, Den_{SIFT} is chosen to represent *Relief*, *Compactness* is chosen to represent *Angularity* and SP_{Cpixel} is chosen to represent *Layering*.

4.4 Fuzzy expert system

While the geological attributes can be represented by visual features, the next step is to use those geological attributes to calculate the science value of rocks. Generally, geologists will use natural language to describe the process of rock science value evaluation. For example, a geologist would give the following sentence to analyse the layering structure of a rock:

If the rock has a **distinct** layered structure, its science value is **very high**.

It can be seen that geologists will use adjectives (descriptions) such as **distinct** and **very high**. As such descriptions refer to the concept of natural language, it is illogical to represent them by discrete singleton values (e.g. 1 for layered, 0 for non-layered). In most cases, there is no obvious boundary between two opposite descriptions of a geological attribute (e.g. *layered* and *unlayered*, *round* and *angular*, *high science value* and *medium science value*). Hence, approaches which can express geological knowledge in the way of natural language would be preferable to represent the geologists' thinking. Therefore, it is realised that many science target attributes can be likened to fuzzy linguistic variables and that the process of rock science evaluation can be likened to fuzzy reasoning (fuzzification, inference and defuzzification). Like the previous system KSTIS [Pugh, 2010], a fuzzy expert system has been established for converting the attribute values of a rock to its science value.

The expert system consists of three components¹: **Structure**, **Texture** and **Composition**, representing the three primary types of geological attributes. Each component can be regarded as a fuzzy subsystem. The configurations of all three components' subsystems are the same, listed in Table 4.13.

Table 4.13: Fuzzy system configuration

Type	Mamdani	Defuzzification	centroid(COG)
AND method	min	OR method	max
Implication	min	Aggregation	max

The Matlab fuzzy logic toolbox was used, whose graphical interface (see Fig. 4.25) is available to help with membership function and rule design.

¹This architecture is the same as the KSTIS 1.0 system [Pugh, 2010], derived from the knowledge elicitation [Pullan, 2006] of a geologist.

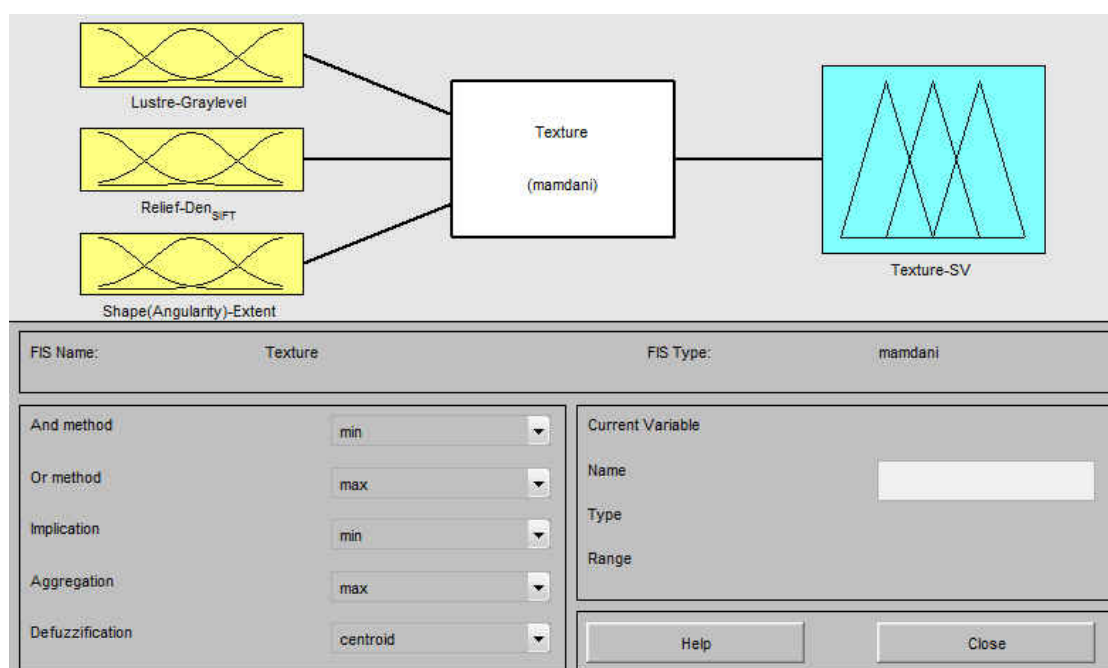


Figure 4.25: MATLAB fuzzy toolbox interface. This figure shows the example of the **Texture** component.

During the design stage (membership functions and rules), discussions were conducted with a geological expert¹.

4.4.1 Membership function

In fuzzy logic, the concept of membership function is closely related to the process of fuzzification and defuzzification. A membership function represents the degree of truth as an extension of valuation. Correspondingly, the membership degree reflects the grade of membership of an element to a set. For instance, if the colour of a rock is only classified into three colour sets, red, green and blue, a yellow rock can be represented as: 0.5 belongs to red and 0.5 belongs to green.

The shapes and parameters of the membership functions in our system were derived from the KSTIS 1.0 system [Pugh, 2010; Pugh et al., 2010a] and have been reviewed by the geologist mentioned before. The membership functions of the **Structure**, **Texture** and **Composition** components are introduced separately.

¹This geologist is the same as the one who provided the ground truth of attribute values.

4.4.1.1 Structure

Unlike KSTIS which includes the attributes *Layering Type* and *Layering Scale*, only one attribute (feature) has been selected to reflect the structure information of rocks. That is:

- *The presence of layering*: the feature SP_{Cpixel} is scaled to $[0, 10]$ to justify if a rock shows a layering structure.

Hence, the input membership functions (MFs) referring to the structure component is only about *Layering* (Fig. 4.26).

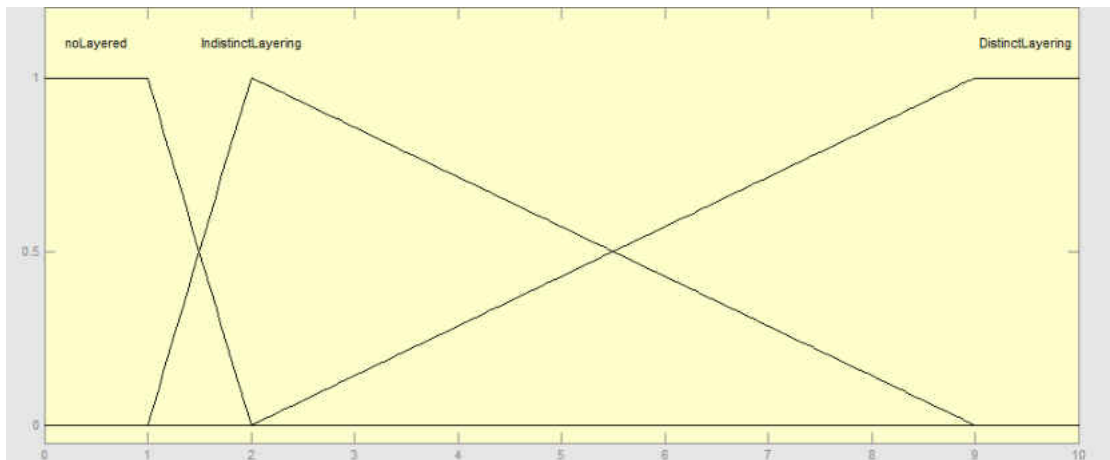


Figure 4.26: Membership functions of Layering (SP_{Cpixel})

The *Layering* MFs include three parts: *noLayered*, *IndistinctLayering* and *DistinctLayering*. Triangular and trapezoidal types of memberships are used. There is a small overlap between *noLayered* and *IndistinctLayering*, which can be used to distinguish if a rock has a layering structure. And the overlap between *IndistinctLayering* and *DistinctLayering* is relatively larger to reflect the distinct level of the layering structure.

4.4.1.2 Texture

As with KSTIS, three attributes are selected for processing texture:

- *Lustre*: the average grayscale intensity is used to indicate the surface glossiness of a rock.

- *Relief*: the feature Den_{SIFT} is scaled to $[0, 10]$ to indicate the roughness of a rock.
- *Shape (Angularity)*: the feature $Compactness$ is scaled to $[0, 10]$ to represent how angular a rock is.

Thus, corresponding to the attributes, the input membership functions are also expressed respectively, named *Lustre* (Fig. 4.27), *Relief* (Fig. 4.28) and *Angularity* (Fig. 4.29).

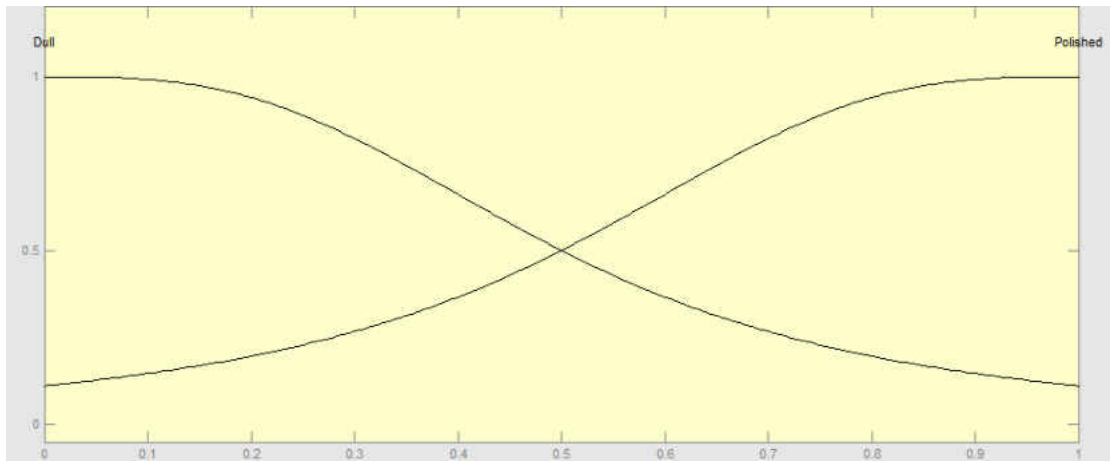
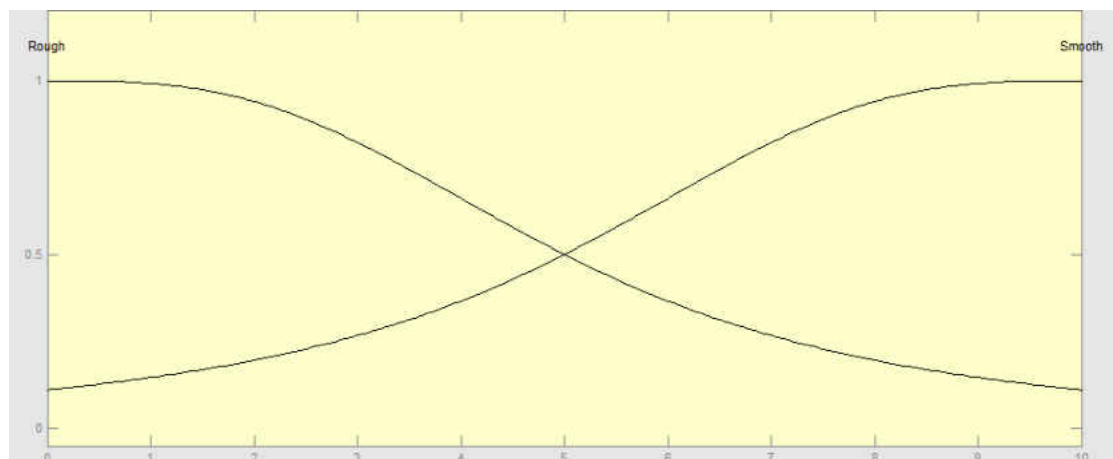
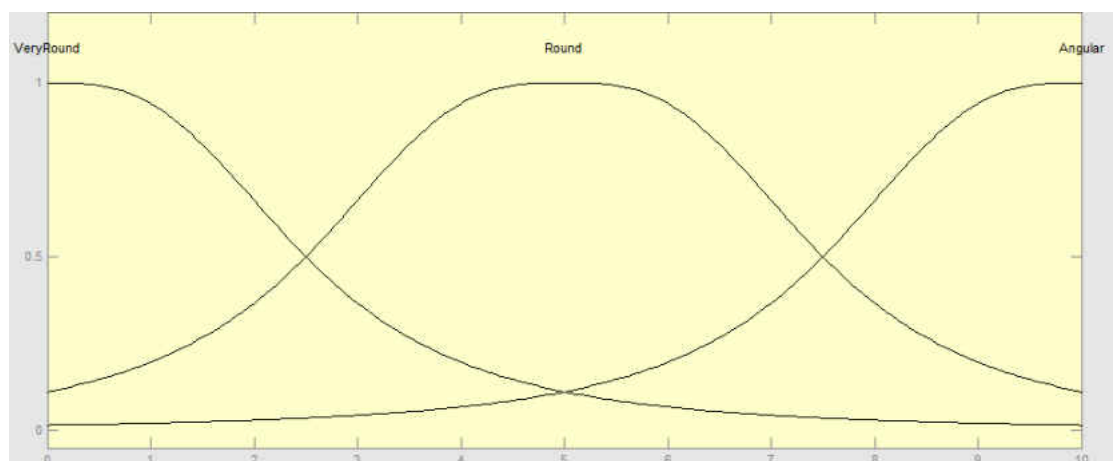


Figure 4.27: Membership functions of Lustre (grayscale intensity)

The *Lustre* MFs provide a measure of the surface glossiness of the observed target. The two membership functions dull and polished are modelled by two bell-shaped curves. These curves can help to represent the gentle change when the polished look of a targets surface, increased or decreased. The input ranges from 0 to 1, where 0 is “perfectly” dull, 1 is “perfectly” polished and 0.5 means “half” dull and “half” polished.

The *Relief* MFs represent the level of variations in the elevation of the targets surface. The two membership functions are rough and smooth, where rough indicates a high amount of elevation variations on the target surface while a smooth target has low or no variation. Again, these membership functions are expressed by two bell-shaped curves which can model the slow transition between the two extremes. The input range is $[0, 10]$, 0 being “perfectly” rough and 10 being “perfectly” smooth.

Figure 4.28: Membership functions of Relief (Den_{SIFT})Figure 4.29: Membership functions of Angularity ($Compactness$)

The *Angularity* MFs capture the angularity (roundness) of a rock. The three membership functions are very round, round and angular. These three are again modelled by bell-shaped curves as the attributes gently transitioned as the level of roundness increases. The input range is $[0, 10]$, 0 being “perfectly” round, 5 being “generally” round and 10 being “very” angular. Specifically, the “round” membership function is placed in the middle as float rocks are generally round.

4.4.1.3 Composition

Colour information has been used to reflect the composition of rocks. Specifically, an assumption has been made that every rock consists of only one material and hence all pixels in a detected rock region represent the same component. Thus, in a rock region, the colours (intensities in RGB channels) are first averaged. Then the average RGB values are transformed into HSV space to reflect the global composition of a rock. Accordingly, the three components of HSV space are regarded as the rock composition attributes. They are:

- *Hue*: the colour of a rock, which expresses the rock composition information.
- *Saturation (Coloured/BW)*: the saturation of the HSV space has been used to indicate if a rock is coloured and hence indicate if the hue is determinable.
- *Value (Albedo)*: the value component is used to represent the albedo of a rock in the situation that the light condition is unknown.

Correspondingly, the input membership functions are also divided into three parts: *Hue* (Fig. 4.30), *Coloured/BW* (Fig. 4.31) and *Albedo* (Fig. 4.32).

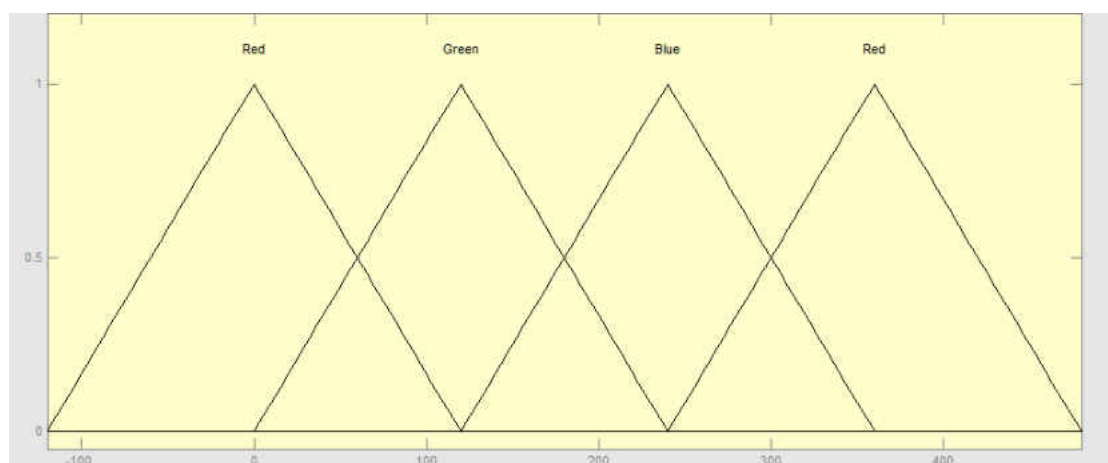


Figure 4.30: Membership functions of Hue

The *Hue* MFs represent the colour of the identified target. The hue input ranges from 0 to 360, where 0 denotes pure red, 120 denotes pure green and 240 denotes pure blue. However the membership functions cover from -120 to 480 in

order to keep the shape intactness of membership functions. There is another red component at the position 360 due to the circularity of *Hue*. By adding such an extra red membership function, the colour mixed by red and blue can be represented correctly. In addition, although the two “red” components both indicate the same colour, in real fuzzy operation, they are processed separately. All *Hue* membership functions are modelled by triangular curves, according to the definition of hue.

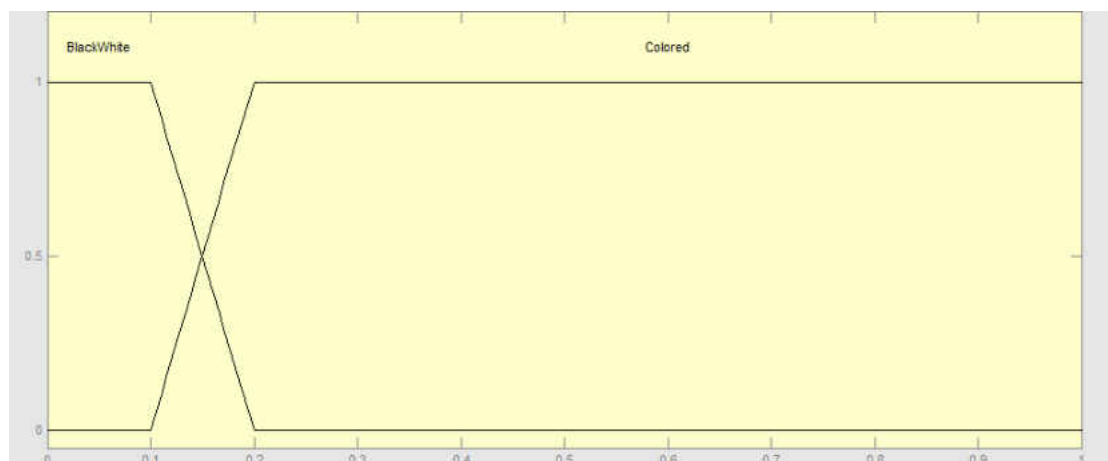


Figure 4.31: Membership functions of Coloured/BW

The *Coloured/BW* MFs indicate whether a rock is a coloured rock (e.g. red rock) or a black-white rock (e.g. gray rock) and hence indicate if the hue of the target was determinable. Two trapezoidal membership functions, coloured and blackwhite, are established between which there is a narrow overlap. Since the input is the saturation component of HSV space, the input range is 0 to 1. Once a rock is determined as a coloured rock, its composition science value can be defined by both its hue and albedo. Otherwise, only the albedo attribute plays the role.

The *Albedo* MFs provide a measure of the reflectivity of the observed target. Three membership functions are included: low, medium and high. Low and high are triangular membership functions which represent the steep change in interest towards the extremes. The central MF which represents medium is trapezoidal, reflecting the relative smooth science value change over the intermediate albedo region. The input range is $[0, 1]$, 0 describes a “perfectly” dark rock, 1 describes a bright rock.

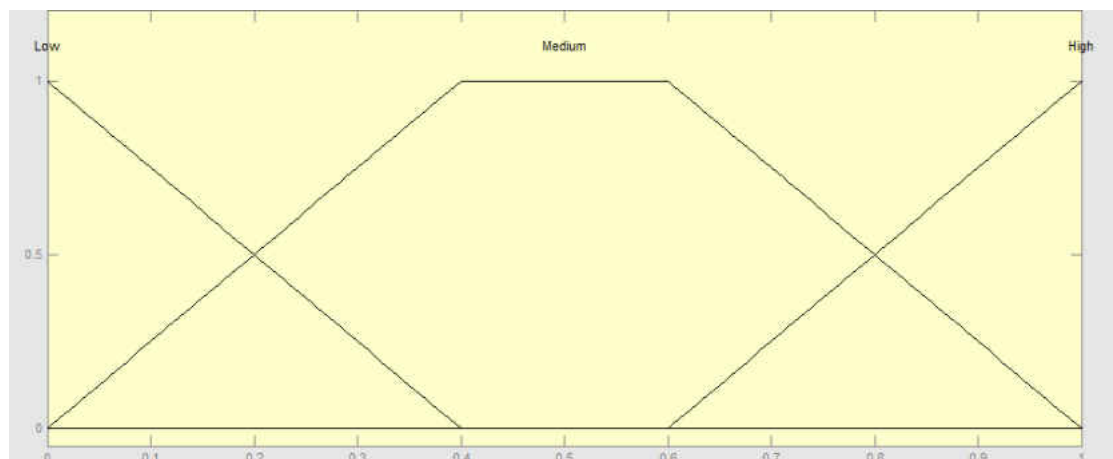


Figure 4.32: Membership functions of Albedo

4.4.1.4 Output

The outputs of the fuzzy system are the science values of rocks. The science value of **Structure**, **Texture** and **Composition** are calculated independently. However, as the outputs of the three components will be summed together to produce the final science value, it is important to ensure that all three outputs are of the same magnitude and on the same scale. Hence, the output membership functions of all three components are identical (see Fig. 4.33).

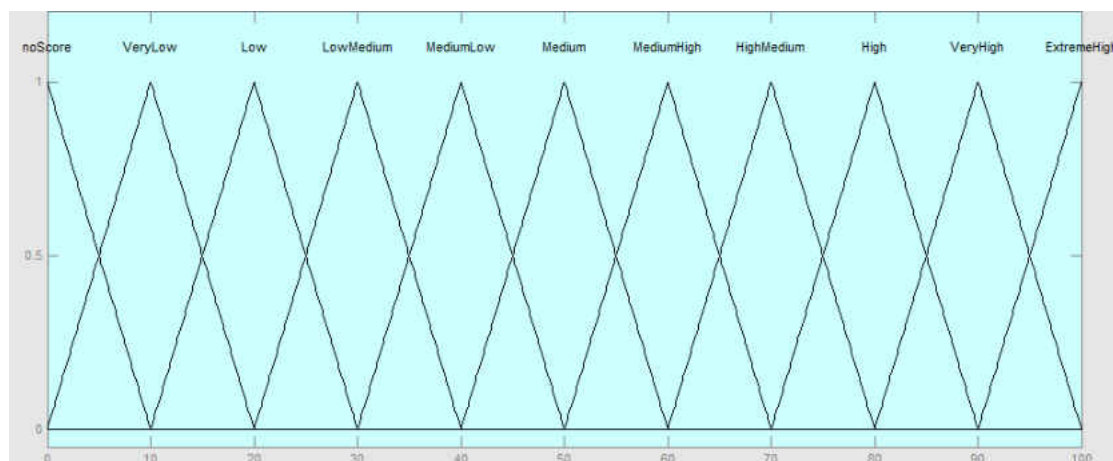


Figure 4.33: Membership functions of the output: the science value of a rock

For each component of the fuzzy system, the 11 membership functions are set. They are noScore, VeryLow, Low, LowMedium, MediumLow, Medium, Medi-

umHigh, HighMedium, high, VeryHigh and ExtremeHigh, representing the science values from low to high. After defuzzification, the outputs of the three components can be converted to digital science values, namely $SV_{Structure}$, $SV_{Texture}$ and $SV_{Composition}$ respectively. They can be simply added together to create a final science value as they are of the same magnitude.

4.4.2 Rule base

The rule base is the crucial element in fuzzy systems for the purpose of inference. Generally, a rule in the rule base has a IF-THEN structure to simulate a process of human linguistic inference. A rule example is like:

If Lustre is *Polished* **and** Relief is *Rough* **then** $SV_{Texture}$ is *Low*

Each rule can be used for analysing rock science value in one aspect. Hence, through integrating every single rule together, a rule base is capable of providing comprehensive analyses of rocks. Furthermore, although there is a general science goal in Mars exploration, the rules are not “set in stone”. Depending on detailed scientific objectives and also the environment, the rule base could be adjusted. For example, one day scientists may be focusing on green rocks (e.g. chlorite) and ignoring layering; another day layered rocks may become the keystone of research and hence the composition part becomes relatively unimportant.

Here, we applied a rule base simplified from KSTIS system¹ as we have a small number of attributes. These rules can deal with general rock science value evaluation. As mentioned, they can be tuned to adapt to particular requirements.

Corresponding to the membership functions, the rule base is partitioned into three parts.

Structure includes 3 rules:

1. **If** (Layering is *noLayered*) **then** (Structure SV is *noScore*)
2. **If** (Layering is *IndistinctLayering*) **then** (Structure SV is *Low*)
3. **If** (Layering is *DistinctLayering*) **then** (Structure SV is *High*)

Texture includes 12 rules:

¹The author [Pugh, 2010] stated that the rules were based on the knowledge elicitation of [Pullan, 2006]. This statement has been reconfirmed.

1. **If** (Lustre is *Dull*) **and** (Relief is *Rough*) **and** (Angularity is *VeryRound*) **then** (Texture SV is *VeryLow*)
2. **If** (Lustre is *Polished*) **and** (Relief is *Rough*) **and** (Angularity is *VeryRound*) **then** (Texture SV is *LowMedium*)
3. **If** (Lustre is *Dull*) **and** (Relief is *Smooth*) **and** (Angularity is *VeryRound*) **then** (Texture SV is *LowMedium*)
4. **If** (Lustre is *Polished*) **and** (Relief is *Smooth*) **and** (Angularity is *VeryRound*) **then** (Texture SV is *Medium*)
5. **If** (Lustre is *Dull*) **and** (Relief is *Rough*) **and** (Angularity is *Round*) **then** (Texture SV is *VeryLow*)
6. **If** (Lustre is *Polished*) **and** (Relief is *Rough*) **and** (Angularity is *Round*) **then** (Texture SV is *Low*)
7. **If** (Lustre is *Dull*) **and** (Relief is *Smooth*) **and** (Angularity is *Round*) **then** (Texture SV is *Low*)
8. **If** (Lustre is *Polished*) **and** (Relief is *Smooth*) **and** (Angularity is *Round*) **then** (Texture SV is *MediumLow*)
9. **If** (Lustre is *Dull*) **and** (Relief is *Rough*) **and** (Angularity is *Angular*) **then** (Texture SV is *VeryLow*)
10. **If** (Lustre is *Polished*) **and** (Relief is *Rough*) **and** (Angularity is *Angular*) **then** (Texture SV is *Low*)
11. **If** (Lustre is *Dull*) **and** (Relief is *Smooth*) **and** (Angularity is *Angular*) **then** (Texture SV is *Low*)
12. **If** (Lustre is *Polished*) **and** (Relief is *Smooth*) **and** (Angularity is *Angular*) **then** (Texture SV is *LowMedium*)

Composition includes 12 rules¹:

1. **If** (Color/BW is *Blackwhite*) **and** (Albedo is *Low*) **then** (Composition SV is *Low*)

¹Practically, there are 15 rules in the inference stage as it has two “red” membership functions. However, for each “red”, the rules are identical.

2. **If** (Color/BW is *Blackwhite*) **and** (Albedo is *Medium*) **then** (Composition SV is *MediumLow*)
3. **If** (Color/BW is *Blackwhite*) **and** (Albedo is *High*) **then** (Composition SV is *MediumHigh*)
4. **If** (Hue is *Red*) **and** (Color/BW is *Colored*) **and** (Albedo is *Low*) **then** (Texture SV is *VeryLow*)
5. **If** (Hue is *Green*) **and** (Color/BW is *Colored*) **and** (Albedo is *Low*) **then** (Texture SV is *HighMedium*)
6. **If** (Hue is *Blue*) **and** (Color/BW is *Colored*) **and** (Albedo is *Low*) **then** (Texture SV is *Low*)
7. **If** (Hue is *Red*) **and** (Color/BW is *Colored*) **and** (Albedo is *Medium*) **then** (Texture SV is *Low*)
8. **If** (Hue is *Green*) **and** (Color/BW is *Colored*) **and** (Albedo is *Medium*) **then** (Texture SV is *High*)
9. **If** (Hue is *Blue*) **and** (Color/BW is *Colored*) **and** (Albedo is *Medium*) **then** (Texture SV is *LowMedium*)
10. **If** (Hue is *Red*) **and** (Color/BW is *Colored*) **and** (Albedo is *High*) **then** (Texture SV is *LowMedium*)
11. **If** (Hue is *Green*) **and** (Color/BW is *Colored*) **and** (Albedo is *High*) **then** (Texture SV is *ExtremeHigh*)
12. **If** (Hue is *Blue*) **and** (Color/BW is *Colored*) **and** (Albedo is *High*) **then** (Texture SV is *MediumLow*)

4.5 Examples of science value calculation

In previous sections, details of visual feature generation, mapping from features to attributes and fuzzy expert system are given. By linking them together, a whole autonomous science evaluation system can be established. Once the region of a rock is detected, its rough science value of the rock can be evaluated. Here, we demonstrate two examples of rock science value calculation (evaluation): one smooth rock without layering structure and one layered rock. The details of the two examples¹ are shown in Figs. 4.34 and 4.35 respectively.

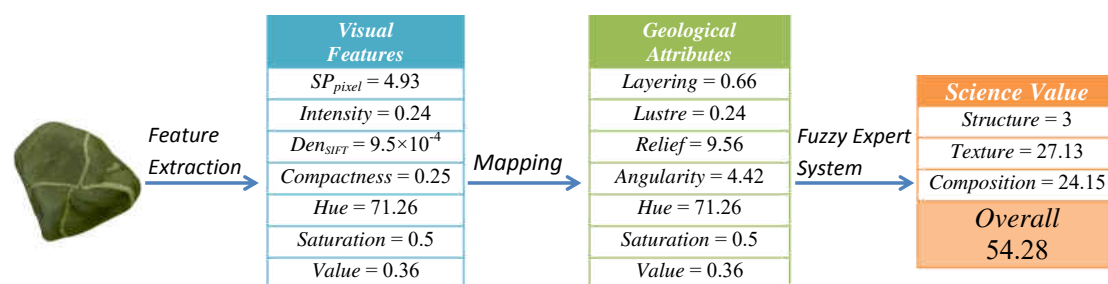


Figure 4.34: Example of science value evaluation on a smooth rock

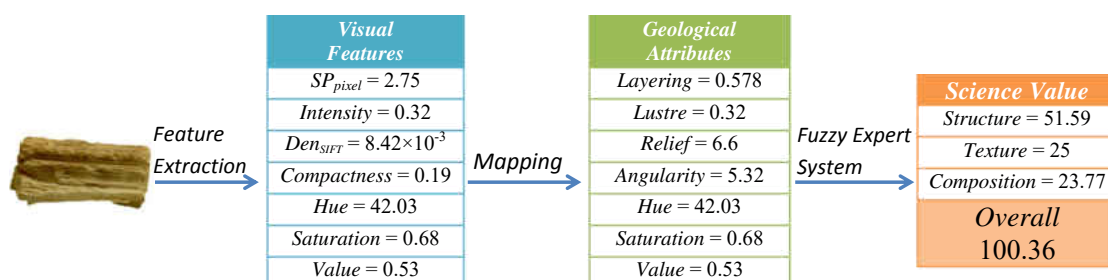


Figure 4.35: Example of science value evaluation on a layered rock

As can be seen, our science evaluation system can reflect the geological attributes and science values of rocks relatively accurately. The *Relief* attribute score of the smooth rock was evaluated relatively higher and the layered rock was endowed with a high *Layering* score. Compared to being smooth, having a layering structure is more science significant. Hence the layering rock was calculated with more science value. From the examples, it can be found that the proposed geology-oriented science evaluation mechanism can indeed perform rock science evaluation in a way similar to human geologists autonomously.

¹More examples can be found in Chapter 6, integrated with other parts of the proposed system.

4.6 Summary

In this chapter, a mechanism for rock science value evaluation on rock image regions has been presented. This mechanism bridges computer vision techniques and geological knowledge representation. Firstly, a number of visual features were extracted. A series of methods have been proposed to map the features (both single features and combination features) to corresponding geological attributes. After the mapping process, a fuzzy system was applied to convert attribute values to science values based on the knowledge elicitation of a geological expert. Specifically, our science value evaluation component is independent to rock detection and further execution components, meaning that the mechanism can receive the rock detection results generated from some methods other than the algorithms mentioned in this thesis. In addition, not only our proposed system, but also the ranking and planning parts of other Mars exploration systems can benefit from this mechanism.

Chapter 5

Executive Agent

5.1 Introduction

The executive agent is related to the construction and control of instruments (hardware), providing a platform to support the software system such as rock detection and rock science value evaluation. For a real rover, the executive agent includes chassis, camera, arm, communication instruments, science instruments and corresponding control systems. However, due to the limited condition, the executive agent only consists of two components in our work: a camera agent and an arm agent. Fig. 5.1 shows the layout of our experimental platform (the hardware of the executive agent).

It can be seen that, although it has been simplified, the platform is still analogous to a real rover. The camera agent provides the capability to capture data remotely (including general image data and multispectral data) and the arm agent is constituted for placing science instruments (if installed at the end of the arm) to a position close to a science target. In addition, these simple instruments provide an environment to integrate and implement partial algorithms mentioned in previous chapters. The effectiveness of those algorithms can therefore be tested and demonstrated.

5.2 Camera Agent

The structure of our camera agent is similar to the camera agent in the ASTIA system [Barnes et al., 2009] and the Aberystwyth University PanCam Emulator

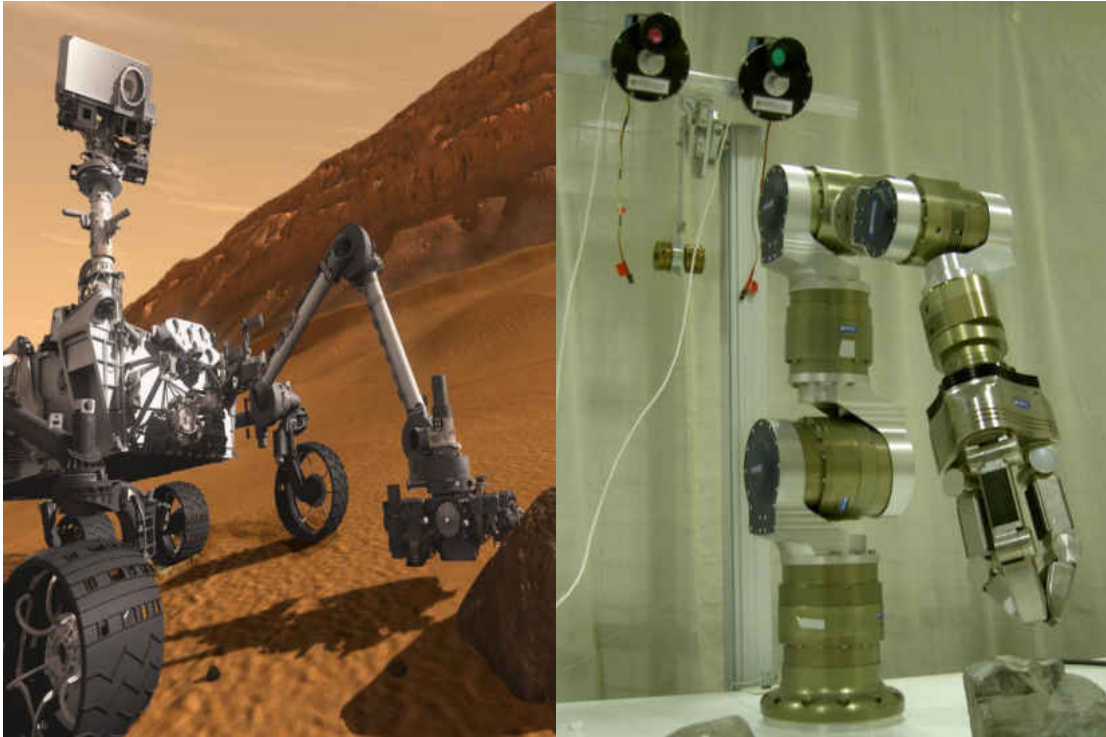


Figure 5.1: Experiment platform (right) containing cameras and an arm. It is analogous to a real rover such as the Curiosity rover (left).

(AUPE-1) [Pugh et al., 2012]. A pair of monochrome cameras was used in front of which filter wheels have been installed to endow the cameras with the capability to capture colour and multispectral data. In addition, a simple tilt unit (no pan unit currently) has been installed for adjusting the range of camera view. This camera system plays a role equivalent to the MER Pancam.

5.2.1 Cameras

The cameras used in the platform are two off-the-shelf wide angle cameras (WACs) manufactured by Imaging Source Ltd. The cameras have 1024×768 pixel resolution and panchromatic sensors without built-in infra-red filters. Their spectral response can be extended into the near infra-red (up to approx. 1000nm) which makes them ideal for working with filters. The data captured by the cameras is transferred through IEEE1394 cables. Table 5.1 gives details of the camera and lens specifications.

Table 5.1: Camera specifications

Model	DMK 31BF03	Image type	Y800
Sensor	Sony ICX204AL	Resolution	1024 × 768
Pixel size	4.65 μm	Sensor size	4.76 × 3.57 mm
Focal length	8 mm	Field of view	45° × 35°
Shutter	1/10000 - 30 s	Iris	f / 1.4

5.2.2 Multispectral Filters

In front of each camera, a filter wheel (see Fig. 5.2) is mounted thereby enabling the monochrome camera to capture colour and multispectral data. The framework of the wheels is made from aluminium on which nine filters (glasses) are mounted. For protection, the filter wheels are housed between carbon fibre sheets.

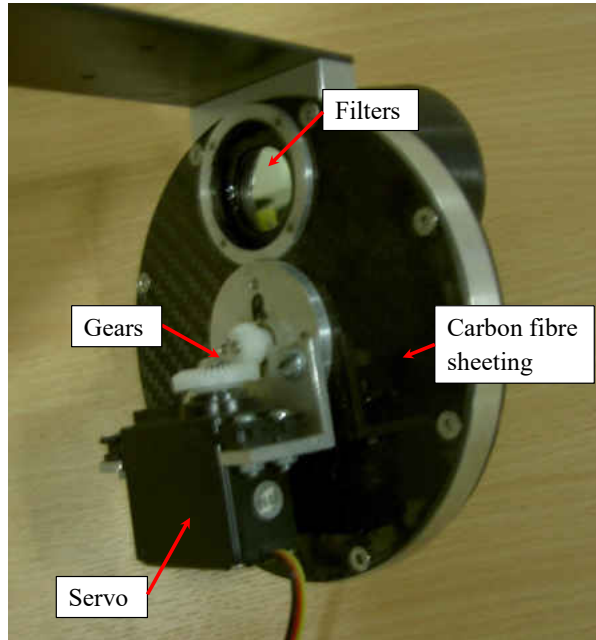











Figure 5.2: Filter wheel structure

On each wheel, three of filters are designed for colour imaging and hence are broadband ($\sim 100\text{nm}$) filters. The remaining twelve filters (six on each wheel) are narrowband interference filters with pass bands of width about 10nm. The details of the filters are given in Table 5.2.

The broadband red, green and blue filters allow regular colour images to be taken while the narrowband filters can be used for terrain composition analysis,

Table 5.2: Filter specifications

Left Filter Wheel				Right Filter Wheel			
Filter No.		Centre(nm)	Width(nm)	Filter No.		Centre(nm)	Width(nm)
1) Blue		460	~100	1) Blue		460	~100
2) Green		550	~100	2) Green		550	~100
3) Red		660	~100	3) Red		660	~100
4) Geol1		440	10	4) Geol7		720	10
5) Geol2		470	10	5) Geol8		760	10
6) Geol3		510	10	6) Geol9		830	10
7) Geol4		560	10	7) Geol10		880	10
8) Geol5		600	10	8) Geol11		950	10
9) Geol6		660	10	9) Geol12		1000	10

rock segmentation or detection of other interesting object. In addition, by using the visible spectra (390nm–700nm) captured by the narrowband filters on left filter wheel, true colour images can be generated which can represent the scene more closely to what would be seen by human eyes.

Each filter is mounted on a stainless steel pivot which is actuated by a servo. The servos can guarantee the accurate positioning of filters, thereby facilitating processing such as dark frames and flat field frames [Gunn, 2013].

5.2.3 Camera mount

On a general rover, panoramic cameras are placed behind a robotic arm. One reason is that the sensing range of cameras is further than the workspace of the arm. In addition, cameras behind an arm can provide feedback of the arm's motion, thereby facilitating the control of the arm. Hence, in our experimental platform, the cameras were mounted on a mast behind a robotic arm. The mounting of the cameras is shown in Fig. 5.3.

As can be seen in the figure, the two cameras are fixed on an optical bench. The bench is installed on a rotation slide platform through a right angle bracket. The platform is regarded as the tilt unit which can tilt the cameras from 0° (horizontally forward) to 90° (vertically downward). There is a laser-engraved scale on the slide platform, allowing adjustment of the tilt angle every 1°. Unfortunately, the tilt unit can only be rotated manually and hence its precision and repeatability are relatively low.

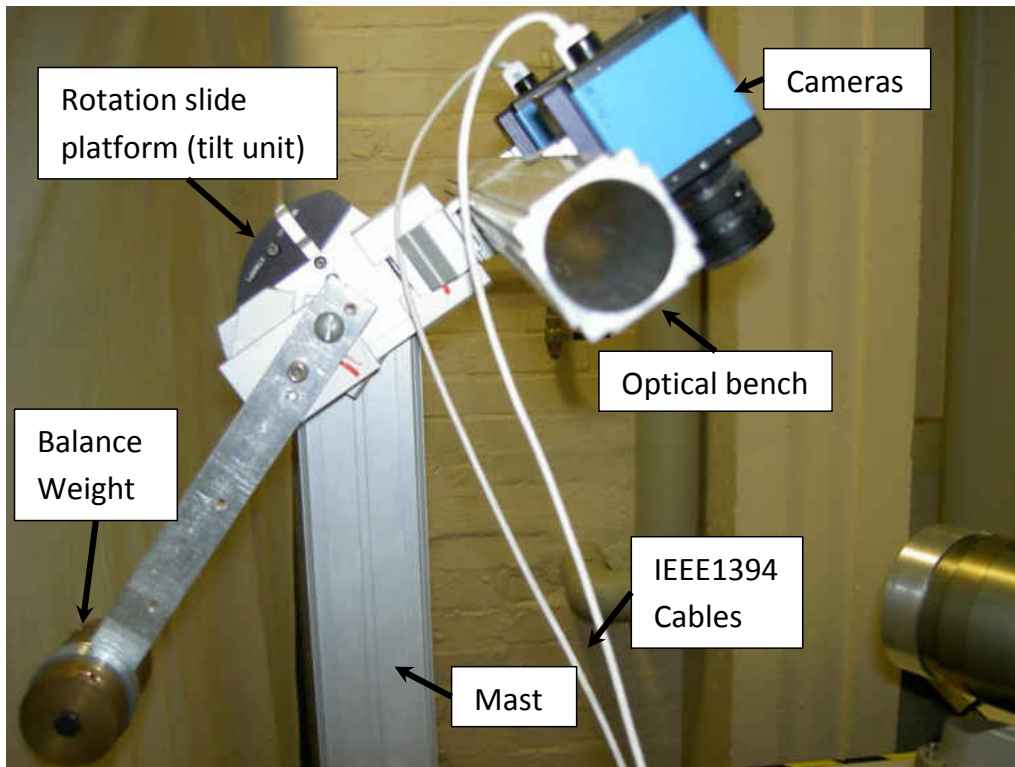


Figure 5.3: Camera mounting (without filter wheels)

5.2.4 Coordinate transformation

When an interesting rock has been detected in an image, it is necessary to convert its position in the image (scene) coordinate frame to the position in the world (camera) coordinate frame. Although stereo technologies [Xu and Zhang, 1996] can pinpoint rock positions in the real world more accurately, in our system a monocular method whose process is much simpler has been applied. In this method, the intrinsic parameters such as camera distortion have been ignored and hence only extrinsic parameters (dimensions of camera mounting and tilt angle) have been involved. In addition, an assumption has been made that rocks are placed on absolutely horizontal floor to simplify the transformation. The tilt angle of the camera is the only parameter to adjust the field of view of the camera. Here it is denoted by θ_t .

The world (camera) coordinate frame is defined as shown in Fig. 5.4. The origin point O is located on the base of the mast, Z axis is along the mast upwards and Y axis is parallel to the bench. The direction of X axis can be derived through

the right-hand rule.

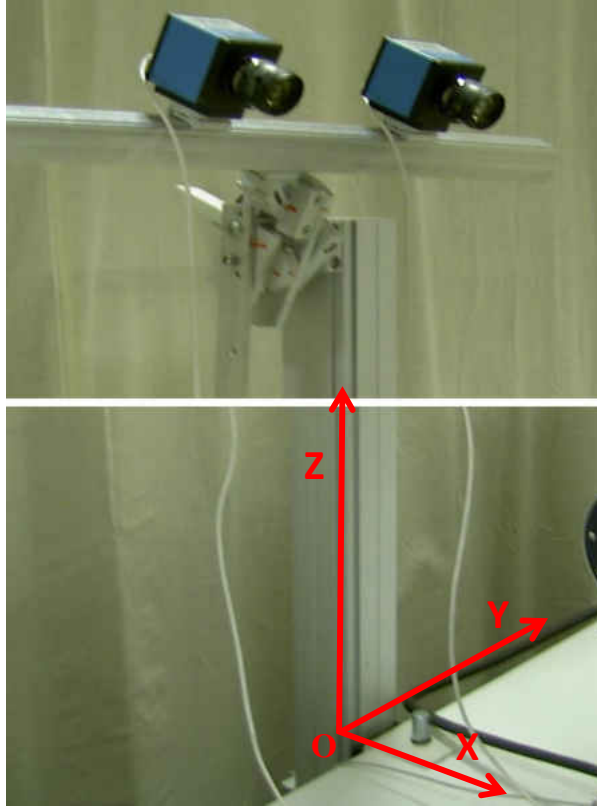


Figure 5.4: Camera (World) coordinate frame

Since the algorithm is based on a monocular camera, the right camera is taken as the example to demonstrate the process of coordinate transformation. Firstly, the camera position (lens position) is determined by the tilt angle. Thus, the lens position in world coordinate $(X_{lens}, Y_{lens}, Z_{lens})$ can be calculated as:

$$\begin{cases} X_{lens} = X_{offset} \times \cos(\theta_t) + Z_{offset} \times \sin(\theta_t) \\ Y_{lens} = Y_{offset} \\ Z_{lens} = H_{mast} + Z_{offset} \times \cos(\theta_t) - X_{offset} \times \sin(\theta_t) \end{cases} \quad (5.1)$$

where H_{mast} is the height of the mounting mast (in the Z direction), from the floor to the rotation centre of the tilt unit. X_{offset} , Y_{offset} and Z_{offset} are the offsets between positions of the tilt unit rotation centre and the camera lens. An illustration of the offsets is shown in Fig. 5.5.

The image coordinate system has been defined with the origin point at the

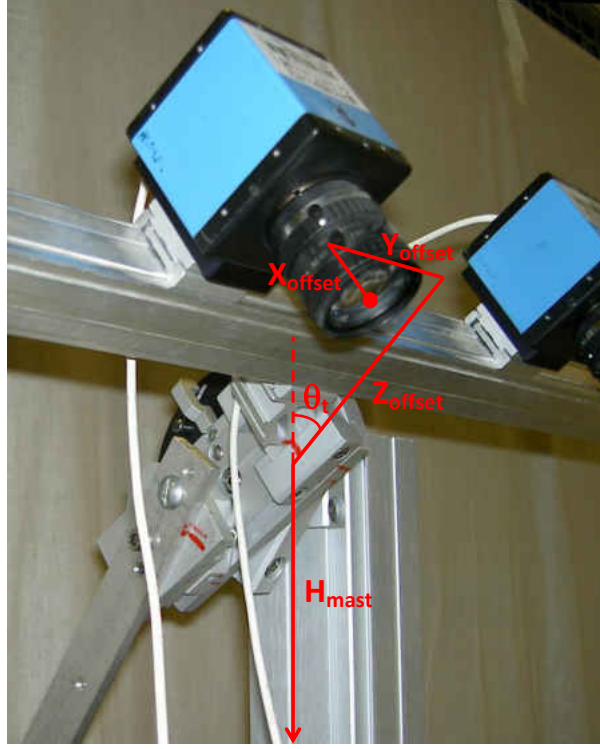


Figure 5.5: Offsets between camera lens and tilt unit

image centre. Thus, the rock position (represented by its centroid) in an image can be defined as (X_{img}, Y_{img}) , measured in pixels. The corresponding position in the world coordinate is $(X_{rock}, Y_{rock}, Z_{rock})$, measured in millimetres.

As it has been assumed that the rock is on the floor, Z_{rock} is approximated to 0. For convenience, the Z_{rock} of every rock is always set as 0 in our method, and thus the (X_{img}, Y_{img}) can be transformed to (X_{rock}, Y_{rock}) through projective relations. Fig. 5.6 illustrates the geometric relationships between world coordinates and image coordinates.

Through geometric relationships shown in the figure, X_{rock} can be calculated using α_x which is the angle between rock position and the centre of the camera view in the X direction:

$$\alpha_x = -\arctan(Y_{img} \times S_{pixel}/f) \quad (5.2)$$

in which S_{pixel} denotes the pixel size and f denotes the focal length of the camera

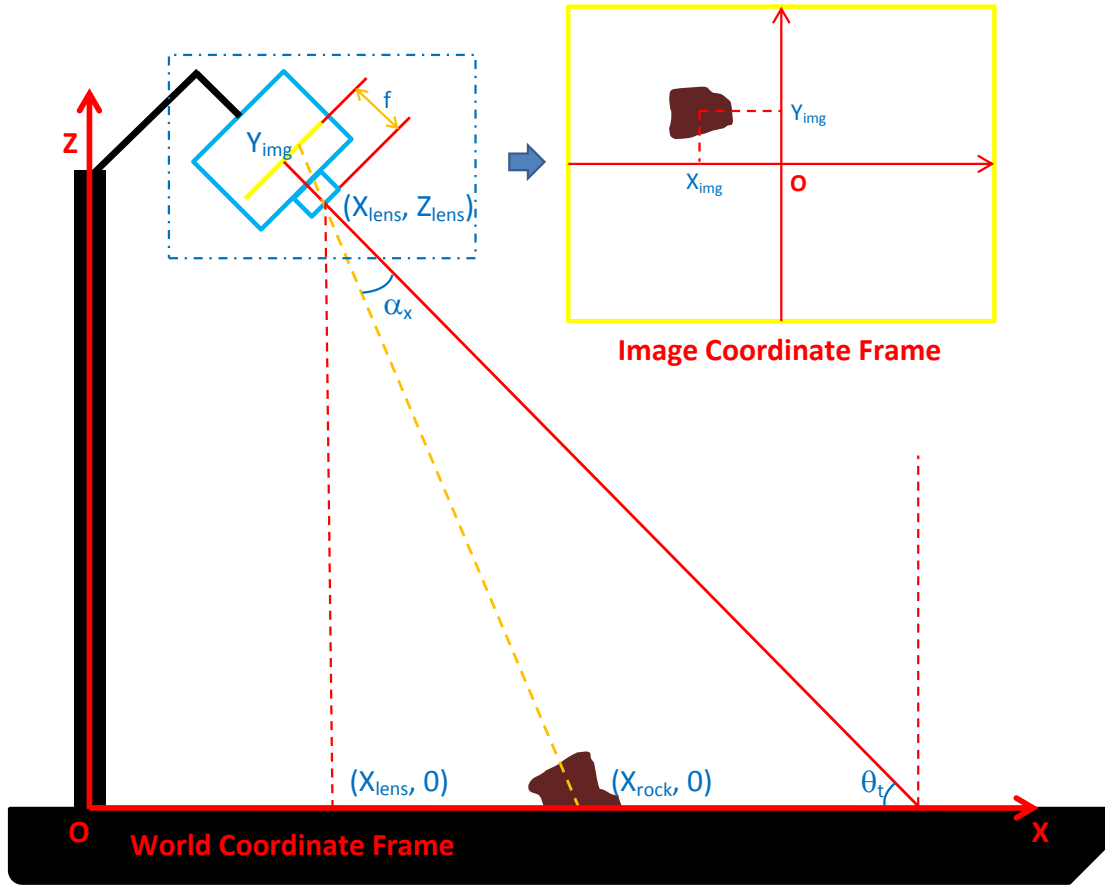


Figure 5.6: Image coordinate frame to world coordinate frame

(details can be found in Table. 5.1). Then X_{rock} is calculated as:

$$X_{rock} = X_{lens} + Z_{lens} \times \tan(\pi/2 - \theta_t + \alpha_x) \quad (5.3)$$

Similarly, Y_{rock} can be calculated as:

$$Y_{rock} = Y_{lens} - X_{img} \times S_{pixel} \times (\sqrt{(X_{rock} - X_{lens})^2 + Z_{lens}^2} \times \cos(\alpha_x) / f) \quad (5.4)$$

Thus, rock positions in images are mapped into the real world. A simulation example of a transformation is shown in Fig. 5.7. If a rock has been detected in the path of a rover, it is possible to give an alarm to the rover. When an “interesting” rock has been detected, the rover can know its relative position and manipulate

science instruments to access and investigate the rock.

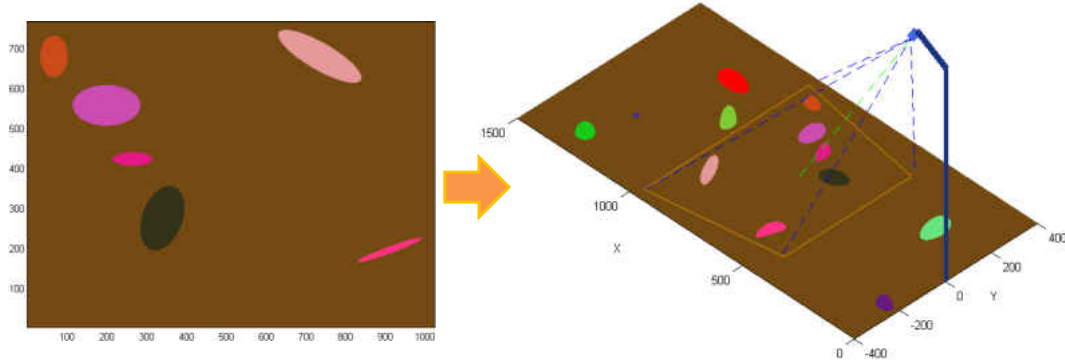


Figure 5.7: Simulation of coordinate transformation. Rocks are represented by ellipses and ellipsoids. The orange trapezoid denotes the view range on the floor, and the green dashed line denotes the centre view line.

5.3 Arm Agent

As mentioned, a robotic arm has been installed in front of the camera system. This section introduces the arm agent referring to corresponding kinematics and control.

5.3.1 Robotic arm

The arm used is an off-the-shelf robotic arm (shown in Fig. 5.8) manufactured by SCHUNK[®]. The arm has seven joints and each joint has one degree of freedom (DOF), thereby endowing the arm with seven degrees of freedom. Generally, six DOFs can fulfill the requirement for placing the end effector of an arm to any position and orientation in the motion space (workspace). An arm with seven DOFs is more dexterous than a 6-DOF arm. While introducing an extra DOF, there are infinite solutions (gestures) when the end effector needs to be moved to a specified position. Thus, if there is an obstacle in the motion space of the arm, the end effector cannot reach some positions with only six DOFs. However, the 7-DOF arm can generate a solution which is not blocked by the obstacle and hence guarantees that the target position can be reached.

The joints of the arm are powered by seven Powercube units. The joints are named as J_1 to J_7 , from the base to the end effector. However, due to the default



Figure 5.8: Robotic arm at the “0” position

setting of the PowerCube module, the Powercube units are numbered #3 to #9. Each joint can rotate in a range from -2 rad to 2 rad. The directions of the joints are illustrated in Fig. 5.9 (“+” and “-” mean the positive and negative directions).

In addition, a 7-DOF gripper has been fitted at the end of the arm. Currently, in our experiments, it is unnecessary to manipulate the gripper. Hence, the gripper remains fixed and is assumed to be a science instrument in the experiment.

5.3.2 Kinematic analysis

The kinematic analysis of the arm contains two parts: forward kinematics and inverse kinematics. Forward kinematics refers to the use of the kinematic equations to compute the position of the end-effector from specified values for joint parameters while the inverse kinematics is the reverse process of forward kinematics, denoting the calculation of the joint parameters when the position and orientation of an end effector are specified.

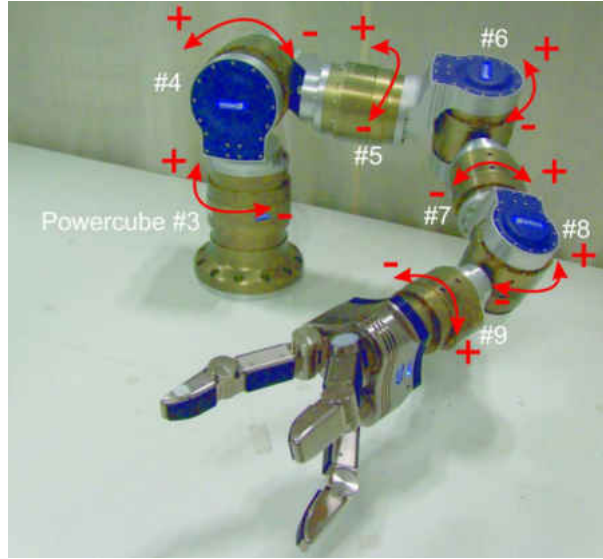


Figure 5.9: Positive and negative directions of the rotation of the seven joints

5.3.2.1 Forward kinematics

All seven DOFs were used in the forward kinematics. The Denavit-Hartenberg method (DH) was introduced to simplify the progress. According to the positive direction of each joint, the DH coordinate frames of all joints can be established (Fig. 5.10).

Thus, the DH parameters can be obtained. The DH parameters of the joints are shown in Table 5.3. Specifically, the parameter θ is the variable which represents the rotation angle of each joint. The d_1 , d_2 , d_3 and d_4 are the link lengths of the SCHUNK arm.

Table 5.3: DH parameter settings of the arm

	a	α	d	θ
J_1	0	-90°	$-d_1$	θ_1
J_2	0	90°	0	θ_2
J_3	0	-90°	$-d_2$	θ_3
J_4	0	90°	0	θ_4
J_5	0	-90°	$-d_3$	θ_5
J_6	0	90°	0	θ_6
J_7	0	-90°	$-d_4$	θ_7

On the basis of these DH parameters, the matrices for performing the trans-

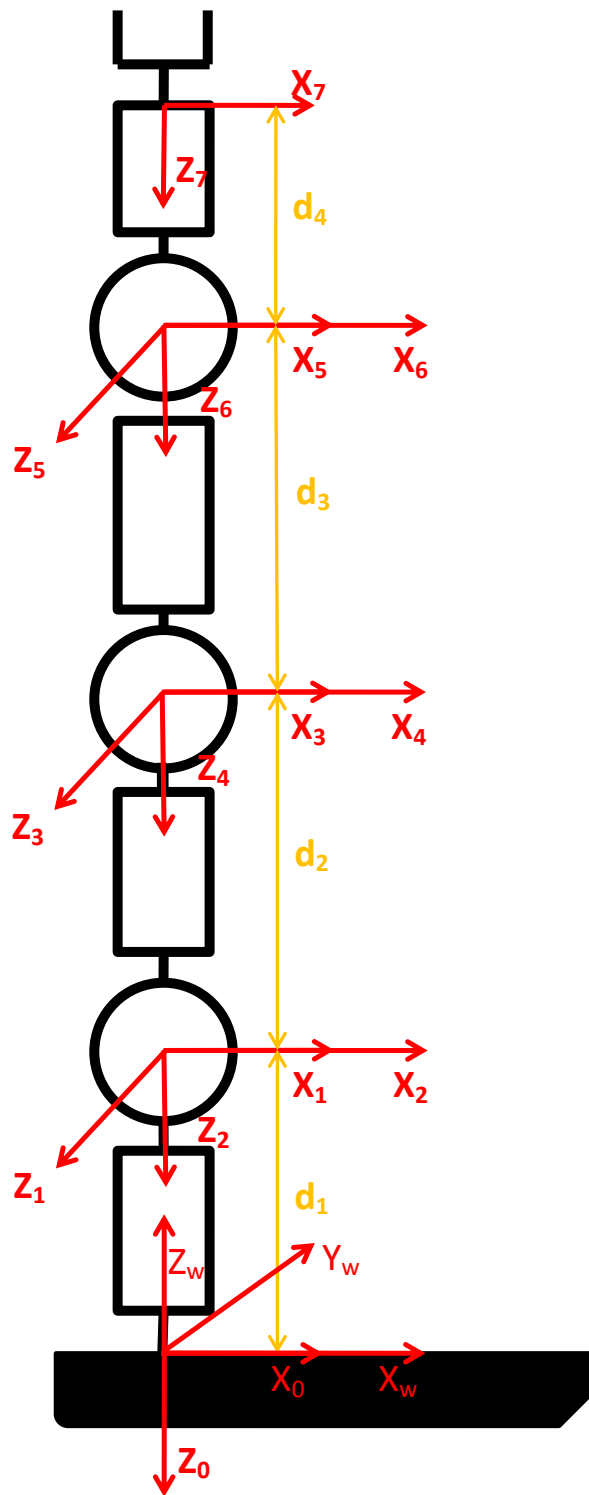


Figure 5.10: Establishment of the DH coordinates

formation between adjacent DH coordinate frames can be obtained as follows:

$${}^0A_1 = \begin{bmatrix} c_1 & 0 & -s_1 & 0 \\ s_1 & 0 & c_1 & 0 \\ 0 & -1 & 0 & -d_1 \\ 0 & 0 & 0 & 1 \end{bmatrix} \quad (5.5)$$

$${}^1A_2 = \begin{bmatrix} c_2 & 0 & s_2 & 0 \\ s_2 & 0 & -c_2 & 0 \\ 0 & 1 & 0 & 0 \\ 0 & 0 & 0 & 1 \end{bmatrix} \quad (5.6)$$

$${}^2A_3 = \begin{bmatrix} c_3 & 0 & -s_3 & 0 \\ s_3 & 0 & c_3 & 0 \\ 0 & -1 & 0 & -d_2 \\ 0 & 0 & 0 & 1 \end{bmatrix} \quad (5.7)$$

$${}^3A_4 = \begin{bmatrix} c_4 & 0 & s_4 & 0 \\ s_4 & 0 & -c_4 & 0 \\ 0 & 1 & 0 & 0 \\ 0 & 0 & 0 & 1 \end{bmatrix} \quad (5.8)$$

$${}^4A_5 = \begin{bmatrix} c_5 & 0 & -s_5 & 0 \\ s_5 & 0 & c_5 & 0 \\ 0 & -1 & 0 & -d_3 \\ 0 & 0 & 0 & 1 \end{bmatrix} \quad (5.9)$$

$${}^5A_6 = \begin{bmatrix} c_6 & 0 & s_6 & 0 \\ s_6 & 0 & -c_6 & 0 \\ 0 & 1 & 0 & 0 \\ 0 & 0 & 0 & 1 \end{bmatrix} \quad (5.10)$$

$${}^6A_7 = \begin{bmatrix} c_7 & 0 & -s_7 & 0 \\ s_7 & 0 & c_7 & 0 \\ 0 & -1 & 0 & -d_7 \\ 0 & 0 & 0 & 1 \end{bmatrix} \quad (5.11)$$

in which $c_i = \cos \theta_i$, $s_i = \sin \theta_i$.

In addition, because the directions of rotation are clockwise, the direction of the coordinate axis Z_0 is downward, causing the problem that the coordinate frame X_0Z_0 is opposite to world coordinate frame $X_wY_wZ_w$ ¹. To deal with this problem, another transformation matrix was introduced to convert the position in the X_0Z_0 coordinate frame to the world coordinate frame. That is:

$${}^wA_0 = \begin{bmatrix} 1 & 0 & 0 & 0 \\ 0 & -1 & 0 & 0 \\ 0 & 0 & -1 & 0 \\ 0 & 0 & 0 & 1 \end{bmatrix} \quad (5.12)$$

Thus, given the rotation angles of all joints, the position of the end effector in the world coordinate frame (P_w) can be calculated by its coordinate value in X_7Z_7 (P_7) and those transformation matrices:

$$P_w = {}^wA_0 {}^0A_1 {}^1A_2 {}^2A_3 {}^3A_4 {}^4A_5 {}^5A_6 {}^6A_7 P_7 \quad (5.13)$$

5.3.2.2 Inverse kinematics

As mentioned above, the arm has a redundant DOF, making the inverse kinematics complicated. However, in the experimental environment, there are no obstacles in the workspace of the arm and hence the path planning of the end effector need not to be considered very carefully. Therefore, in the preliminary state of the experiment, the gesture (orientation) of the end effector should be less complicated. Thus, not all DOFs are used in the inverse kinematics. Here, joints J_3 , J_5 and J_7 are locked (the rotation angles are fixed as 0), reducing the number of the arm's DOFs to four. In addition, the orientation of the end effector is set as always downwards², which needs another DOF to be ensured. The other three DOFs are for the purpose of moving the coordinate frame of the end effector to the target position. Thus the inverse kinematics is simplified remarkably. Unlike the forward kinematics using DH matrices, a cylindrical coordinate method based on fundamental geometry is applied to solve the inverse issue.

Suppose that the target point is $P (X_p, Y_p, Z_p)$ in the world coordinate (shown

¹This world coordinate frame is different from the world coordinate of the camera. Its origin point is at the base of the arm and hence it can also be called the arm coordinate frame. However, the direction of each axis is the same as the camera coordinate frame.

²Originally, the inverse kinematics was designed for grasping rocks using the gripper fitted at the end of the arm. Hence, the downwards direction is regarded as the best gesture for grasping.

in Fig. 5.11), P 's projective point on the ground plane XOY is $P_g (X_p, Y_p, 0)$.

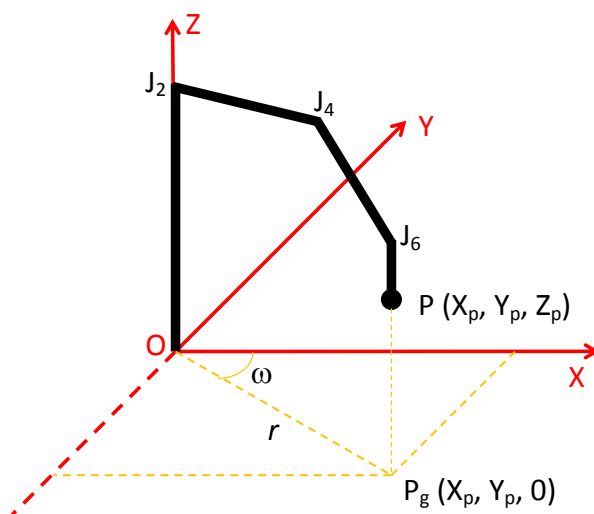


Figure 5.11: Solving procedure of the J_1

It can be seen that the rotation angle θ_1 of the joint J_1 can be simply solved as:

$$\theta_1 = -\omega = -\tan(Y_p/X_p) \tag{5.14}$$

The rotation angle θ_1 of J_1 is related to the azimuth while the rotation angles of the other three joints are used to determine the radius r and height Z_p . This is to say that, the calculation of θ_2 , θ_4 and θ_6 is independent to the calculation of θ_1 . Here, the three angle are calculated on the plane $OJ_2J_4J_6$ (Fig. 5.12).

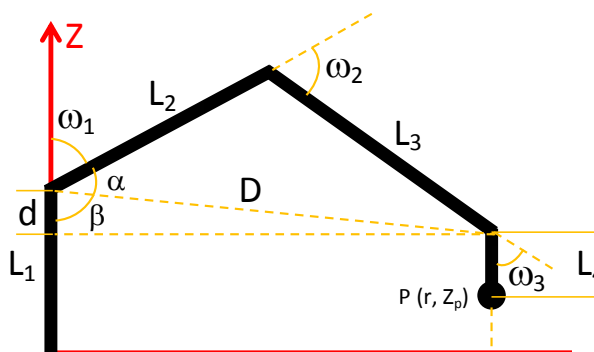


Figure 5.12: Solving procedure of J_2 , J_4 and J_6 .

The r can be calculated by the coordinate value of the target position:

$$r = \sqrt{X_p^2 + Y_p^2} \quad (5.15)$$

Here we defined two parameters to represent the computing procedure more conveniently. These are d , referring to the height difference between J_2 and J_4 , and D referring to the distance between joints J_2 and J_4 :

$$d = L_1 - L_4 - Z_p \quad (5.16)$$

$$D = \sqrt{d^2 + r^2} \quad (5.17)$$

Afterwards, ω_2 can be calculated by the cosine theorem:

$$\omega_2 = \pi - \arccos\left(\frac{L_2^2 + L_3^2 - D^2}{2L_2L_3}\right) \quad (5.18)$$

Two temporary angles α and β are introduced. These are:

$$\alpha = \arccos\left(\frac{L_2^2 + D^2 - L_3^2}{2DL_2}\right) \quad (5.19)$$

$$\beta = \text{atan2}(r, d) \quad (5.20)$$

ω_1 is the supplementary angle of $(\alpha + \beta)$.

$$\omega_1 = \pi - (\alpha + \beta) \quad (5.21)$$

ω_3 can be computed by using ω_1 and ω_2 .

$$\omega_3 = \pi - \omega_1 - \omega_2 \quad (5.22)$$

Due to the defined direction of each joint, the rotation angles θ_2 , θ_4 and θ_6 are the inverse angles of ω_1 , ω_2 and ω_3 .

$$\begin{cases} \theta_2 = -\omega_1 \\ \theta_4 = -\omega_2 \\ \theta_6 = -\omega_3 \end{cases} \quad (5.23)$$

In addition, if the position of a target point is out of the workspace, the end effector cannot reach the target. Under such a situation, it will generate imaginary number(s) in the procedure of the inverse kinematics. Thus, the appearance of an imaginary number can be used as an indicator to judge whether the target position is in the workspace envelope.

5.3.3 Workspace of the arm

The workspace here represents all positions where an end effector (e.g. the gripper) can reach. One way to obtain the workspace is to record the positions of the end effector with different settings of joint angles. Generally, a simulation system will be established to facilitate the calculation of the workspace. Hence, a simulation system of the Schunk arm with a graphic user interface (GUI) was built using Matlab (shown in Fig. 5.13) to save time for calculating the workspace as it need not move the real arm. In addition, the graphic interface of the simulation system can provide a visualisation of the arm by which we can quickly analyse the kinematics.

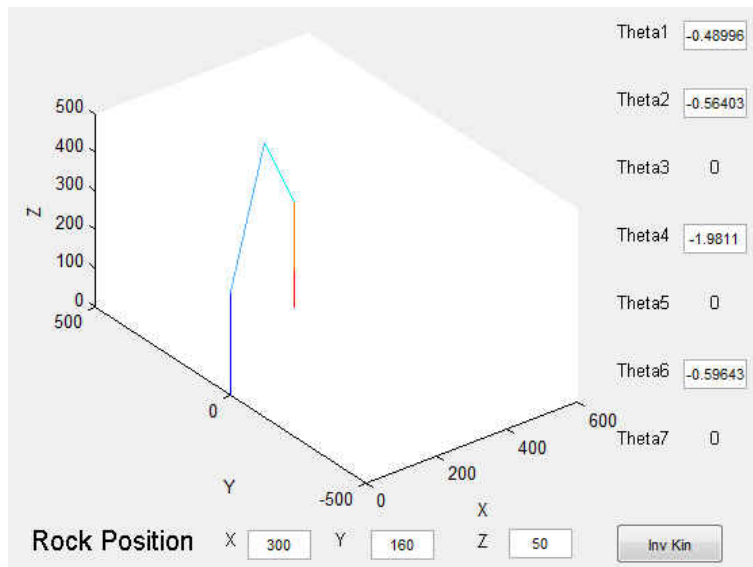


Figure 5.13: GUI of the kinematic simulation system

A workspace is always limited by some restrictions. In the case of our arm, the main restrictions are:

- **The constraint of the real space**

The workspace of the arm is limited by the real physical space where it can

move. For example, the end effector cannot be in a position beneath the table supporting the arm ($z < 0$). Moreover, the x coordinate value of any part of the arm should not be less than 0, which may lead the arm to hit the wall behind it.

- **The solvability of the kinematics**

As mentioned above, there are some situations where no kinematic solution exists. It means that the arm cannot reach the position under such a kinematics condition. Since the number of arm DOFs have been reduced to four, the arm is more likely to encounter this restriction.

- **The range of joint angles**

Each joint of the arm has range of rotation (-2 rad to 2 rad) due to the mechanical or electronic limitations. If any rotation angle is out of its range, the arm could be damaged.

- **The collision of links**

The collision of links will also damage the arm, which could occur in the process of moving. However, due to the limitations added in the inverse kinematics (the end effector is perpendicular to the ground), the collision restriction is mostly avoided.

All the target points which satisfy these restricted conditions form the workspace. The workspace generally consists of an infinite number of points and has an irregular shape. Here, the workspace is illustrated by a point cloud (see Fig. 5.14). The blue points are the positions the end effector can reach (within the workspace).

To illustrate the shape of the workspace more precisely, the projections of the point cloud on the coordinate XOZ , YOZ and XOY are shown in Fig. 5.15, corresponding to the side view, the front view and the plan view respectively. By observing the point cloud, the approximate range and shape of the workspace can be obtained. It can be seen that the shape of the workspace is similar to a quarter sphere with 600 mm radius, cut by a cylinder with 250 mm radius.

5.4 Camera to arm

Combining the coordinate transformation and kinematics in the camera agent and the arm agent together, it is feasible to manipulate the arm (end effector) to access rocks detected in images. The detailed procedure is listed in Fig. 5.16.

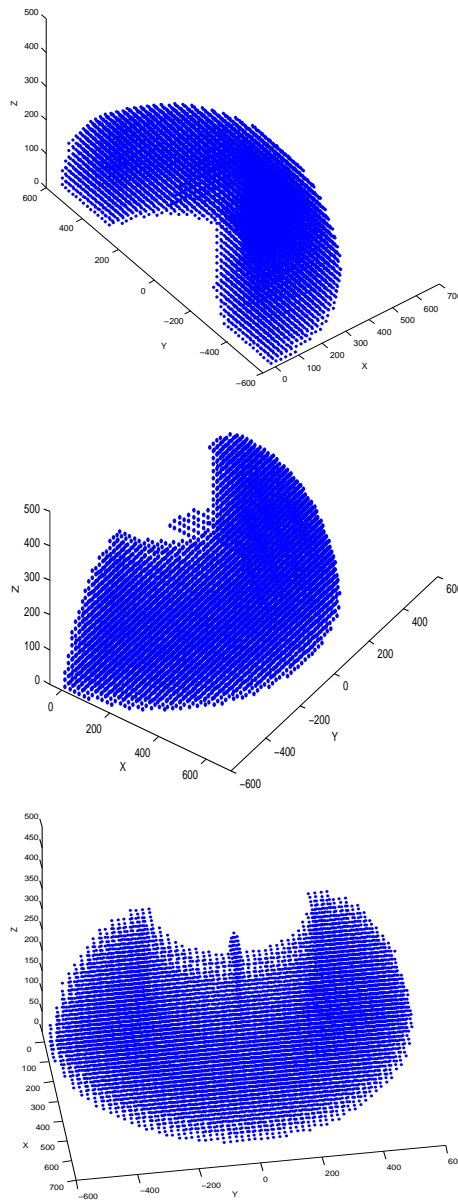


Figure 5.14: Workspace of the end effector demonstrated by blue point cloud. The distance between adjacent points is 20 mm.

Since the defined axes of the camera coordinate frame and arm coordinate frame are in the same direction but the origin points are different, it needs an extra transformation between them. Suppose the position of a point is (X_c, Y_c, Z_c) in the camera coordinate frame and is (X_a, Y_a, Z_a) in the arm coordinate

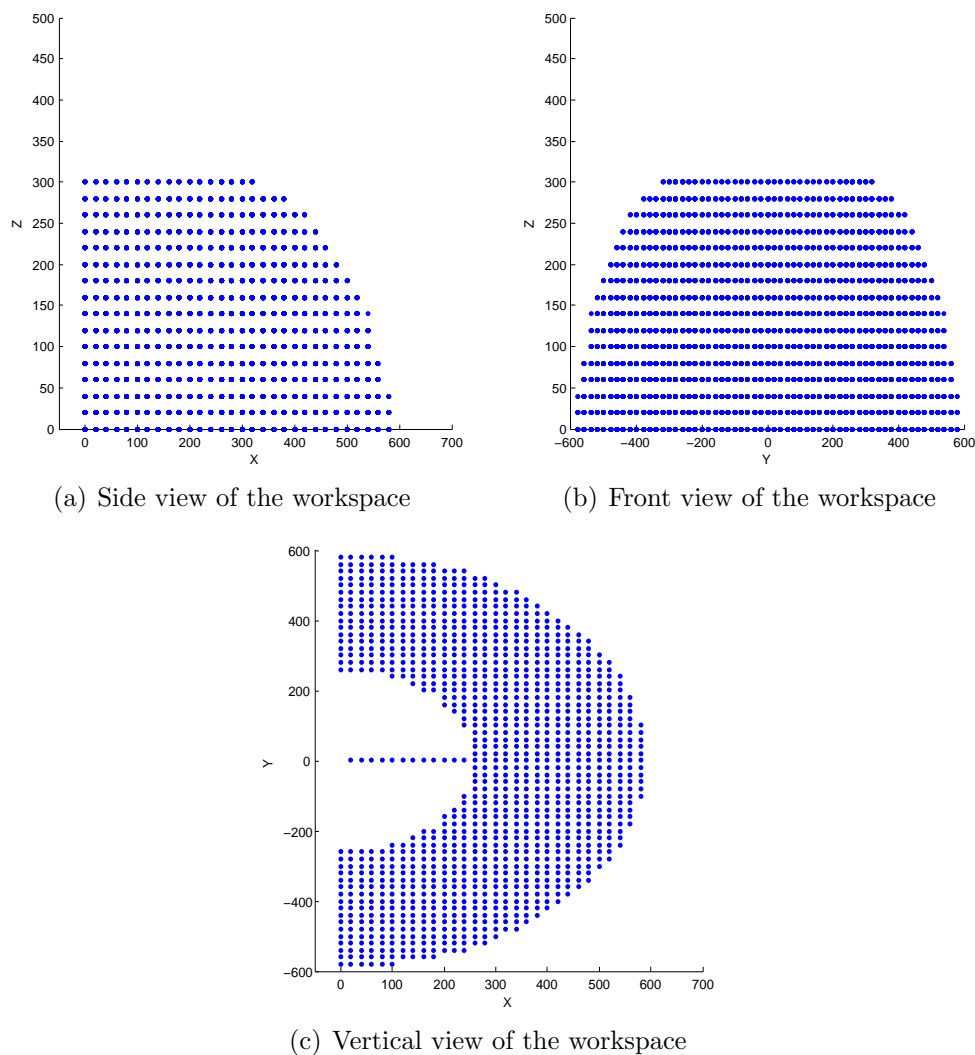


Figure 5.15: Projections of the workspace on the three base coordinate planes

frame. The transformation can be expressed as:

$$\begin{bmatrix} X_a \\ Y_a \\ Z_a \end{bmatrix} = \begin{bmatrix} X_c \\ Y_c \\ Z_c \end{bmatrix} + \begin{bmatrix} d_x \\ d_y \\ 0 \end{bmatrix} \quad (5.24)$$

where d_x and d_y are the distances between the arm base and camera base in the x -axis direction and the y -axis directions respectively. A simulation diagram is given in Fig. 5.17.

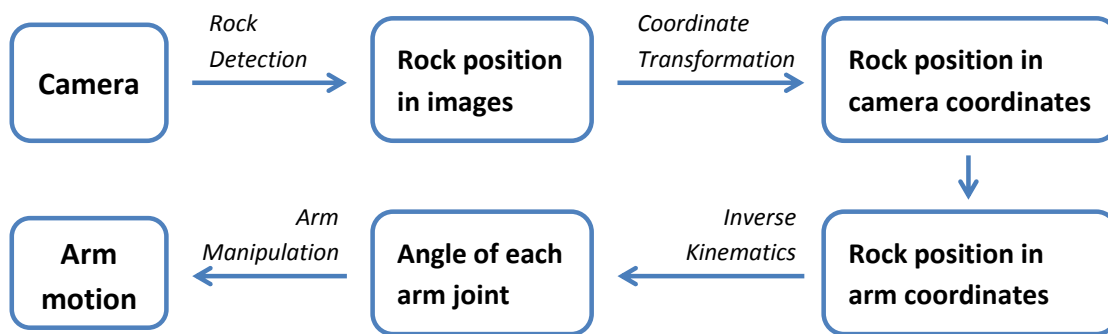


Figure 5.16: Procedure of the transformation between arm and camera

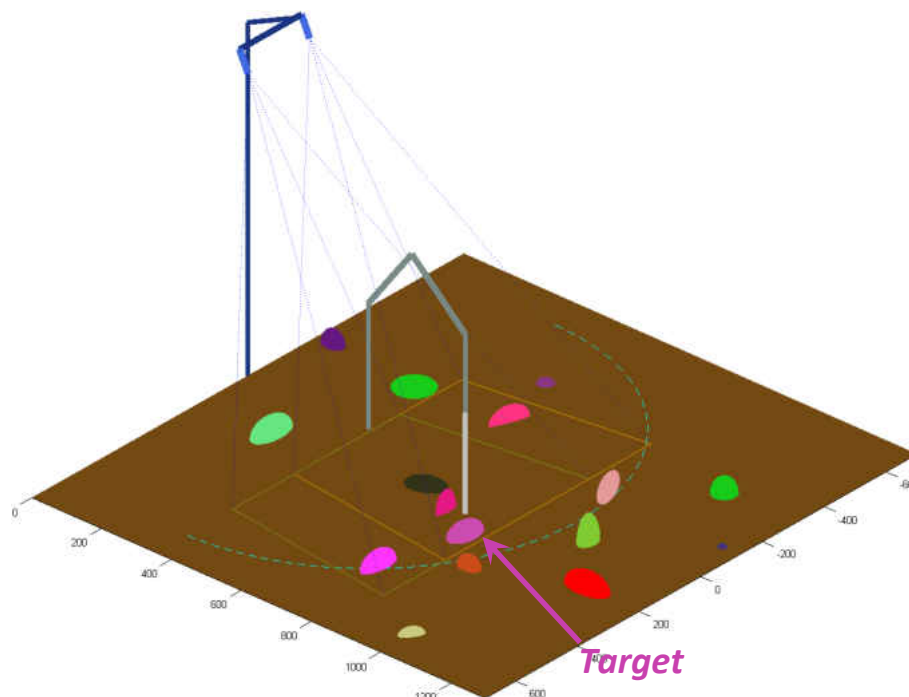


Figure 5.17: Integration of the camera agent and the arm agent. Firstly, an interesting rock is detected as the target, and through a series of calculations, the end effector of the arm accesses the rock.

5.5 Summary

In this chapter, an executive agent designed as the emulator of some parts of a real rover is discussed. The agent consists of two cameras with the capability of capturing colour and multispectral images and a 7-DOF robotic arm to perform manipulations such as accessing rocks. Specifically, the related kinematic calcula-

tions of the agent are given in detail, including the forward and inverse kinematics of the robotic arm, the coordinate transformation from captured images to the real world, and the coordinate transformation between camera coordinates and arm coordinates. The executive agent can be regarded as a good platform to support and test the algorithms of rock detection and science value evaluation.

Chapter 6

Experiments and Demonstrations

In the previous chapters, the details of rock detection, rock science value evaluation and executive system have been described separately. In this chapter, the three parts are integrated together, forming a relatively complete system. Rocks which hold different geological characteristics have been selected and scattered in front of the cameras and robotic arm (see Fig. 6.1) to simulate a typical environment a rover could encounter. However, the experimental environment is different to a real Mars environment to some degree. The background of rocks is the top of the table where the robotic arm is installed. On the one hand, compared to the complex Mars regolith (soil), the background with only a single colour is relatively simple, facilitating the segmentation of rocks. On the other hand, this background is inconsistent with some suppositions¹ in the rock detection chapter and therefore the performance of corresponding algorithms may be different. In addition, the experimental environment is an indoor environment and hence the light source is not sunlight but fluorescent light which lacks infrared components. Therefore, it is hard to capture multispectral data in infrared wavelengths. Although restricted, this environment can be used to carry out preliminary experiments for validating the algorithms mentioned before and testing the overall performance of whole system.

A demonstration experiment has been conducted firstly to demonstrate the integration of final system, linking the instruments and algorithms mentioned before together. The procedure and corresponding results of each part were exhibited in

¹Mainly refer to a supposition in Section 3.3. The supposition is that rock regions will be darker or brighter than of background regions and hence the intensities of background regions will be between the intensities of darker rock regions and brighter rock regions. In this case however, the background regions are always brighter than rock regions.

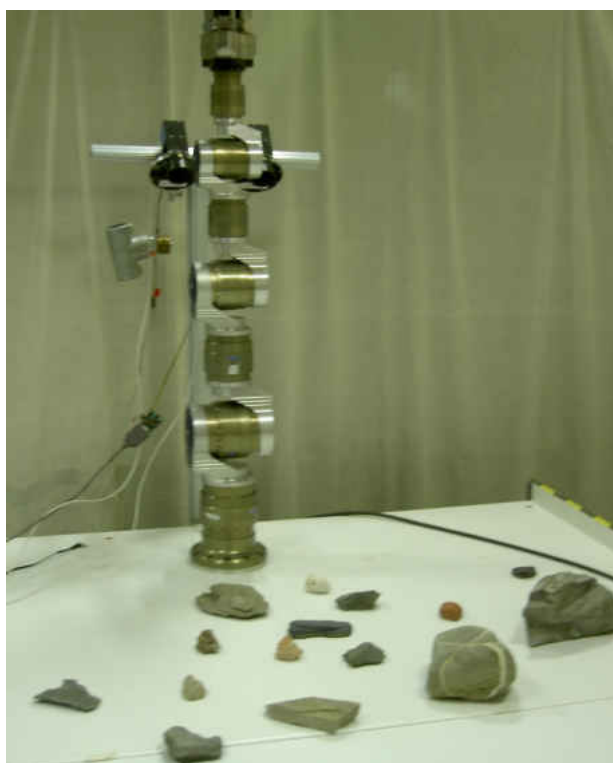


Figure 6.1: Experimental environment. Rocks with different characteristics are scattered around the robotic arm.

detail, from capturing images to accessing rocks. Then several experiments have been done with different rock layouts to evaluate the stability and repeatability of the system.

6.1 System integration

As described before, the proposed autonomous rock science analysis system mainly consists of three components: rock detection, science value evaluation and corresponding executive agent. The relation of the three components is exhibited in Fig. 6.2. The rock detection component addresses the image and multispectral data captured by the executive agent, generating detected rock regions for the rock science value evaluation component and rock position calculating (included in the executive agent). The science evaluation component uses the image and region information to extract geological attribute information and calculate rough rock science value which can guide the further motion of executive agent. By

connecting the three components together, we can establish the final integrated system which is competent to perform autonomous rock analysis tasks.

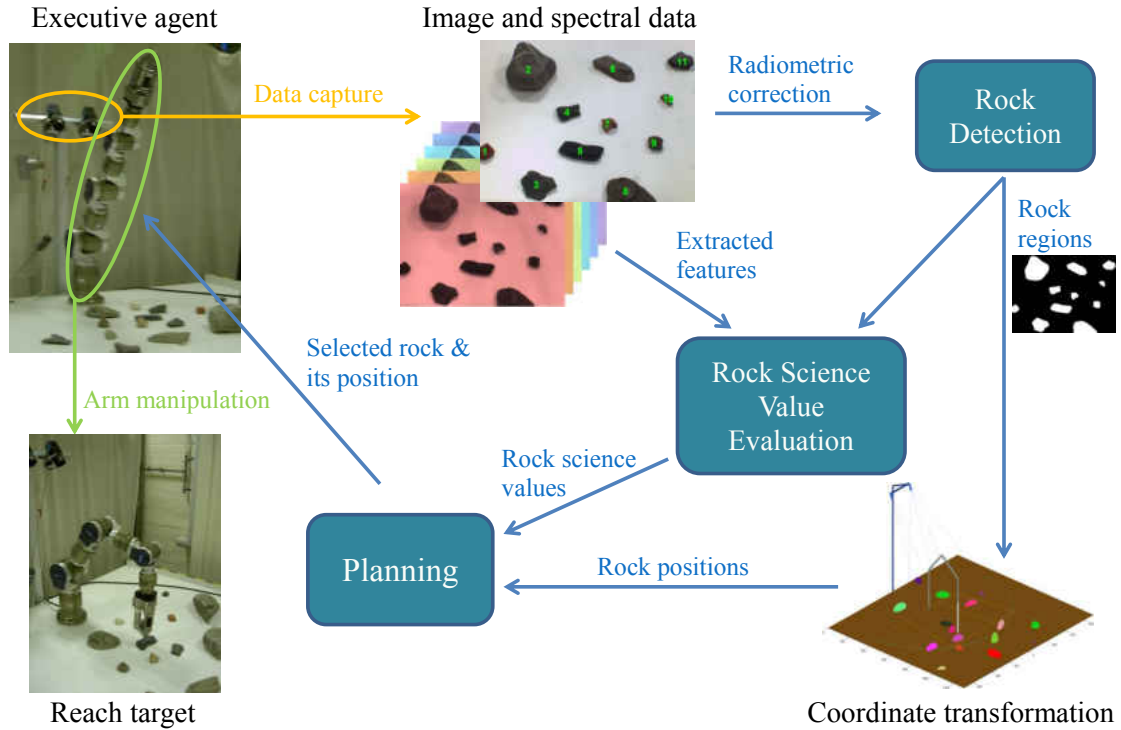


Figure 6.2: Relation between the three components of proposed system

6.1.1 Image capture and preprocessing

The first step of the system is to capture images of rocks. In order to fit in with the workspace of the arm, the tilt angle is set to 49° . Since we require only multispectral data in the range of visible light, and our rock position calculation algorithm is based on a single camera, only the left camera has been used to capture rock image data. The broadband red, green and blue filters were used to capture the images of the RGB channels separately. The RGB data can be used for rock detection (saliency methods) as well as for rock science value calculation (composition part). False colour images can also be generated from the RGB data. An example of the captured RGB images is shown in Fig. 6.3. This instance is also used for demonstrating other components of the ARSAS system.

The narrowband geological filters whose wavelengths range from 440nm to 660nm were used to capture raw multispectral data. In addition, a ColorChecker[®]

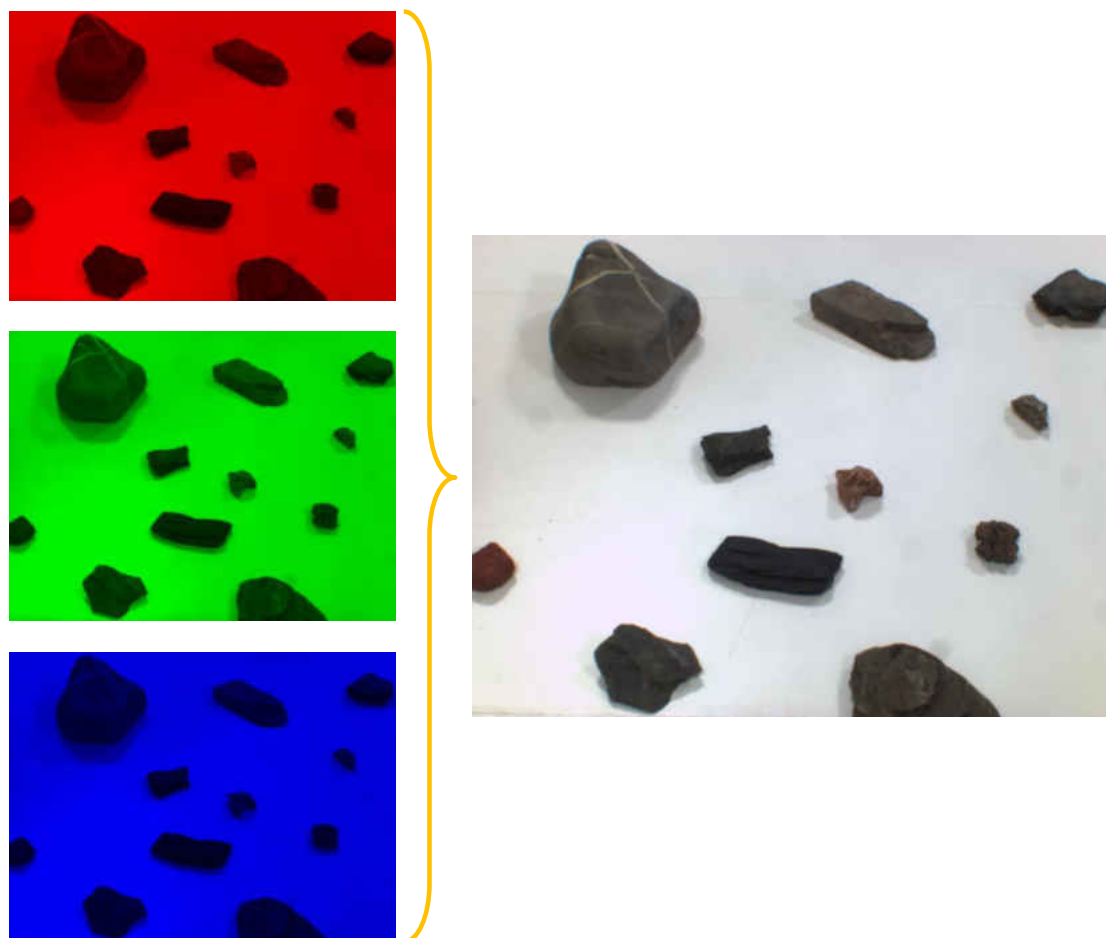


Figure 6.3: Example of an RGB image captured by the camera system. The images of the R, G and B channels are captured independently and can be used to generate false colour images. This image was used as an instance (example) image and experiments have conducted on it to demonstrate whole procedure of the proposed system.

colour radiation chart (shown in Fig. 6.4) has been used as a calibration target (CT). Through use of the calibration target, the light condition of the experimental environment can be measured, by which the raw multispectral data can be transformed to R^* data. Details of the transformation process can be found in [Barnes et al., 2011]. Fig. 6.5 illustrates the R^* data corresponding to the example image, showing the relative reflectance of rocks under light of different wavelengths.

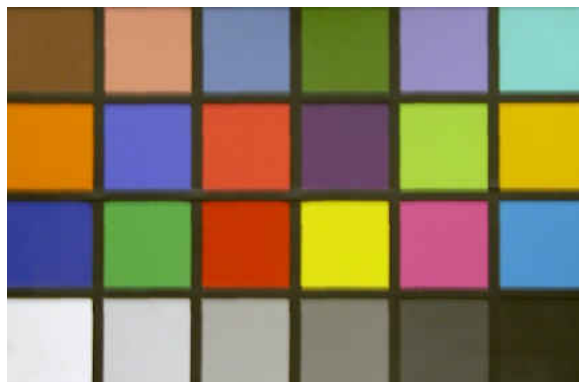


Figure 6.4: Calibration target: ColorChecker[®] colour radiation chart

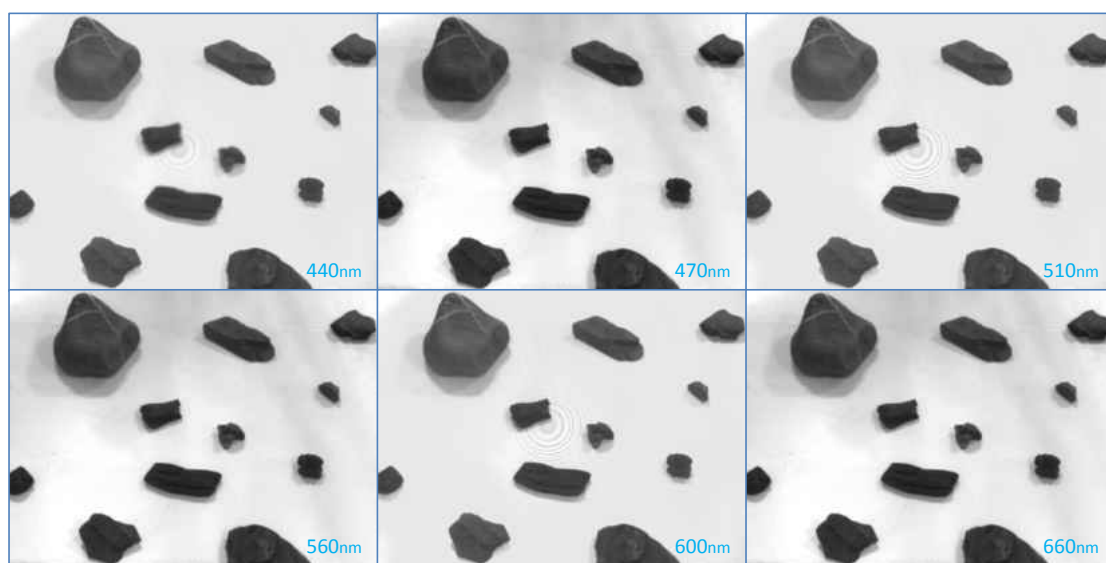


Figure 6.5: Experimental R^* data

6.1.2 Rock detection

In Chapter 3, three types of rock detection methods (i.e. multispectral classification method, two-threshold thresholding¹ method and saliency method) have been presented and each type of method contains several algorithms. Here, all those algorithms were tested on the example image captured in the experimental environment. The parameter settings of those algorithms has been kept the same as the settings discussed in Chapter 3. Multispectral classification algorithms were tested using the multispectral data (R^* data). Specifically, training

¹The result of one-threshold OTSU method is also presented.

pixels¹ were manually labeled for selecting features and training classifiers (clusters). Two-threshold thresholding algorithms were tested on the grayscale image corresponding to the green filter as this type of algorithms only addresses single-channel images. Saliency algorithms were tested on the composed RGB image. The detection results of the three methods are shown in Figs. 6.6, 6.7 and 6.8 respectively.

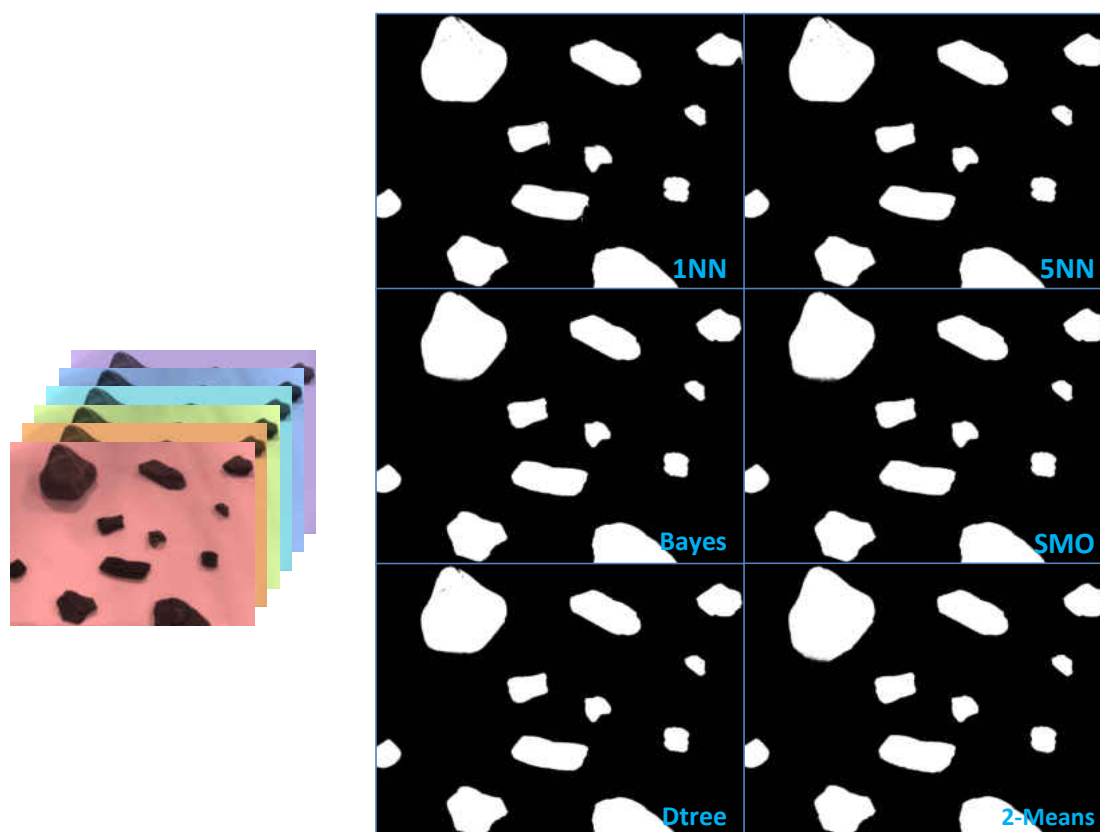


Figure 6.6: Detection results of multispectral classification algorithms on the example image

It can be seen that, even though the experimental environment is unlike the real Mars environment, the performance of multispectral methods are relatively better. The contours of detected rock regions are clearer and fewer shadow and noisy regions are detected. The good performance may benefit from the amount of data and the training processes with labeled ground truth. Through labeling and

¹As with previous settings, the training set contains 100 pixels: 50 pixels denote rock regions and 50 pixels denote background regions.

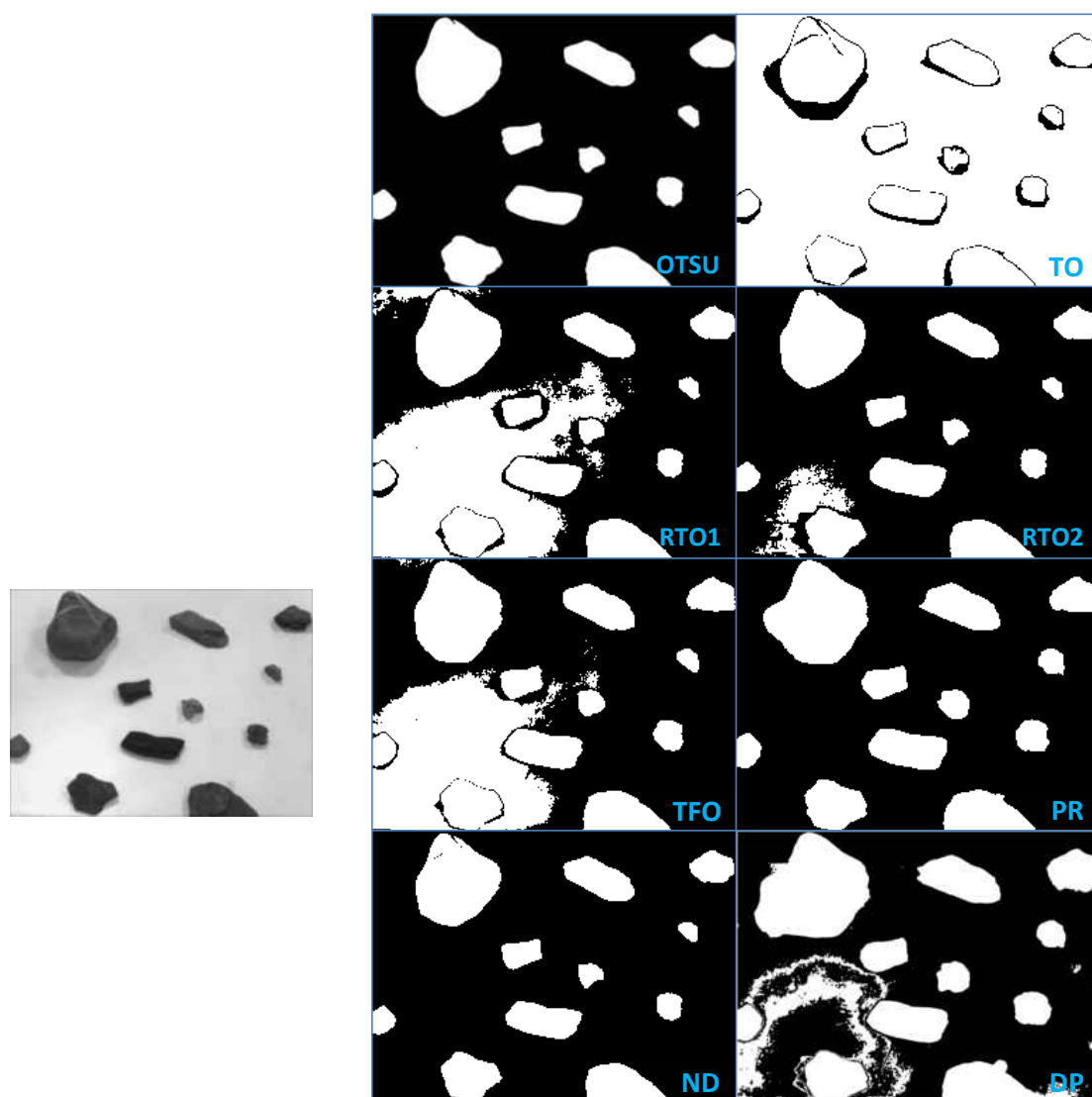


Figure 6.7: Detection results of thresholding algorithms on the example image

training, different classifiers can be generated, adapting for different environments.

On the other hand, due to the differences between the experimental and Mars environments, the supposition that background intensities are higher or lower than rock intensities is no longer correct. Hence, in the experimental case, the two-threshold algorithms do not gain better performance than traditional one-threshold OTSU algorithms. However, in terms of each two-thresholding algorithm, the performance on the example image is similar to the previous performance (see Fig. 3.19 and 3.20). The TO, RTO1 and TFO algorithms still obtain bad rock detection

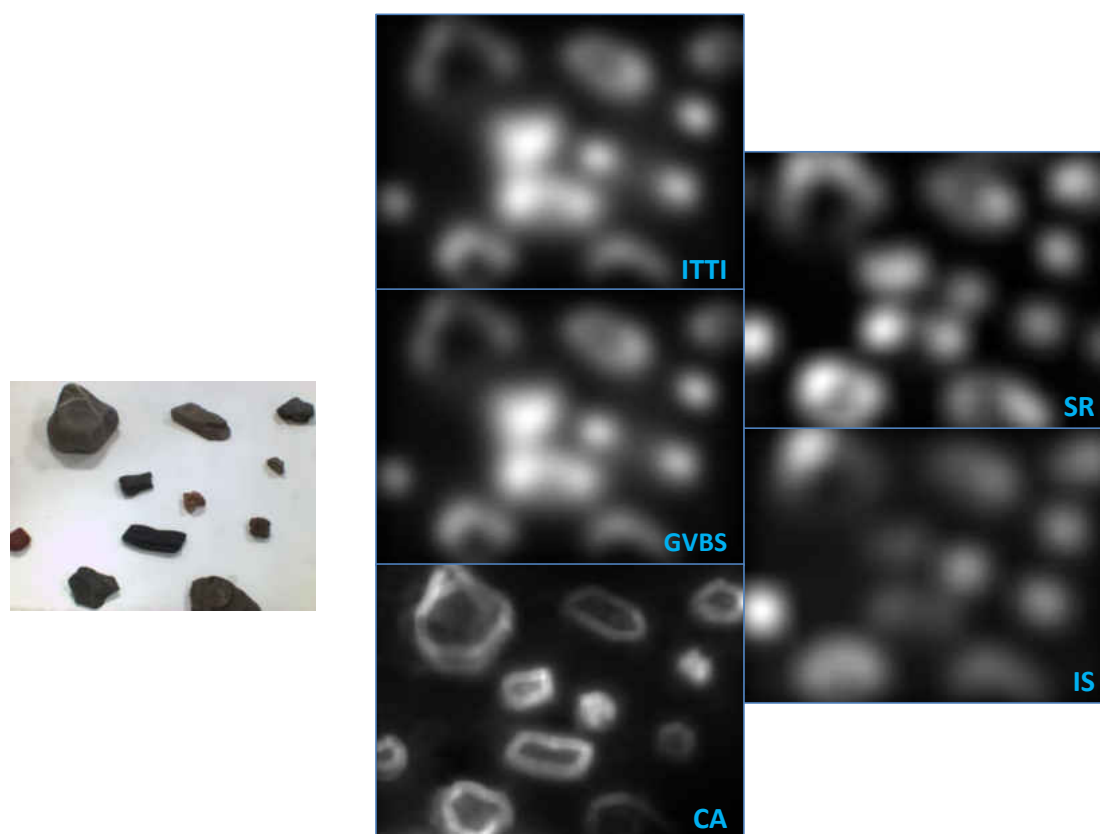


Figure 6.8: Detection results of saliency algorithms on the example image

results. The DP algorithm, sensitive to parameter settings, does not obtain a good detection result since the parameters have not been adjusted for this specific experimental environment. Nevertheless, the PR and, especially ND algorithms, have good adaptability. Their detection results are similar to the OTSU method, implying that these two algorithms can also deal with one-threshold problems. In contrast with classification algorithms, thresholding methods cannot detect the shadow region precisely. Hence generally, classification methods will obtain better performance than thresholding methods.

With regard to saliency algorithms, although rough rock regions were approximately recognised, the clear contours of rock regions cannot be determined. It can be seen that the saliency algorithms are very sensitive to rock edges and shadow regions as discussed before. Hence, although these can be used to point out approximate rock positions, saliency methods are not suitable for defining precise rock regions which are important for further rock science value evaluation.

Although the experimental environment has been simplified, rock regions still cannot be detected perfectly. This is an inevitable problem and may affect the rock detection result to some extent.

6.1.3 Attribute extraction and science value calculation

After rock regions have been identified, the next step is to extract the geological attributes from the rock regions from which the science value of the rocks can be calculated. Specifically, we used the SMO classification method to generate the rock regions. For easy reference, the rocks are labelled as shown in Fig. 6.9.



Figure 6.9: Rock labels for the experiment

The geological attributes that need to be extracted are *Lustre*, *Relief*, *Angularity*, *Layering*, *Hue*, *Saturation* and *Value*, in which *Hue*, *Saturation* and *Value* are extracted directly, and *Lustre*, *Relief*, *Angularity* and *Layering* are scaled from average graylevel, $DENSIFT$, $Compactness$ and SP_{Cpixel} respectively as in Chapter 4. The extracted attribute values of the rocks are listed in Table 6.1.

Table 6.1: Attribute extraction

Rock No.	<i>Layering</i>	<i>Lustre</i>	<i>Relief</i>	<i>Angularity</i>	<i>Hue</i>	<i>Saturation</i>	<i>Value</i>
1	0	0.16	6.94	4.03	8.8	0.51	0.32
2	0.03	0.26	6.82	4.67	33.9	0.14	0.28
3	4.66	0.22	6.91	4.62	42.1	0.07	0.22
4	5.23	0.21	6.76	4.92	33.1	0.04	0.19
5	10	0.14	6.86	5.4	229.5	0.1	0.16
6	8.43	0.29	6.86	5.2	28.3	0.19	0.28
7	3.02	0.24	6.66	4.57	16.4	0.38	0.36
8	1.29	0.18	6.89	5.27	33.4	0.21	0.23
9	1.11	0.18	6.78	4.88	21.9	0.25	0.23
10	5.2	0.2	6.43	4.67	32.8	0.23	0.29
11	7.12	0.28	6.87	4.49	27.2	0.11	0.22

Using these geological attribute values as the input of the fuzzy expert system¹, the science value of each rock can be calculated, based on which a rover can plan what to do next. Table 6.2 lists the science value outputs of the fuzzy expert system. $SV_{Structure}$, $SV_{Texture}$ and $SV_{Composition}$ were generated separately and were added together to calculate the comprehensive science value SV_{total} .

Table 6.2: Science value calculation

Rock No.	$SV_{Structure}$	$SV_{Texture}$	$SV_{Composition}$	SV_{total}
1	3	25.14	18.65	46.79
2	3	25.06	27.53	55.59
3	45.08	24.84	30.54	100.46
4	48.42	24.3	29.59	102.31
5	80	23.37	28.63	132
6	71.85	24.88	21.59	118.33
7	32.91	24.98	20.53	78.41
8	11.59	23.83	18.93	54.35
9	7.74	24.09	17.91	49.74
10	48.27	24.29	20.02	92.57
11	59.98	25.55	29.05	114.58

In the results of attribute extraction and science value calculation, it can be seen that the science value evaluation system can indeed reflect the geological

¹The fuzzy expert system adopted the rule base mentioned in Section 4.4.2. Hence it is for the purpose of general exploration, preferring rocks with layered structures, smooth surfaces, green colours, high albedos and so on.

expert's thinking. For example, the 5th rock has an obvious layered structure and therefore it has a very high science value in structure aspect. The 7th rock has a relatively brighter colour, and hence it gained a slightly higher composition science value.

6.1.4 End effector manipulation

In the previous parts of the ARSAS system, the transformation from image data to science value has been done. As with the architectures of other classical autonomous systems, the next stage is the planning phase where commands will be generated to guide the rover motion. However, in our executive agent, except for the camera system for capturing rock images, the robotic arm is the only instrument. It means that it is impossible to change the relative position between the arm and the rocks. Hence, in order to adapt this situation, the planning phase has been extremely simplified. The planning procedure is as follows:

1. Choose the rock with highest comprehensive science value.
2. Calculate its position in the world coordinate frame.
3. Manipulate the end effector of the arm to access (reach) the rock if it is in the workspace of the arm¹.

The 5th rock had been evaluated as the rock with the highest comprehensive value in this scene and hence was regarded as the science target with the highest priority. Through coordinate transformation, it was confirmed that its position was within the range of the arm. Finally, the arm was controlled automatically to access the rock (see Fig. 6.10).

6.2 Repeatability experiments

In this section, the rocks were shuffled and eight experiments were conducted with different rock layouts. The procedures of these experiments were almost the

¹In real Mars situations, if a rock with the highest science value has been identified out of the arm workspace, the rover should be moved to a place where the rock can be assessed by the end effector (science instruments). However, in our restricted experimental condition, we can only deal with the rocks in the fixed workspace.



Figure 6.10: Robotic arm controlled to reach the rock which has highest science value

same as the procedure of the demonstration experiment. Particularly in the rock detection part, not all algorithms were performed. The SMO classification method was selected as the rock detection method since it obtained good performance in the previous demonstration experiment. The corresponding results of each experiment are illustrated in Figs. 6.11, 6.12, 6.13, 6.14, 6.15, 6.16, 6.17 and 6.18 respectively. Specifically, the experimental results are shown by four parts. Taking Fig. 6.11 which represents the results of experiment I for example, the top-left image is the RGB colour image synthesised by the data captured by the camera agent. The top-right image shows the rock detection result generated by the SMO classification algorithm. Specifically, the detected rock regions are marked with number in order to facilitate rock reference. The bottom-left image is a heat map representing the calculated science values of detected rocks. The colour closer to red means that the corresrock has higher science value. The bottom-right image is the photo demonstrating the status of rock approaching by the arm agent.



Figure 6.11: Results of experiment I

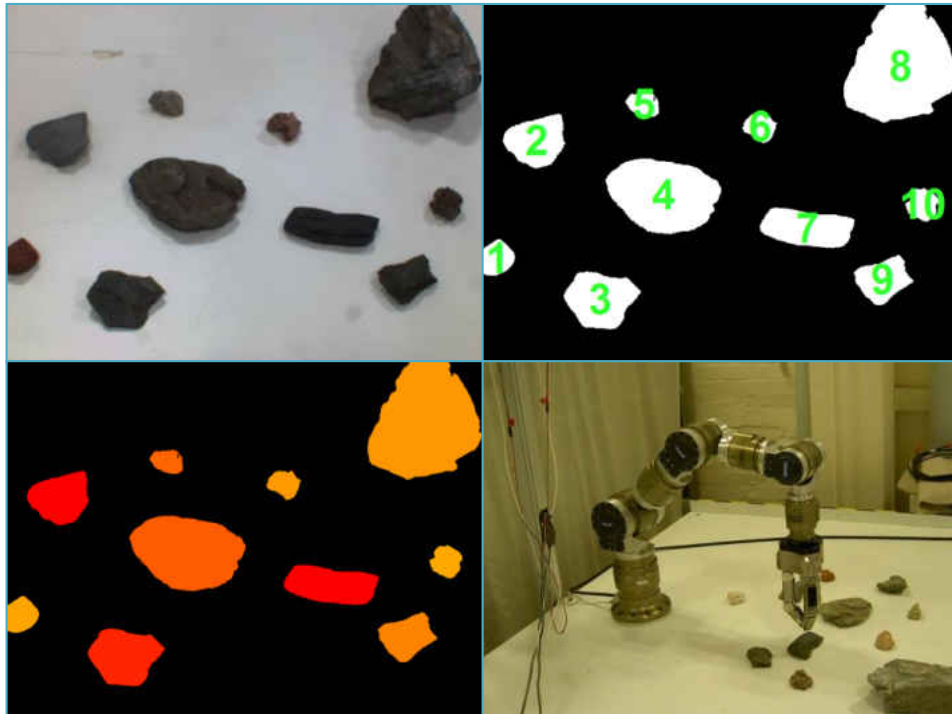


Figure 6.12: Results of experiment II

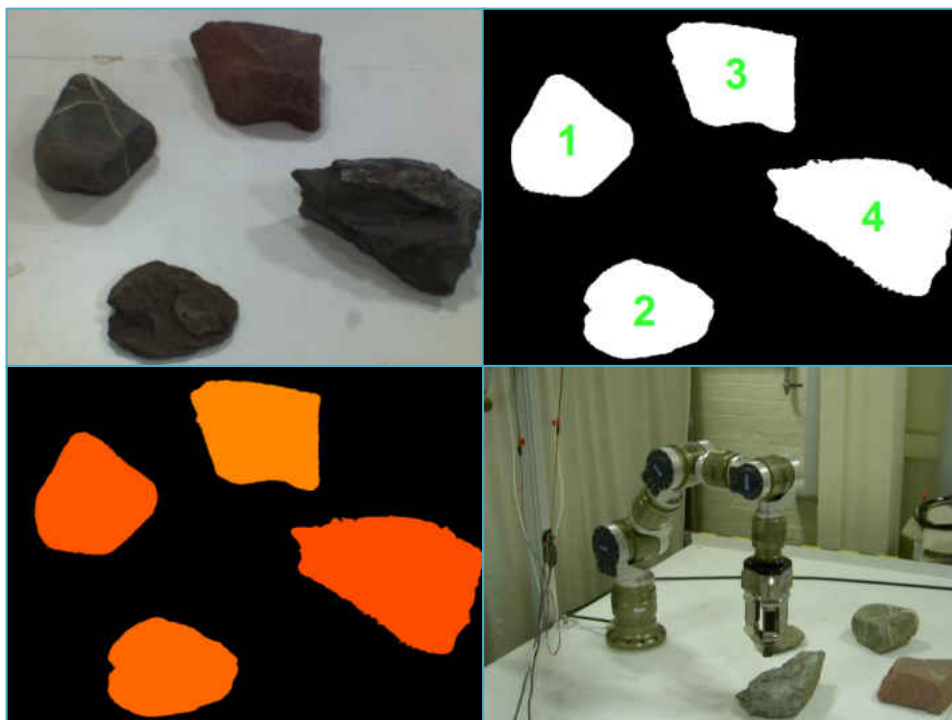


Figure 6.13: Results of experiment III

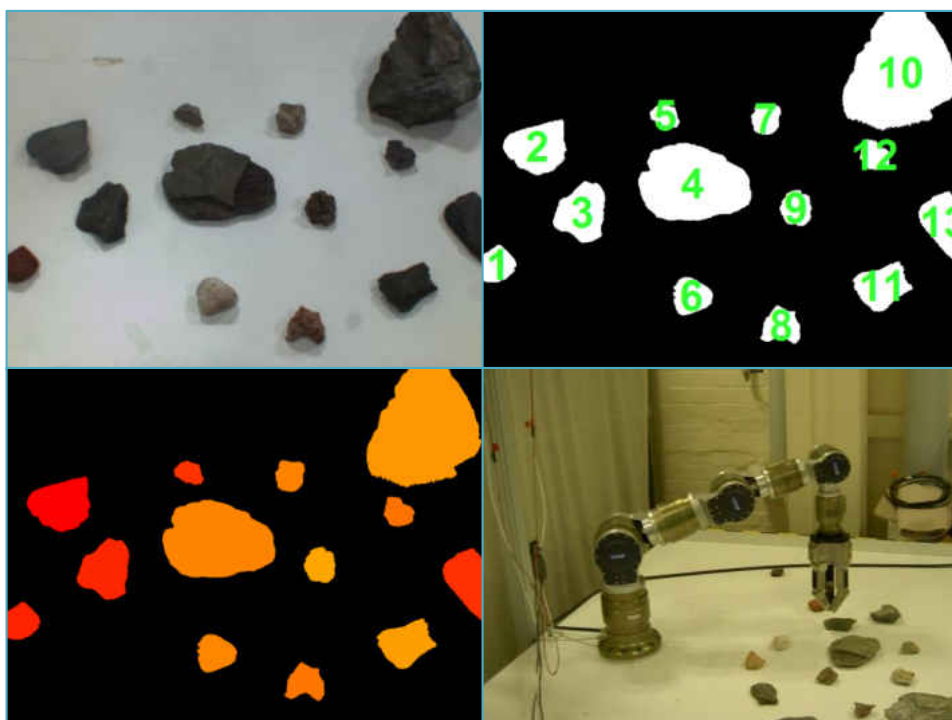


Figure 6.14: Results of experiment IV



Figure 6.15: Results of experiment V

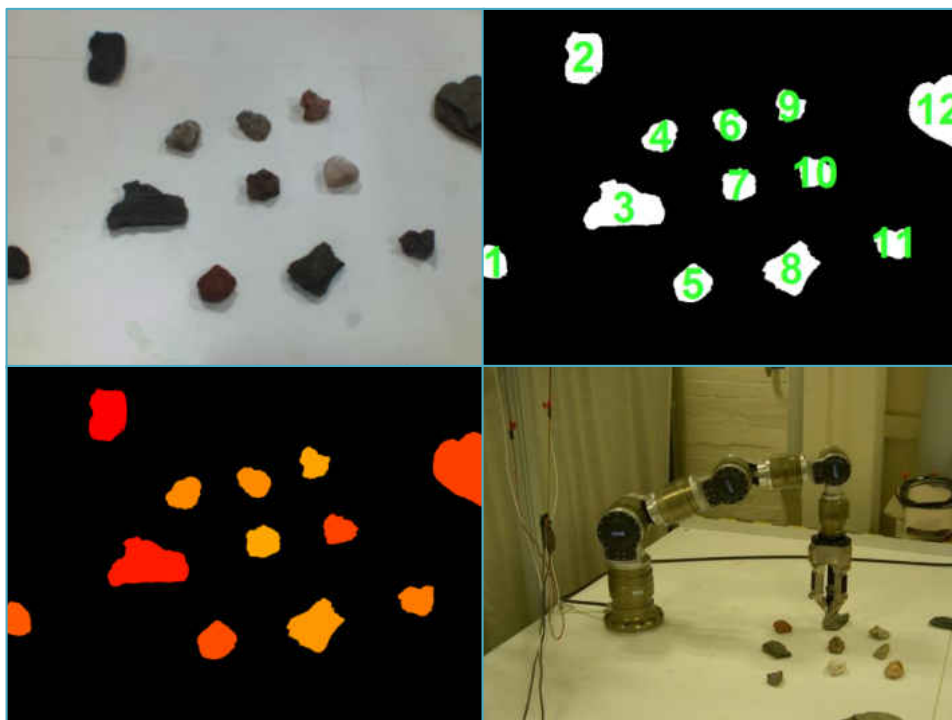


Figure 6.16: Results of experiment VI

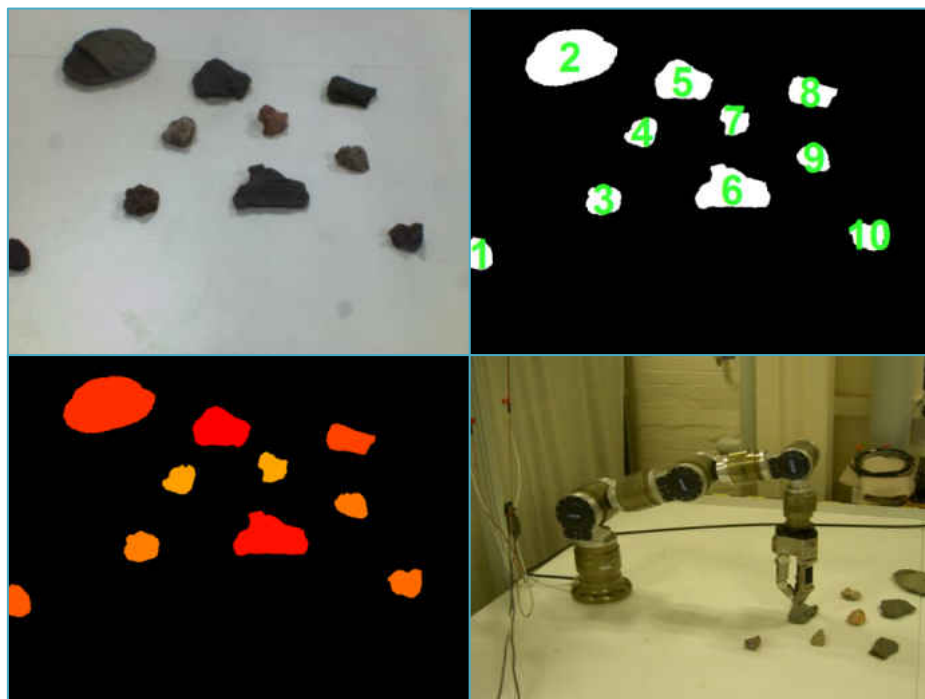


Figure 6.17: Results of experiment VII

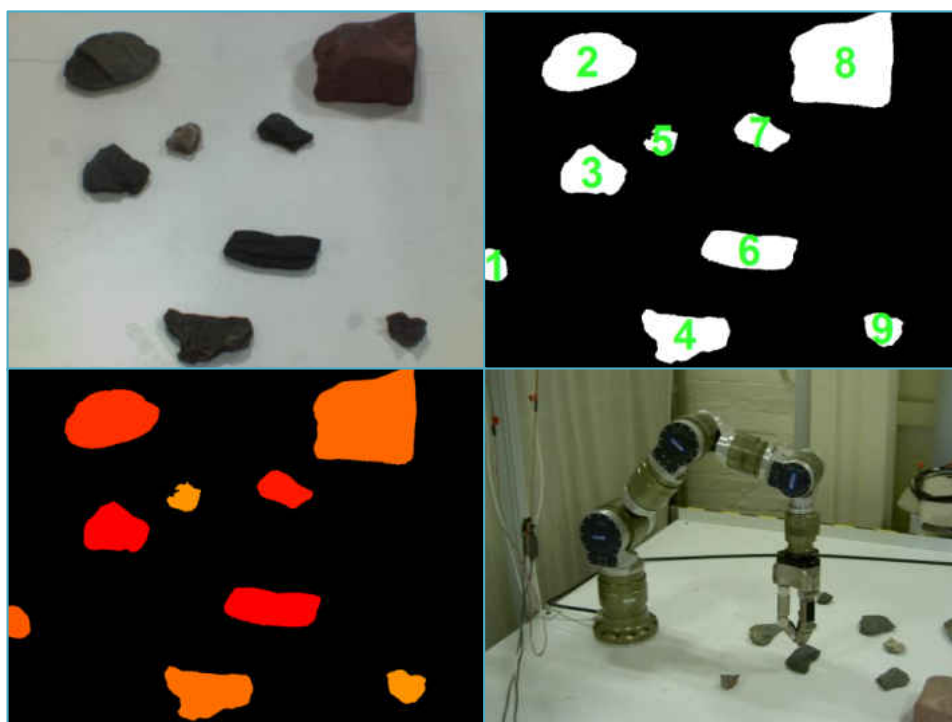


Figure 6.18: Results of experiment VIII

In addition, the intermediate outputs of the science value evaluation of these experiments are listed in Appendix A, indicating the distribution of every attribute and science value.

Both by inspecting the resultant images and by analysing the quantitative data, it can be seen that the proposed system is of good stability and repeatability. As to the rock detection component, all rock regions were extracted appropriately, although the experiments were conducted in a relatively simple environment. The component of executive agent also worked well. After a target rock within the workspace of arm is selected, the end effector can always move to the target position accurately.

In particular, an extra quantitative analysis has been done to show the performance consistency of the science evaluation component. There are 20 rocks which have been used in the experiments of integrated system, in which 10 rocks were appeared in more than four experiments. For easy reference, these 10 rocks are relabelled from “A” to “J”. The mapping between original and new labels can be seen in Table 6.3, where the experiment 0 denotes the initial experiment described in Section 6.1.

Table 6.3: Mapping between original and new labels

Exp	A	B	C	D	E	F	G	H	I	J
0	1	3	4	5	7	8	9	10	×	×
1	1	3	4	6	5	8	10	7	9	×
2	1	3	9	7	6	4	10	5	2	×
3	×	×	×	×	×	2	×	×	×	×
4	1	3	11	×	8	4	9	5	2	7
5	7	×	11	9	8	×	6	5	2	4
6	5	3	8	×	9	12	7	6	×	4
7	×	6	8	×	7	2	3	9	5	4
8	×	4	×	6	×	2	×	×	3	5

The original rock labels are depended on images while the new labels are based on rocks. Through using the new labels, the output of different runs of experiments can be compared more directly. Here, we show the comparison between the calculated science values of different rocks and experiment runs in Table 6.4.

As can be seen in the table, the performance of science value evaluation is generally stable, in spite of some fluctuations. The average coefficient of variation of all experiments is 20.29%. One reason leading to the inconsistency could be the heterogeneity of rocks. The 2D projection of a 3D rock from different directions is

different, hence generating different science value evaluation scores. For example, the “C” rock, placing with different directions, showed layering structure in the 0, 1 and 7 experiment runs but did not show layering structure in the 2, 4, 5 and 6 runs. The output science values were therefore varied.

Table 6.4: Rock science value comparison between different experiment runs

Exp	A	B	C	D	E	F	G	H	I	J
0	46.8	100.5	102.3	132.0	78.4	54.4	49.7	92.6		
1	45.0	114.4	98.8	108.8	84.7	84.3	44.2	84.3	102.4	
2	45.4	111.0	62.3	130.7	78.9	83.9	44.4	78.9	137.0	
3						77.4				
4	112.3	136.2	49.5		70.2	62.9	45.2	104.1	136.2	63.4
5	112.8		50.0	130.6	73.4		62.8	95.2	136.7	75.9
6	91.2	117.1	53.4		46.6	96.9	45.0	69.6		59.9
7		122.1	96.7		46.8	106.5	66.3	70.3	132.9	48.7
8				130.3		105.4			133.4	53.8

6.3 Summary

In this chapter, the three parts of the proposed system described in previous chapters were integrated together. In addition, the experimental environment was established in which experiments have been conducted to demonstrate how the whole system works. Due to the lack of mobility, this system cannot reach rocks out of the workspace of the robotic arm. However, the limited experimental results can also show that the proposed system owns good autonomy, stability and repeatability. It is relatively reliable to complete autonomous rock analysis missions.

Chapter 7

Conclusion

This chapter presents a high level summary of the research as detailed in the preceding chapters. A number of thoughts about the directions for future research are also presented.

7.1 Summary of the thesis

A major mission driver for space exploration is to minimise ground(Earth)-based human intervention and hence associated operations costs, thereby maximising science data return. In terms of rover-based exploration, greater autonomy becomes an essential requirement. Previous autonomous systems such as OASIS, AEGIS and ASTIA, which were discussed in Chapter 1, have clearly exhibited the benefits of planetary autonomy.

In this thesis, a new autonomous system named *Autonomous Rock Science Analysis System* (ARSAS) was derived from ASTIA (an autonomous system for rock identification and acquisition). Like other classical autonomous systems, ARSAS consists of three components: rock detection, rock science value evaluation and corresponding executive agents. In each component, a number of new techniques have been introduced.

In terms of the rock detection component, three methods were presented. The first method refers to multispectral data. A fuzzy-rough feature selection method has been used to select the multispectral features which can reflect the difference between rocks and regolith (background). Then, classifiers¹ were trained using the

¹A clustering method was also mentioned.

selected features. Through the trained classifiers, rock regions could be identified in images. The second method is based on two-threshold thresholding. This method addresses grayscale images, the most common image type acquired in real Mars exploration¹. Several thresholding algorithms were presented. Some algorithms were derived from the traditional OTSU method (TO, RTO1, RTO2 and TFO) and some algorithms were based on other information of the shape of image histograms (PR, ND and DP). All algorithms were tested on real Mars images and laboratory images, and corresponding detection results were compared both qualitatively and quantitatively. The third method was inspired by saliency concepts, trying to detect rock regions in a bottom-up way. Five existing saliency algorithms were tested on MER, *McMurdo* and laboratory images, attempting to point out the conspicuous targets in them.

In terms of the performance evaluation of the presented algorithms, since part of the image data lacks labeled ground truth, quantitative comparisons have not been fully provided. However, through inspection, the performance of multispectral classification algorithms is generally good. The rock detection results are less affected by the soil dust covering the surface of rocks. Shadow regions can be also detected more correctly. The reason for the better detection performance could be due to the supervised mechanisms of these algorithms. The labeled ground truth is used to select efficient features which can increase the distance between rocks and regolith. Hence good classifiers can be trained using these features, by which the rock regions can therefore be detected more accurately. As for the two-threshold thresholding algorithms, although they did not obtain results as good as the multispectral classification methods, they generally obtained detection results better than those of traditional one-threshold algorithms when dealing with the Mars images. Particularly, in the experimental results of the MER data, the F_1 coefficient of the PR algorithm was 0.682 while the traditional OTSU algorithm only attained 0.501. With respect to saliency algorithms, we found that they not only can detect novel objects but also can reflect the novelty level of detected objects. However, as a bottom-up method, the detection performance is relatively unstable. Non-rock regions were often detected. On the one hand, the detected non-rock regions may represent rare targets which hold extremely high science value. On the other hand, shadow regions which look locally different were often detected as interesting regions but have lower science values, weakening the overall performance of saliency algorithms. In addition, the boundaries of the rock regions detected by saliency

¹The multispectral data can also be regarded as a series of grayscale images in different channels.

algorithms were relatively vague. Hence, the saliency algorithms are more suitable for alerting to the emergence of novelty (rocks or other novel targets) rather than providing the precise regions for further analysis.

The component of rock science value evaluation is the kernel of the system. A methodology has been presented for bridging the gap between computer vision and geological representation. One hundred and three images were collected and labeled with rock regions from which 63 image visual features were extracted to reflect different characteristics of rocks. A geologist was invited to provide the ground truth of the abstract geological attributes *Relief*, *Angularity* and *Layering*. Correlation coefficients were used to reflect the consistency between the visual features and the geological attributes. For each geological attribute, the feature with the highest consistency was selected as its indicator. Thus, the density of SIFT corner Den_{SIFT} , the ratio of a rock's area to the square of its perimeter *Compactness* and the direction histogram sharpness of Canny-detected pixels SP_{Cpixel} were selected as the indicators of *Relief*, *Angularity* and *Layering* respectively. We found that the correlation between SP_{Cpixel} and *Layering* was 0.738, proving that this visual feature is highly consistent with the geological attribute. However, the correlation between *Compactness* and *Angularity* was only 0.391, implying it was not an ideal mapping. In addition, combination features were tried but did not obtain repeatable results.

Except for the three attributes mentioned above, the composition attributes of rocks such as hue and albedo were directly extracted from rock regions according to the suggestion of the geologist. Afterwards, a fuzzy system was established to convert the values of those geological attributes to overall rock science values. Compared to some previous science systems (e.g. OASIS) which use weighted summation to integrate the features (attributes), using a fuzzy system makes the science value evaluation more similar to that of real human geologists, especially in the case that several attributes are synergistic.

The executive agent mainly contains two parts: a camera agent and an arm agent, for simulating the partial structure of a real rover. In the camera agent, a pair of monochrome cameras was employed. Through the filters mounted in front of the cameras, colour images and multispectral data could be acquired. A simple method was presented to convert the rock positions in images to their positions in real world. Also, the kinematics of the arm was implemented, allowing the arm to access rocks. Although restricted, the executive agent can be regarded as a good platform to support the previous two components and hence can be used to test

and demonstrate the usefulness of the system.

Finally, demonstrating experiments have been carried out, exhibiting the procedure of the whole system: capturing images, detecting rock regions, extracting attributes, calculating science values, choosing the rock target with the highest science value and finally using the robotic arm to access it. In the experiment, the system showed good autonomous and automatic capabilities. It is adequate to execute a mission for identifying and accessing rocks with high science value adaptively and hence reaches the E3 autonomy level (Table 1.5).

7.2 Thesis contributions

In this thesis, an autonomous rock science analysis system for Mars exploration has been presented. A number of techniques have been proposed and introduced in the system, which can be regarded as the original contributions of this thesis. In particular, the contributions can be reflected in the following three aspects:

1. Presenting three kinds of novel rock detection methods which detect rocks using different information of rocks.
2. Proposing a geology-oriented mechanism for converting rock region information to rock science value. Specifically, a mapping procedure has been introduced, bridging the gap between visual features and rock attributes.
3. Building a practicable experimental platform and developing corresponding coordinate transformation algorithms, linking the software and hardware systems together. Hence, demonstration and more complicated experiments can be conducted.

7.3 Future work

Although promising, much can be done to further improve the work presented in this thesis. The following addresses a number of interesting issues whose successful solution would help strengthen the current research. The issues are divided into two parts: one part discusses relatively big directions; the other part deals with detailed problems in specific aspects.

7.3.1 Macro issues

Architecture of the system: As illustrated in Fig. 1.5, due to instrument limitations, only a pair of cameras and a robotic arm have been involved into our system. Although it is adequate to demonstrate the process of rock detection and science value evaluation, the planning and executing parts are very limited. Lacking moving components such as chassis and wheels, the system can only carry on experiments as a lander but not as a rover. In the future, adding moving mechanisms and other instruments into the executive agent will make the system more similar to a real rover.

Standard dataset¹: In contrast to other mature research domains in computer science (e.g. medical imaging, face recognition, etc.), developing AI techniques for Mars exploration is a relatively niche domain. Hence, as far as the author knows, there is no public standard dataset for rock detection and rock science value evaluation. Hence, when someone needs to do related research, it is necessary to spend a large amount of time to collect data and label ground truth. Especially in the cases referring to expertise (e.g. geological knowledge), more time is needed for studying related knowledge or communicating with domain experts. Such a research procedure is very inefficient. In addition, although working for similar objectives, different researchers will use different data sets. This inconsistency leads to another problem that the results of different works cannot be directly compared. If a performance comparison needs to be done between a new algorithm and an existing algorithm, it is necessary to re-implement the corresponding algorithm. Even so, the comparison results cannot be generalised to other works. Such an incomparability makes the conclusions presented in this domain sound less reliable. Particularly, in this thesis, with respect to the autonomous science evaluation, a database of geological attributes was presented. Through further extension and amendment, it could become a standard dataset for rock science value evaluation. And in the future, we are looking forward to establishing more standard datasets which can facilitate the research in this domain.

Running speed: The running speed of an algorithm is a very important indicator to evaluate its performance. Particularly in a real rover environment where the power and computing ability of an on-board computer are very limited, the speed

¹A so-called standard dataset means a dataset especially established for related experiments. A standard dataset must contain labeled data, providing expert ground truth, which can be used to objectively compare the performance of various methods.

of algorithms is extremely important. In the thesis, the speed issue has been rarely mentioned since most algorithms have not been optimised specifically and the algorithms were programmed and compiled under different environments (e.g. C++, Java and Matlab). On the other hand, even if all algorithms had been optimised, there is a tendency that a more complicated algorithm will have both better performance and more running time. Hence, how to choose an index¹ which can evaluate the performance and running speed of an algorithm comprehensively is an issue that deserves to be discussed further.

Experimental environment: The experiments were carried out in a laboratory environment which is obviously different from a Mars environment². The differences mainly rest in the terrain background (red regolith vs gray table surface) and light source (sun light vs luminescence light). In the future, more reliable results could be expected if the experiments were carried out in field environments, especially those sites whose landscapes look like Mars such as Tenerife island and Atacama desert.

7.3.2 Micro issues

Rock region ground truth: With regard to rock detection, the ground truths of rock regions are labeled by the author. However, as the boundaries between rock and regolith regions were relatively vague, the ground truth provided by geologists would be preferable.

More multispectral features: In this thesis, for convenience, only the multispectral data of the left camera was used. If registration techniques are applied, the multispectral information of both left and right cameras can be used together thereby increasing the amount of raw data. In addition, the features used in this thesis are all based on single pixel position. In future work, introducing more features from the relations between pixels (e.g. standard deviation of 8-connected neighborhoods [Shang and Barnes, 2013]) may generate better features to reflect the difference between rocks and regolith, hence improving the performance of rock detection.

Other feature selection methods: Only one feature selection method (i.e. the

¹A simple example index in rock detection could be $\frac{Precision}{RunningTime}$.

²This also leads to the problem that some algorithms work well for Mars rock images but work badly in the experimental environment.

fuzzy-rough feature selection method based on fuzzy similarity [Jensen and Shen, 2009]) was mentioned. Although the method achieved a good selection result, other feature selection methods [Diao, 2014] could provide more efficient selections.

Saliency method improvement: Only five off-the-shelf saliency methods have been tested and none of them has been optimised for Mars application. It is supposed that a saliency method specifically developed for the Mars environment could identify rocks and novelty targets more effectively and efficiently.

Rock detection method combination: As mentioned, rocks can be identified either top-down or bottom-up. Top-down methods can identify rocks according to prior knowledge but may overlook some novel rocks. Bottom-up methods can detect different rocks but may misfocus on wrong targets such as shadows. Combining these two ways together, the shortcomings of each may be overcome, and hence better rock detection results could be expected.

More geological experts: Geologists play an important role in rock science value evaluation. In this research, a geologist who has worked on several Mars-related projects was invited to guide the processing of autonomous rock science value evaluation. However, although having a lot of experience, a geologist may provide uncertain information. It is hard to guarantee that all information provided by a geologist is correct. Hence, if more geologists are involved in the provision of geological knowledge, the experimental results could be more reliable. On the other hand, human geological evaluation is relatively subjective. If there is more than one expert, it is very important to develop some methods to aggregate their knowledge together, especially in the case where different experts hold conflicting opinions.

More geological attributes: This thesis used seven basic geological attributes to assess rock science value. However, the evaluation of rocks could use more attributes such as layering type and surface fabric. Increasing the number of geological attributes in the future will allow the system to perform more complicated evaluation. Correspondingly, the rule base of the fuzzy system would be extended.

More appropriate features for geology: Currently, in terms of the geological attribute *Angularity*, the highest correlation attained was only about 0.4, which means that all the presented visual features cannot represent this attribute very well. In the future, more visual features (e.g. 3D shape information) could be

used, hence allowing the possibility of finding features which can express geological attributes more appropriately.

Nonlinear feature combination method: In this thesis, combination features didn't achieve their expected performance. One of the reasons is that only linear combinations have been considered. It is possible to generate good combination features¹ through using nonlinear combination methods (e.g. neural network).

Geologist reevaluation: The mapping from visual features to geological attributes discussed in this thesis was mainly dependent on the correlation coefficients between the output values of visual algorithms and the attribute scores provided by a geological expert. However, the attribute scores may contain some uncertainties, introducing some bias into the performance evaluation of features. In the future, it is desirable to perform a geologist reevaluation. The reevaluation could judge the performance of visual algorithms more similarly to how the geologist's mind would, thereby selecting features which can represent geological knowledge more appropriately.

More complex kinematics: As mentioned, the robotic arm has seven degrees of freedom but only four of which have been used in inverse kinematics. In the future, the other three DOFs can be developed thereby endowing the arm with the ability to complete more flexible motions. Therefore, the arm would be more adaptive when encountering uncommon situations.

Rock grasping: The original aim of this thesis was to attempt building a system which can collect rock samples using a gripper-like actuator. However due to time limitations, the research of rock grasping has not been completed. Compared to the current rock acquisition approach—drilling [Zacny et al., 2011], using a gripper to acquire rock samples has several advantages. Firstly, it can deal with small rocks, which are hard to sample with a drill. Secondly, a grasping process need not damage the intactness of a rock. Lastly, if a rock has been held by the gripper, through moving the robotic arm, the cameras of the corresponding rover can observe the appearance of the rock from different viewpoints. Such a process is similar to the way that a real human geologist investigates an isolated rock. Hence, introducing a grasping mechanism into Mars exploration is a very promising direction in future research.

¹A good combination feature means that it can be generated through a fixed combination and can always represent a specified attribute accurately.

Appendix A

Science Value Evaluation Output of Integrated System Experiments

In Chapter 6, the science value output of repeatability experiments is illustrated by colour maps. To reflect the performance of science value evaluation stage in more detail, here we show the corresponding intermediate output of each experiment in Tables A.1 to A.16.

Table A.1: Attribute output of experiment I

Rock No.	<i>Layering</i>	<i>Lustre</i>	<i>Relief</i>	<i>Angularity</i>	<i>Hue</i>	<i>Saturation</i>	<i>Value</i>
1	0	0.14	6.94	3.87	11.67	0.54	0.24
2	0	0.21	6.89	5.18	45.01	0.17	0.21
3	7.26	0.17	6.91	4.5	55.59	0.09	0.16
4	5.11	0.16	6.89	4.86	48.98	0.1	0.13
5	4.07	0.2	6.7	4.76	21.62	0.39	0.28
6	6.79	0.16	6.86	5.06	221.29	0.09	0.12
7	3.94	0.19	6.53	4.38	35.47	0.22	0.24
8	4.16	0.17	6.91	4.02	39.15	0.22	0.17
9	5.18	0.23	6.88	4.38	45.12	0.08	0.17
10	0	0.14	6.89	4.89	27.4	0.35	0.17

Table A.2: Science value output of experiment I

Rock No.	$SV_{Structure}$	$SV_{Texture}$	$SV_{Composition}$	SV_{total}
1	3	24.93	17.12	45.05
2	3	24.2	22.9	50.1
3	61.05	24.66	28.66	114.37
4	47.75	24.04	27.05	98.84
5	41.35	24.42	18.89	84.66
6	57.73	23.79	27.23	108.75
7	40.43	24.69	19.2	84.32
8	41.97	25.23	18.26	85.46
9	48.16	25.31	28.89	102.36
10	3	23.83	17.37	44.2

Table A.3: Attribute output of experiment II

Rock No.	<i>Layering</i>	<i>Lustre</i>	<i>Relief</i>	<i>Angularity</i>	<i>Hue</i>	<i>Saturation</i>	<i>Value</i>
1	0	0.15	6.94	3.9	9.63	0.53	0.25
2	10	0.29	6.85	4.64	34.68	0.05	0.25
3	6.66	0.21	6.91	4.46	42.3	0.07	0.17
4	3.6	0.21	6.91	4.55	29.93	0.18	0.2
5	2.65	0.3	6.79	5.21	30.16	0.16	0.29
6	1.12	0.21	6.68	4.78	16.31	0.37	0.29
7	10	0.14	6.91	5.44	227.02	0.08	0.12
8	0.8	0.17	6.92	4.86	28.37	0.13	0.19
9	1.59	0.16	6.8	4.9	43.58	0.15	0.14
10	0	0.14	6.83	4.53	23.89	0.29	0.17

Table A.4: Science value output of experiment II

Rock No.	$SV_{Structure}$	$SV_{Texture}$	$SV_{Composition}$	SV_{total}
1	3	25.11	17.24	45.35
2	80	25.43	31.56	136.99
3	56.9	25.05	29.01	110.96
4	37.93	24.91	21.05	83.89
5	29.07	24.88	24.98	78.93
6	8.12	24.47	18.7	51.28
7	80	23.38	27.27	130.65
8	3	24.18	25.62	52.8
9	15.26	23.92	23.07	62.25
10	3	24.31	17.04	44.35

Table A.5: Attribute output of experiment III

Rock No.	<i>Layering</i>	<i>Lustre</i>	<i>Relief</i>	<i>Angularity</i>	<i>Hue</i>	<i>Saturation</i>	<i>Value</i>
1	3.42	0.24	6.91	4.55	47.38	0.15	0.21
2	3.15	0.17	6.91	4.5	41.97	0.22	0.18
3	2.07	0.17	6.93	4.79	9.4	0.35	0.22
4	4.27	0.11	6.91	5.63	44.6	0.13	0.15

Table A.6: Science value output of experiment III

Rock No.	$SV_{Structure}$	$SV_{Texture}$	$SV_{Composition}$	SV_{total}
1	36.5	25.17	24.61	86.29
2	34.17	24.65	18.61	77.43
3	21.14	24.28	16.51	61.92
4	42.63	22.99	25.12	90.75

Table A.7: Attribute output of experiment IV

Rock No.	<i>Layering</i>	<i>Lustre</i>	<i>Relief</i>	<i>Angularity</i>	<i>Hue</i>	<i>Saturation</i>	<i>Value</i>
1	8.28	0.14	6.94	4.17	11.92	0.53	0.25
2	10	0.28	6.92	4.83	67.83	0.05	0.23
3	6.6	0.21	6.9	4.62	55.58	0.07	0.17
4	1.41	0.22	6.9	4.63	43.35	0.14	0.18
5	6.49	0.23	6.67	4.64	42.2	0.17	0.24
6	1.27	0.42	6.83	4.87	35.07	0.21	0.43
7	1.84	0.29	6.65	4.68	32.73	0.22	0.31
8	2.49	0.2	6.81	5.25	21.85	0.43	0.29
9	0.61	0.16	6.65	4.22	26.68	0.26	0.18
10	0.39	0.16	6.92	4.92	40.63	0.13	0.17
11	0.59	0.15	6.8	5.06	49.37	0.16	0.14
12	1.81	0.19	6.74	4.48	3.7	0.09	0.17
13	6.22	0.16	6.94	5.22	56.11	0.04	0.13

Table A.8: Science value output of experiment IV

Rock No.	$SV_{Structure}$	$SV_{Texture}$	$SV_{Composition}$	SV_{total}
1	70.14	24.83	17.3	112.27
2	80	25.12	31.08	136.2
3	56.49	24.82	28.96	110.27
4	13.29	24.85	24.72	62.86
5	55.85	24.76	23.5	104.11
6	11.32	26.87	23.28	61.47
7	17.84	25.25	20.31	63.4
8	27.07	23.95	19.14	70.17
9	3	24.81	17.44	45.24
10	3	23.98	25.66	52.63
11	3	23.71	22.77	49.48
12	17.48	24.68	29.12	71.29
13	54.18	23.71	27.6	105.48

Table A.9: Attribute output of experiment V

Rock No.	<i>Layering</i>	<i>Lustre</i>	<i>Relief</i>	<i>Angularity</i>	<i>Hue</i>	<i>Saturation</i>	<i>Value</i>
1	3.22	0.16	6.94	4.03	3.4	0.1	0.14
2	10	0.28	6.88	4.48	63.58	0.05	0.23
3	0	0.2	6.89	4.97	55.37	0.08	0.17
4	2.78	0.29	6.78	4.91	32.48	0.23	0.31
5	5.2	0.23	6.67	4.64	40.01	0.18	0.25
6	2.04	0.16	6.83	4.22	23.86	0.25	0.18
7	9.37	0.14	6.89	4.02	9.78	0.51	0.24
8	2.83	0.14	6.76	4.66	19.62	0.39	0.26
9	10	0.16	6.88	5.39	222.96	0.09	0.12
10	10	0.22	6.94	4.06	346.87	0.1	0.19
11	0	0.16	6.84	4.98	52.87	0.15	0.13

Table A.10: Science value output of experiment V

Rock No.	$SV_{Structure}$	$SV_{Texture}$	$SV_{Composition}$	SV_{total}
1	34.8	25.11	27.75	87.66
2	80	25.52	31.13	136.65
3	3	24.26	29.06	56.32
4	30.53	25.08	20.32	75.94
5	48.27	24.81	22.16	95.23
6	20.69	24.93	17.21	62.83
7	80	24.88	16.91	121.78
8	31.07	24.07	18.27	73.41
9	80	23.52	27.07	130.59
10	80	25.75	29.6	135.35
11	3	23.86	23.2	50.05

Table A.11: Attribute output of experiment VI

Rock No.	<i>Layering</i>	<i>Lustre</i>	<i>Relief</i>	<i>Angularity</i>	<i>Hue</i>	<i>Saturation</i>	<i>Value</i>
1	3.01	0.16	6.94	4.01	6.1	0.1	0.14
2	10	0.16	6.94	4.61	201.93	0.03	0.14
3	7.74	0.18	6.84	5.5	73.23	0.04	0.16
4	1.49	0.29	6.64	4.42	33.27	0.22	0.29
5	5.38	0.15	6.89	4.14	9.7	0.5	0.24
6	1.45	0.29	6.8	4.18	36.18	0.2	0.26
7	0.1	0.17	6.71	4.2	21.06	0.27	0.18
8	0	0.17	6.73	5.21	48.98	0.11	0.14
9	0.67	0.24	6.78	4.94	19.1	0.38	0.29
10	4.88	0.46	6.8	4.89	30.82	0.22	0.42
11	1.72	0.16	6.94	4.71	6.42	0.09	0.15
12	6.2	0.2	6.94	4.9	40.97	0.22	0.17

Table A.12: Science value output of experiment VI

Rock No.	$SV_{Structure}$	$SV_{Texture}$	$SV_{Composition}$	SV_{total}
1	32.72	25.12	27.35	85.19
2	80	24.39	27.82	132.21
3	64.89	23.64	28.57	117.11
4	14.21	25.57	20.11	59.89
5	49.31	24.95	16.94	91.19
6	13.79	26.03	19.75	59.58
7	3	25	17.04	45.03
8	3	23.7	26.7	53.4
9	3	24.61	19.01	46.62
10	46.39	27.44	22.95	96.78
11	16.55	24.26	28.32	69.13
12	54.04	24.42	18.46	96.92

Table A.13: Attribute output of experiment VII

Rock No.	<i>Layering</i>	<i>Lustre</i>	<i>Relief</i>	<i>Angularity</i>	<i>Hue</i>	<i>Saturation</i>	<i>Value</i>
1	2.99	0.16	6.94	3.95	8.53	0.1	0.13
2	6.82	0.22	6.93	4.57	44.36	0.16	0.19
3	2.24	0.17	6.77	4.09	26.93	0.27	0.18
4	1.01	0.29	6.79	4.96	34.65	0.24	0.29
5	9.21	0.19	6.94	4.59	45.12	0.04	0.15
6	8.27	0.17	6.86	5.45	59	0.02	0.15
7	0.09	0.23	6.78	4.78	19.2	0.38	0.30
8	4.81	0.11	6.85	5.13	51.55	0.1	0.13
9	2.41	0.2	6.79	4.38	35.84	0.23	0.24
10	2.2	0.17	6.94	4.64	9.1	0.09	0.15

Table A.14: Science value output of experiment VII

Rock No.	$SV_{Structure}$	$SV_{Texture}$	$SV_{Composition}$	SV_{total}
1	32.72	25.15	27.71	85.58
2	57.9	24.94	23.68	106.51
3	23.67	25.1	17.54	66.31
4	3.53	25.04	20.09	48.66
5	80	24.67	28.26	132.94
6	70.05	23.6	28.45	122.1
7	3	24.71	19.06	46.77
8	45.99	23.31	27.4	96.69
9	26.07	25	19.27	70.34
10	23.17	24.47	28.28	75.92

Table A.15: Attribute output of experiment VIII

Rock No.	<i>Layering</i>	<i>Lustre</i>	<i>Relief</i>	<i>Angularity</i>	<i>Hue</i>	<i>Saturation</i>	<i>Value</i>
1	3	0.15	6.94	4.07	11.32	0.1	0.13
2	6.72	0.21	6.93	4.52	47.81	0.17	0.19
3	9.11	0.2	6.94	4.4	80.62	0.06	0.15
4	2.47	0.16	6.91	5.5	52.97	0.15	0.16
5	1.17	0.28	6.76	5.3	37.51	0.24	0.26
6	10	0.14	6.88	5.44	212.45	0.09	0.11
7	7.87	0.16	6.86	4.98	53.32	0.09	0.13
8	3.55	0.12	6.94	4.65	11.2	0.36	0.2
9	0.78	0.17	6.94	4.38	19.2	0.11	0.16

Table A.16: Science value output of experiment VIII

Rock No.	$SV_{Structure}$	$SV_{Texture}$	$SV_{Composition}$	SV_{total}
1	32.72	25.02	27.39	85.13
2	57.29	24.97	23.1	105.36
3	80	25.02	28.38	133.4
4	26.77	23.46	23.83	74.06
5	9.34	24.64	19.77	53.75
6	80	23.35	26.91	130.26
7	66.04	23.87	27.44	117.35
8	37.56	24.06	16.29	77.9
9	3	24.82	26.76	54.58

References

- J. Amos. Lost Beagle2 probe found “intact” on Mars, 2015. URL <http://www.bbc.co.uk/news/science-environment-30784886>. Last accessed Jan. 2015. 76
- R.B. Anderson and J.F. Bell. Correlating multispectral imaging and compositional data from the Mars exploration rovers and implications for Mars science laboratory. *Icarus*, 223(1):157 – 180, 2013. ISSN 1019-1035. 37, 48
- P. Backes, A. Diaz-Calderon, M. Robinson, M. Bajracharya, and D. Helmick. Automated rover positioning and instrument placement. In *Aerospace Conference, 2005 IEEE*, pages 60–71, March 2005. 15
- D. Barnes, M. Grande, L. Tyler, and A. Cook. The europlanet ri transnation access planetary analogue terrain laboratory (PATLab). *European Planetary Science Congress, EPSC*, 3, 2008. 68, 105
- D. Barnes, S. Pugh, and L. Tyler. Autonomous science target identification and acquisition (ASTIA) for planetary exploration. In *Intelligent Robots and Systems, 2009. IROS 2009. IEEE/RSJ International Conference on*, pages 3329–3335, October 2009. 16, 26, 27, 28, 88, 140
- D. Barnes, M.C. Wilding, M. Gunn, S. Pugh, L. Tyler, A.J. Coates, A.D. Griffiths, C.R. Cousins, N. Schmitz, A. Bauer, and G. Paar. Multi-Spectral Vision Processing for the ExoMars 2018 Mission. In *Proceedings of 11th Symposium on Advanced Space Technologies in Robotic and Automation (ASTRA)*, 2011. 38, 69, 165
- D.L. Bekker, D.R. Thompson, W.J. Abbey, N.A. Cabrol, R. Francis, K.S. Manatt, K.F. Ortega, and K.L. Wagstaff. Field Demonstration of an Instrument Performing Automatic Classification of Geologic Surfaces. *Astrobiology*, 14:486–501, June 2014. 14
- J.F. Bell, S.W. Squyres, K.E. Herkenhoff, J.N. Maki, H.M. Arneson, D. Brown, S.A. Collins, A. Dingizian, S.T. Elliot, E.C. Hagerott, A.G. Hayes, M.J. Johnson, J.R.

- Johnson, J. Joseph, K. Kinch, M.T. Lemmon, R.V. Morris, L. Scherr, M. Schwochert, M.K. Shepard, G.H. Smith, J.N. Sohl-Dickstein, R.J. Sullivan, W.T. Sullivan, and M. Wadsworth. Mars exploration rover athena panoramic camera (Pancam) investigation. *Journal of Geophysical Research: Planets*, 108(E12), 2003. [32](#)
- J.F. Bell, S.W. Squyres, R.E. Arvidson, H.M. Arneson, D. Bass, D. Blaney, N. Cabrol, W. Calvin, J. Farmer, W.H. Farrand, W. Goetz, M. Golombek, J.A. Grant, R. Greeley, E. Guinness, A.G. Hayes, M.Y. H. Hubbard, K.E. Herkenhoff M.J. Johnson, J.R. Johnson, J. Joseph, K.M. Kinch, M.T. Lemmon, R. Li, M.B. Madsen, J.N. Maki, M. Malin, E. McCartney, S. McLennan, H.Y. McSween Jr., D.W. Ming, R.V. Morris J.E. Moersch, E.Z. Noe Dobrea, T. J. Parker, J. Proton, J.W Rice Jr., F. Seelos, J. Soderblom, L.A. Soderblom, J.N. Sohl-Dickstein, R.J. Sullivan, M.J. Wolff, and A. Wang. Pancam multispectral imaging results from the Spirit rover at Gusev crater. *Science*, 305(5685):800–806, 2004. [34](#)
- J.F. Bell, J. Joseph, J.N. Sohl-Dickstein, H.M. Arneson, M.J. Johnson, M.T. Lemmon, and D. Savransky. In-flight calibration and performance of the Mars exploration rover panoramic camera (Pancam) instruments. *Journal of Geophysical Research: Planets*, 111(E2), 2006. [36](#)
- J.F. Bell, M.C. Malin, M.A. Caplinger, M.A. Ravine, A.S. Godber, M.C. Jungers, M.S. Rice, and R.B. Anderson. Mastcam multispectral imaging on the Mars science laboratory rover: Wavelength coverage and imaging strategies at the Gale Crater field site. In *Lunar and Planetary Science Conference*, volume 43, March 2012. [32](#)
- G. Bianciardi, J.D. Miller, P.A. Straat, and G.V. Levin. Complexity analysis of the Viking labeled release experiments. *IJASS*, 13(1):14–26, 2012. [4](#)
- K. Biemann and J.L. Bada. Comment on “Reanalysis of the Viking results suggests perchlorate and organics at midlatitudes on Mars” by Rafael Navarro-Gonzalez et al. *Journal of Geophysical Research: Planets*, 116(E12), 2011. [4](#)
- J.J. Biesiadecki and M.W. Maimone. The Mars exploration rover surface mobility flight software driving ambition. In *Aerospace Conference, 2006 IEEE*, 2006. [14](#)
- C.A. Brooks and K.D. Iagnemma. Self-supervised classification for planetary rover terrain sensing. In *Aerospace Conference, 2007 IEEE*, pages 1–9, March 2007. [14](#)
- L.D.C Cadapan. Autonomous rock acquisition for a microrover to be used in planetary exploration. Master’s thesis, Massachusetts Institute of Technology, 1997. [15](#)
- J. Canny. A computational approach to edge detection. *Pattern Analysis and Machine Intelligence, IEEE Transactions on*, PAMI-8(6):679–698, November 1986. [22](#), [90](#)

- J. Carsten, A. Rankin, D. Ferguson, and A. Stentz. Global path planning on-board the Mars exploration rovers. In *IEEE Aerospace Conference*, 2007. 14
- A. Castano, R.C. Anderson, R. Castano, T. Estlin, and M. Judd. Intensity-based rock detection for acquiring onboard rover science. In *35th Lunar and Planetary Science Conference*, March 2004. 30
- R. Castano, T. Mann, and E. Mjolsness. Texture analysis for Mars rover images. In *Applications of Digital Image Processing XXII, Proc. SPIE*, pages 162–173, 1999. 20, 31, 96
- R. Castano, R.C. Anderson, T. Estlin, D. DeCoste, F. Fisher, D. Gains, D. Mazzoni, and M. Judd. Rover traverse science for increased mission science return. In *IEEE Aerospace Conference Proceedings*, March 2003. 81, 88
- R. Castano, M. Judd, T. Estlin, R.C. Anderson, D. Gaines, A. Castano, B. Bornstein, T. Stough, and K. Wagstaff. Current results from a rover science data analysis system. In *Proceedings of the IEEE Aerospace Conference*, 2005. 21
- R. Castano, T. Estlin, R.C. Anderson, D. Gaines, A. Castano, B. Bornstein, C. Chouinard, and M. Judd. OASIS: Onboard autonomous science investigation system for opportunistic rover science. *Journal of Field Robotics*, 24(5):379–397, 2007a. 14, 19, 31, 81
- R. Castano, T. Estlin, D. Gaines, C. Chouinard, B. Bomstein, R.C. Anderson, M. Burl, D. Thompson, A. Castano, and M. Judd. Onboard autonomous rover science. In *Proc. of Aerospace Conference, 2007 IEEE*, pages 1–13, march 2007b. 19, 81
- Y. Cheng, A. Johnson, and L. Matthies. MER-DIMES: a planetary landing application of computer vision. In *Computer Vision and Pattern Recognition, 2005. CVPR 2005. IEEE Computer Society Conference on*, volume 1, pages 806–813, June 2005. 13
- R.C. Crida and G. De Jager. Rock recognition using feature classification. In *Communications and Signal Processing, 1994. COMSIG-94., Proceedings of the 1994 IEEE South African Symposium on*, pages 152–157, Oct 1994. 30
- J.A. Crisp, M. Adler, J.R. Matijevic, S.W. Squyres, R.E. Arvidson, and D.M. Kass. Mars exploration rover mission. *Journal of Geophysical Research: Planets*, 108(E12), 2003. ISSN 2156-2202. 8
- M. Dash and H. Liu. Feature selection for classification. *Intelligent Data Analysis*, 1: 131–156, 1997. 39

- K. Di, Z. Yue, Z. Liu, and S. Wang. Automated rock detection and shape analysis from Mars rover imagery and 3D point cloud data. *Journal of Earth Science*, 24(1): 125–135, 2013. [31](#), [81](#), [86](#), [88](#)
- R. Diao. *Feature Selection with Harmony Search and its Applications*. PhD thesis, Aberystwyth University, February 2014. [186](#)
- H. Dunlop. Automatic rock detection and classification in natural scenes. Master’s thesis, Carnegie Mellon University, 2006. [14](#)
- H. Dunlop, D.R. Thompson, and D. Wettergreen. Multi-scale features for detection and segmentation of rocks in Mars images. In *Computer Vision and Pattern Recognition, 2007. CVPR ’07. IEEE Conference on*, pages 1–7, 2007. [31](#)
- T. Estlin, D. Gaines, C. Chouinard, R. Castano, B. Bornstein, M. Judd, I. Nesnas, and R. Anderson. Increased Mars rover autonomy using AI planning, scheduling and execution. In *Proceedings of the IEEE International Conference on Robotics and Automation (ICRA 2007)*, 2007. [20](#)
- T. Estlin, R. Castano, B. Bornstein, D. Gaines, R.C. Anderson, C. de Granville, D. Thompson, M. Burl, M. Judd, and S. Chien. Automated targeting for the MER rovers. In *Space Mission Challenges for Information Technology, 2009. SMC-IT 2009. Third IEEE International Conference*, pages 257–263, July 2009. [21](#), [22](#), [31](#), [81](#), [86](#)
- T. Estlin, B.J. Bornstein, D. Gaines, R.C. Anderson, D.R. Thompson, M. Burl, R. Castano, and M. Judd. AEGIS automated science targeting for the MER opportunity rover. *ACM Trans. Intell. Syst. Technol.*, 3(3), May 2012. [21](#), [81](#), [84](#)
- T. Estlin, D. Gaines, B. Bornstein, S. Schaffer, V. Tompkins, D.R. Thompson, A. Altinok, R.C. Anderson, M. Burl, R. Castano, D. Blaney, L. De Flores, T. Nelson, and R. Wiens. Automated targeting for the MSL rover ChemCam spectrometer. In *International Symposium on Artificial Intelligence, Robotics and Automation in Space (i-SAIRAS) 2014*, 2014. [21](#)
- C. Farfán, R.A. Salinas, and G. Cifuentes. Rock segmentation and measures on gray level images using watershed for sizing distribution in particle systems. In *International Conference on System Engineering, Communications and Information Technologies*, 2001. [31](#)
- W. Fink, A Datta, J.M. Dohm, M.A Tarbell, F.M. Jobling, R. Furfaro, J.S. Kargel, D. Schulze-Makuch, and V.R. Baker. Automated global feature analyzer - a driver for tier-scalable reconnaissance. In *Aerospace Conference, 2008 IEEE*, pages 1–12, March 2008. [31](#), [81](#), [90](#), [96](#)

- A Fitzgibbon, M. Pilu, and R.B. Fisher. Direct least square fitting of ellipses. *Pattern Analysis and Machine Intelligence, IEEE Transactions on*, 21(5):476–480, May 1999. 88
- J. Fox, R. Castano, and R.C. Anderson. Onboard autonomous rock shape analysis for Mars rovers. In *Aerospace Conference Proceedings, 2002. IEEE*, volume 5, pages 5–2052 vol.5, 2002. 21, 88
- P.R. Gazis and T. Roush. Autonomous identification of carbonates using near-IR reflectance spectra during the February 1999 Marsokhod field tests. *Journal of Geophysical Research: Planets*, 106(E4):7765–7773, 2001. 14
- M.S. Gilmore, R. Castano, T. Mann, R.C. Anderson, E.D. Mjolsness, R. Manduchi, and R.S. Saunders. Strategies for autonomous rovers at mars. *Journal of Geophysical Research*, 2000. 32
- S. Goferman, L. Zelnik-manor, and A. Tal. Context-aware saliency detection. In *IEEE Conf. on Computer Vision and Pattern Recognition*, 2010. 66
- S.B. Goldberg, M.W. Maimone, and L. Matthies. Stereo vision and rover navigation software for planetary exploration. In *Aerospace Conference Proceedings, 2002. IEEE*, volume 5, pages 2025–2036, 2002. 14
- X. Gong and J. Liu. Rock detection via superpixel graph cuts. In *Image Processing (ICIP), 2012 19th IEEE International Conference on*, pages 2149–2152, Sept 2012. 31
- V. Gor, R. Castano, R. Manduchi, R.C. Anderson, and E. Mjolsness. Autonomous rock detection for Mars terrain. In *Proceedings of AIAA Space*, Albuquerque, NM, 2001. 30, 31
- A.D. Griffiths, A.J. Coates, R. Jaumann, H. Michaelis, G. Paar, D. Barnes, and J. Josset. Context for the ESA ExoMars rover: the panoramic camera (PanCam) instrument. *International Journal of Astrobiology*, 5:269–275, 7 2006. 32
- J.P. Grotzinger, J. Crisp, A.R. Vasavada, R.C. Anderson, C.J. Baker, R. Barry, D.F. Blake, P. Conrad, K.S. Edgett, B. Ferdowski, R. Gellert, J.B. Gilbert, M. Golombek, J. Gmez-Elvira, D.M. Hassler, L. Jandura, M. Litvak, P. Mahaffy, J. Maki, M. Meyer, M.C. Malin, I. Mitrofanov, J.J. Simmonds, D. Vaniman, R.V. Welch, and R.C. Wiens. Mars science laboratory mission and science investigation. *Space Science Reviews*, 170 (1-4):5–56, 2012. ISSN 0038-6308. 8

- C. Gui. *Autonomous Science Target Detection and Touchability Assessment for Planetary Exploration*. PhD thesis, Aberystwyth University, 2015. [31](#)
- C. Gui, D. Barnes, and L. Pan. An approach for matching desired non-feature points on Mars rock targets based on SIFT. In *Towards Autonomous Robotic Systems (TAROS)*, 2012. [31](#)
- C. Gui, D. Barnes, and L. Pan. Planetary exploration autonomous science target touchability evaluation using a fuzzy rule-based approach. In *the 12th ESA Workshop on Advanced Space Technologies for Robotics and Automation (ASTRA)*, 2013. [15](#)
- V.C. Gulick, R.L. Morris, M.A. Ruzon, and T.L. Roush. Autonomous image analyses during the 1999 Marsokhod rover field test. *Journal of Geophysical Research: Planets*, 106(4):7745–7763, 2001. [14](#), [31](#), [90](#), [91](#), [93](#)
- M. Gunn. *Spectral imaging for Mars exploration*. PhD thesis, Aberystwyth University, 2013. [143](#)
- R.M. Haralick, K. Shanmugam, and I. Dinstein. Textural features for image classification. *Systems, Man and Cybernetics, IEEE Transactions on*, SMC-3(6):610–621, Nov 1973. [101](#)
- J. Harel, C. Koch, and P. Perona. Graph-based visual saliency. In *ADVANCES IN NEURAL INFORMATION PROCESSING SYSTEMS 19*, pages 545–552. MIT Press, 2007. [66](#)
- C.G. Harris and M.J. Stephens. A combined corner and edge detector. In *In Proceedings of Fourth Alvey Vision Conference*, pages 147–151, 1988. [100](#)
- D. Helmick, S. McCloskey, A. Okon, J. Carsten, W. Kim, and C. Leger. Mars science laboratory algorithms and flight software for autonomously drilling rocks. *Journal of Field Robotics*, 30(6):847–874, 2013. [15](#)
- X. Hou and L. Zhang. Saliency detection: A spectral residual approach. In *Computer Vision and Pattern Recognition, 2007. CVPR '07. IEEE Conference on*, pages 1–8, June 2007. [66](#)
- X. Hou, J. Harel, and C. Koch. Image signature: Highlighting sparse salient regions. *Pattern Analysis and Machine Intelligence, IEEE Transactions on*, 34(1):194–201, Jan 2012. [66](#)
- P.V.C. Hough. Method and means for recognizing complex patterns, U.S. Patent 3069654, December 1962. [94](#)

- M.K. Hu. Visual pattern recognition by moment invariants. *Information Theory, IRE Transactions on*, 8(2):179–187, February 1962. 90
- T. Huntsberger, Y. Cheng, A. Stroupe, and H. Aghazarian. Closed loop control for autonomous approach and placement of science instruments by planetary rovers. In *Proc. of IEEE/RSJ International Conference on Intelligent Robots and Systems*, volume numer WPII-13 in Planetary Rover, 2005. 15
- L. Itti and C. Koch. A saliency-based search mechanism for overt and covert shifts of visual attention. *Vision Research*, 40:1489–1506, 2000. 67
- L. Itti, C. Koch, and E. Niebur. A model of saliency-based visual attention for rapid scene analysis. *IEEE Trans. Pattern Anal. Mach. Intell.*, 20(11):1254–1259, November 1998. 66
- R. Jensen and Q. Shen. *Computational Intelligence and Feature Selection: Rough and Fuzzy Approaches*. IEEE Press and Wiley, 2008. 39
- R. Jensen and Q. Shen. New approaches to fuzzy-rough feature selection. *Fuzzy Systems, IEEE Transactions on*, 17(4):824–838, Aug 2009. 39, 186
- T. Kachanuban and S. Udomhunsakul. Natural rock images classification using spatial frequency measurement. In *Intelligent and Advanced Systems, 2007. ICIAS 2007. International Conference on*, pages 815 –818, nov. 2007. 31
- J.S. Kargel. *Mars - A Warmer, Wetter Planet*. Springer and Praxis, 2004. 5
- W.S. Kim, I.A. Nesnas, M. Bajracharya, R. Madison, A.I. Ansar, R.D. Steele, J.J. Biesiadecki, and K.S. Ali. Targeted driving using visual tracking on Mars: From research to flight. *Journal of Field Robotics*, 26(3):243–263, 2009. 15
- H.P. Klein. The Viking biological experiments on Mars. *Icarus*, 34:666–674, 1978. 4
- L. Lepistö, I. Kunttu, and A. Visa. Color-based classification of natural rock images using classifier combinations. In *Proceedings of the 14th Scandinavian conference on Image Analysis*, pages 901–909, Berlin, Heidelberg, 2005. 32
- L. Lepistö, I. Kunttu, J. Autio, and A. Visa. Rock image classification using non-homogenous textures and spectral imaging. In *Spectral Imaging, WSCG SHORT PAPERS proceedings, WSCG 2003, Plzen, Czech Republic*, 2003a. 31
- L. Lepistö, I. Kunttu, J. Autio, and A. Visa. Classification method for colored natural textures using gabor filtering. In *Proceedings of the 12th International Conference on Image Analysis and Processing*, pages 397–401, 2003b. 31

- L. Lepistö, I. Kunttu, and A. Visa. Rock image classification based on k-nearest neighbour voting. *Vision, Image and Signal Processing, IEEE Proceedings of*, 153(4):475 – 482, August 2006. 31
- R. Li, K. Di, A.B. Howard, L. Matthies, J. Wang, and S. Agarwal. Rock modeling and matching for autonomous long-range Mars rover localization. *Journal of Field Robotics*, 24(3):187–203, 2007. 31
- P.S Liao, T.S Chen, and P.C Chung. A fast algorithm for multilevel thresholding. *Journal of Information Science and Engineering*, 17:713–727, 2001. 49, 51
- D.G. Lowe. Distinctive image features from scale-invariant keypoints. *International Journal of Computer Vision*, 60(2):91–110, 2004. 100
- P.R. Mahaffy, C.R. Webster, S.K. Atreya, H. Franz, M. Wong, P.G. Conrad, D. Harpold, J.J. Jones, L.A. Leshin, H. Manning, T. Owen, R.O. Pepin, S. Squyres, M. Trainer, and MSL Science Team. Abundance and isotopic composition of gases in the Martian atmosphere from the Curiosity rover. *Science*, 341(6143):263–266, 2013. 8
- M.W. Maimone, I.A. Nesnas, and H. Das. Autonomous rock tracking and acquisition from a Mars rover. In *Proc. of iSAIRAS*, page 99, 1999. 15
- M.W. Maimone, P.C. Leger, and J.J. Biesiadecki. Overview of the mars exploration rovers autonomous mobility and vision capabilities. In *IEEE International Conference on Robotics and Automation (ICRA)*, 2007. 13
- MEPAG. Science priorities for mars sample return. *ASTROBIOLOGY*, 8(3), March 2008. 14, 15
- T.M. Mitchell. *Machine Learning*. McGraw-Hill, Inc., New York, NY, USA, 1997. 40
- S. Mkwelo. A machine vision-based approach to measuring the size distribution of rocks on a conveyor belt. Master’s thesis, University of Cape Town, May 2004. 31
- NASA. Mars Science Laboratory: Mission objectives, 2015a. URL <http://mars.nasa.gov/msl/mission/science/objectives/>. Last accessed March 2015. 7
- NASA. Mars exploration rovers objectives, 2015b. URL <http://mars.nasa.gov/mer/science/objectives.html>. Last accessed March 2015. 5
- R. Navarro-Gonzalez, E. Vargas, J. de la Rosa, A.C. Raga, and C.P. McKay. Reanalysis of the Viking results suggests perchlorate and organics at midlatitudes on Mars. *J. Geophys. Res.*, 115(E1), 2010. 4

- S. Niekum. Reliable rock detection and classification for autonomous science. Honor Bachelor Thesis, Carnegie Mellon University, 2005. [31](#), [32](#)
- N. Otsu. *IEEE Transactions on Systems, Man and Cybernetics*, 9(1):62–66. [49](#)
- G. Paar, M. Woods, C. Gimkiewicz, F. Labrosse, A. Medina, L. Tyler, D. Barnes, G. Fritz, and K. Kapellos. PRoViScout: a planetary scouting rover demonstrator. *Proc. SPIE*, 8301:83010A–83010A–14, 2012. [105](#)
- L. Pan, C. Gui, D. Barnes, and C. Shang. Mars multispectral image classification using machine learning techniques. In *12th Symposium on Advanced Space Technologies in Automation and Robotics*, 2013. [31](#)
- M. Partio, B.n Cramariuc, M. Gabbouj, and A Visa. Rock texture retrieval using gray level co-occurrence matrix. *Entropy*, 75:8–14, 2002. [31](#)
- L. Pedersen. *Robotic Rock Classification and Autonomous Exploration*. PhD thesis, Carnegie Mellon University, November 2000. [14](#), [31](#), [32](#), [85](#), [87](#), [90](#)
- L. Pedersen. Science target assessment for mars rover instrument deployment. In *IEEE/RSJ International Conference on Intelligent Robots and Systems (IROS)*, pages 200–2, 2002. [31](#)
- L. Pedersen, D.E. Smith, M. Deans, R. Sargent, C. Kunz, D. Lees, and S. Rajagopalan. Mission planning and target tracking for autonomous instrument placement. In *Aerospace Conference, 2005 IEEE*, pages 34–51, March 2005. [15](#)
- J.C. Platt. Sequential minimal optimization: A fast algorithm for training support vector machines. Technical report, ADVANCES IN KERNEL METHODS - SUPPORT VECTOR LEARNING, 1998. [40](#)
- R. Prakash, P.D. Burkhart, A. Chen, K.A. Comeaux, C.S. Guernsey, D.M. Kipp, L.V. Lorenzoni, G.F. Mendeck, R.W. Powell, T.P. Rivellini, A.M. San Martin, S.W. Sell, A.D. Steltzner, and D.W. Way. Mars Science Laboratory entry, descent, and landing system overview. In *Aerospace Conference, 2008 IEEE*, pages 1–18, March 2008. [14](#)
- S. Pugh. *Autonomous Science For Future Planetary Exploration Operations*. PhD thesis, Aberystwyth University, 2010. [24](#), [25](#), [29](#), [70](#), [81](#), [127](#), [128](#), [135](#)
- S. Pugh, D. Barnes, D. Pullan, and L. Tyler. Knowledge based Science Target Identification System (KSTIS). In *The 10th International Symposium on Artificial Intelligence Robotics and Automation in Space*, 2010a. [27](#), [28](#), [31](#), [81](#), [128](#)

- S. Pugh, L. Tyler, and D. Barnes. Automatic pointing and image capture (APIC) for ExoMars type mission. In *The 10th International Symposium on Artificial Intelligence Robotics and Automation in Space*, 2010b. [23](#)
- S. Pugh, D. Barnes, L. Tyler, M. Gunn, N. Schmitz, G. Paar, A. Bauer, C. Cousins, D. Pullan, A. Coates, and A. Griffiths. AUPE: A PanCam emulator for the ExoMars mission. In *Proc. of 11th International Symposium on Artificial Intelligence, Robotics and Automation in Space (i-SAIRAS)*, 2012. [58](#), [141](#)
- D. Pullan. Scientific autonomy for planetary rover. Technique Report, Department of Physics and Astronomy, University of Leicester, 2006. [24](#), [127](#), [135](#)
- D. Pullan. *Analogue Studies for In Situ Surface Planetary Exploration*. PhD thesis, University of Leicester, July 2008. [81](#), [94](#)
- R.J. Reid, P.H. Smith, M. Lemmon, R. Tanner, M. Burkland, E. Wegryn, J. Weinberg, R. Marcialis, D.T. Britt, N. Thomas, R. Kramm, A. Dummel, D. Crowe, B.J. Bos, J.F. Bell, P. Rueffer, F. Gliem, J.R. Johnson, J.N. Maki, K.E. Herkenhoff, and R.B. Singer. Imager for Mars Pathfinder (IMP) image calibration. *Journal of Geophysical Research: Planets*, 104(E4):8907–8925, 1999. [36](#)
- R. Rieder, R. Gellert, J. Brckner, G. Klingelhöfer, G. Dreibus, A. Yen, and S.W. Squyres. The new athena alpha particle X-ray spectrometer for the Mars exploration rovers. *Journal of Geophysical Research: Planets*, 108(E12), 2003. [8](#)
- T.L. Roush. Essential autonomous science inference on rovers (EASIR). In *Aerospace Conference, 2004. Proceedings. 2004 IEEE*, volume 2, pages 790–800 Vol.2, March 2004. [90](#), [94](#)
- C. Shang and D. Barnes. Combining support vector machines and information gain ranking for classification of mars McMurdo panorama images. In *Image Processing (ICIP), 2010 17th IEEE International Conference on*, pages 1061–1064, 2010. [32](#)
- C. Shang and D. Barnes. Fuzzy-rough feature selection aided support vector machines for Mars image classification. *Computer Vision and Image Understanding*, 117(3):202–213, 2013. ISSN 1077-3142. [14](#), [32](#), [33](#), [39](#), [69](#), [185](#)
- C. Shang, D. Barnes, and Q. Shen. Effective feature selection for Mars McMurdo terrain image classification. In *Intelligent Systems Design and Applications, 2009. ISDA '09. Ninth International Conference on*, pages 1419–1424, 2009. [32](#)
- C. Shang, D. Barnes, and Q. Shen. Facilitating efficient Mars terrain image classification with fuzzy-rough feature selection. *International Journal of Hybrid Intelligent Systems*, 2011. [32](#)

- A. Shaukat, C. Spiteri, Y. Gao, S. Al-Milli, and A. Bajpai. Quasi-thematic feature detection and tracking for future rover long-distance autonomous navigation. In *Proc. ESA Conference on Advanced Space Technologies in Robotics and Automation (ASTRA)*, 2013. [31](#)
- A. Shaw, M. Woods, E. Honary, P. Rendell, D. Pullan, D. Barnes, S. Pugh, and D. Long. CREST robotic scientist. In *Towards Autonomous Robotic Systems (TAROS)*, 2007. [23](#)
- J. Shi and C. Tomasi. Good features to track. In *Computer Vision and Pattern Recognition, 1994. Proceedings CVPR '94., 1994 IEEE Computer Society Conference on*, pages 593–600, June 1994. [100](#)
- S.M. Smith and J.M. Brady. SUSAN - a new approach to low level image processing. *International Journal of Computer Vision*, 23:45–78, 1995. [100](#)
- Y.H. Song. Automated rock segmentation for Mars exploration rover imagery. In *39th Lunar and Planetary Science Conference*, page 2043–2051, 2008. [14](#), [31](#), [32](#)
- Y.H. Song and J. Shan. A framework for automated rock segmentation of the Mars exploration rover imagery. In *Proceedings of ASPRS Annual Conference*, 2006. [31](#)
- S.W. Squyres, R.E. Arvidson, E.T. Baumgartner, J.F. Bell, P.R. Christensen, S. Gorevan, K.E. Herkenhoff, G. Klingelhöfer, M.B. Madsen, R.V. Morris, R. Rieder, and R.A. Romero. Athena Mars rover science investigation. *Journal of Geophysical Research: Planets*, 108(E12), 2003. [5](#)
- H. Tamura, S. Mori, and T. Yamawaki. Textural features corresponding to visual perception. *Systems, Man and Cybernetics, IEEE Transactions on*, 8(6):460–473, June 1978. [104](#)
- D.R. Thompson and R. Castano. Performance comparison of rock detection algorithms for autonomous planetary geology. In *Proc. of Aerospace Conference, 2007 IEEE*, pages 1–9, march 2007. [14](#), [20](#)
- D.R. Thompson, S. Niekum, T. Smith, and D. Wettergreen. Automatic detection and classification of geological features of interest. In *In IEEE Aerospace Conference Proceedings*, March 2005a. [31](#), [32](#)
- D.R. Thompson, T. Smith, and D. Wettergreen. Data mining during rover traverse: From images to geologic signatures. In *8th International Symposium on Artificial Intelligence, Robotics and Automation in Space*, September 2005b. [14](#), [31](#), [32](#), [81](#)

- D.R. Thompson, T. Smith, and D. Wettergreen. Autonomous detection of novel biologic and geologic features in Atacama desert rover imagery. In *Proc. of the Lunar and Planetary Science Conference*, March 2006. 14
- R. Tibshirani. Regression shrinkage and selection via the Lasso. *Journal of the Royal Statistical Society (Series B)*, 58:267–288, 1996. 118
- J. Vago. Science management plan. Review Report EXM-MS-PL-ESA-00002, February 2010. 7
- J. Vago, B. Gardini, G. Kminek, P. Baglioni, G. Gianfiglio, A. Santovincenzo, S. Bayón, and M. van Winnendael. ExoMars - searching for life on the red planet. *ESA Bulletin*, 126:16–23, May 2006. 23
- M. Van Winnendael, P. Baglioni, and J. Vago. Development of the ESA ExoMars rover. In *Proceedings of 8th International Symposium on Artificial Intelligence, Robotics and Automation in Space*, 2005. 23
- R. Volpe, I. Nesnas, T. Estlin, D. Mutz, R. Petras, and H. Das. The CLARAty architecture for robotic autonomy. In *Aerospace Conference, 2001, IEEE Proceedings.*, volume 1, 2001. 15
- M.D. Wagner, D. Apostolopoulos, K. Shillcutt, B. Shamah, R. Simmons, and W. Whittaker. The science autonomy system of the nomad robot. In *Robotics and Automation, 2001. Proceedings 2001 ICRA. IEEE International Conference on*, volume 2, pages 1742–1749, 2001. 31
- L. Wang. Automatic identification of rocks in thin sections using texture analysis. *Mathematical Geology*, 27(7), October 1995. 31
- D.W. Way, R.W. Powell, A. Chen, A.D. Steltzner, A.M. San Martin, P.D. Burkhart, and G.F. Mendek. Mars Science Laboratory: Entry, descent, and landing system performance. In *Aerospace Conference, 2007 IEEE*, pages 1–19, March 2007. 14
- G. Webster. NASA’s Mars curiosity debuts autonomous navigation, 2015. URL <http://www.jpl.nasa.gov/news/news.php?release=2013-259>. Last accessed Jan. 2015. 14
- G. Webster, N.N Jones, and D. Brown. NASA rover finds active and ancient organic chemistry on Mars, 2015. URL <http://www.jpl.nasa.gov/news/news.php?feature=4413>. Last accessed Jan. 2015. 4

- D. Wettergreen, N. Cabrol, V. Baskaran, F. Calderon, S. Heys, D. Jonak, R.A. Luders, D. Pane, T. Smith, J. Teza, P. Tompkins, D. Villa, C. Williams, and M.D. Wagner. Second experiments in the robotic investigation of life in the Atacama desert of Chile. In *8th International Symposium on Artificial Intelligence, Robotics and Automation in Space*, September 2005. [14](#)
- M. Woods, L. Baldwin, G. Wilson, S. Hall, A. Pidgeon, D. Long, M. Fox, R. Aylett, and R. Vituli. MMOPS: Assessing the impact of on-board autonomy for planetary exploration missions. In *Proceedings of SpaceOps 2006 Conference*, 2006. [23](#)
- M. Woods, A. Shaw, E. Honary, D. Barnes, D. Long, and D. Pullan. CREST autonomous robotic scientist: Developing a closed-loop science capability for European Mars missions. In *9th International Symposium on Artificial Intelligence, Robotics and Automation in Space (i-SAIRAS)*, 2008a. [23](#), [24](#), [25](#), [81](#)
- M. Woods, A. Shaw, P. Rendell, D. Barnes, S. Pugh, D. Price, D. Pullan, and D. Long. Developing an autonomous science capability for European Mars missions. In *10th ESA Workshop on Advance Space Technologies for Robotics and Automation*, 2008b. [23](#)
- M. Woods, A. Shaw, D. Barnes, D. Price, D. Long, and D. Pullan. Autonomous science for an ExoMars rover-like mission. *Journal of field robotics*, 26(4):358–390, 2009. [26](#), [70](#), [81](#), [85](#), [105](#)
- G. Xu and Z. Zhang. *Epipolar Geometry in Stereo, Motion and Object Recognition*. Springer, 1996. [144](#)
- K. Zacny, J. Wilson, P. Chu, and J. Craft. Prototype rotary percussive drill for the Mars sample return mission. In *Aerospace Conference, 2011 IEEE*, pages 1–8, march 2011. [187](#)
- L.A. Zadeh. Fuzzy sets. *Information and control*, 8(3):338–353, 1965. [27](#)